
A multi-wavelength study of the interstellar medium in active galactic nuclei at cosmic noon

Chiara Circosta



München 2019

A multi-wavelength study of the interstellar medium in active galactic nuclei at cosmic noon

Chiara Circosta

Dissertation
an der Fakultät für Physik
der Ludwig-Maximilians-Universität
München

vorgelegt von
Chiara Circosta
aus Reggio Calabria, Italien

München, den 13 Juni, 2019

Erstgutachter: Prof. Dr. Andreas Burkert
Zweitgutachter: Prof. Dr. Eiichiro Komatsu
Tag der mündlichen Prüfung: 25 Juli, 2019

TRAVELS

By Pat Metheny
and Lyle Mays

A MELODY
BALLAD ♩ = 02 (EVEN EIGHTHS)

Dsus4 **8** Gmaj7 Gadd2/B
 C C/D Gmaj7 B7 Em Dm
 Cadd2 Em C/D G Dsus4
B
 G F/G G C D Bbmaj7 C
 Fmaj7 G C Bb/C C Fmaj7 G7
 Ebmaj7 F7sus4 F7 Bbmaj7 C Dsus4 D

C Gmaj7 Gmaj7/B Cmaj7 Cmaj7/D
 Gmaj7 B7 Em7 Dm9 Cmaj7
 Em C/D To CODA **C** Gadd2 AFTER SOLOS: D.S. AL CODA **C** C/D
CODA
 Gmaj7 G D/F# Em C/D Gmaj7 B7 Em C/D Gmaj7 G D/F#
 Em C/D Gmaj7 B7 Em C/D Gmaj7 G D/F#
 Em7 C/D Gmaj7

This thesis has been carried out at the European Southern Observatory under the supervision of Dr. Vincenzo Mainieri, Dr. Paolo Padovani and Dr. Christopher M. Harrison.

Contents

| | |
|---|-------------|
| Zusammenfassung | xv |
| Abstract | xvii |
| 1 Introduction | 1 |
| 1.1 Brief history of AGN and galaxy research | 2 |
| 1.2 The structure of an AGN | 3 |
| 1.3 The AGN family and the unified model | 7 |
| 1.4 AGN spectral properties | 8 |
| 1.5 Evolution of AGN and their hosts | 13 |
| 1.5.1 The population of normal galaxies and the comparison with AGN . | 13 |
| 1.5.2 The relevance of the gas reservoir | 15 |
| 1.6 The obscuration of AGN and its connection with the host galaxy | 17 |
| 1.7 AGN feedback | 20 |
| 1.8 Thesis outline | 22 |
| 2 X-ray emission of $z > 2.5$ AGN can be obscured by their host galaxies | 25 |
| 2.1 Introduction | 25 |
| 2.2 Dataset and sample selection | 27 |
| 2.3 X-ray spectral analysis | 28 |
| 2.3.1 Spectral extractions | 28 |
| 2.3.2 Spectral models | 30 |
| 2.4 SED fitting | 32 |
| 2.4.1 Data modeling | 32 |
| 2.5 Results | 33 |
| 2.5.1 X-ray spectral analysis | 33 |
| 2.5.2 SED decomposition | 36 |
| 2.5.3 Gas content of the host galaxies | 40 |
| 2.6 Discussion | 41 |
| 2.6.1 Size of the host galaxies | 41 |
| 2.6.2 ISM column density | 42 |
| 2.6.3 Possible progenitors of the cQGs | 46 |
| 2.7 Conclusions | 47 |

| | | |
|----------|---|------------|
| 3 | SUPER I. Toward an unbiased study of ionized outflows in $z \sim 2$ AGN | 49 |
| 3.1 | Introduction | 49 |
| 3.2 | The survey | 52 |
| 3.2.1 | Sample selection | 54 |
| 3.2.2 | X-ray properties of the sample | 59 |
| 3.3 | Target sample characterization | 60 |
| 3.3.1 | Multi-wavelength dataset | 60 |
| 3.3.2 | Data modeling | 66 |
| 3.4 | Overall properties of the target sample | 70 |
| 3.4.1 | SED-fitting results | 70 |
| 3.4.2 | X-ray vs. optical spectroscopic and SED-fitting classification | 79 |
| 3.4.3 | Radio regime | 81 |
| 3.5 | Summary and future work | 84 |
| 4 | The molecular gas content of active galactic nuclei at $z \sim 2$ | 87 |
| 4.1 | Introduction | 87 |
| 4.2 | The sample | 90 |
| 4.2.1 | Target selection | 90 |
| 4.2.2 | Comparison sample of star-forming galaxies | 90 |
| 4.3 | Multi-wavelength properties of the sample | 92 |
| 4.4 | ALMA data: observations and analysis | 94 |
| 4.5 | Results and discussion | 98 |
| 4.6 | Conclusions | 103 |
| 5 | Conclusions and Future prospects | 105 |
| 5.1 | Summary of this thesis | 105 |
| 5.2 | Future work | 107 |
| 5.2.1 | Unveiling the causes behind low molecular gas contents in AGN | 107 |
| 5.2.2 | Moving to different sizes: study of the impact of AGN on large scale | 108 |
| 5.2.3 | Investigating the correlation between AGN activity and SFR | 110 |
| 5.3 | Final remarks | 112 |
| A | Notes on the targets of Chapter 2 | 113 |
| B | Multi-wavelength properties of the targets | 115 |
| C | Spectral energy distributions | 121 |
| D | Flux maps and spectra of the ALMA observations | 131 |

List of Figures

| | | |
|------|--|-----|
| 1.1 | Schematic representation of the AGN structure and its main components | 4 |
| 1.2 | Schematic representation of the main AGN classes | 8 |
| 1.3 | Optical spectra of type-1 and type-2 AGN from SDSS | 9 |
| 1.4 | Schematic representation of an AGN SED | 10 |
| 1.5 | Main components of the X-ray spectra of unobscured AGN | 11 |
| 1.6 | SMBH masses plotted against the stellar velocity dispersion of the bulge of the host galaxies | 14 |
| 1.7 | SFR density compared to the SMBH accretion rate | 15 |
| 1.8 | The star-forming main sequence shown by stellar mass and SFR | 16 |
| 1.9 | A schematic diagram to illustrate the relationships between fuel supply, galaxy growth and black hole growth | 17 |
| 1.10 | AGN X-ray spectrum with different levels of obscuration | 18 |
| 1.11 | Ratio of stellar mass to halo mass as a function of halo mass | 21 |
| | | |
| 2.1 | 7 Ms <i>Chandra</i> spectra of the targets | 34 |
| 2.2 | Spectral decomposition of the rest-frame SEDs of the target sample | 38 |
| 2.3 | ISM column density vs X-ray column density for the target sample | 43 |
| | | |
| 3.1 | Summary of IFS observations from the literature characterizing ionized outflows in AGN host galaxies | 53 |
| 3.2 | Two examples of rest-frame SEDs | 71 |
| 3.3 | Bolometric corrections in the hard 2 – 10 keV band versus bolometric luminosities. | 74 |
| 3.4 | Eddington ratios versus BH masses | 76 |
| 3.5 | Distribution of host galaxy properties in the SFR- M_* plane | 78 |
| 3.6 | AGN bolometric luminosities versus column densities of the whole target sample | 80 |
| 3.7 | Radio properties of the target sample | 82 |
| | | |
| 4.1 | Distribution of host galaxy properties in the SFR- M_* plane | 93 |
| 4.2 | L'_{CO} as a function of L_{FIR} for our AGN sample and normal galaxies | 99 |
| 4.3 | L'_{CO} versus stellar masses for our sample of AGN and normal galaxies | 101 |
| | | |
| 5.1 | SINFONI maps of an ionized outflow from SUPER | 108 |

| | | |
|-----|---|-----|
| 5.2 | Median CO SLEDs | 109 |
| 5.3 | VIMOS spectrum of one background quasars | 110 |
| 5.4 | Comparisons of ALMA and <i>HST</i> observations for inactive galaxies | 111 |
| C.1 | Rest-frame SEDs of the AGN | 122 |
| D.1 | CO velocity-integrated maps and spectra | 132 |

List of Tables

| | | |
|-----|---|-----|
| 2.1 | AGN sample summary | 29 |
| 2.2 | Summary of source parameters from the 7 Ms CDF-S data | 30 |
| 2.3 | Best-fit parameters of the X-ray spectral analysis | 35 |
| 2.4 | Best-fit parameters of the SED decomposition | 39 |
| 2.5 | Half-light radii and column densities derived from both the SED-fitting and the X-ray analyses | 45 |
| 2.6 | Surface densities of SFR, gas and stars together with gas depletion timescales of the target sample | 47 |
| 3.1 | Summary of the target AGN sample | 58 |
| 3.2 | Summary of the photometric data used for the SED-fitting modeling | 65 |
| 3.3 | Input parameter values used in the SED-fitting procedure | 69 |
| 4.1 | Summary of the target AGN sample | 91 |
| 4.2 | Summary of ALMA observations and analysis | 97 |
| B.1 | Summary of AGN host galaxies properties | 116 |
| B.2 | Summary of AGN properties | 119 |

Zusammenfassung

Eine der bemerkenswertesten Entdeckungen der letzten zwei Jahrzehnte ist, dass alle massereichen Galaxien ein supermassereiches schwarzes Loch (SMBH) in ihrem Zentrum haben, das eine aktive Wachstumsphase erlebt hat, bekannt als aktiver Galaxienkern (AGN). Obwohl Galaxienentwicklungsmodelle AGN Feedback benötigen, um die beobachteten Eigenschaften von Galaxien zu reproduzieren, müssen direkte Hinweise auf die Mechanismen durch die sich SMBH und Galaxien gemeinsam entwickeln noch gefunden werden. Der Spitzenzeitraum der Galaxienentstehung und des SMBH-Wachstums, der sogenannte “kosmische Mittag” ($1 < z < 3$), repräsentiert eine Schlüsselepoche, um zu verstehen, wie sich die Verbindung zwischen AGN und ihren Wirtsgalaxien etabliert wurde.

In dieser Arbeit präsentiere ich beobachtungsbasierte Untersuchungen des interstellaren Mediums (ISM) von Röntgen-ausgewählter AGN im kosmischen Mittag. Der Gasgehalt ist streng mit der Evolution von AGN und dessen Wirtsgalaxie verbunden. Tatsächlich treibt das Gas sowohl die Entstehung von neuen Sternen in der Galaxie als auch das Wachstum des zentralen SMBHs an. Das Gas in der Wirtsgalaxie entlang unserer Sichtlinie könnte auch eine ausschlaggebende Rolle in der Verdunklung der zentralen Kernquelle haben. Letztendlich könnten die Bewegungen im Gas und dessen Zusammensetzung durch die Energie, die vom zentralen AGN freigegeben wird, das sogenannte AGN Feedback, beeinflusst werden. Um eine umfassende Untersuchung des ISM zu erreichen, übernehme ich eine Herangehensweise in multiplen Wellenlängen und nutze eine Großzahl von Daten, vom Röntgen zum Radiobereich, indem Techniken wie das Fitten von spektralen Energieverteilungen (SED) in mehreren Bändern, Röntgenspektralanalyse und sub-mm Spektroskopie benutzt werden.

Zuerst untersuche ich, ob die Verdunklung, die in den Röntgenspektren von AGN beobachtet werden, vom ISM der Wirtsgalaxie verursacht werden kann. Für eine Stichprobe von Ferninfrarot-ausgewählter AGN mit $z > 2.5$ finde ich, dass die Gesamtpaltendichte von Wasserstoff entlang der Sichtlinie, gemessen im Röntgenbereich, vergleichbar ist mit der Spaltendichte, die mit dem ISM der Wirtsgalaxie assoziiert wird, gemessen über SED Fits und Abschätzungen von Galaxiegrößen. Das ISM der Wirtsgalaxie scheint daher im Stande zu sein, eine signifikante Absorption auf kpc Skalen zu verursachen. Eine solche Absorption ergänzt (oder sogar ersetzt) diejenige, die auf pc Skalen durch das kernumgebende Material verursacht wird, wodurch die Dichotomie von verdunkelter/unverdunkelter AGN as Effekt von Inklination allein in Frage gestellt wird.

Eine systematische Studie einer Anzahl von blind gewählter AGN mit $z \sim 2$, die einen

breiten Bereich von Leuchtkräften abdecken, ist entscheidend um die Bedeutung von AGN Feedback auf die Galaxienentwicklung angemessen einzugrenzen. Für solch eine repräsentative Auswahl führe ich zwei sich ergänzende Untersuchungen durch, welche die ionisierte und molekulare Phase des ISM erforschen. Die erste, genannt SUPER, spürt ionisierte Ausflüsse über die [OIII] Linie mit hochauflösenden, räumlich-aufgelösten Integralfeldspektroskopischen Beobachtungen (SINFONI) auf. In dieser Arbeit lege ich die Grundlagen für die Studie, indem ich eine Multi-Wellenlängen Charakterisierung der Eigenschaften von AGN und deren Wirtsgalaxien durchführe und zeige, dass der Vergleich von Erkenntnissen von verschiedenen Techniken/Beobachtungen entscheidend ist, um Ergebnisse von SED Fits und Spektroskopie zu bestätigen und zusätzliches Vertrauen in die Methoden zu erlangen. Die Multi-Wellenlängen Eigenschaften werden dann mit den Eigenschaften der Ausflüsse verbunden, die mit SINFONI ausgespiert wurden. Die zweite Untersuchung nutzt ein Set von ALMA Beobachtungen des CO($J=3-2$) Übergangs, um CO-Eigenschaften von AGN mit denen einer Kontrollstichprobe von inaktiven Galaxien, die gleiche Rotverschiebungen, stellare Massen und Sternentstehungsraten haben, zu vergleichen. Ich zeige, dass die AGN Gruppe leuchtschwach in CO scheint im Vergleich zur Kontrollstichprobe und dass der Unterschied ist signifikant bei hohen Massen, $\log(M_*/M_\odot) > 11$. Diese Beobachtungen demonstrieren, dass die AGN einen möglichen Einfluss auf das ISM der Wirtsgalaxie haben, auch wenn die genauen Mechanismen weitere Beobachtungen benötigen, um verstanden zu werden.

Diese Projekte bilden den Rahmen für zukünftige Untersuchungen, die unser Verständnis der Rolle von AGN in der Galaxienentwicklung wesentlich verbessern werden.

Abstract

One of the most remarkable discoveries of the last two decades is that all massive galaxies host a supermassive black hole (SMBH) at their center, which has gone through an active phase of growth known as active galactic nucleus (AGN). Although galaxy evolution models need AGN feedback to reproduce the observed properties of galaxies, direct observational evidence for the mechanisms through which SMBHs and galaxies co-evolve has still to be proven. The peak epoch of galaxy assembly and SMBH growth, the so-called “cosmic noon” ($1 < z < 3$), represents a key laboratory to understand how the connection between AGN and their host galaxies was established.

In this thesis, I presented observational studies of the interstellar medium (ISM) of X-ray selected AGN at cosmic noon. The gas content is directly linked to the evolution of the AGN and its host galaxy. Indeed, it feeds both the formation of new stars in the galaxy and the growth of the central SMBH. The gas in the host along our line of sight may also have a pivotal role in obscuring the central nuclear source. Finally, the kinematics and composition of the gas could be affected by the energy released by the central AGN, through the so-called AGN feedback. To achieve a comprehensive study of the ISM, I adopted a multi-wavelength approach and exploited a variety of data, from the X-ray to the radio regime, by using techniques such as broad-band spectral energy distribution (SED) fitting, X-ray spectral analysis and submm spectroscopy.

I first investigated whether the obscuration observed in the X-ray spectra of AGN can be produced by the ISM of the host galaxy. For a sample of far-IR detected AGN at $z > 2.5$ I found that the total hydrogen column density along the line of sight, measured in the X-ray band, is comparable to the column density associated with the ISM of the host, derived through SED-fitting analysis and assuming galaxy sizes. Therefore, the ISM of the host appears to be capable of providing significant absorption on kpc scales. Such absorption adds to (or even replaces) that produced on pc scales by any circumnuclear material, challenging the view of the obscured/unobscured AGN dichotomy as due to inclination effects only.

Then, I conducted two complementary studies to probe the ionized and molecular phases of the ISM in a blindly-selected sample of AGN at $z \sim 2$ that covers a wide range in luminosities. Such studies are necessary to properly constrain the impact of AGN feedback on galaxy evolution. The first, called SUPER, traces ionized outflows through the [OIII] line by using high-resolution spatially-resolved integral field spectroscopic observations (SINFONI). In this work I laid the foundations of the survey, by performing a multi-wavelength

characterization of AGN and host galaxy properties, and showed how comparing insights from different techniques/observations is crucial to confirm and provide extra confidence in SED-fitting as well as spectroscopic results. These multi-wavelength properties will then be connected with those of the outflows as traced by SINFONI. The second study used a set of ALMA observations of the CO($J=3-2$) transition, to carry out a comparison of the CO properties of AGN with those of a control sample of inactive galaxies matched in redshift, stellar mass and star-formation rate. I found that the AGN sample appears to be underluminous in CO with respect to the control sample and the difference is especially significant at high masses, $\log(M_*/M_\odot) > 11$. These observations demonstrated that the AGN may have an effect on the ISM of the hosts, although the exact mechanisms in place require further observations to be understood.

These projects set the scene for future investigations, which will significantly improve our understanding of the role of AGN in galaxy evolution.

Chapter 1

Introduction

Supermassive black holes (SMBHs) are among the most fascinating objects in the Universe. They are incredibly compact with masses $M_{\text{BH}} > 10^6 M_{\odot}$, making them extreme cases of curved space-time described by general relativity. Over the last two decades, one of the most remarkable astronomical discoveries is that all massive galaxies in the local Universe host a SMBH at their center, which has gone through an active phase of growth known as active galactic nucleus (AGN). AGN have always captured my interest, since they can produce incredible amounts of energy concentrated in a very small region but still they can be so powerful that they are among the most distant sources yet observed.

Apart from being intriguing objects to study in their own right, during the last decades AGN have become crucial for galaxy evolution research. This is mainly due to observational results showing a tight connection between SMBHs and galaxy properties, despite a difference of several orders of magnitude in physical size scales. Moreover, they are key ingredients in galaxy evolution models, which need AGN to reproduce the observed properties of galaxies.

Although AGN are expected to play a pivotal role in shaping the evolution of their host galaxies, researchers are still seeking observational evidence for the mechanisms through which SMBHs and galaxies co-evolve. To address this issue, studying the ISM properties of AGN host galaxies in every gas phase is fundamental. Indeed, the reservoir of gas is the candidate linking host galaxy and SMBH growth, since it fuels both star formation and AGN activity. Crucially for this work, the gas is an important component that may contribute to the obscuration of the AGN emission along our line of sight, and through which AGN feedback is thought to regulate star formation. In this framework, some open questions of outstanding relevance are: how can AGN activity, a small-scale process, influence the star-formation activity across the galaxy? And is the gas forming stars on large scale able to produce obscuration to the observed AGN emission, usually ascribed to small-scale material?

In this thesis, I addressed these open questions of galaxy and AGN evolution by adopting a multi-wavelength approach. I exploited a variety of data, from X-rays to the radio regime, in order to retrieve the physical properties of galaxies and AGN at the so-called cosmic noon (i.e., the peak of SMBH growth and star-formation activity, $1 < z < 3$),

needed to understand how their growth is linked. In addition to the detailed panchromatic approach, a key focus of my work is the careful selection of representative samples of targets, spanning a wider range of physical parameters than previous work. This introductory Chapter provides the background and motivation to the research presented in this thesis.

1.1 Brief history of AGN and galaxy research

During the last century, astronomy saw the birth and development of the extragalactic branch. Extragalactic sources started to be noticed in 1780s as “nebulous objects” (Messier, 1781; Herschel, 1786), whose origin was highly debated (e.g., Smith, 2008). Herschel reckoned that some of them may be star systems external to our Galaxy, but it was in 1860s that Huggins used spectroscopy to examine some of these nebulae revealing the presence of stars (e.g., Huggins & Miller, 1864), which were found to have velocities larger than any star in the Milky Way. Later, Hubble used the luminosity-period relationship of Cepheid variable stars to eventually confirm the true extragalactic nature of these nebulae (Hubble, 1925). Since these discoveries, huge progress has been made in building instruments to observe the variety of galaxies we know today and understanding their properties. Nowadays we can count on very deep surveys to collect large samples of galaxies and understand their evolution, such as the Hubble Ultra Deep Field - a view of nearly 10 000 galaxies obtained with the Hubble Space Telescope (*HST*), and the current record for the furthest galaxy known is $z = 11.1$ (Oesch et al., 2016). One of the most recent estimates for the number of galaxies in the Universe, thanks to the observations performed by *HST*, is around 2 trillion (Conselice et al., 2016).

AGN started to be discovered later than galaxies. Fath (1909) obtained an optical spectrum of the nebula NGC 1068 at the Lick Observatory, that showed strong emission lines (recognizable as those seen in the spectra of gaseous nebulae), although its appearance on the image was similar to a star. Some years later, Curtis (1918) reported the following notes for the nebula NGC 4486, also photographed at the Lick Observatory: “Exceedingly bright; nearly round; no spiral structure is discernible. A curious straight ray lies in a gap in the nebulosity [...], apparently connected with the nucleus by a thin line of matter” (which was later identified with the optical jet in the elliptical galaxy M87; Baade & Minkowski 1954). Although such examples of uncommon activity in the nuclei of galaxies were reported in the literature, the official discovery of AGN dates back to the work of Seyfert (1943), who studied six spiral galaxies with unusually bright and starlike nuclei. Seyfert galaxies did not receive further attention until two of them were identified as radio sources by Baade & Minkowski (1954). Indeed, this was the period when the first radio surveys were performed, and the positions of some radio sources were found to be coincident with star-like optical objects (based on this association the name “quasi-stellar radio sources” or quasars was introduced), whose spectra showed strong and broad emission lines at unidentified wavelengths. Schmidt (1963) identified the emission lines seen in the spectra of these sources to be at very high redshift ($z = 0.158$, among the largest ever measured at the time), implying an enormous luminosity. Since Seyfert galaxies found

locally were radio quiet (i.e., no detected radio emission) and showed optical luminosities lower than quasars, it took some time for a link with quasars to be widely accepted. The problem to be faced with such objects was how to generate an extraordinary amount of energy in a tiny volume, since the nuclei were unresolved (e.g., Matthews & Sandage, 1963). The source associated with these physical extremes was debated for a long time and eventually ascribed to mass accretion onto a SMBH (e.g., Salpeter, 1964; Lynden-Bell, 1969). Since then, SMBHs have not stopped fascinating researchers and have been subject of intense study in every frequency band, from radio to gamma rays. The idea of the presence of a SMBH at the core of AGN, lurking in the center of galaxies when they are not active, was originally just a working hypothesis. In order to prove it, observations at very high resolution have been pursued until some flagship results have been recently reached. One example is the most detailed observation of material orbiting close to the massive object at the center of the Milky Way, which confirms the identity of Sagittarius A*, the SMBH at the heart of our Galaxy (Gravity Collaboration et al., 2018). Another recent result is the first radio-wave image of a SMBH candidate, at the scales of the innermost emitting region around it, in the center of the giant elliptical galaxy M87, providing powerful support for SMBHs as the central engines of AGN (Event Horizon Telescope Collaboration et al., 2019).

1.2 The structure of an AGN

In this Section, we briefly outline the main components of the AGN structure as given by the currently most accepted model. The physical structure of an AGN and the corresponding formation mechanisms are, at present, not perfectly known and still matter of debate. Since different components are concentrated in very small volumes, direct investigations are extremely difficult due to observational limitations that prevent the study of their innermost region (\lesssim parsec). Nevertheless, some information on the sizes of the central regions can be obtained through variability studies or, for the region immediately surrounding the SMBH, direct imaging with interferometric techniques, as recently obtained with the Event Horizon Telescope (Event Horizon Telescope Collaboration et al., 2019). Understanding the different components of an AGN is key to discern the mechanisms building up their observed emission (see Sect. 1.4).

A schematic representation of the AGN structure is shown in Fig. 1.1 along with the corresponding approximate sizes.

SMBH: the central engine of the AGN. According to the current theory, a black hole (BH) can be completely described by only three properties: mass, charge and angular momentum. The mass of a SMBH, M_{BH} , ranges between $\sim 10^6$ and $\sim 10^{10} M_{\odot}$. The most basic characteristic that defines a BH is the presence of an event horizon, that is a boundary from which matter and even light can never re-emerge. It is described by the gravitational radius, defined as $r_g = GM_{\text{BH}}/c^2$, where G and c are the gravitational constant and the speed of light, respectively. Charge is usually assumed to be zero, which corresponds to neutral black holes. The angular

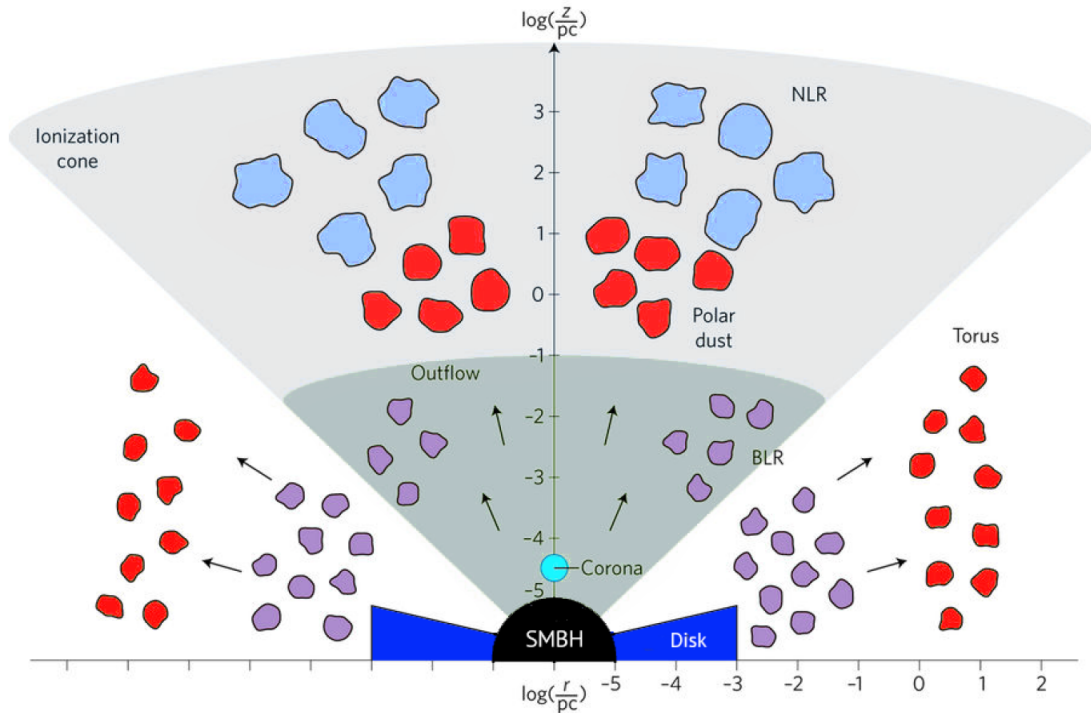


Figure 1.1: Schematic representation of the AGN structure and its main components, illustrating the physical scales of the key regions mentioned in the text (from Ramos Almeida & Ricci, 2017). Accretion disk, corona, BLR, and dusty torus reside within the gravitational influence of the SMBH. The NLR is on a larger scale and under the gravitational influence of the host galaxy.

momentum J is described by the adimensional parameter per unit mass, called spin $a = Jc/GM_{\text{BH}}^2$. This quantity can assume all values between $+1$ and -1 : it is positive if the direction of BH rotation is the same of that of the accreted inflowing material, it is negative otherwise. The radius of the event horizon, in units of r_g , is given by $r_{\pm} = 1 \pm (1 - a^2)^{1/2}$. If $a = 0$ the BH is called “static”, with an event horizon described by the Schwarzschild radius $R_s = 2GM_{\text{BH}}/c^2$. Instead, if $a = 1$, the BH is maximally rotating and is described by the Kerr metric.

The process at work in an active nucleus is the conversion of gravitational potential energy into electromagnetic radiation. In particular, energy is generated by gravitational infall of material which is heated to high temperatures in a dissipative accretion disk. The accretion luminosity, that is the radiative bolometric output of the AGN, is given by $L_{\text{acc}} = \eta \dot{M} c^2$ where η is the mass-to-luminosity conversion efficiency (usually assumed to be 0.1 but it depends on the spin of the BH, with an expected range of 0.05–0.42) and \dot{M} is the mass accretion rate. A theoretical upper limit on the accretion luminosity is given by the Eddington luminosity, calculated assuming spherical accretion of fully ionized hydrogen onto the central object. The

Eddington luminosity is the maximum average luminosity a system can attain, when the outward radiation pressure equals the inward gravitational force. Above the Eddington limit, radiation pressure overcomes gravity and the gas is pushed away. It is described by the equation:

$$L_{\text{Edd}} = \eta \dot{M}_{\text{Edd}} c^2 = \frac{4\pi c G M_{\text{BH}} \mu m_{\text{p}}}{\sigma_{\text{T}}} \simeq 1.5 \times 10^{38} \left(\frac{M_{\text{BH}}}{M_{\odot}} \right) \text{ erg s}^{-1} \quad (1.1)$$

where \dot{M}_{Edd} is the Eddington accretion rate, μ is the mean molecular weight, m_{p} is the proton mass and σ_{T} is the Thomson cross section for an electron.

The ratio of the accretion luminosity to the Eddington luminosity is called Eddington ratio $\lambda_{\text{Edd}} = L_{\text{acc}}/L_{\text{Edd}}$. This is a useful quantity for defining how powerful an AGN is with respect to the Eddington luminosity (and therefore the SMBH mass). Sources with high values of λ_{Edd} (i.e., $\lambda_{\text{Edd}} \gtrsim 0.1$) are referred to as “high-accretion” rate AGN.

Accretion disk: a disk of material which emits thermally because of viscosity. The energy lost during accretion can be converted into electromagnetic radiation with high efficiency (6%–40%), and thus large luminosities can be produced for a modest amount of accretion, making AGN the most powerful non-explosive objects in the Universe. AGN disks can be optically thick or thin, depending on the column density, the level of ionization of the gas and the mass accretion rate (e.g., Netzer, 2013). A commonly assumed model of accreting disks is the optically thick, geometrically thin accretion disk (Shakura & Sunyaev, 1973). The gas within the disk has a wide range of temperatures (with the temperature being an inverse function of the distance from the SMBH) and, consequently, the emission is produced over a broad wavelength range. The overall emission can be explained as the sum of different temperature blackbody spectra and the total spectrum takes the shape of a power law with a spectral index equal to 1/3. In particular, for a disk surrounding a $10^8 M_{\odot}$ black hole accreting at the Eddington rate, the maximum temperature is roughly $T \sim 10^5$ K and most of the emission is in the range 30–300 nm, that is the UV-optical part of the spectrum.

Hot corona: a hot, rarefied gas ($T \sim 10^{8-9}$ K), located above the disk (Haardt & Maraschi, 1993, see Fig. 1.1). It has been proposed as a mechanism to explain the energetic X-ray emission of AGN. The soft thermal photons produced by the disk are upscattered to their observed X-ray energy by the hot electrons in the corona. The simplest model involves an optically thin corona with a small scale height, whose temperature is determined by the fraction of the total accretion power deposited into the corona itself. Even a small fraction can result in temperatures of $\sim 10^8$ K (Netzer, 2013). The heating mechanism and the exact geometry are, at present, open issues.

Broad Line Region (BLR): made of gaseous clouds under the direct gravitational influence of the SMBH (see Fig. 1.1), the BLR is extended up to 0.1–1 pc (Peterson et al.,

2004). The gas reprocesses the energy produced by the continuum source at ionizing ultraviolet energies through emission lines from recombination or de-excitation of photoionized atoms. The BLR electron densities are sufficiently high ($>10^8 \text{ cm}^{-3}$; Osterbrock & Ferland 2006) that essentially all forbidden lines are collisionally suppressed. The gas temperature is about 10^4 K . The central engine dominates the bulk motion of this region, therefore the permitted emission lines from the BLR are broad, characterized by typical Full Width at Half Maximum (FWHM) $\Delta v_{\text{FWHM}} \sim 10^3 - 10^4 \text{ km s}^{-1}$. The broadening of such emission lines is used to estimate the masses of SMBHs (Vestergaard & Peterson, 2006). The BLR is dust-free, being within the dust sublimation radius.

Narrow Line Region (NLR): extended for hundreds of parsecs ($\sim 10^2 - 10^4 \text{ pc}$; Tadhunter et al., 1989; Greene et al., 2011), the NLR represents the largest spatial scale where the ionizing radiation escaping from the central source can excite the surrounding medium (see Fig. 1.1). The electron densities are low enough ($<10^6 \text{ cm}^{-3}$; Osterbrock & Ferland 2006) to allow the production of forbidden lines, which are not collisionally suppressed, through recombination processes. Permitted lines are also produced in the NLR. The electron temperatures are in the range $10\,000 - 25\,000 \text{ K}$. Typical FWHM of the narrow lines is in the range $250 \lesssim \Delta v_{\text{FWHM}} \lesssim 2\,000 \text{ km s}^{-1}$, therefore this gas has a narrower distribution of velocities than the BLR. The NLR arises outside the dust sublimation radius, hence significant amounts of dust are present as the radiation field is much weaker. The boundary between the BLR and NLR is likely delineated by the radius where dust sublimates. Moreover, this is the only AGN component that has been spatially resolved in the optical with current instrumentation, often revealing an axisymmetric morphology with two opposite ionization cones centered on the nuclear source (e.g., Evans et al., 1999).

Obscuring torus: an optically and geometrically thick structure composed of dust and gas between ~ 0.1 and 10 pc from the central SMBH. The dusty phase is made of carbonaceous and amorphous silicate grains, while the gas is composed of a broad range of gaseous states, from fully ionized gas to neutral and molecular gas. It is characterized by gas densities of about $10^4 - 10^7 \text{ cm}^{-3}$ and velocities of about $1\,000 \text{ km s}^{-1}$. Its inner radius is set by the dust sublimation radius within which the medium is ionized by the central source, while a natural scale for the outer edge of the torus is the gravitational sphere of influence of the SMBH ($\sim 10 \text{ pc}$ for nearby systems). The geometry of this dusty structure is expected to be toroidal, but is the subject of ongoing research and several studies confirm a clumpy distribution of the dust (e.g., Jaffe et al., 2004; Burtscher et al., 2013; Combes et al., 2019, see Fig. 1.1).

Jets: extended, collimated and relativistic linear structures, shown by $\sim 10\%$ of powerful AGN. Launched close to the accretion disk and aligned with the symmetry axis of the system, they mostly emit through synchrotron, from the radio band to γ -rays. The formation mechanism may be related to a fast rotating black hole and the magnetic field that can collimate the outflow of charged particles. This leads to jet structures

which transport energy and particles from the central compact source to the extended regions. Jets are affected by “Doppler beaming”, a relativistic effect that enhances the surface brightness of the jet that is approaching the observer. The most powerful jets propagate into the interstellar and intergalactic medium up to Mpc scales, much more extend than the stellar component (tens of kpc). The interaction between jets and the environment causes the formation of hot spots and large-scale radio lobes.

1.3 The AGN family and the unified model

AGN are divided in several classes based on their emission properties at different wavelengths. The full family of AGN is a zoo of names reflecting different detection criteria and spectral characteristics. We refer the reader to Padovani et al. (2017) for a complete description of AGN classes. The AGN unification scheme (Antonucci, 1993; Urry & Padovani, 1995), the favored picture for the physical structure of AGN, was introduced to explain the features of the principal AGN classes based on orientation, coupled with intrinsic differences in a small number of physical parameters (such as luminosity). Fig. 1.2 depicts a schematic representation of the main AGN classification based on the inclination angle of the source. This axisymmetric model explains a different appearance of AGN as due to the inclination of the object with respect to the observer’s line of sight. For example, the distinction between the so-called type-1 and type-2 AGN implies that the observer’s line of sight passes through the obscuring medium for type-2 AGN while it is free from obscuration for type-1s (see Fig. 1.2). These are the two main classes in which AGN can be divided and are identified by the characteristics of their optical and ultraviolet spectra, as shown in Fig. 1.3. Specifically, type-1 AGN are characterized by bright continua and broad emission lines, as the line of sight does not intercept the obscuring torus. Type-2 present weak continua and only narrow emission lines, because of obscuration along the line of sight (essentially almost all optical-UV radiation from the inner parsec is absorbed). Another feature that divides AGN into two big classes is the presence or absence of jets, which are then referred to as either “jetted” or “non-jetted” AGN, respectively (Padovani, 2017). These nomenclature supersedes the previous distinction in “radio loud” and “radio quiet”. Finally, blazars are jetted AGN for which the line of sight is close to the radio jet axis.

AGN are also separated according to their luminosity. Seyfert galaxies are AGN with lower luminosity, whereas quasars (QSOs) are more luminous members of the AGN family. The dividing line between Seyfert galaxies and quasars has never been defined properly. Historically, QSOs were defined as having magnitudes $M_v < -23$, since preliminary samples of Seyferts/QSOs were selected in the optical-UV. The boundary is usually at AGN bolometric luminosities $L_{\text{bol}} \sim 10^{45} \text{ erg s}^{-1}$. In terms of X-ray luminosity, this division corresponds to $L_X \sim 10^{44} \text{ erg s}^{-1}$ (Netzer, 2013). Typical X-ray luminosities of AGN are in the range $10^{42} < \log(L_X/\text{erg s}^{-1}) < 10^{46}$, where $10^{42} \text{ erg s}^{-1}$ in the 2–10 keV band is the luminosity that can be reached by combined emission of X-ray binaries in a galaxy, therefore discriminating between a star-forming galaxy and an AGN. The threshold at

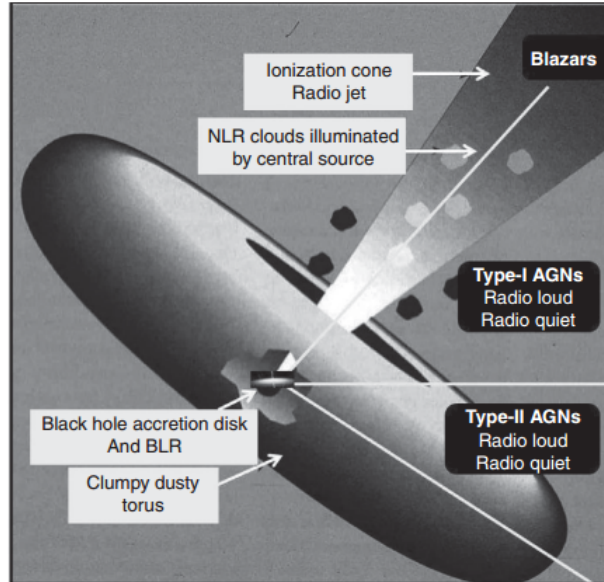


Figure 1.2: Schematic representation of the main AGN classes and AGN components, based on the inclination angle of the observer’s line of sight with respect to the torus axis (from Netzer, 2013). Type-1 and type-2 classes refer to the optical/UV properties of the AGN spectrum, while the division between radio-loud and radio-quiet AGN is based on the loudness of their radio emission (here we adopt the classification of Padovani 2017 in “jetted” and “non-jetted”). Blazars are viewed along the jet direction.

X-ray luminosities $\sim 10^{42}$ erg s $^{-1}$ was also adopted in this work to select AGN.

1.4 AGN spectral properties

AGN are characterized by detectable emission covering the whole electromagnetic spectrum, allowing them to be discovered through almost all spectral bands. The different physical components of the AGN structure, described in Section 1.2, contribute to build up the overall spectral energy distribution (SED) of AGN. A schematic representation of an AGN SED from radio frequencies to hard X-rays is shown in Fig. 1.4. It can be described, to a first-order approximation, as a power law $S_\nu \propto \nu^{-\alpha}$, whose spectral index α ranges generally from 0 to 1. The primary radiation from the central engine is the driving force for all other secondary processes, each one producing specific spectral features. The description of the different emission components discernible in AGN SEDs is particularly relevant for this work, in which I carried out detailed fitting of models to estimate key physical quantities of AGN and their host galaxies (see Chapters 2 and 3).

Across the whole electromagnetic spectrum, the following continuum properties can be distinguished (see, e.g., Elvis et al., 1994; Peterson, 2003; Risaliti & Elvis, 2004; Padovani et al., 2017):

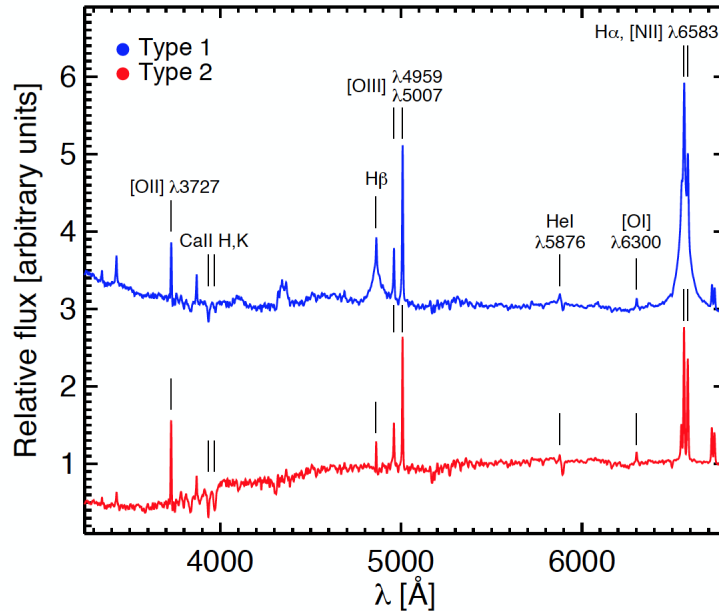


Figure 1.3: Optical spectra of type-1 (blue) and type-2 (red) AGN from the Sloan Digital Sky Survey (SDSS) (from Hickox & Alexander, 2018). Some emission features are marked in the spectra. Type-1 AGN show the presence of a bluer nuclear continuum and broad permitted emission lines (by definition).

- The radio emission is significantly different for jetted and non-jetted sources. In jetted AGN, a strong, non-thermal continuum extends from the radio to the far-infrared (FIR), while in non-jetted objects the SED decreases rapidly at low frequencies (the so-called “submillimeter break”), as shown in Fig. 1.4. The emission of jetted AGN is due to rapidly accelerated charged particles and magnetic fields producing a power-law continuum spectrum through synchrotron emission, which can extend to the X-rays or even the γ -rays. The radio emitting regions are the compact core, and the extended regions (i.e., jets, lobes and hot spots). However, the radio contribution to the bolometric luminosity is small. In non-jetted AGN, any detected radio emission can be due to supernovae and compact (non relativistic) radio jets.
- The submm/FIR, for the majority of AGN, is dominated by thermal emission from cooler dust heated by the star formation in the host galaxy, with a minimal contribution from the AGN itself. For the most radio-luminous quasars the non-thermal emission in this regime can be substantial.
- The infrared (IR) between a few μm up to about $70 \mu\text{m}$ is mainly produced by thermal emission of hot dust close to the central engine, with temperatures ranging between 50 and 1000 K. It has a spectral shape characterized by a bump at typical wavelengths of about $10\text{--}30 \mu\text{m}$ and a steep fall-off at longer wavelengths due to the decreasing emitting efficiency of dust grains (e.g., Pier & Krolik, 1992; Polletta

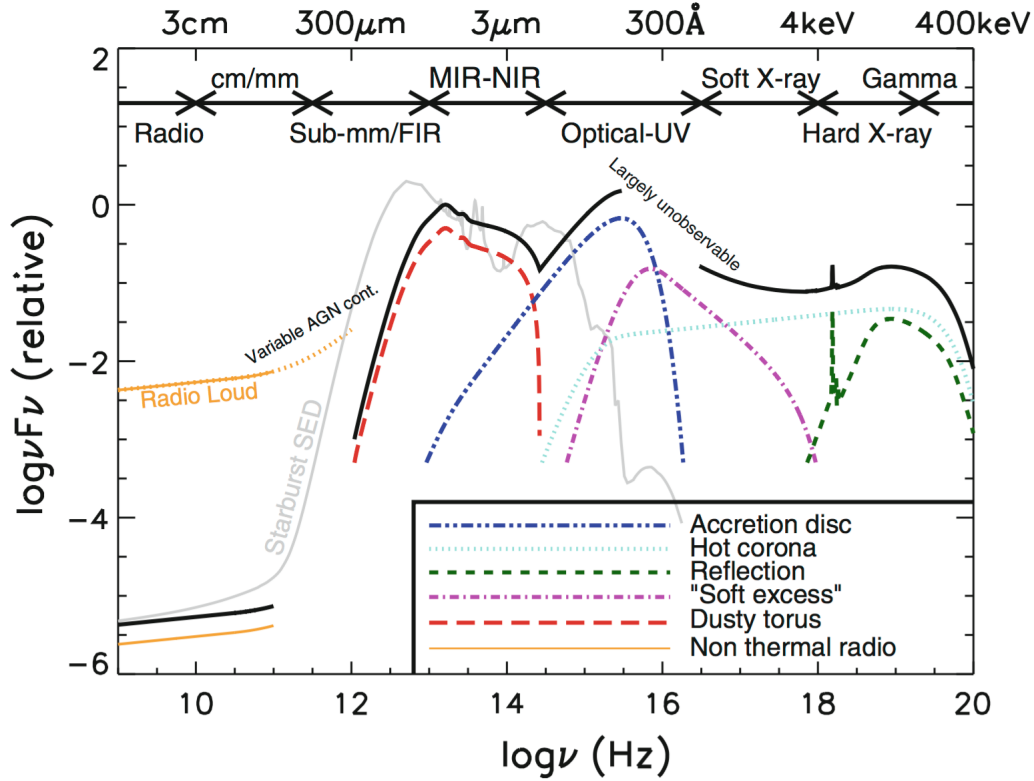


Figure 1.4: Schematic representation of an AGN SED, from Harrison (2014). The thick solid curve represents the total SED, mainly based on the observed SED of non-jetted quasars, and the other curves represent the individual components. The primary emission from the AGN accretion disk peaks in the UV region. The radio emission of jetted AGN (labelled as radio-loud in the plot) is also shown, and can be orders of magnitude higher than non-jetted AGN. An example radio-UV SED of a starburst galaxy is depicted in gray as a comparison.

et al., 2000). This wavelength range, for jetted AGN, can also be associated with non-thermal emission, produced by the same synchrotron emission that dominates in the radio regime. For type-2 AGN, whose disk emission is absorbed, stellar emission from the host also contributes to the near-infrared (NIR) regime. It therefore allows for an estimate of the mass of the galaxy.

- The peak in the optical-UV continuum is referred to as the “big blue bump”, ascribed to thermal emission from the accretion disk. It dominates the emission between $\sim 300 \text{ \AA}$ and $\sim 3000 \text{ \AA}$, and the spectrum can be well approximated by a power law (as normally implemented in models; e.g., Fritz et al. 2006). The majority of the bolometric luminosity of AGN is thought to be in the UV, which is a region of the electromagnetic spectrum not easily observable from Earth. An additional feature, the “small blue bump”, consists of blended Fe emission lines and Balmer continuum.

Moreover, several emission lines are present in quasar spectra at these wavelengths: broad lines (such as $\text{Ly}\alpha\lambda 1216$, $\text{CIV}\lambda 1549$, $\text{NV}\lambda\lambda 1239, 1243$, $\text{OVI}\lambda 1035$) emitted from the BLR, and narrow (forbidden) lines (such as $[\text{OIII}]\lambda 5007$, $[\text{NII}]\lambda 6583$, $[\text{OII}]\lambda 3727$) from the NLR. Observations in the optical regime are the most effective at gathering information about AGN classification and redshift.

- The X-ray domain (from ~ 0.1 keV up to ~ 300 keV) is one of the key energy ranges to study and select AGN (X-ray selection is indeed the method adopted in this work). This regime is also particularly suitable to estimate the obscuration affecting the AGN emission (see Section 1.6). X-ray emission accounts for $\sim 10\%$ of the AGN bolometric luminosity. In particular, for increasing bolometric luminosities the X-ray luminosity becomes less dominant (as given by the correlation between the bolometric correction $k_{\text{bol}} = L_{\text{bol}}/L_{\text{X}}$ and the bolometric luminosity; Marconi et al. 2004; Lusso et al. 2012).

Since I performed extensive X-ray analysis for the targets of this work, the different components that build up the overall emission are described in the following and shown in Fig. 1.5. This will be useful to understand the models and assumptions adopted later (see, especially, Chapter 2).

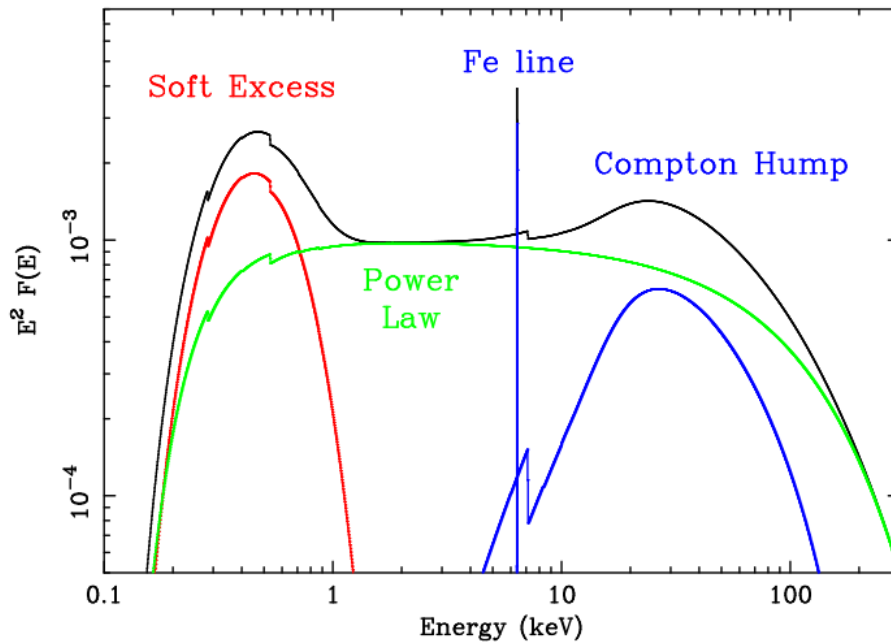


Figure 1.5: Main components of the X-ray spectra of unobscured AGN (from Fabian & Miniutti, 2005), namely soft emission from the accretion disk (red line), primary emission from thermal Comptonization of the soft X-rays from the hot corona (green line), reflected emission and Fe line due to reflection of hard X-rays from dense gas (blue line). The total emission is shown in black.

Primary emission: The intrinsic X-ray spectra of quasars take the form of a power-law component extending from about 1 keV to so-called hard energies of up to ~ 200 keV. It results from the superposition of many scattering orders between the incident black body emission from the disk and the corona. The high energy exponential cut-off at 100–300 keV corresponds to the temperature at which electrons and photons are thermalized (Lanzuisi et al., 2019). In addition to the main power-law continuum, there is also a soft emission component with characteristic temperature $kT \sim 0.2 - 1$ keV called “soft excess”, which is probably the exponential tail of the “blue bump” at high energy, produced by thermal emission from the accretion disk. Alternatively, this emission could be due to ionized reflection from the accretion disk (Fabian & Miniutti, 2005).

Reflection component: While about half of the primary photons can reach the observer, the remaining part is directed back to the accretion disk, giving rise to the reflection spectrum through Compton scattering and photoelectric absorption. Since these processes are energy dependent, the incident soft X-rays are mostly absorbed, while hard photons are Compton scattered off the disk. Indeed, the reflection continuum peaks at $\sim 20-30$ keV, with a broad hump-like shape named the “Compton hump”. The cut-off at 4–5 keV is due to photoelectric absorption of the lower energy incident radiation. Above a few tens of keV, the emission decreases because absorption dominates again. The reflected emission is typically a few percent of the primary in the 2–10 keV band (e.g., Comastri et al., 2010; Baloković et al., 2014; Ricci et al., 2017).

Iron line: The most important feature in the 2–10 keV band is a neutral iron emission line at a rest-frame energy of 6.4 keV. It arises from the material surrounding the SMBH and is produced by the same mechanism responsible for the reflection component. Photoelectric absorption of photons from the corona causes the ejection of one of the two electrons in the K-shell (i.e., $n = 1$) of the iron atom (or ion), which is followed by fluorescent line emission at 6.4 keV (34% probability), or the ejection of an Auger electron (66% probability). A threshold energy of 7.1 keV is required to have absorption by neutral iron¹. If we consider ionized iron, the lower number of electrons is less able to screen the K-electrons from the nuclear charge, therefore the energies of both the photoelectric threshold and $K\alpha$ line increase (6.7 keV for helium-like iron and 6.96 keV for hydrogen-like iron). This line is so prominent because iron, among all metals, has the best combination of fluorescent yield (i.e., the probability that a photoelectric absorption event is followed by fluorescent line emission rather than the Auger effect) and abundance (Fabian et al., 2000).

A measure of the intensity of the line with respect to the continuum emission is given by the equivalent width (EW), defined as:

¹Additionally, this produces a feature in the spectrum (see the blue line in Fig. 1.5), the so-called Compton edge, due to absorption of the majority of incident photons just above the photoelectric threshold.

$$EW = \int \frac{F_1(\lambda) - F_c(\lambda)}{F_c(\lambda)} d\lambda \quad (1.2)$$

where $F_1(\lambda)$ is the observed flux of the emission line at the wavelength λ and $F_c(\lambda)$ is the underlying continuum at the line energy. This quantity is a function of the geometry of the system, the element abundances, the inclination angle of the observer’s line of sight and the ionization state.

1.5 Evolution of AGN and their hosts

The pivotal role of AGN in galaxy evolution was first revealed through a series of ground-breaking observational results pointing to a direct connection between SMBH and galaxy growth, despite the very different physical size scales at which they occur (i.e., nine orders of magnitude).

The first key result is the discovery of a tight correlation between SMBH masses and the properties of their host galaxies, such as masses of the host galaxy bulge (Magorrian et al., 1998), as well as the velocity dispersions (Ferrarese & Merritt, 2000; Bennert et al., 2011), as shown in Fig. 1.6.

The second result is the similar evolution with redshift of the cosmic SMBH growth and star formation rate (SFR; Madau & Dickinson, 2014), both peaking at $z \sim 1 - 3$ and declining toward the local Universe, as shown in Fig. 1.7. Notably, the ratio between cosmic star formation and the black hole accretion rate at a given redshift is roughly 10^3 , which is the same factor as the $M_{\text{BH}}-M_{\text{bulge}}$ relation. Moreover, a coeval cosmic “downsizing” has been observed for both AGN and galaxies, meaning that more luminous AGN and more massive galaxies formed earlier than less luminous AGN and less massive galaxies (e.g., La Franca et al., 2005; Delvecchio et al., 2014).

These observational arguments suggest that SMBHs and their galaxies are causally connected, although these results only provide indirect evidence for such a connection without placing strong constraints on the form of the connection itself. Indeed, the physical processes driving the average trends described above are still far from clear. The scenario in which BH and galaxy evolution are coupled is referred to as “BH-galaxy co-evolution” (see Kormendy & Ho, 2013, for a review).

1.5.1 The population of normal galaxies and the comparison with AGN

A promising approach to understand these connections is to compare the AGN population with the corresponding “inactive” galaxy population. The dominant population of galaxies is represented by star-forming galaxies, where most of star formation in the Universe occurs, which sit on the “main sequence” (MS; Noeske et al., 2007; Whitaker et al., 2012; Speagle et al., 2014). The MS is a correlation between SFR and stellar mass and a useful tool to

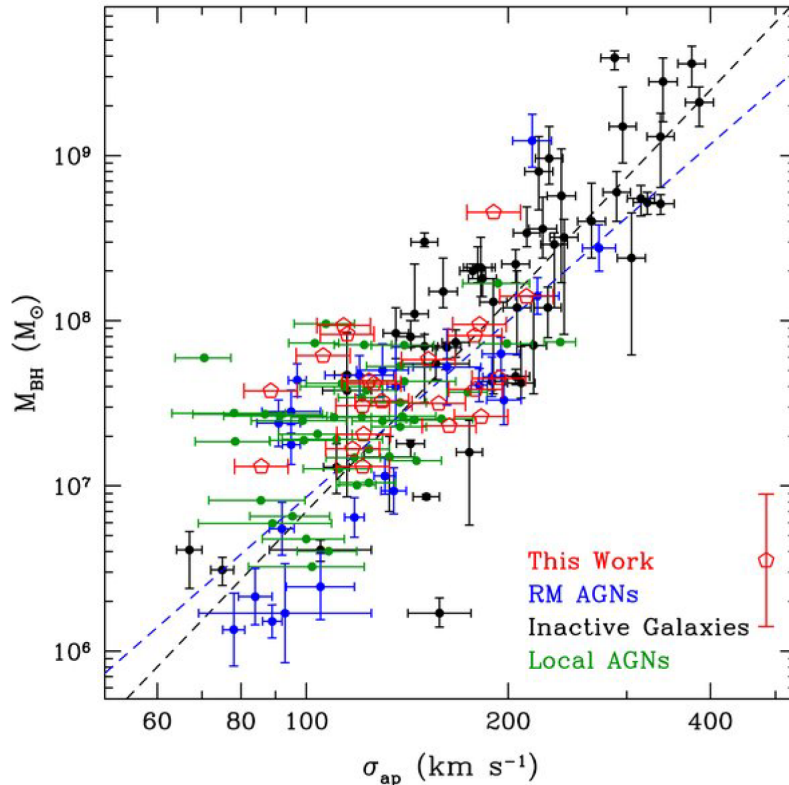


Figure 1.6: Collection of SMBH masses plotted against the stellar velocity dispersion of the bulge of the host galaxies, from Bennert et al. (2011).

classify galaxies. Fig. 1.8 shows an example of the MS and its evolution with redshift. The population of galaxies lying significantly (~ 4 times) above the MS is called starbursts and have higher SFRs compared to stellar mass matched MS galaxies (e.g., Rodighiero et al., 2011). Viceversa, the quenched population of galaxies is located below the MS. Several studies have measured SFRs and stellar masses for galaxies hosting growing black holes and the non-AGN population and searched for either correlations or differences. The *Herschel* Space Observatory has played a major role in providing an obscuration-independent view of star formation that is relatively uncontaminated by emission from the AGN. The typical result is that the average SFRs of AGNs trace that of star-forming galaxies (e.g., Harrison et al., 2012a; Santini et al., 2012; Rosario et al., 2013). However, these findings are based on mean-stacked results, which can be biased toward higher values by a few bright outliers. More recent results comparing the distribution of SFRs with respect to the main sequence for X-ray selected AGN and normal galaxies, based on individual detections, are presented by Mullaney et al. (2015). They find that the distribution of SFRs is broader than that of normal galaxies and peaks slightly below the main sequence (see also Scholtz et al., 2018).

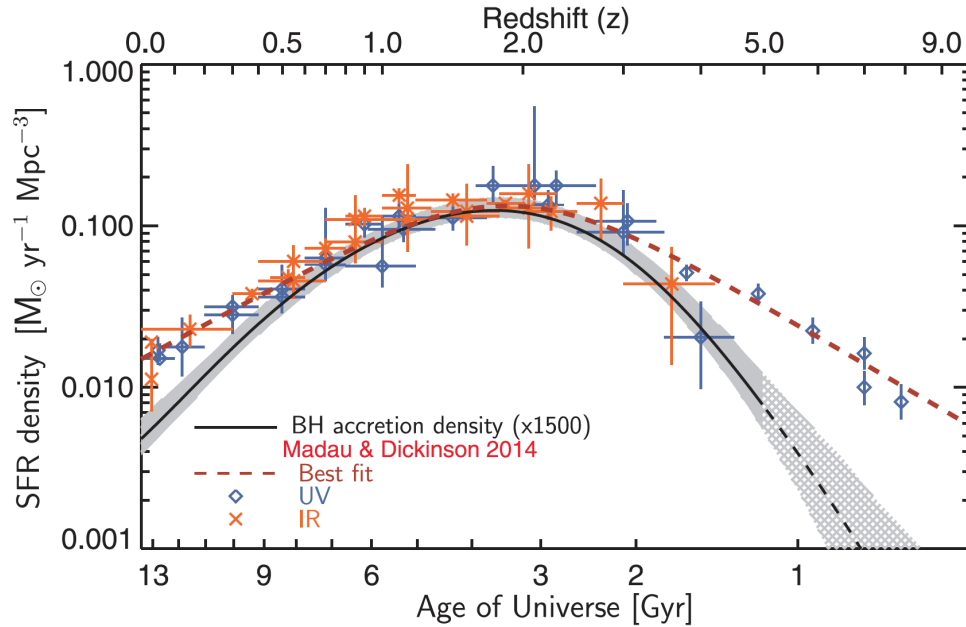


Figure 1.7: SFR density compared to the SMBH accretion rate, from Aird et al. (2015). The former is shown by the dashed red line, as well as the blue and orange points (see Madau & Dickinson, 2014), while the latter is depicted by the solid black line and is scaled up by an arbitrary factor of 1 500. Shaded regions indicate the 99% confidence interval. Both galaxy and SMBH growth peak at $z \sim 2$.

1.5.2 The relevance of the gas reservoir

The fundamental ingredient for SMBH-galaxy co-evolution, fueling both star formation and AGN activity, is the cold gas residing in the galaxy (Madau & Dickinson, 2014; Vito et al., 2014). In particular, recent results constraining the cosmic evolution of the molecular gas density find that it closely matches the evolution of the cosmic star formation rate density (Decarli et al., 2019), and therefore of the SMBH accretion rate. This similarity supports the relevance of the gas reservoir of galaxies as the key candidate linking star formation and SMBH growth. Therefore, obtaining information on the gas content of AGN host galaxies, for different galaxy properties (e.g., stellar mass) and redshift is of paramount relevance (see Chapter 4). The gaseous fuel, star-formation and AGN activity are all connected by a complex interplay that shapes the evolution of galaxies across cosmic time, which is depicted in Fig. 1.9. The supply of material for the formation of new stars and SMBH accretion originates from a gas reservoir inside the galaxy halo (potentially hot gas). It can be fed by phenomena such as accretion of gas from intergalactic medium, gas-rich mergers or recycled fuel from internal galactic processes. Out of this reservoir (red clouds in Fig. 1.9), the gas that is able to cool will fuel star formation (i.e., galaxy growth) and AGN activity (i.e., the growth of the SMBH), shown by the green arrows in Fig. 1.9. These two processes are also responsible for reducing the availability of cold gas (red arrows in

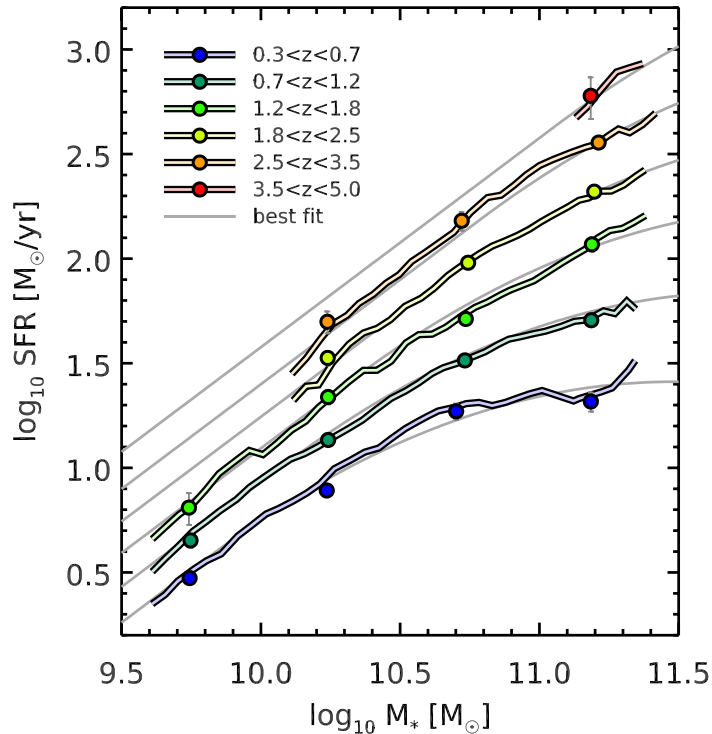


Figure 1.8: The star-forming main sequence shown by stellar mass and SFR and its evolution with redshift, from Schreiber et al. (2015).

Fig. 1.9), by injecting energy and momentum into the galaxy through radiation, winds and jets and are therefore able to ionize, heat, shock or expel material. They represent feedback mechanisms which are thought to be able to self-regulate the growth of the galaxy. A particularly important role is attributed to the AGN and its impact on star formation in the galaxy.

An interesting laboratory to study the interplay between star formation and AGN activity is the high-redshift regime during the peak epoch of galaxy assembly and SMBH growth (which is the focus of this thesis). An evolutionary picture commonly adopted to explain the formation of passive galaxies predicts that, once the gas starts to be accreted onto the galaxy through the mechanisms described above, it activates the AGN and also triggers high rates of star formation in the host galaxy (Sanders et al., 1988; Alexander et al., 2005). During the growth phase, the large reservoirs of gas and dust produce heavy obscuration to much of SMBH growth (e.g., Iwasawa et al., 2011). Subsequently, the energy produced during the rapid phase of AGN accretion and intense star formation clear the galaxy of gas in a short-lasting ($\sim 10^7$ yr) “blow-out phase” and the galaxy eventually evolves into a passive system (e.g., Hopkins et al., 2006; Lapi et al., 2014). Of this evolutionary picture, the most relevant phases for this thesis are: the obscuration of AGN, to test whether the star-forming gas in the galaxy is able to obscure the AGN emission (Chapter 2); the feedback phenomena (Chapters 3 and 4), thought to be the

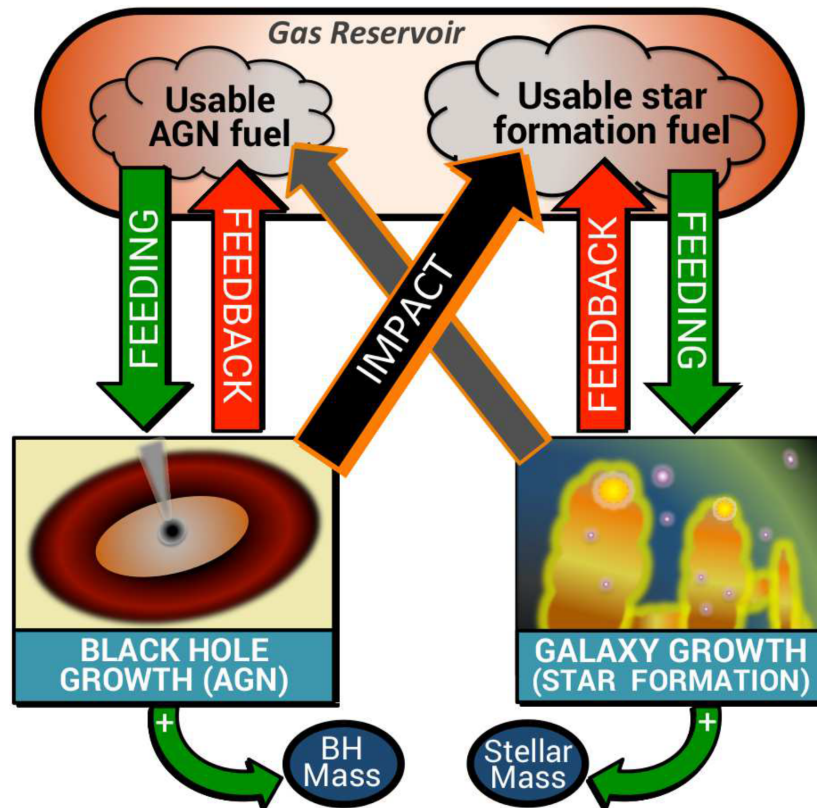


Figure 1.9: A schematic diagram to illustrate the relationships between fuel supply, galaxy growth and black hole growth, from Harrison (2017). See text for details.

key actors which established a long-lasting link between SMBHs and their hosts. Further details are provided in the next Sections.

1.6 The obscuration of AGN and its connection with the host galaxy

The characteristic emission of AGN can be affected by the presence of gas and dust between the accretion disk and the observer. Such material produces obscuration, meaning that it absorbs and/or scatters away from the observer's line of sight a fraction of the emission, modifying the spectral shape as follows. In the optical-UV regime the continuum is heavily attenuated by dust and thermally re-radiated at infrared wavelengths, while narrow emission lines dominate the spectrum. In the X-ray band, obscuration is produced by gas (usually measured with the neutral hydrogen equivalent column density N_{H}) and depends on the rest-frame energy of the photons. As shown in Fig. 1.10, the incidence of absorption at $1 < E < 10$ keV becomes more and more important and the spectrum is absorbed toward higher energies as N_{H} increases. In particular, low-energy photons (be-

low ~ 10 keV) suffer from photoelectric absorption while high-energy photons are mainly affected by Compton scattering² and subsequent absorption. The direct X-ray emission with energies >10 keV can penetrate the absorber emerging as transmitted emission when $N_{\text{H}} \lesssim 10^{25} \text{ cm}^{-2}$. Viceversa, if $N_{\text{H}} \gtrsim 10^{25} \text{ cm}^{-2}$, no direct emission can survive and the only detectable emission is the reflected one (e.g., Risaliti & Elvis, 2004). A prominent spectral feature, which is an unambiguous signature of obscuration, is the iron $\text{K}\alpha$ line, whose EW increases as a function of the column density, since it is measured against an absorbed continuum. For $N_{\text{H}} < 10^{23} \text{ cm}^{-2}$, a typical EW of about 100 eV is observed, while for higher column densities it reaches values of a few keV. Being produced by a cold reflector far from the central SMBH, this line is usually narrow ($\sigma = 0.1 - 0.01$ keV). In addition, a soft component in excess of the absorbed power law is also observed at low energies, whose origin is not well known and may involve different processes: scattering of the primary power law by hot gas, a fraction of the primary emission escaping the obscuring medium, and/or the sum of unresolved emission lines from photoionized gas. It is usually a few percent of the primary emission (e.g., Gilli et al., 2007).

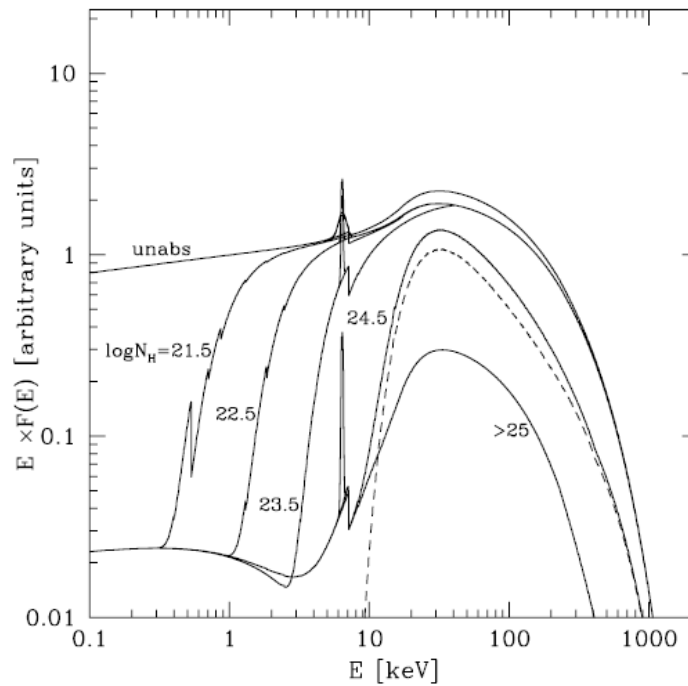


Figure 1.10: AGN X-ray spectrum with different levels of obscuration, from Gilli et al. (2007). From top to bottom, solid lines refer to increasing values of the column density N_{H} . The emission feature is the Fe $\text{K}\alpha$ line at 6.4 keV. The dashed line represents the transmitted emission in objects with $\log(N_{\text{H}}/\text{cm}^{-2}) = 24.5$, which dominates above 10 keV.

²The cross sections for Compton scattering and photoelectric absorption are approximately the same for energies of ~ 10 keV, hence above this threshold Compton scattering is the dominant process.

X-ray spectroscopy provides one of the most reliable methods of indentifying obscured AGN and measuring the amount of absorption. Consequently, AGN are often classified according to the amount of X-ray absorption affecting their spectra. Compton-thin AGN are characterized by $N_{\text{H}} < 1 \times 10^{24} \text{ cm}^{-2}$, while AGN with $N_{\text{H}} \geq 1 \times 10^{24} \text{ cm}^{-2}$ are called Compton-thick³. Moreover, AGN with $N_{\text{H}} > 3 \times 10^{23} \text{ cm}^{-2}$ are identified as heavily obscured (e.g., Lanzuisi et al., 2015). The presence of a strong reflection component at $E > 10 \text{ keV}$ and a prominent Fe $K\alpha$ line at 6.4 keV (with EW typically $>1 \text{ keV}$) are clear signatures of Compton-thick absorption.

AGN obscuration is usually modeled as being produced by a single-scale absorber (i.e., the torus) but it is increasingly clear that it could be due to material distributed over a range of scales and characterized by different physical conditions (e.g., circumnuclear gas associated with central starbursts and galaxy-scale material associated with galaxy disks and mergers; see Hickox & Alexander 2018). Spatially resolved *Chandra* observations of local AGN have found evidence for Fe $K\alpha$ lines produced up to $\sim\text{kpc}$ away from the nucleus (Fabbiano et al., 2017). These emission features, previously attributed to a compact absorber, may therefore originate from material with very different geometries, and obscuration can be produced by gas on the scales of the entire galaxy ($>\text{kpc}$).

The period of obscured AGN activity has a pivotal role in galaxy evolution, as it represents the key phase for building up the mass of the SMBH (peaking at high redshift). However, interpreting AGN obscuration is quite complex, especially at high redshift, when the gas content of galaxies is higher and therefore an evolutionary link of this phenomenon with the host galaxy may come into play. This possibility is supported by some observational evidence, but a direct proof is still missing. The fraction of obscured AGN is found to increase at high redshift (e.g., Maiolino & Rieke, 1995; Gilli et al., 2001; Ueda et al., 2014; Vito et al., 2014, 2018). This result is thought to be related to a larger available gas supply and higher SFRs in galaxies at earlier cosmic times (e.g., Carilli & Walter, 2013; Bothwell et al., 2013). For a galaxy with a high enough gas mass, even large-scale ($\sim\text{kpc}$) obscuring clouds could be heavily absorbing. The same galaxy-scale dust and gas that obscure the AGN may also be expected to produce enhanced star formation. Therefore, studies comparing the star-forming properties of obscured and unobscured AGN should be able to confirm a potential link between AGN obscuration and star formation. Some works focusing on luminous quasars show that obscured sources exhibit stronger emission from cold dust (this conclusion holds for obscuration measured in X-rays and IR-optical SEDs). In particular, the fraction of quasars that are obscured increases strongly with FIR luminosity, consistent with a picture in which obscuration in luminous AGN is frequently associated with galaxy-scale dust (Chen et al., 2015b). However, less luminous sources do not present comparable differences in average FIR emission (Merloni et al., 2014). Providing further support for the connection between AGN obscuration and host galaxies is the correlation between the hydrogen column density and the stellar mass of the host galaxy (Buchner & Bauer, 2017; Lanzuisi et al., 2017). These are crucial points for this work, since

³ $N_{\text{H}} \sim 1.5 \times 10^{24} \text{ cm}^{-2}$ corresponds to optical depths ~ 1 for Compton scattering, meaning that the column density is equal to the inverse of the Thomson cross section σ_{T} .

they open up the possibility of a connection between AGN obscuration and the properties of host galaxies.

Obscuration of AGN due to material distributed on parsec and galaxy-wide scales has profound implications on our understanding of AGN structure and evolution, making the high-redshift obscured AGN population a particularly interesting target to study the bulk of SMBH accretion. Specifically, in this work I investigated the possibility that AGN obscuration is produced by the host galaxy (see Chapter 2).

1.7 AGN feedback

AGN feedback has been invoked by simulations and semi-analytical models as a popular mechanism to reproduce the observed properties of galaxies. One of the most remarkable examples is the different shapes of the dark matter halo mass function and the galaxy stellar mass function when feedback is taken into account, as shown in Fig. 1.11. The latter, unlike the predictions of models without feedback, shows a break at the low and high mass ends (Somerville et al., 2008; Behroozi et al., 2013; Harrison, 2017). This has been ascribed to feedback from supernovae and AGN, respectively, which prevents the galaxy from converting the baryons into stars. Other examples are the color bimodality of galaxies (Strateva et al., 2001), the decrease of the cosmic star formation density at $z < 1$ (see Fig. 1.7; Madau & Dickinson, 2014; Aird et al., 2015), and the rates of gas cooling in galaxy clusters (Fabian, 2012).

AGN can release an incredible amount of energy during their growth phases. For example, the energy produced to build a SMBH with mass $M_{\text{BH}} = 10^8 M_{\odot}$ is $E_{\text{BH}} \sim 10^{61}$ erg, assuming $E = 0.1 M_{\text{BH}} c^2$. Such energy is a few orders of magnitude (2–3) higher than the binding energy of the bulge of the galaxy, which can be derived assuming that the black hole is close to the $M_{\text{BH}}-M_{\text{bulge}}$ relation (i.e., $E \sim 10^{58}$ erg), and is likely to be comparable to, or higher than, the thermal energy of the gas in the dark matter halo in which the galaxy resides. Only the coupling of a small fraction (i.e., $\sim 0.1-1\%$) of the accretion energy to the gas is sufficient to have an impact on the evolution of the host galaxy and regulate black hole growth as well as star formation. This represents a feedback mechanism which can prevent further accretion of cold gas by injecting material and/or energy into the interstellar medium (ISM).

A possible (and commonly accepted) form of feedback are outflows driven by strong AGN radiation or jets. AGN-driven outflows gained huge attention in the field of galaxy evolution during the last 20 years (see Harrison et al., 2018, for a review), after the publication of some key papers (Silk & Rees, 1998; Benson et al., 2003; Di Matteo et al., 2005), presenting models where a few percent of the AGN luminosity is able to drive galaxy-wide outflows and establish the observed correlation between SMBH and galaxy properties. Since then, AGN became a fundamental component of semi-analytical models and hydrodynamical simulations and a huge amount of work attempts to connect AGN-driven outflows with galaxy evolution.

Although outflows and feedback are a fundamental aspect of galaxy evolution, several

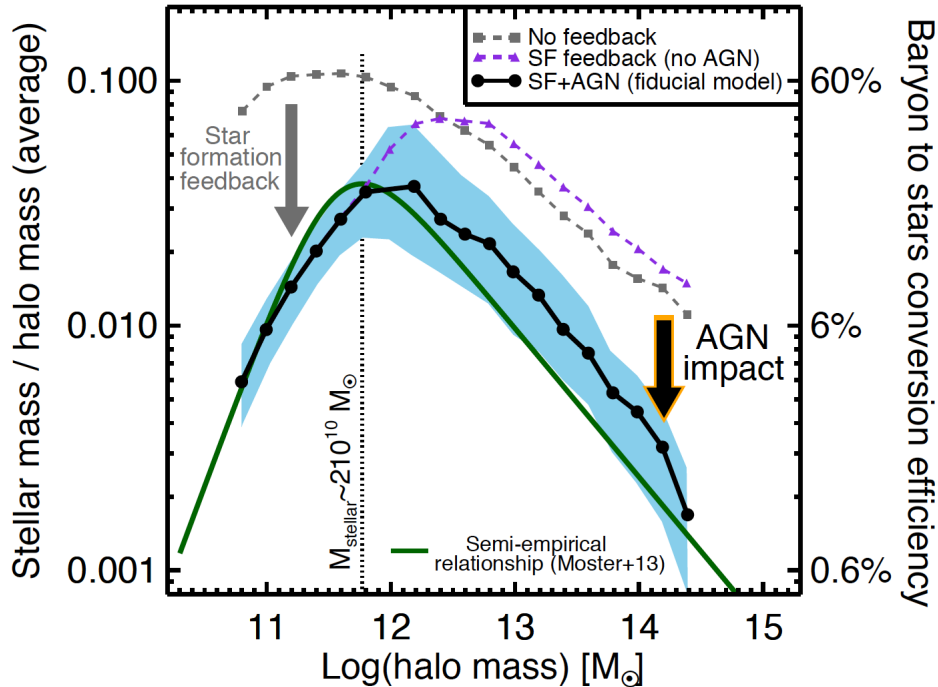


Figure 1.11: The ratio of stellar mass to halo mass as a function of halo mass for three different runs of a simulation and for a semi-empirical relationship, from Harrison (2017). The shaded region depicts the fiducial model that includes energy injection from AGN and star formation. The right y-axis represents the efficiency of turning baryons into stars. Star formation and AGN feedback reduce the efficiency of converting baryons into stars in low and high mass haloes, respectively.

observational challenges have to be faced. For example, key open topics are the launching mechanisms of outflows (Wylezalek & Morganti, 2018; Jarvis et al., 2019) and their eventual fate (i.e., whether they are able to escape the galaxy or are accreted back; Fluetsch et al. 2019). Outflows are multi-phase, therefore observations of the different gas phases (e.g., ionized, neutral, molecular) are needed to have a comprehensive view of their effects (Cicone et al., 2018). Additionally, in order to test AGN feedback models, observed outflow properties have to be derived which can be affected by heavy uncertainties and rely on assumptions (Harrison et al., 2018).

A key cosmic epoch to explore feedback effects is the cosmic noon ($1 < z < 3$), when the SMBH activity is at its peak. Observations of AGN in this redshift range have usually studied unusual objects (e.g., very bright or with known outflows), and therefore are not representative of the overall AGN population. To understand how common outflows are and their role in affecting star formation we need observations for AGN over a wide range of properties, especially bolometric luminosity. In this work I started addressing this observational limitation by introducing SUPER (a SINFONI Survey for Unveiling the Physics and Effect of Radiative feedback), an ESO’s VLT/SINFONI Large Programme

which performs the first systematic investigation of ionized outflows, and the star formation activity in the hosts, in a sizeable and blindly-selected sample of X-ray AGN (Chapter 3). Another necessary approach to probe feedback effects is to trace the cool gas of AGN hosts, out of which stars form. These studies, in a systematic fashion, are now possible thanks to the Atacama Large Millimeter Array (ALMA), the largest radio interferometer in the world. In this thesis, I presented a systematic investigation probing the molecular gas content of AGN and comparing the results with normal star-forming galaxies (Chapter 4).

1.8 Thesis outline

In this thesis I presented observational studies of the ISM of X-ray selected AGN at cosmic noon. In particular, I addressed outstanding open issues of galaxy evolution, namely the possibility that AGN obscuration is produced by the host galaxy and the impact of AGN activity on the ISM of the galaxy. A multi-wavelength approach to derive physical properties of galaxies and AGN has been adopted. Indeed, the detailed characterization of their properties is paramount in order to understand the link between SMBHs and their hosts. I exploited data from the X-ray to the radio regime and used techniques such as broad-band SED fitting, X-ray spectral analysis and submm interferometry. An outline of this thesis is as follows.

- **Chapter 2:** Here I tested the possibility that AGN obscuration observed in the X-rays can be produced by the gas distributed on the scales of the host galaxy ($> \text{kpc}$). A multi-wavelength study of seven $z > 2.5$ AGN in the *Chandra* Deep Field-South (CDF-S), selected to have good FIR detections, is performed using the highest-quality data currently available for a deep field. I estimated the total hydrogen column density as derived from X-ray spectra and compared it to the column density associated with the ISM of the host. The similarity between these quantities suggests that, at least at high redshift, the ISM in the host galaxy may have a significant role in absorbing AGN emission. This work has been published as Circosta et al. (2019).
- **Chapter 3:** In this Chapter I introduced the SUPER survey, its characteristics and goals, as well as the selection of the targets. SUPER aims to perform the first systematic investigation of ionized outflows in a sizeable and blindly-selected sample of 39 X-ray AGN at $z \sim 2$. The key focus of this work is the uniform and systematic characterization of the multi-wavelength properties of the sample. These parameters are fundamental in order to place the targets in the context of galaxy evolution and to connect the properties of outflows with those of AGN and host galaxies. Such analysis laid the foundations for the survey. This work has been published as Circosta et al. (2018).
- **Chapter 4:** The first systematic and uniform analysis of the molecular gas content of AGN at $z \sim 2$ is presented in this Chapter. The main goal is to infer whether AGN activity affects the ISM of the host galaxy. As a tracer, I used the $\text{CO}(J=3-2)$

emission line. The AGN sample, made of 25 targets, benefits from the same multi-wavelength characterization presented in Chapter 3. The CO emission properties of the AGN sample are compared with those of star-forming galaxies, matched in redshift, stellar mass and SFR. Additionally, the comparison sample only consists of targets observed in the same CO($J=3-2$) transition, to avoid the uncertainties connected with a priori assumptions on excitation factors. AGN result to be under-luminous in CO and this could be ascribed to the effects of AGN activity.

- **Chapter 5:** an overall summary of the work presented in the thesis along with the current and future prospects are outlined in this Chapter.

Chapter 2

X-ray emission of $z > 2.5$ active galactic nuclei can be obscured by their host galaxies

Published as C. Circosta, C. Vignali, R. Gilli, A. Feltre, F. Vito, F. Calura, V. Mainieri, M. Massardi, C. Norman; A&A, 623A, 172C (2019)

2.1 Introduction

The emission observed in active galactic nuclei (AGN) is thought to be produced by gas accretion onto a supermassive black hole (SMBH). Tracing the accretion history of AGN at different cosmic epochs is crucial to understand the way SMBHs have formed and evolved. A key phase of this accretion history occurs at $z = 1 - 3$, when the peak of AGN activity is observed (e.g., Aird et al., 2010; Delvecchio et al., 2014). The amount of gas required to sustain the build-up of the SMBH population in place at high redshift may contribute to the obscuration of the AGN emission itself. Several studies have confirmed that the majority of AGN is obscured by column densities $N_{\text{H}} > 10^{22} \text{ cm}^{-2}$ (e.g., Ueda et al., 2014; Buchner et al., 2015), and mounting evidence does support a positive evolution of the obscured AGN fraction with redshift (e.g., Vito et al., 2014, 2018; Aird et al., 2015).

The gas content of galaxies is also observed to have been higher in the past (Carilli & Walter, 2013). This gas fuels star formation activity in galaxies, and the evolution of the star formation rate (SFR) density in the Universe matches that observed for the BH accretion rate (Madau & Dickinson, 2014). The same gas that produces stars is therefore a potential contributor to the obscuration of the AGN. This connection intimately links the history of SMBH accretion to that of the star formation activity of their host galaxies.

Several scaling relations between the BH mass and the large-scale properties of the host galaxy have been found, such as stellar mass (Magorrian et al., 1998) or velocity dispersion (Ferrarese & Merritt, 2000). The tightness of these relations suggests a direct link between

the origin of galaxies and SMBHs, leading to the concept of BH-galaxy coevolution (see Kormendy & Ho, 2013, for a review). This evolutionary scenario matches the BH accretion phase with strong star formation episodes. Hence, studying the bulk of SMBH accretion also means seeking sites where intense star formation is taking place. The most powerful star-forming sources at high redshift are submillimeter galaxies (SMGs), which commonly are detected at a median redshift $z \sim 2 - 3$ (e.g., Simpson et al., 2014). They are defined as submm sources with flux densities $\gtrsim 1$ mJy at $850 \mu\text{m}$, corresponding to typical $L_{\text{IR}} \sim 10^{12} L_{\odot}$ and estimated SFRs $\sim 100 - 1000 M_{\odot} \text{ yr}^{-1}$ (Blain et al., 2002). SMGs present large reservoirs of cold gas, $\gtrsim 10^{10} M_{\odot}$ (e.g., Coppin et al., 2010; Bothwell et al., 2013; Wang et al., 2013a). A significant fraction ($\sim 20\%$; Wang et al., 2013b) of SMGs has been found to host X-ray detected AGN, most of which are obscured with $N_{\text{H}} > 10^{23} \text{ cm}^{-2}$.

The SMG phase is thought to be part of a broader evolutionary scenario, where a major merger event between gas-rich galaxies (e.g., Hopkins et al., 2006) or an early phase of fast collapse characterizing massive halos (e.g., Lapi et al., 2014, 2018) trigger starburst activity and BH accretion, funneling the gas toward the center. After this initial phase, when the BH is obscured by gas and dust, with column densities reaching even the Compton-thick regime (i.e., $N_{\text{H}} \geq 10^{24} \text{ cm}^{-2}$), feedback from the BH and supernova-driven winds disperse the gas, then revealing the system as a bright powerful quasar that eventually evolves into a passive galaxy. The physical properties characterizing the different phases of this evolutionary cycle are not well understood. However, the study of the obscured and active phase, especially for high-redshift sources where most of the mass accretion occurred, can be crucial for better comprehending the interplay between the BH and its host.

Obscuration of the AGN emission is usually ascribed to a parsec-scale absorber, that is, the nuclear (~ 10 pc) torus of dust and gas surrounding the central engine, postulated by the unified model (e.g., Urry & Padovani, 1995). However, with the framework of the BH-galaxy coevolution in mind, gas on galaxy-wide scales could also have a role in obscuring the AGN. This role may be not negligible especially at high redshift, when galaxies were smaller (e.g., van der Wel et al., 2014; Shibuya et al., 2015; Allen et al., 2017) and richer in gas content (e.g., Scoville et al., 2017; Tacconi et al., 2018), and therefore featured a denser interstellar medium (ISM).

The potential contribution of the host galaxy in obscuring the AGN has been investigated by Gilli et al. (2014), who found that the column density associated with the ISM of the host can be on the same order as the column density inferred from the X-ray spectral analysis. Their analysis was performed on a single target, specifically, an SMG hosting a Compton-thick AGN at $z = 4.755$. This type of study requires multiwavelength data, from the X-rays to the submm, which can be challenging in the distant Universe. On the one hand, X-ray spectra provide us with a direct measurement of the total hydrogen column density along the line of sight affecting the X-ray emission of AGN through absorption and Compton scattering. On the other hand, estimating the column density associated with the ISM of the host galaxy requires measurements of the gas mass (which is dominated by the molecular phase at high redshift, e.g., Calura et al., 2014) and the size of the galaxy. The former can be inferred, for example, via low-J transitions of CO, a commonly used tracer of cold molecular gas in galaxies. An alternative method requires dust emission

measurements and the use of an empirical calibration to convert the monochromatic luminosity at $850\ \mu\text{m}$ into a molecular gas mass (Scoville et al., 2016, 2017; Privon et al., 2018). As for the sizes, high-resolution observations of the gas and/or dust emission are necessary (e.g., Hodge et al., 2016; Talia et al., 2018).

Following Gilli et al. (2014), we explore the possibility that the obscuration as seen in the X-rays is produced by the ISM of the host galaxy. This study is performed for the first time on a sample of seven X-ray selected AGN, for which we present a multiwavelength analysis in order to characterize both the host galaxy and the active nucleus. This Chapter is organized as follows. In Sec. 2.2 we present the dataset used and the sample selection. In Sec. 2.3 we describe the X-ray spectral extraction procedure and models used for the spectral analysis. In Sec. 2.4, the code and parameter setup used for modeling the SEDs of our targets are outlined. The results obtained from our analyses as well as the assumptions we made to estimate the molecular gas mass of each source are presented in Sec. 2.5. We discuss our findings together with the way ISM sizes and column densities have been derived in Sec. 2.6. We finally draw our conclusions in Sec. 2.7.

Throughout this Chapter, a standard ΛCDM cosmology with $\Omega_{\text{M}} = 0.3$, $\Omega_{\Lambda} = 0.7$ and $H_0 = 70\ \text{km s}^{-1}\ \text{Mpc}^{-1}$ is assumed (Ade et al., 2016).

2.2 Dataset and sample selection

Deep X-ray surveys are very powerful tools because they offer the possibility of efficiently selecting large samples of AGN in the distant Universe, including low-luminosity AGN (e.g., down to $L_{\text{X}, [2-10\text{keV}]} \sim 10^{43}\ \text{erg s}^{-1}$, Luo et al., 2017). Our study focuses on the *Chandra* Deep Field South (CDF-S; Luo et al., 2017), which provides the deepest X-ray spectral information currently available for distant AGN through its 7 Ms exposure. This field benefits from an extraordinary multiband coverage, allowing us to extend our analysis to a broad range of wavelengths. The Great Observatories Origins Deep Survey South field (GOODS-S; Giavalisco et al., 2004) covers, along with the Cosmic Assembly Near-IR Deep Extragalactic Legacy Survey (CANDELS; Grogin et al., 2011), the central area of the CDF-S and about one-third of the whole field. GOODS-S has been imaged with the major facilities providing a wide combination of multi-epoch data available in several bands (e.g., optical imaging with *Hubble*/ACS, optical/near-IR observations with the Subaru Suprime-Cam Intermediate Band Filters, observations in the mid-IR in the *Spitzer*/IRAC and MIPS bands, as well as far-IR in the *Herschel*/PACS and SPIRE bands). The UV-to-mid-IR (MIR) data used in this study are taken from Hsu et al. (2014), who provide photometric data for all the sources detected in the Extended *Chandra* Deep Field-South (E-CDF-S; Xue et al., 2016; Lehmer et al., 2005). We complemented these data with far-IR (FIR) data from *Herschel*/PACS and SPIRE, using the catalogs provided by Magnelli et al. (2013) and Oliver et al. (2012), respectively. We used a positional matching radius of $2''$ to associate a FIR counterpart with the sources in the UV-to-MIR catalog, taking into account that we used $24\ \mu\text{m}$ -priorred catalogs that in turn are IRAC- $3.6\ \mu\text{m}$ priorred. Detections with a signal-to-noise ratio $S/N < 3$ were converted into 3σ upper limits. The photometric data

used in this work are corrected for Galactic extinction (Schlegel et al., 1998).

In order to select our sample, we searched for X-ray AGN in the CDF-S that satisfy the following requirements:

1. Redshift higher than 2.5, to find a compromise between the increasing gas content in the host galaxy with redshift and the sample size.
2. Secure spectroscopic redshift, z_{spec} , as given by Luo et al. (2017) (quality flag “Secure”), in order to avoid the large photometric redshift uncertainties that propagate on different measurements.
3. At least one $> 3\sigma$ detection at $\lambda_{\text{obs}} \geq 100 \mu\text{m}$, in order to constrain the emission produced by cold dust that is heated by star formation activity, and as a result, to derive the intrinsic luminosity at $850 \mu\text{m}$ and estimate the molecular gas mass (Scoville et al., 2016; Privon et al., 2018).

Out of the 29 targets that match criteria 1 and 2, we found a total of 7 AGN that also satisfy requirement 3. ID, redshift and coordinates of the final sample are presented in Table 2.1. XID42 is part of the ALESS sample (Chen et al., 2015a). XID337 was studied by Mainieri et al. (2005), who presented a complete SED analysis. XID551 is the first high- z Compton-thick QSO discovered in the CDF-S by Norman et al. (2002) and was also studied by Comastri et al. (2011) in the 3.3 Ms XMM-*Newton* survey of the CDF-S. XID539 is the most distant Compton-thick AGN known (Gilli et al., 2011), hosted by a luminous SMG (Coppin et al., 2010; De Breuck et al., 2014; Gilli et al., 2014). XID666 is a Compton-thick QSO hosted by an infrared-luminous galaxy studied by Feruglio et al. (2011) and Del Moro et al. (2016). XID170 and XID746 are known since the 1 Ms observation of the CDF-S (Szokoly et al., 2004). It is relevant to mention that all the targets emerging from the sample selection are obscured, meaning that they are characterized by obscuring column densities $N_{\text{H}} \gtrsim 10^{23} \text{ cm}^{-2}$, according to the value given by the 7 Ms catalog and derived using the hardness ratio ($HR = \frac{H-S}{H+S}$, where H and S are the number of counts in the hard 2 – 7 keV and soft 0.5 – 2 keV bands, respectively). This would point to a connection between the presence of dust in the ISM that is heated by star formation, and nuclear absorption that may be produced by the same ISM (see Chen et al., 2015b).

2.3 X-ray spectral analysis

2.3.1 Spectral extractions

We used the data products publicly available in the *Chandra* Data Archive¹ for each of the 103 observations of the 7 Ms dataset. For each target, the final spectrum was obtained

¹<http://cxc.harvard.edu/cda/>

| XID | CID | XID | RA | DEC | z_{spec} |
|-----|------------------|------------------|---|--------------|-------------------|
| (1) | (2) | (3) | (4) | (5) | (6) |
| 42 | 326 ^a | 34 ^b | 03 ^h 31 ^m 51 ^s .95 | -27°53'27".2 | 2.940 |
| 170 | 14781 | 137 | 03 ^h 32 ^m 07 ^s .99 | -27°46'57".2 | 2.612 |
| 337 | 5479 | 262 | 03 ^h 32 ^m 18 ^s .85 | -27°51'35".7 | 3.660 |
| 539 | 273 | 403 ^c | 03 ^h 32 ^m 29 ^s .27 | -27°56'19".8 | 4.755 |
| 551 | 6294 | 412 | 03 ^h 32 ^m 29 ^s .86 | -27°51'6".1 | 3.700 |
| 666 | 9834 | 490 | 03 ^h 32 ^m 35 ^s .72 | -27°49'16".4 | 2.578 |
| 746 | 10578 | 546 | 03 ^h 32 ^m 39 ^s .68 | -27°48'51".1 | 3.064 |

Table 2.1: AGN sample summary. (1) Source identification number in the 7 Ms CDF-S catalog by Luo et al. (2017); (2) CANDELS identification number; (3) Source identification number in the 4 Ms CDF-S catalog by Xue et al. (2011); (4) J2000 right ascension and (5) declination of the X-ray source; (6) spectroscopic redshift as given by Luo et al. (2017).

^aID from GEMS (Häussler et al., 2007).

^bAlso known as ALESS57.1.

^cAlso known as ALESS73.1.

by combining the spectra extracted from each *Chandra* pointing. Since individual spectral extractions depend on off-axis angle and roll-angle, a source lying at the edges of the field of view can be outside some observations. This was the case for XID42 and XID539, the targets with the largest off-axis angle, for which such observations were excluded from the analysis. The off-axis angles of the sample are listed in Table 2.2 and range between 1.9' and 9.5'.

To extract the spectra, we followed the extraction procedure described in Vito et al. (2013). Images were inspected by means of SAOImage DS9². The source extraction regions were centered on the target coordinates (see Table 2.1), while the respective backgrounds were taken from nearby source-free regions in the full 7 Ms exposure image. The choice of the extraction radii was made taking into account the source position in the field of view (because the point spread function, PSF, broadens and distorts as the off-axis angle increases) and the number of counts (because fainter sources require smaller radii in order to reduce the number of background counts, hence increasing the S/N). We selected circular source regions with radii in the range 2.3 – 7", and verified that most of the counts were included. The values chosen for each source are reported in Table 2.2. Background regions were chosen in nearby areas that are free from contamination due to either close detected objects or the source itself. The background extraction region is larger than the corresponding source extraction region by a factor of $\sim 10 - 15$ in order to ensure a good sampling of the background itself.

Spectra, response matrices, and ancillary files were extracted with the *specextract* tool included in the *Chandra* Interactive Analysis of Observations³ (CIAO, v.4.8) software suite.

²<http://hea-www.harvard.edu/RD/ds9/>

³<http://cxc.harvard.edu/ciao/>

| XID | Counts | Off-axis angle | Extraction radius |
|-----|---------------|----------------|-------------------|
| (1) | (2) | (3) | (4) |
| 42 | 250 ± 16 | 9.51 | 7.0 |
| 170 | 1807 ± 43 | 4.70 | 3.5 |
| 337 | 326 ± 18 | 3.84 | 2.6 |
| 539 | 74 ± 9 | 7.96 | 3.5 |
| 551 | 707 ± 27 | 2.75 | 2.5 |
| 666 | 115 ± 11 | 1.88 | 2.3 |
| 746 | 2056 ± 45 | 2.56 | 2.5 |

Table 2.2: Summary of source parameters from the 7 Ms CDF-S data. (1) X-ray source ID (see Table 2.1); (2) net counts in the full 0.5–7 keV band collected for the whole sample in this work, referred to the 7 Ms dataset (errors are computed assuming a Poisson statistic); (3) off-axis angle in arcmin, that is the angular separation between the X-ray source and the CDF-S average aimpoint, from the 7 Ms source catalog (Luo et al., 2017); (4) radius, in arcsec, of the circular area selected for the source spectral extraction.

The final spectra were grouped to one count per bin with the *grppha* tool, and the Cash statistics with direct background subtraction was adopted (Cash, 1979; Wachter et al., 1979). The net counts in the full (0.5 – 7 keV) band for each source are reported in Table 2.2. They range between ~ 74 and ~ 2056 , with a median value of ~ 326 , and are in good agreement with the values reported in the Luo et al. (2017) catalog.

Some spectra were analyzed in a narrower energy range (e.g., XID42, XID539) in order to exclude spectral regions that are affected by a high background and to maximize the S/N.

2.3.2 Spectral models

To derive obscuring column densities and X-ray luminosities, we performed a spectral analysis using XSPEC⁴ (Arnaud, 1996), v.12.8.2. Because of the low photon statistics, we first adopted a simple power-law model including Galactic absorption⁵ (POWERLAW and PHABS models in XSPEC). The spectral slopes were found to be significantly flatter than the typical intrinsic slope of AGN ($\Gamma = 1.8 \pm 0.2$; e.g., Nandra & Pounds, 1994; Mainieri et al., 2002; Mateos et al., 2005; Tozzi et al., 2006). These hard slopes ($\Gamma \sim 0.0 - 1.0$) are in fact characteristic of obscured sources with low-counting statistics (e.g., Del Moro et al., 2016), and if coupled with prominent iron $K\alpha$ emission features ($EW \gtrsim 1$ keV), they are highly suggestive of heavy obscuration (e.g., Feruglio et al., 2011).

We therefore adopted more complex models to fit the spectra while keeping a minimum number of free parameters. All models have fixed geometric parameters of the obscuring

⁴<https://heasarc.gsfc.nasa.gov/xanadu/xspec/>

⁵The Galactic column density along the line of sight to the CDF-S is $N_{\text{H}} = 8.8 \times 10^{19} \text{ cm}^{-2}$ (e.g., Stark et al., 1992).

material because these are not known a priori and the data quality does not allow us to obtain them from the fitting process itself. For the majority of the targets, we could not simultaneously place tight constraints on the photon index and column density because these parameters are degenerate for low-count spectra. Hence we fixed the photon index to 1.8. Because the AGN emission is obscured, we also fixed the width of the iron line to 10 eV, which only accounts for the narrow component produced by the obscuring medium far away from the central black hole (e.g., Risaliti & Elvis, 2004).

We used the models described below.

- A transmission-dominated model, which reproduces the fraction of the primary emission transmitted through the obscuring medium. It is modeled by PLCABS (Yaqoob, 1997), which considers transmitted emission for a cold, spherical, and uniform distribution of matter surrounding an X-ray source. This model takes into account Compton scattering and works for column densities up to $\sim 5 \times 10^{24} \text{ cm}^{-2}$, as well as a maximum observed energy of 10 – 18 keV. We added a Gaussian line (ZGAUSS) to model the iron line and an unabsorbed power law to account for the soft-energy emission component (e.g., radiation that is scattered or leaking from the absorber). The photon index of this secondary power law is the same as that adopted for the primary one, as in the case of Thomson scattering.
- A reflection-dominated model, which implies $N_{\text{H}} \gtrsim 10^{25} \text{ cm}^{-2}$, therefore the direct nuclear emission is entirely absorbed and only emission reflected by the obscuring medium can be observed. It is parametrized by the PEXRAV model (Magdziarz & Zdziarski, 1995), fixing $\Gamma = 1.8$, and by a Gaussian line. Moreover, we fixed the cutoff energy to 100 keV and the viewing angle to the default value of 60° .
- The MYTorus model (Murphy & Yaqoob, 2009), which adopts a toroidal geometry for the reprocessor (a tube-like, azimuthally symmetric torus) with a half-opening angle of 60° and assumes that the reprocessing material is uniform, neutral, and cold. It is valid for column densities in the range $10^{22} - 10^{25} \text{ cm}^{-2}$. This model self-consistently reproduces the main components that usually characterize AGN emission (i.e., the “transmitted” and the “reflected” continuum, and the emission line). The inclination of the line of sight is fixed to 75° . We adopted a power-law continuum as primary spectrum, with the photon index fixed to 1.8 and a maximum energy $E_{\text{T}} = 500 \text{ keV}$ (even if a lower value is not expected to significantly affect our results, given the spectral energy range).

The results of the X-ray spectral analysis are presented in Section 2.5.1. Notes on individual targets are reported in Appendix A.

2.4 SED fitting

2.4.1 Data modeling

We analyzed the multiwavelength data of our targets in order to derive stellar masses, SFRs, and AGN bolometric luminosities, as well as to model the long-wavelength emission and infer the $850 \mu\text{m}$ luminosity (Scoville et al., 2016). To this aim, we used the SED-fitting code originally presented by Fritz et al. (2006) and Hatziminaoglou et al. (2008) and improved by Feltre et al. (2013). For a detailed description of the code, we refer to Feltre et al. (2013) and summarize below some of its main features.

The code adopts a multicomponent fitting approach that accounts for three distinct emission components: (i) stellar emission, which mainly prevails between ~ 0.3 and $\sim 5 \mu\text{m}$ (rest frame); (ii) emission due to hot dust heated by the AGN whose emission peaks in the mid-infrared (MIR); (iii) emission by cold dust dominating the FIR regime that is associated with star-forming activity.

The first component was modeled with a set of simple stellar populations (SSPs) of solar metallicity and assuming a Salpeter (1955) IMF, convolved with an exponentially declining star formation history (SFH), the so-called direct- τ model (e.g., Santini et al., 2015), in a time interval ranging between the formation redshift of the galaxy z_{form} and the source redshift z :

$$\text{SFR}(t) = \left(\frac{T_G - t}{T_G} \right) \exp\left(-\frac{T_G - t}{T_G \cdot \tau_B} \right), \quad (2.1)$$

where T_G is the age of the galaxy (or the age of the oldest SSP), which depends on z_{form} , and τ_B is the duration of the initial burst normalized to the age of the galaxy. The effect of attenuation was taken into account adopting the Calzetti et al. (2000) law, and applying a common value of attenuation to stars of all ages.

The AGN contribution was modeled with the templates presented by Fritz et al. (2006) and updated by Feltre et al. (2012), which assume that dust, composed of silicate and graphite, is smoothly distributed around the central engine with a flared-disk geometry. They have been extensively used in various analyses at different redshifts (Hatziminaoglou et al., 2010; Vignali et al., 2011; Pozzi et al., 2012). The extent and morphology of the nuclear dust distribution were resolved through high-resolution interferometric observations in the MIR revealing a clumpy or filamentary dust structure (Jaffe et al., 2004; Tristram et al., 2007; Burtscher et al., 2013). However, models assuming both a smooth and clumpy (e.g., Nenkova et al., 2008a,b) dust distribution are widely used and provide a good reproduction of the observed AGN SEDs. According to Feltre et al. (2012), the majority of the differences in the model SEDs are mainly due to different model assumptions and not to the clumpiness or smoothness of the dust distribution. We here focus on the global characteristics of the SEDs and not on the details of the torus structure and geometry.

Finally, the cold dust component was modeled with empirical templates that are representative of starburst galaxies (such as Arp220, M82, and NGC4102; see Polletta et al., 2007). The best fit was determined by a standard χ^2 minimization. The results of the SED-

fitting analysis are presented in Section 2.5.2. Notes on individual targets are reported in Appendix A.

2.5 Results

2.5.1 X-ray spectral analysis

The best-fit parameters obtained from the X-ray spectral analysis (see Sec. 2.3.2) are reported in Table 2.3 for each model we used in the fitting procedure. Figure 2.1 shows X-ray spectra for the whole sample fit by the transmission model. Errors are given at the 90% confidence level for one parameter of interest (Avni, 1976). The whole sample is characterized by very high column densities in the range $\sim 7 \times 10^{22} - 3 \times 10^{24} \text{ cm}^{-2}$. In particular, four out of seven sources are Compton-thick candidates. The equatorial column densities obtained with the MYTorus model were converted into the corresponding value along the line of sight (Murphy & Yaqoob, 2009). An iron emission line is detected in five out of seven sources, and in terms of EW, it is consistent within the errors with the prominent line (EW $\sim 1 \text{ keV}$) that is typically observed in obscured AGN spectra. Because of the limited photon statistics, some physical quantities are poorly constrained and characterized by loose limits.

The hard X-ray luminosities were computed in the rest-frame energy range 2 – 10 keV and corrected for absorption. These luminosities were found to be in the quasar luminosity domain with values in the range $(2 - 7) \times 10^{44} \text{ erg s}^{-1}$. Because there is no information on the intrinsic luminosity in the pure reflection model, we estimated it by assuming a reflection efficiency (i.e., the observed-to-intrinsic luminosity ratio) of 2% in the 2 – 10 keV band. This efficiency is admittedly very uncertain because it depends on the exact geometry of the absorbing-reflecting medium, but we note that reflection efficiencies on the order of $\sim 1 - 3\%$ have been reported in the literature (Maiolino et al., 1998; Comastri et al., 2010; Baloković et al., 2014; Ricci et al., 2017) and are usually assumed for Compton-thick AGN in synthesis models of the X-ray background (Gilli et al., 2007; Akylas et al., 2012). The observed fluxes in the same energy range are between $(1 - 7) \times 10^{-15} \text{ erg cm}^{-2} \text{ s}^{-1}$.

Errors on luminosities were derived taking into account the uncertainties on the column density as well as on the flux. Specifically, we considered a 90% confidence level for two parameters of interest (column density and power-law normalization). Our sample partially overlaps those studied by Liu et al. (2017) and Vito et al. (2018). Our results are in good agreement with their analysis.

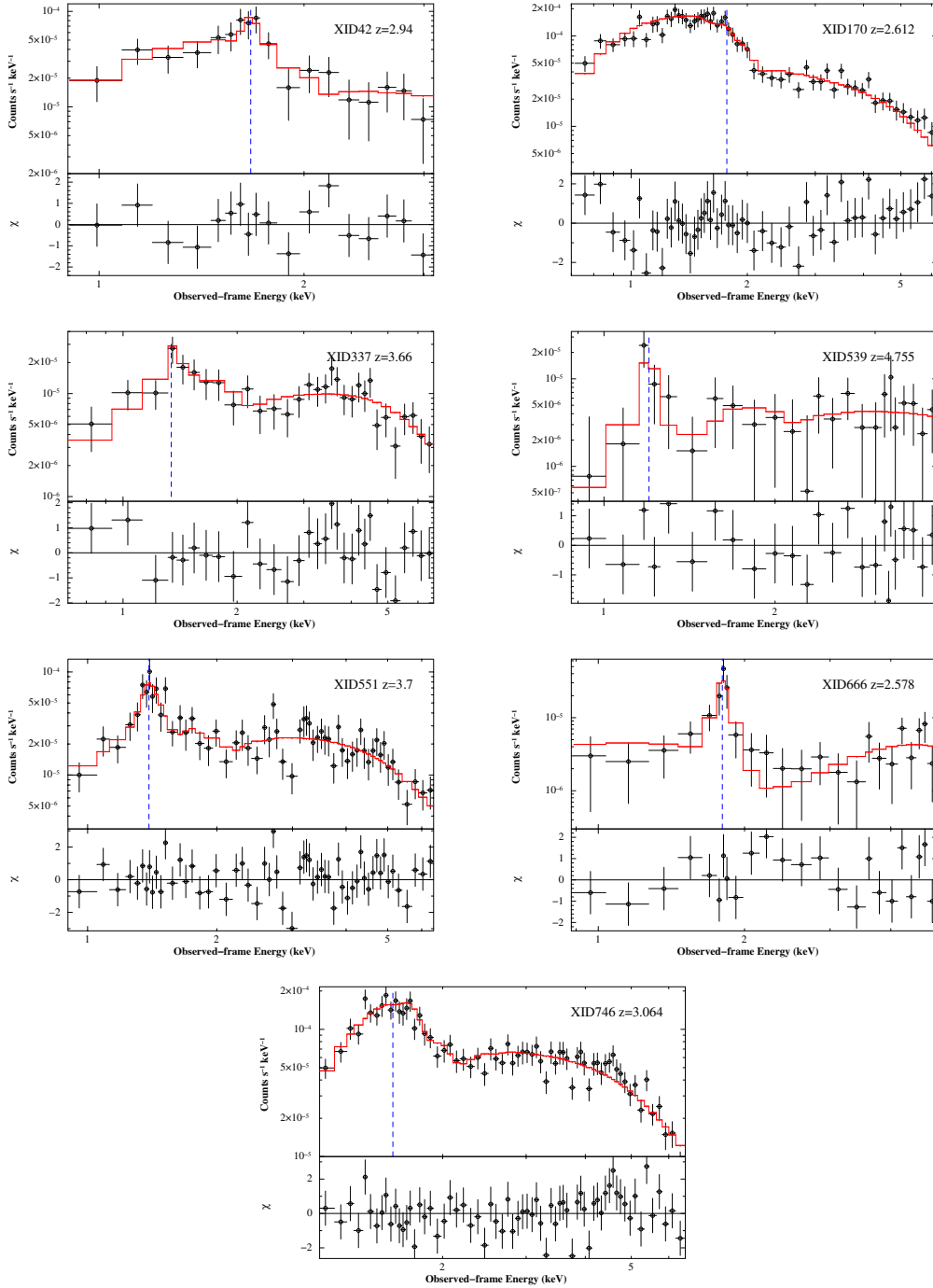


Figure 2.1: 7 Ms *Chandra* spectra of the targets fit using the transmission model. Observations are shown in black and the best-fit model in red. The data-to-model ratios in units of σ are shown at the bottom of each panel. The spectra are rebinned here for presentation purposes. The position of the iron line, as reported in Table 2.3, is marked by a blue dashed line.

| XID (1) | Model (2) | C-stat/dof (3) | N_{H} (4) | Γ (5) | $E_{\text{Fe line}}$ (6) | EW (7) | $F_{[2-10\text{keV}]}$ (8) | $L_{[2-10\text{keV}]}$ (9) |
|------------|--------------|-------------------|-----------------------|-----------------|-----------------------------|------------------------|-------------------------------|-------------------------------|
| 42 | Transmission | 146.9/172 | $2.0^{+1.0}_{-0.9}$ | 1.8 | $6.57^{+0.20}_{-0.35}$ | 386^{+335}_{-288} | $3.0^{+0.8}_{-0.8}$ | $1.9^{+0.8}_{-0.6}$ |
| | Reflection | 154.8/173 | - | 1.8 | $6.54^{+0.19}_{-0.36}$ | 504^{+504}_{-339} | $6.7^{+1.0}_{-0.9}$ | $34.5^{+5.0}_{-5.1}$ |
| | MYTorus | 151.8/177 | $2.4^{+1.0}_{-0.9}$ | 1.8 | 6.4 | 290^{+394}_{-261} | $3.4^{+0.6}_{-0.6}$ | $2.2^{+1.0}_{-0.6}$ |
| 170 | Transmission | 355.7/391 | $0.7^{+0.1}_{-0.1}$ | 1.8 | 6.4 | < 141 | $3.7^{+0.2}_{-0.2}$ | $1.7^{+0.2}_{-0.2}$ |
| | Reflection | 972.5/389 | - | 1.8 | 6.4 | 260^{+137}_{-123} | $9.3^{+0.5}_{-0.4}$ | $33.9^{+1.3}_{-1.7}$ |
| | MYTorus | 354.3/389 | $0.7^{+0.1}_{-0.1}$ | 1.8 | 6.4 | < 150 | $3.7^{+0.2}_{-0.1}$ | $1.6^{+0.1}_{-0.1}$ |
| 337 | Transmission | 207.4/240 | $10.0^{+3.0}_{-2.0}$ | 1.8 | $6.25^{+0.27}_{-0.24}$ | 610^{+596}_{-508} | $1.8^{+0.2}_{-0.3}$ | $3.1^{+1.3}_{-0.3}$ |
| | Reflection | 197.4/242 | - | 1.8 | 6.32 | < 503 | $1.6^{+0.2}_{-0.2}$ | $12.0^{+2.1}_{-1.0}$ |
| | MYTorus | 190.7/241 | $14.0^{+6.8}_{-3.4}$ | 1.8 | 6.4 | 502^{+537}_{-391} | $2.0^{+0.2}_{-0.4}$ | $3.8^{+2.7}_{-1.2}$ |
| 539 | Transmission | 29.2/45 | $17.0^{+11.7}_{-6.8}$ | 1.8 | $6.91^{+0.39}_{-0.21}$ | 3240^{+2325}_{-2946} | $1.5^{+0.3}_{-1.2}$ | $6.7^{+27.0}_{-4.0}$ |
| | Reflection | 32.4/47 | - | 1.8 | 6.9 | < 2089 | $1.0^{+0.4}_{-0.2}$ | $14.5^{+4.5}_{-2.7}$ |
| | MYTorus | 30.9/45 | $15.5^{+24.9}_{-6.9}$ | 1.8 | $6.95^{+0.59}_{-0.27}$ | 2618^{+2514}_{-1973} | $1.5^{+0.4}_{-1.2}$ | $5.0^{+16.8}_{-1.7}$ |
| 551 | Transmission | 268.1/307 | $11.8^{+2.4}_{-1.9}$ | 1.8 | $6.53^{+0.14}_{-0.14}$ | 630^{+338}_{-310} | $2.6^{+0.3}_{-0.3}$ | $5.0^{+1.7}_{-1.1}$ |
| | Reflection | 282.1/309 | - | 1.8 | $6.56^{+0.17}_{-0.17}$ | 376^{+259}_{-230} | $2.4^{+0.2}_{-0.2}$ | $19.2^{+1.2}_{-1.5}$ |
| | MYTorus | 276.5/316 | $9.5^{+1.7}_{-1.7}$ | 1.8 | 6.4 | 382^{+313}_{-267} | $2.6^{+0.3}_{-0.3}$ | $4.1^{+0.9}_{-0.7}$ |
| 666 | Transmission | 83.6/113 | $32.8^{+15.4}_{-8.4}$ | 1.8 | $6.44^{+0.09}_{-0.11}$ | 1470^{+980}_{-560} | $0.9^{+0.4}_{-0.2}$ | $5.6^{+1.2}_{-1.2}$ |
| | Reflection | 87.9/114 | - | 1.8 | $6.44^{+0.10}_{-0.10}$ | 1707^{+895}_{-712} | $0.6^{+0.2}_{-0.2}$ | $3.0^{+0.9}_{-0.4}$ |
| | MYTorus | 85.9/115 | > 39 | 1.8 | 6.4 | 1589^{+477}_{-524} | $1.3^{+3.2}_{-0.2}$ | > 3.4 |
| 746 | Transmission | 372.7/382 | $5.5^{+0.4}_{-0.3}$ | 1.8 | 6.4 | < 100 | $7.0^{+0.3}_{-0.4}$ | $6.1^{+0.6}_{-0.5}$ |
| | Reflection | 492.8/376 | - | 1.8 | $6.25^{+0.21}_{-0.15}$ | < 325 | $8.2^{+0.3}_{-0.3}$ | $43.5^{+1.5}_{-1.2}$ |
| | MYTorus | 368.8/382 | $5.5^{+0.3}_{-0.3}$ | 1.8 | 6.4 | < 204 | $7.2^{+0.3}_{-0.4}$ | $6.4^{+0.6}_{-0.5}$ |

Table 2.3: Best-fit parameters of the X-ray spectral analysis. (1) X-ray source ID (see Table 2.1); (2) model used to fit the source spectrum; (3) ratio between the Cash statistic value and the number of degrees of freedom; (4) column density, in units of 10^{23} cm^{-2} ; (5) spectral index; (6) rest-frame energy of the iron emission line in keV; (7) rest-frame equivalent width of the iron line in eV; (8) observed flux in the hard (2 – 10 keV) band, in units of $10^{-15} \text{ erg cm}^{-2} \text{ s}^{-1}$; (9) rest-frame absorption corrected luminosity in the hard (2 – 10 keV) band, in units of $10^{44} \text{ erg s}^{-1}$.

Errors are given at the 90% confidence level.

2.5.2 SED decomposition

In Table 2.4 we report the most relevant physical parameters derived by fitting the SEDs of our targets: M_* , the stellar mass of the galaxy; L_{IR} , the total infrared luminosity integrated in the $8 - 1000 \mu\text{m}$ rest-frame interval; L_{bol} , the AGN bolometric luminosity; $E(B - V)$, the total attenuation to the stellar emission; f_{AGN} , the fractional AGN contribution to the total infrared luminosity in the range $8 - 1000 \mu\text{m}$; SFR, the star formation rate obtained from L_{IR} by using the Kennicutt (1998b) calibration and subtracting the AGN fraction; and M_{gas} , the gas mass (atomic and molecular hydrogen).

Our galaxies are found to be massive, with stellar masses in the range $(1.7 - 4.4) \times 10^{11} M_{\odot}$ and characterized by an intense IR emission, $L_{\text{IR}} = (1.0 - 9.6) \times 10^{12} L_{\odot}$. In terms of AGN bolometric luminosities, our targets are in the quasar regime, with values between 1.9×10^{12} and $4.8 \times 10^{12} L_{\odot}$. The AGN contributes to the IR $8 - 1000 \mu\text{m}$ luminosity up to a few tens of percent. The attenuation to the host galaxy emission is in the range $E(B - V) = 0.24 - 0.48$.

We determined the uncertainties on the best-fit parameters by considering all the acceptable solutions within 1σ confidence level, which means within a given range $\Delta\chi^2$ that depends on the free parameters of the SED-fitting procedure. There are 11 free parameters (see Pozzi et al., 2012): 6 are related to the AGN (see Feltre et al., 2012), 2 to the stellar component (τ_{B} and $E(B - V)$), 1 to the starburst component (i.e., the selected best-fit template among the starburst library), and 2 further free parameters are represented by the normalizations of the stellar and starburst components. The normalization of the AGN component, instead, is estimated by difference after the other two components (the stellar and FIR components) were fixed by the fitting procedure. Therefore, we considered all the solutions within a χ^2 interval $\Delta\chi^2 = \chi^2 - \chi_{\text{min}}^2 \lesssim 12.65$ (Lampton et al., 1976). The resulting relative errors are $\sim 20\%$ for bolometric as well as IR luminosities, and of a few percent for the stellar masses. This uncertainty is clearly underestimated and is on the order of the statistical errors of the photometric measurements. Comparisons between the stellar masses obtained with the code used in this analysis and other codes (adopting different libraries and IMFs) provide instead a scatter of $\sim 30\%$. A similar range was also found by Santini et al. (2015), who investigated the influence of systematic effects in the stellar mass estimate produced by different assumptions, mainly due to poor constraints on the stellar population properties (e.g., metallicity, attenuation curves, and IMF) and the lack of a proper reconstruction of the SFH. They collected stellar mass measurements for the sources observed in the CANDELS field (where our targets lie) by ten teams in the CANDELS collaboration, who fit the same photometry, but adopted different assumptions. The comparison of the resulting estimates was quite satisfactory: the majority of the results were around the median value. They therefore claimed that the stellar mass is a stable parameter against the different assumptions, except for the IMF, which introduces a constant offset⁶. They also quantified the scatter around the median value, which is roughly $25\% - 35\%$. We compared our measurements of the stellar mass with the results presented

⁶In order to rescale the stellar mass from the Salpeter to the Chabrier IMF, 0.24 dex needs to be subtracted.

in their GOODS-S catalog⁷, in particular with the median values and the results obtained with the method whose assumptions are the most similar to ours (method 2d_τ in Santini et al., 2015), that is, the χ^2 minimization to estimate the goodness of fits, the Salpeter IMF, an exponentially declining SFH, and the Calzetti attenuation law. The quantity $\langle \log(M_{*, \text{literature}}/M_{*, \text{this work}}) \rangle$ is equal to -0.13 dex and -0.07 dex for their median stellar masses (rescaled to a Salpeter IMF) and those obtained with the method 2d_τ, respectively. The standard deviation is 0.1 dex in both cases. According to the results mentioned above, we assumed a relative error of 30% for the stellar masses derived in this work.

Overall, the observed SEDs, shown in Fig. 2.2, are well reproduced by the models. The optical/NIR regime of our SEDs is densely sampled by several photometric datapoints. The AGN contamination to the optical/NIR regime is negligible, as can be seen from the best fits, because we study obscured AGN. The coverage is sparser in the MIR and FIR regimes. The *Spitzer*/MIPS data at 24 μm account for the wavelength range where the AGN emission dominates, but in our targets, the AGN contribution can be important in this regime. The FIR part of the SEDs is differently sampled for the different sources. In general, all the targets have *Herschel*/PACS and SPIRE photometry, to which we added SCUBA (Rigopoulou et al., 2009) and ALMA submm data (in Bands 7, 6, and/or 4), when available. ALMA data constrain the declining part of the FIR peak (at long wavelengths), which corresponds to the Rayleigh-Jeans tail, associated with dust in the optically thin regime. The dust continuum can therefore be used as an indicator of dust mass, and through the dust-to-gas ratio, of the ISM mass in the galaxy (see Sec. 2.5.3). The FIR data also allowed us to estimate the SFRs of the sample, which is characterized by an intense star-formation activity, with values in the range between ~ 190 and $\sim 1680 M_{\odot} \text{yr}^{-1}$.

We compared our estimates of X-ray luminosities with those predicted by the relations found by Lusso et al. (2012) with bolometric luminosities, and Gandhi et al. (2009) with 12.3 μm luminosities. Our results are in good agreement with the predicted values, and they agree on average to within a difference of 0.1 dex and 0.3 dex for the Lusso et al. (2012) and Gandhi et al. (2009) relations, respectively.

⁷http://candels.ucolick.org/data_access/GOODS-S.html.

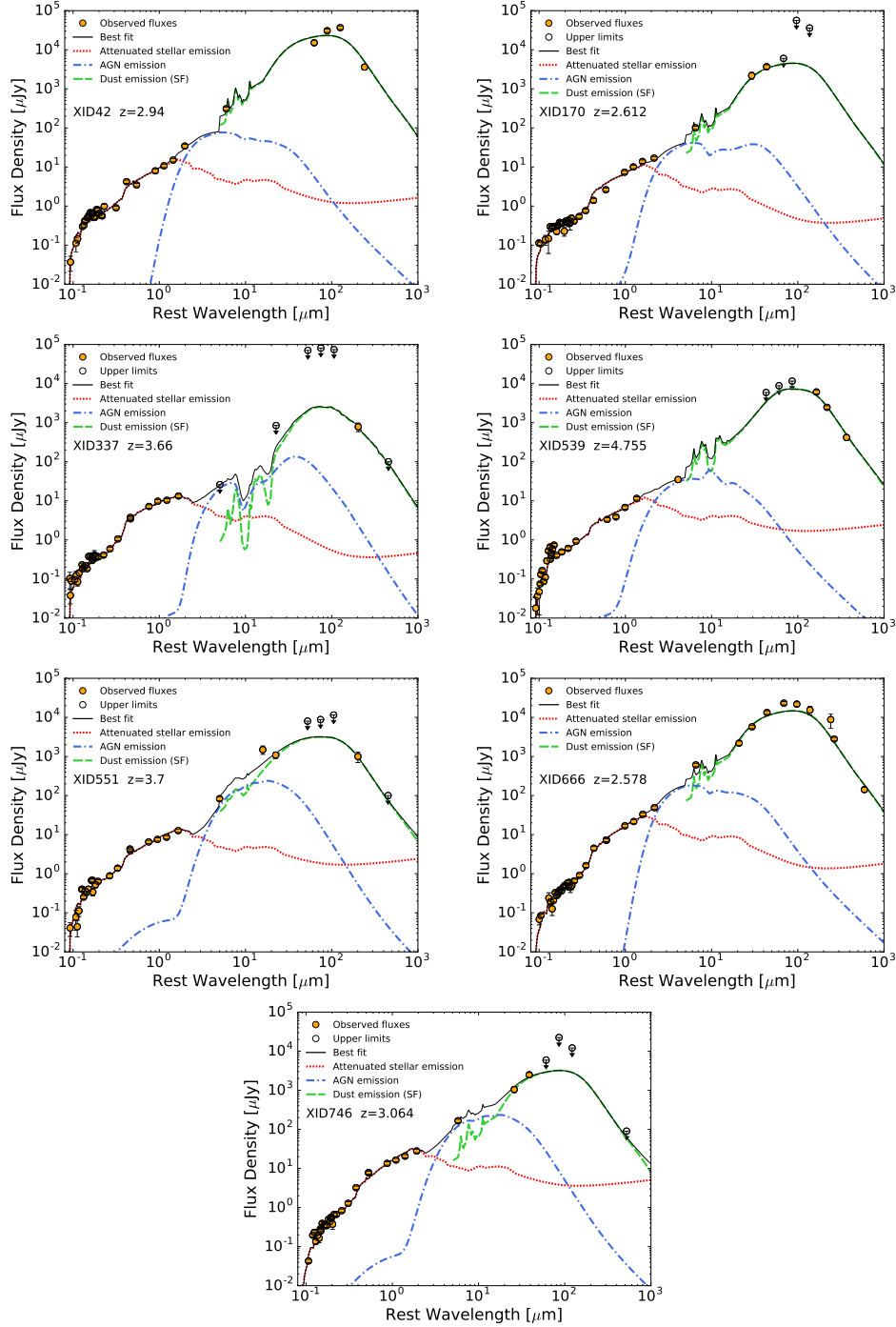


Figure 2.2: Spectral decomposition of the rest-frame SEDs of the target sample. The X-ray source ID (from Luo et al., 2017) and the redshift are shown in the middle-left part of each panel. The orange-filled dots depict photometric data, empty dots indicate 3σ upper limits. The black solid line is the total best-fit model, the red dotted line represents the stellar emission attenuated by dust, the AGN model is reproduced by the blue dot-dashed line and the green dashed line accounts for dust emission heated by star formation.

| XID | M_* | L_{IR} | L_{bol} | $E(B - V)$ | f_{AGN} | SFR | M_{gas} |
|-----|-----------------|-----------------|------------------|------------|------------------|----------------|------------------|
| (1) | (2) | (3) | (4) | (5) | (6) | (7) | (8) |
| 42 | 2.16 ± 0.65 | 9.62 ± 1.92 | 2.60 ± 0.78 | 0.31 | 0.01 | 1679 ± 336 | 5.41 ± 3.21 |
| 170 | 1.74 ± 0.52 | 1.57 ± 0.31 | 1.89 ± 0.57 | 0.24 | 0.02 | 276 ± 55 | 0.87 ± 0.51 |
| 337 | 3.43 ± 1.03 | 1.01 ± 0.20 | 3.11 ± 0.93 | 0.24 | 0.09 | 192 ± 38 | 0.85 ± 0.51 |
| 539 | 2.15 ± 0.64 | 4.90 ± 0.98 | 2.66 ± 0.80 | 0.37 | 0.02 | 864 ± 173 | 4.55 ± 2.70 |
| 551 | 2.19 ± 0.66 | 2.27 ± 0.45 | 2.92 ± 0.88 | 0.36 | 0.14 | 456 ± 91 | 0.88 ± 0.52 |
| 666 | 4.41 ± 1.32 | 4.90 ± 0.98 | 4.82 ± 1.44 | 0.38 | 0.03 | 872 ± 175 | 2.76 ± 1.63 |
| 746 | 4.33 ± 1.30 | 1.44 ± 0.29 | 2.84 ± 0.85 | 0.48 | 0.17 | 299 ± 60 | 0.80 ± 0.47 |

Table 2.4: Best-fit parameters of the SED decomposition. (1) X-ray source ID (see Table 2.1); (2) stellar mass, in units of $10^{11}M_{\odot}$; (3) total infrared luminosity integrated in the rest-frame $8 - 1000 \mu\text{m}$ range, in units of $10^{12}L_{\odot}$; (4) AGN bolometric luminosity, in units of $10^{12}L_{\odot}$; (5) attenuation to the stellar emission; (6) fractional AGN contribution to the total IR luminosity; (7) SFR in units of $M_{\odot} \text{ yr}^{-1}$; (8) $M_{\text{gas}} = M_{\text{H}_2} + M_{\text{HI}}$ in units of $10^{10} M_{\odot}$.

Errors are given at the 68% confidence level. Relative errors are $\sim 30\%$ for stellar masses and $\sim 20\%$ for IR luminosities and AGN bolometric luminosities.

2.5.3 Gas content of the host galaxies

In order to estimate the gas content of the host galaxies, we derived the molecular gas mass, which is the dominant component in these sources, using the results obtained by Scoville et al. (2016). They analyzed both long-wavelength dust-continuum emission and CO($J=1-0$) line luminosities for a large sample of galaxies that consists of local star-forming galaxies, low- z ultra-luminous infrared galaxies (ULIRGs) and high- z SMGs. All galaxies show the same linear correlation between CO($J=1-0$) luminosity L'_{CO} and the luminosity at $850 \mu\text{m}$ $L_{850 \mu\text{m}}$ rest frame, $L'_{\text{CO}} = 3.02 \times 10^{-21} L_{850 \mu\text{m}}$ (see left panel of Fig. 1 in Scoville et al., 2016), probing the molecular gas mass and the dust emission, respectively. We estimated the luminosity at $850 \mu\text{m}$ rest frame from the model SEDs of our targets and recovered L'_{CO} through the observed correlation. The molecular gas mass can then be quantified assuming a CO-to- H_2 conversion factor α_{CO} , $M_{\text{H}_2} = \alpha_{\text{CO}} L'_{\text{CO}}$. However, the ISM mass estimate relies on several assumptions and systematic uncertainties. For instance, to translate observations at different rest-frame wavelengths into luminosities at $850 \mu\text{m}$, the observed dust emission needs to be modeled, and the common assumption is that of a single-temperature modified blackbody in the long-wavelength optically thin regime. This in turn requires the assumption of a dust absorption coefficient and a dust temperature (e.g., Bianchi, 2013). Neither of these parameters is well known, and they can vary for different classes of galaxies. Moreover, the conversion factor α_{CO} is affected by large uncertainties and likely depends on local ISM conditions, such as pressure, gas dynamics, and metallicity (e.g., Carilli & Walter, 2013, and references therein). Highly star-forming systems usually show values in the range $0.3 - 1.3$ (Carilli & Walter, 2013), with an average value of $\alpha_{\text{CO}} = 0.8 M_{\odot}/(\text{K km s}^{-1} \text{pc}^2)$ (e.g., Tacconi et al., 2008; Magdis et al., 2012; Magnelli et al., 2012; Bothwell et al., 2013). This is lower than what is observed in normal galaxies ($\alpha_{\text{CO}} = 4.5$), implying more CO emission per unit molecular gas mass, and it is likely related to the different physical conditions in the ISM (e.g., Papadopoulos et al., 2012). We therefore assumed $\alpha_{\text{CO}} = 0.8 \pm 0.5 M_{\odot}/(\text{K km s}^{-1} \text{pc}^2)$ for our highly star-forming systems. Moreover, to account for the atomic hydrogen mass M_{HI} , we considered the results by Calura et al. (2014). They converted the [CII] $158 \mu\text{m}$ line luminosity into atomic gas mass for a sample of high- z AGN host galaxies, obtaining an average ratio $M_{\text{H}_2}/M_{\text{HI}} \sim 5$ for the whole sample. Theoretical results agree with this estimate (e.g., Lagos et al., 2011). Our gas masses, obtained as the sum of the molecular and neutral hydrogen masses $M_{\text{gas}} = M_{\text{H}_2} + M_{\text{HI}}$, are in the range $(0.8 - 5.4) \times 10^{10} M_{\odot}$, as reported in Table 2.4. Errors take into account a 20% error on the luminosity at $850 \mu\text{m}$, the 0.2 dex dispersion of the Scoville et al. (2016) relation, and the range of α_{CO} values mentioned above.

2.6 Discussion

2.6.1 Size of the host galaxies

In order to infer the column density of the ISM in the host galaxy, we need to estimate the gas extension. As a probe of the gas size, we can consider observations of the thermal FIR continuum, produced by dust heated by young, massive stars, hence representing the regions of active star formation; CO transitions, tracing molecular gas that serves as the fuel for star formation; and [CII] line emission, probing the photodissociation regions (PDRs) and the interstellar medium.

High-redshift QSOs and SMGs tend to have significant masses of cold dust ($M_{\text{dust}} \sim 10^8 - 10^9 M_{\odot}$) as well as substantial reservoirs of molecular gas ($M_{\text{gas}} \sim 10^{10} - 10^{11} M_{\odot}$). Several analyses of the stellar component and the molecular gas as well as dust hosted in these sources have confirmed that they have compact sizes. For example, Swinbank et al. (2010) performed a detailed study of the stellar structure for a sample of 25 SMGs (including both AGN and starburst galaxies) at redshift $z \sim 2$. They used deep *HST* *I*- and *H*-band images and derived typical half-light radii of about 2 kpc. Tacconi et al. (2008) obtained sub-arcsec resolution observations of CO rotational transitions in four SMGs at $z \sim 2$ using the IRAM Plateau de Bure Interferometer (PdBI). The observed emission had a compact intrinsic size, with $r_{\text{half}} \lesssim 2$ kpc. Half-light radii in the range $\sim 1 - 4$ kpc have also been measured for the ISM of very distant ($z \sim 6 - 7$) quasar hosts by means of ALMA observations of the [CII] fine structure line and dust continuum emission (see, e.g., Decarli et al. 2018; Venemans et al. 2018 and references therein). Other compelling results are provided by Harrison et al. (2016b), who presented high-resolution ALMA 870 μm imaging of five high-redshift ($z \sim 1.5 - 4.5$) AGN host galaxies. They measured angular sizes of $\sim 0.2'' - 0.5''$ for the rest-frame FIR emission of their targets, corresponding to star formation scales of 1 – 3 kpc. However, FIR/submm observations at these redshifts are usually just marginally resolved, and therefore these data do not probe the source morphology and just place tight constraints on the spatial extent of the observed objects. All these sources are characterized by physical parameters similar to those derived for our targets, which means stellar masses $M_* \sim 10^{10} - 10^{11} M_{\odot}$, gas masses $M_{\text{gas}} \sim 10^{10} - 10^{11} M_{\odot}$, and IR luminosities $L_{\text{IR}} \gtrsim 10^{12} L_{\odot}$, some of them showing obscured AGN activity detected through X-ray observations.

We lack measurements that would trace the gas component for our sample. We assumed that the molecular gas and dust are cospatial. Although not many observations have so far probed both the dusty and molecular component for targets similar to ours, some works have reported compact sizes of the molecular gas and similar or slightly smaller extensions of the dust (e.g., Hodge et al., 2015; Spilker et al., 2016; Tadaki et al., 2017a,b; Talia et al., 2018, but see also Calistro Rivera et al. 2018). Therefore, we used the size of the dust-emitting region as a probe of the gas size for the sources for which this information is available (see Table 2.5). For the remaining targets, we assumed that the size of the heated-dust region is half of that of the total stellar emission (e.g., Tadaki et al., 2017b) as derived from CANDELS *HST* *H*-band data (i.e., rest-frame optical) using GALFIT

(van der Wel et al., 2012). This assumption is in agreement with the results of Hodge et al. (2016): by means of ALMA observations at $0.16''$ resolution, they found that for the distant (median redshift ~ 2.6) SMGs in the ALESS survey, the size of the central dusty and starbursting region is on average ~ 2.5 times smaller than that of stellar emission as measured in CANDELS. These results have been confirmed by Fujimoto et al. (2017) on a larger sample of star-forming galaxies at a similar median redshift and observed by both ALMA and *HST*. In spite of a large scatter in their measurements, these authors found that FIR-measured sizes are on average ~ 1.5 times smaller than those measured at UV/optical (rest-frame) wavelengths.

We have solid multiwavelength observational constraints on the extension of the source XID539 from previous works. De Breuck et al. (2014) presented ALMA Band 7 (345 GHz, i.e., $870 \mu\text{m}$) observations of the [CII] line emission and dust continuum, which are confined in a region with a radius smaller than 2 kpc. A continuum Band 6 (230 GHz, $1300 \mu\text{m}$) observation of this target was analyzed by Gilli et al. (2014), who found an intrinsic source size of 0.27 ± 0.08 arcsec (Gaussian FWHM), corresponding to a dust half-light radius of $r_{\text{half}}^d = 0.9 \pm 0.3$ kpc (see also Hodge et al. 2016). In the *HST*/WFC3 *H*-band ($\sim 2800 \text{ \AA}$ rest-frame), the source is not resolved, which places an upper limit on the UV rest-frame emission of 1.2 kpc (Chen et al., 2015a). As discussed in Gilli et al. (2014), we assumed a stellar half-light radius of $r_{\text{half}}^* \sim 1$ kpc, which is comparable to what has been found for the dust emission. For XID42 and XID666, we used data from a recent ALMA Band 4 observation at $0.15''$ resolution (PI: Gilli). The two sources appear resolved in the ALMA data, with half-light radii for the dust-continuum emission of about 1.2 ± 0.4 and 0.6 ± 0.3 kpc, respectively (D’Amato et al., in prep.). These values are lower than the half-light radii of the stellar component in the *HST*/WFC3 *H*-band, which are 2.2 ± 0.1 kpc (Chen et al., 2015a) and ~ 3 kpc (van der Wel et al., 2012) for XID42 and XID666, respectively. Overall, for the three sources in our sample with both high-resolution ALMA and *HST* *H*-band data, the rest-FIR size is from 1.1 to 5 times smaller than the rest-optical size, in agreement with the general trend found in the literature, and again indicating that SMGs have central dusty starbursts that are more compact than the whole stellar distribution. For the remaining sources, XID170, XID337, XID551, and XID746, we assumed that the extension of the ISM is half of that measured for the total stellar emission, as derived from CANDELS *HST* *H*-band data (van der Wel et al., 2012). The adopted ISM half-light radii are reported in Table 2.5.

2.6.2 ISM column density

In order to estimate the equivalent column density associated with the gas in the host galaxy, we considered a simple geometrical approximation assuming a spherical gas distribution with uniform density. Hence, under the assumption that both molecular and atomic gas are cospatial with dust, and considering that half of the total gas mass $M_{\text{gas}} = M_{\text{H}_2} + M_{\text{HI}}$ is confined within $r_{\text{half}}^{\text{ISM}}$, we computed the ISM column densities for the seven

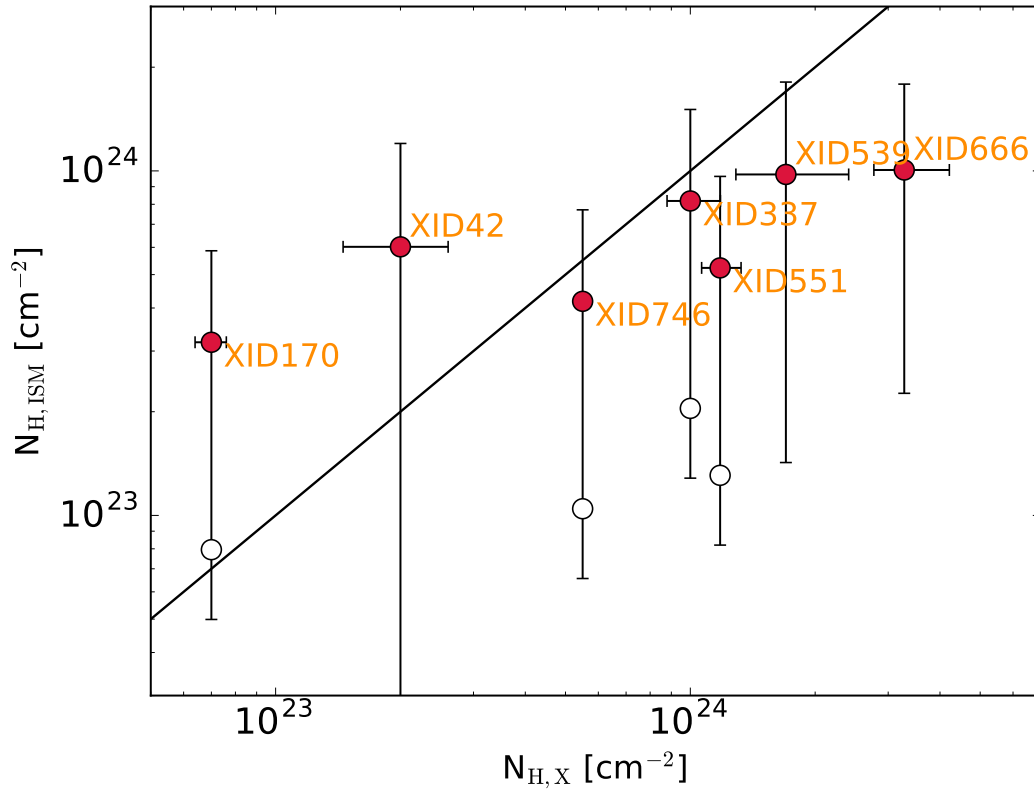


Figure 2.3: ISM column density vs X-ray column density for our targets. The solid line shows the 1:1 relation. Filled circles were derived assuming $r_{\text{half}}^{\text{ISM}}$ as reported in Table 2.5. For the targets with no ALMA data, the ISM densities that would be obtained by assuming $r_{\text{half}}^{\text{ISM}} = r_{\text{half}}^*$ instead of $r_{\text{half}}^{\text{ISM}} = r_{\text{half}}^*/2$ are also shown as open circles.

sources of our sample:

$$N_{\text{H}} = \int_0^{r_{\text{h}}} n_{\text{H}} ds, \quad (2.2)$$

which is the volume density n_{H} of hydrogen atoms inside the sphere of radius r_{h} integrated over the path length ds .

The values obtained are reported in Table 2.5 and range between $\sim 10^{23}$ and $\sim 10^{24}$ cm^{-2} , which are on the same order as those derived from the X-ray spectral analysis. Because the geometry adopted for the host ISM is similar to that assumed by the transmission-dominated model used to analyze the X-ray spectra, we consider as fiducial results for $N_{\text{H}, \text{x}}$ those derived by using the transmission model (see Table 2.3). The outcome of this comparison is that the host ISM can significantly contribute to the observed X-ray obscuration.

In Fig. 2.3 the ISM column densities are plotted against the values derived from the X-ray spectral analysis. For the four sources without any direct measurement of the FIR-rest size, we also plot (open circles) the ISM column density that would be obtained by assuming a dust-to-stellar size ratio of 1 instead of 0.5. Clearly, the derived ISM columns would decrease by a factor of 4. Moreover, we note that Calistro Rivera et al. (2018) reported a CO($J3-2$) half-light radius for the target XID42 of 3.1 ± 0.5 kpc. By assuming this value, the column density would decrease by a factor of 7, but still represent 40% of the value derived from the X-rays. In general, the similarity between the ISM column densities and the X-ray column densities suggests that the host ISM is capable of providing significant absorption on large (kpc) scales that adds to (or even replaces) the absorption produced on small (pc) scales by any circumnuclear material (i.e., the torus). The presence of hot dust surrounding the central engine and heated by its emission is indeed supported by the mid-IR “excess” observed in the SED. This component, which is also observed in X-ray unobscured AGN, does not necessarily account for the whole obscuration.

If we consider that complex merging phenomena, gas inflows toward the central engine and inhomogeneous collapse of gas, are expected during the evolution of these sources (e.g., Hopkins et al. 2006; Lapi et al. 2014), a simple unification model based on torus-like absorbers and ordered gas motions may not apply, and nuclear radiation may then be absorbed by gas located at different physical scales. In particular, the medium in the host galaxy is an ingredient that should be considered, as also suggested by the evidence for an increase in X-ray column density with the stellar mass of the AGN host, as has recently been found by Buchner & Bauer (2017) and Lanzuisi et al. (2017).

Hopkins et al. (2005, 2006) studied the AGN obscuration during a major merger event by computing the column density along several lines of sight and modeling the ISM through a hot (diffuse) and a cold (molecular and neutral) phase, with most of the mass distributed in dense and cold structures. They found that the column density does not depend considerably on the assumptions regarding the small-scale physics of the ISM and obscuration, as the central regions of the merging galaxies are expected to be highly chaotic. Moreover, the scales associated with obscuration are related to starburst activity and obscured quasar growth, and were found to be larger ($\gtrsim 100$ pc) than the typical scales of traditional tori. In particular, the galaxy ISM is able to generate an important contribution to the obscuration

| Source | $r_{\text{half},''}^*$ | $r_{\text{half},''}^{\text{d}}$ | $r_{\text{half},\text{kpc}}^{\text{ISM}}$ | $N_{\text{H, ISM}}$ | $N_{\text{H, X}}^a$ |
|--------|------------------------|---------------------------------|---|---------------------|-----------------------|
| (1) | (2) | (3) | (4) | (5) | (6) |
| 42 | 0.28 ± 0.01 | 0.15 ± 0.07 | 1.2 ± 0.4 | 6.0 ± 5.9 | $2.0_{-0.9}^{+1.0}$ |
| 170 | 0.16 ± 0.01 | - | 0.7 ± 0.3 | 3.2 ± 2.7 | $0.7_{-0.1}^{+0.1}$ |
| 337 | 0.11 ± 0.01 | - | 0.4 ± 0.2 | 8.2 ± 6.9 | $10.0_{-2.0}^{+3.0}$ |
| 539 | < 0.2 | 0.13 ± 0.04 | 0.9 ± 0.3 | 9.8 ± 8.3 | $17.0_{-6.8}^{+11.7}$ |
| 551 | 0.14 ± 0.01 | - | 0.5 ± 0.2 | 5.2 ± 4.4 | $11.8_{-1.9}^{+2.4}$ |
| 666 | 0.38 ± 0.01 | 0.08 ± 0.02 | 0.6 ± 0.3 | 10.0 ± 7.8 | $32.8_{-8.4}^{+15.4}$ |
| 746 | 0.14 ± 0.01 | - | 0.5 ± 0.2 | 4.2 ± 3.5 | $5.5_{-0.5}^{+0.6}$ |

Table 2.5: Half-light radii and column densities derived from both the SED-fitting and the X-ray analyses. (1) XID; (2) stellar half-light radius in arcsec as derived from *HST*/WFC3 *H*-band observations (see Chen et al. 2015a for XID42 and XID539, and van der Wel et al. 2012 for the remaining sources); (3) dust continuum half-light radius in arcsec from ALMA data (see text); (4) ISM half-light radius in kpc. We assumed $r_{\text{half}}^{\text{ISM}} = r_{\text{half}}^{\text{d}}$ when ALMA data were available, and $r_{\text{half}}^{\text{ISM}} = r_{\text{half}}^*/2$ (with $\sim 30\%$ errors, similar to those on $r_{\text{half}}^{\text{d}}$) otherwise (see text for details); (5) column density associated with the ISM of the host galaxy, in units of 10^{23} cm^{-2} ; (6) column density derived from the X-ray spectral analysis, in units of 10^{23} cm^{-2} .

^aSince the geometry adopted for the host ISM is similar to that assumed by the transmission-dominated model used to analyze X-ray spectra, we consider as fiducial results for $N_{\text{H, X}}$ those derived by using the transmission model (see Table 2.3).

across most lines of sight toward the nucleus (Trebitsch et al., 2019) (a few sightlines may still be free from obscuration as witnessed in, e.g., unobscured quasars hosted by gas-rich galaxies, Fu et al., 2017; Decarli et al., 2018). In this scenario, the obscuring column density could be an evolving function of time, luminosity, and host galaxy properties, dominated by gas inflows that fuel the central BH in different evolutionary stages. In particular, because of the larger gas content and smaller size of high-redshift galaxies, kpc-scale obscuration by the host ISM may be responsible for the observed increase of the obscured AGN fraction toward high redshifts (Vito et al., 2014; Aird et al., 2015; Buchner et al., 2015; Vito et al., 2018).

The role of the host galaxy ISM in obscuring the AGN emission has also been studied through numerical simulations (e.g., Bournaud et al., 2011a,b). Thick gaseous disks in high-redshift galaxies subject to violent instability can produce strong obscuration toward the central AGN, characterized by very high column densities ($N_{\text{H}} > 10^{23} \text{ cm}^{-2}$) that even reach the Compton-thick regime. Juneau et al. (2013) pointed out that at high redshift, in addition to small-scale absorption (i.e., the pc-scale torus), large amounts of gas in galaxies might contribute to absorbing X-rays. In particular, they found a more frequent X-ray absorption in galaxies hosting an AGN with higher sSFRs (i.e., SFR/M_*). A possible explanation for this observed trend is that the gas reservoir that fuels the intense star formation also acts as a relevant source of obscuration for the AGN. This situation

could be more likely at high redshift, where the AGN hosts show an increase in SFR and gas content (e.g., Carilli & Walter, 2013).

The kinematics and spatial distribution of the ISM might be better constrained by observing molecular lines, which provide the most direct insight into the physics and behavior of these systems. SMGs and QSOs often exhibit double-peaked CO spectra, which are a potential indicator of either the existence of kinematically distinct components within these systems or a rotating disk-like component (e.g., Tacconi et al., 2008; Bothwell et al., 2013). However, galaxy-integrated line fluxes are mainly measured at high redshift, and spatially resolved molecular gas observations are restricted to a few bright sources (Carilli & Walter, 2013). Therefore, inferring the size of the CO reservoir and studying the kinematic mode that determines the gas dynamics, as well as how the ISM takes part in the obscuration of the central AGN, is very challenging at these redshifts.

2.6.3 Possible progenitors of the cQGs

We constrained the surface densities of SFRs, gas, and stellar masses as derived from SED fitting (see Table 2.4), assuming a uniform distribution with radius r_{half} . The results are reported in Table 2.6. The surface density of star formation, $\Sigma_{\text{SFR}} = (\text{SFR}/2)/(\pi r_{\text{half}}^2)$, ranges between ~ 108 and $\sim 338 M_{\odot} \text{ yr}^{-1} \text{ kpc}^{-2}$, in line with the range found by, for example, Harrison et al. (2016b) for a sample of X-ray selected AGN at $z \sim 1.5 - 4.5$ and observed with ALMA (see also Genzel et al., 2010; Hodge et al., 2013). Similarly, we estimated the gas surface density, $\Sigma_{\text{gas}} = \Sigma_{\text{HI+H}_2} = (M_{\text{gas}}/2)/(\pi r_{\text{half}}^2)$, with values in the range $(0.3 - 1.1) \times 10^{10} M_{\odot} \text{ kpc}^{-2}$. These values are in agreement with those typically found for SMGs (see, e.g., Daddi et al. 2010 and Swinbank et al. 2010 for a comparison with Σ_{gas} and Σ_{*} obtained for SMGs). Finally, we combined the size and stellar mass estimates to derive the stellar surface density, $\Sigma_{*} = (M_{*}/2)/(\pi r_{\text{half}}^2)$, where r_{half} is the stellar half-light radius. Our results are in the range $(0.7 - 8.7) \times 10^{10} M_{\odot} \text{ kpc}^{-2}$: the stellar density is about one dex higher than what is found for local elliptical galaxies of similar mass (e.g., as derived by Hopkins et al. 2010 based on the *HST* data of Lauer et al. 2007), and is instead similar to what is found in compact quiescent galaxies (cQGs) at $z \gtrsim 1$ (Trujillo et al., 2007; Cimatti et al., 2008).

High-redshift QSOs and SMGs are thought to be complex systems of dense gas, massive star formation, and even AGN activity. Tacconi et al. (2008) suggested that a significant fraction of the stellar mass of these objects ($\sim 50\%$) formed and assembled during their most active phase, while the rest formed over a longer period of time. Taking into account the high SFRs, we can estimate the gas depletion timescale, that is, the time that the available gas needs to be depleted assuming a constant SFR. Hence, $t_{\text{dep}} = M_{\text{gas}}/\text{SFR}$ is found to be in the range $\sim (2 - 5) \times 10^7 \text{ yr}$. After the SMG phase, which ends when the gas supply is depleted or if star formation is quenched and further prevented by negative feedback from AGN and supernovae, the galaxy will end up as a compact passive system (e.g., Lapi et al., 2014). It has been argued that SMGs at high redshift (e.g., Tacconi et al., 2008; Gilli et al., 2014) could be the best progenitors of cQGs (see, e.g., Barro et al., 2013; Fu et al., 2013) observed at $1 \lesssim z \lesssim 3$. These objects indeed show compact morphologies,

| Source | Σ_{SFR} | Σ_{gas} | Σ_* | t_{dep} |
|--------|-----------------------|-----------------------|---------------|------------------|
| (1) | (2) | (3) | (4) | (5) |
| 42 | 198 ± 41 | 6.4 ± 3.8 | 0.7 ± 0.2 | 3.2 ± 2.0 |
| 170 | 108 ± 23 | 3.4 ± 2.0 | 1.7 ± 0.5 | 3.1 ± 2.0 |
| 337 | 195 ± 40 | 8.7 ± 5.1 | 8.7 ± 2.6 | 4.5 ± 2.8 |
| 539 | 169 ± 41 | 10.4 ± 6.1 | 2.1 ± 0.6 | 5.3 ± 3.3 |
| 551 | 288 ± 59 | 5.5 ± 3.3 | 3.5 ± 1.0 | 1.9 ± 1.2 |
| 666 | 338 ± 69 | 10.7 ± 6.3 | 0.8 ± 0.2 | 3.2 ± 2.0 |
| 746 | 166 ± 35 | 4.4 ± 2.6 | 6.0 ± 1.8 | 2.7 ± 1.7 |

Table 2.6: Surface densities of SFR, gas and stars together with gas depletion timescales of the target sample. (1) XID; (2) SFR surface density in units of $M_{\odot} \text{ yr}^{-1} \text{ kpc}^{-2}$; (3) gas surface density in units of $10^9 M_{\odot} \text{ kpc}^{-2}$; (4) stellar surface density in units of $10^{10} M_{\odot} \text{ kpc}^{-2}$; (5) depletion timescale in units of 10^7 yr .

with stellar half-light radii $r_{\text{half}} \sim 0.5 - 2 \text{ kpc}$ and stellar surface densities $\Sigma_* > 10^{10} M_{\odot} \text{ kpc}^{-2}$. The formation channels of the cQGs are still an open issue. However, we showed that our sources have a compact (sub-kpc for most of the sample) stellar core with stellar surface densities similar to those of cQGs observed at $z > 1$. This is in line with what has been found by Toft et al. (2014), who compared the properties of a sample of $z \gtrsim 3$ SMGs and $z \sim 2$ cQGs and concluded that SMGs evolve into cQGs. Based on the comoving number density of their samples, Toft et al. (2014) derived an SMG duty cycle of $\sim 42 \text{ Myr}$, which is in agreement with our estimates of the gas depletion timescale but is still independent of the arguments we used. According to the values derived for SFR, stellar mass, gas depletion timescale, and size, our targets could therefore be the progenitors of this type of systems.

2.7 Conclusions

We have presented a multiwavelength analysis of a sample of seven heavily obscured AGN and their host galaxies at high redshift in the CDF-S, which were selected because they have good detections in the FIR domain. By exploiting the superb datasets that are available in this field (spanning from the ultra-deep 7 Ms *Chandra* exposure to the broadband photometry of *HST*/CANDELS and *Herschel*, as well as ALMA), we were able to characterize the physical properties of the active nuclei and their hosts, and to place constraints on the role of the host ISM in obscuring the AGN. Our results are summarized below.

- We extracted the X-ray spectra from the 7 Ms *Chandra* dataset and derived obscuring column densities in the range $N_{\text{H}} = (0.07 - 3) \times 10^{24} \text{ cm}^{-2}$ and intrinsic rest-frame luminosities in the range $L_{[2-10 \text{ keV}]} = (2 - 7) \times 10^{44} \text{ erg s}^{-1}$. Moreover, we found that most of our targets feature prominent iron $\text{K}\alpha$ lines with $\text{EW} \gtrsim 0.5 \text{ keV}$, as expected in heavily obscured nuclei. Our combined X-ray and FIR selection hence returned a

sample made only of obscured AGN, which indicates a connection between the dust and gas content in the host ISM and nuclear obscuration.

- We built up the UV-to-FIR SEDs for our targets and analyzed them by means of an SED decomposition technique, from which we derived stellar masses in the range $M_* = (1.7-4.4) \times 10^{11} M_\odot$, total IR ($8-1000 \mu\text{m}$) luminosities $L_{\text{IR}} = (1.0-9.6) \times 10^{12} L_\odot$, and AGN bolometric luminosities $L_{\text{bol}} = (1.9 - 4.8) \times 10^{12} L_\odot$. Moreover, by subtracting the AGN contribution to the total IR luminosity, we measured star formation rates in the range $\text{SFR} = 192 - 1679 M_\odot \text{ yr}^{-1}$.
- We estimated the gas content of the host galaxies using the Scoville et al. (2016) calibration, which relates the intrinsic luminosity at $850 \mu\text{m}$ rest frame (derived from the model SED and interpreted as emission from dust heated by star formation) to the molecular gas mass, that is, the fuel for star formation activity. Our targets host large reservoirs of cold gas, with masses $M_{\text{gas}} = (0.8 - 5.4) \times 10^{10} M_\odot$. Under the assumption that the heated dust and gas are confined within regions of comparable size, we used ALMA dust-continuum data to assess this size for three of the seven targets. For the remaining targets, we assumed that the characteristic size of the region containing both gas and dust is about half the size measured by HST/CANDELS for the optical stellar emission, as seen on average in distant SMGs. The estimated ISM half-light radii for our sample are small, ranging between ~ 0.4 and 1.2 kpc.
- By adopting a simple geometrical model, specifically, a spherical gas distribution of uniform gas, we computed the column densities associated with the ISM of the host galaxy and showed that they are comparable to those measured from the X-ray spectral analysis.

Our result suggests that in high-redshift gas-rich systems, the obscuration of the nucleus may occur on large (kpc) scales and be produced by the ISM of the host. Obscuration by the ISM may then add to that produced by a small-scale circumnuclear medium (e.g., the torus of the unified model) and constitutes an important ingredient for understanding the coevolution of galaxies with their black holes.

Chapter 3

SUPER I. Toward an unbiased study of ionized outflows in $z \sim 2$ active galactic nuclei: survey overview and sample characterization

Published as C. Circosta, V. Mainieri, P. Padovani, G. Lanzuisi, M. Salvato, C. M. Harrison, D. Kakkad, A. Puglisi, G. Vietri, G. Zamorani, C. Cicone, B. Husemann, C. Vignali, B. Balmaverde, M. Bischetti, A. Bongiorno, M. Brusa, S. Carniani, F. Civano, A. Comastri, G. Cresci, C. Feruglio, F. Fiore, S. Fotopoulou, A. Karim, A. Lamastra, B. Magnelli, F. Mannucci, A. Marconi, A. Merloni, H. Netzer, M. Perna, E. Piconcelli, G. Rodighiero, E. Schinnerer, M. Schramm, A. Schulze, J. Silverman, L. Zappacosta; A&A, 620A, 82C (2018)

3.1 Introduction

Supermassive black holes (SMBHs) at the center of galaxies undergo periods of gas accretion becoming visible as active galactic nuclei (AGN). The enormous amount of energy released during these growth episodes is thought to shape the evolutionary path of AGN host galaxies. It may play a significant role in regulating and even quenching star formation in the galaxy by expelling gas out of the galaxy itself or preventing gas cooling. The process by which the energy is injected by the AGN and coupled to the surrounding medium is the so-called AGN feedback (Fabian, 2012; King & Pounds, 2015; Harrison, 2017). It can be particularly crucial at $z \sim 2$, since this redshift corresponds to the peak of star formation and SMBH accretion in the Universe (e.g., Madau & Dickinson, 2014) and therefore the energy injected by the central engine into the host galaxy may be maximized. However, the full details of the specific effects this may have on the host galaxy's life are still not clear.

Feedback of AGN is invoked from a theoretical perspective (e.g., Ciotti & Ostriker, 1997; Silk & Rees, 1998; Di Matteo et al., 2005; King, 2005; Somerville et al., 2008) to explain key observations of the galaxy population, such as the tight correlation between black hole masses and bulge masses as well as velocity dispersions of the host galaxies (Kormendy & Ho, 2013), the bimodal color distribution of galaxies (Strateva et al., 2001), and the lack of very massive galaxies in the most massive galaxy haloes (Somerville et al., 2008; Behroozi et al., 2013). According to some models (e.g., King, 2005; Springel et al., 2005; Debuhr et al., 2012; Costa et al., 2014), fast winds are launched by the accretion disk surrounding the SMBH and driven by radiative and mechanical energy during its active and bright phase. These winds propagate into the host galaxy coupling to the interstellar medium (ISM) and drive fast outflows out to large scales (up to ~ 1000 km s $^{-1}$ on kpc scales), potentially removing the gas which fuels star formation. It is important to test the models with observations by measuring key outflow properties such as kinetic energy and momentum injection rates (Fiore et al., 2017; Harrison et al., 2018).

AGN-driven outflows can therefore be a manifestation of AGN feedback. The presence of outflows in AGN host galaxies is now quite well established: they have been detected at different physical scales (e.g., Feruglio et al., 2010; Tombesi et al., 2015; Veilleux et al., 2017) and in different gas phases (e.g., Cano-Díaz et al., 2012; Cicone et al., 2014; Rupke et al., 2017), both in the nearby (e.g., Rupke & Veilleux, 2013; Perna et al., 2017) and distant Universe (e.g., Nesvadba et al., 2011; Carniani et al., 2015; Cicone et al., 2015). An important property shown by outflows is their multi-phase nature so to fully characterize them we need to trace all the gas phases, neutral and ionized, atomic and molecular (Cicone et al., 2018). The ionized phase has been studied through absorption and emission lines in rest-frame optical (e.g., Bae et al., 2017; Concas et al., 2017; Perna et al., 2017), ultraviolet (UV) (e.g., Liu et al., 2015) and X-ray (e.g., Tombesi et al., 2010). When the velocity shift of these lines with respect to the rest-frame velocity is not representative of ordered motion in the galaxy as traced by stellar kinematics, it can be considered as evidence for the presence of non-gravitational kinematic components, such as outflowing gas (Karouzos et al., 2016; Woo et al., 2016). To understand the impact of AGN outflows on the gas and star formation in the host galaxy, it is necessary to explore large galactic scales (~ 1 – 10 kpc). A commonly used diagnostic for this kind of studies is the forbidden emission line doublet [OIII] λ 5007,4959 Å. It traces the kinematics of ionized gas on galaxy-wide scales, in the narrow line region (NLR), since being a forbidden line it cannot be produced in the high-density environment of the broad line region (BLR) on sub-parsec scales. Therefore asymmetric [OIII] λ 5007 profiles, showing a broad and blue-shifted wing, are used to trace outflowing kinematic components.

Long-slit optical and near-infrared (NIR) spectroscopy is a useful technique to reveal outflow signatures (e.g., Das et al., 2005; Crenshaw & Kraemer, 2007; Brusa et al., 2015). However, it is able to provide spatial information along one direction, therefore lacking a detailed mapping of the outflow distribution in the host galaxy together with its velocity. In recent years, integral-field spectroscopy (IFS) studies have offered a more direct way to identify and interpret outflows, allowing astronomers to spatially resolve the kinematics of ionized gas (e.g., Cresci et al., 2009; Alexander et al., 2010; Gnerucci et al., 2011; Förster

Schreiber et al., 2014; Harrison, 2014). Nevertheless, the observational evidence available so far at $z > 1$, the crucial cosmic epoch to study AGN-driven outflows and on which this work is focused, is sparse, mainly limited to bright objects or observations performed in seeing limited conditions and therefore not able to resolve scales below 3–4 kpc, which limits how well the observations can constrain model predictions (Harrison et al., 2018). In Figure 3.1 we collect IFS results from the literature tracing ionized outflows in AGN host galaxies through the [OIII] emission line. The left panel compares AGN bolometric luminosities and redshift for each target, in order to summarize the state-of-the-art of ionized AGN outflow IFS studies. Contrary to the uniform coverage of the parameter space at $z < 1$ (gray crosses in Figure 3.1, *left panel*), at $z > 1$ it is limited to a small number of objects, mainly at high luminosity ($L_{\text{bol}} > 10^{46}$ erg s $^{-1}$, see points in Figure 3.1, *left panel*). The targets of previous studies are mostly selected to increase the chances to detect an outflow, meaning because they are powerful AGN (e.g., in the IR or radio regime), they have already known outflows or characteristics suitable for being in an outflowing phase (e.g., high mass accretion rate of the SMBH and high column density; Brusa et al., 2015; Kakkad et al., 2016). Because of this observational bias, it is still controversial how common these outflows are especially in sources with low AGN bolometric luminosity. Nevertheless, detailed single object studies have provided evidence that powerful outflows may suppress star formation in the regions where they are detected (e.g., Cano-Díaz et al., 2012; Cresci et al., 2015; Carniani et al., 2016), although it is still not clear the impact that such outflows may have on the global star-forming activity occurring in the host galaxy (i.e., including regions of the galaxies not affected by the outflow). In addition to negative feedback mechanisms, outflows have been proved to be responsible for positive feedback mechanisms in a few cases by triggering star formation (e.g., Cresci et al., 2015; Molnár et al., 2017; Cresci & Maiolino, 2018).

In order to draw a coherent picture and definitively address the impact of such outflows on the galaxy population evolution it is necessary to conduct systematic and unbiased searches for outflows in large samples of objects. The KMOS AGN Survey at High redshift (KASHz; Harrison et al., 2016a, Harrison et al., in prep.; blue rectangle in Figure 3.1, *left panel*) has first started to provide spatially-resolved information for hundreds of X-ray selected AGN. These observations are seeing limited, which sets a limit on the spatial scales that can be resolved at $z > 1$. The range of spatial scales resolved in current observations is shown in the right panel of Figure 3.1, plotted as a function of redshift for the same collection of data as in the left panel. At $z > 1$, the spatial resolution is mainly in the range 3–10 kpc (i.e., $>0.5''$).

To provide higher spatial resolutions (down to ~ 2 kpc at $z \sim 2$), one needs to exploit the possibilities offered by adaptive optics (AO), which corrects for the distortion caused by the turbulence of the Earth’s atmosphere. This has been done by, e.g., Perna et al. (2015), Brusa et al. (2016), Vayner et al. (2017) and Vietri et al. (2018). Such observations require a larger amount of observing time, therefore it is necessary to focus on smaller but still representative samples. Our on-going ESO Large Programme called SUPER (the SINFONI Survey for Unveiling the Physics and Effect of Radiative feedback), represented by the red rectangle in Figure 3.1, is taking advantage of the AO corrections by reaching angular resolutions of $0.2''$. It combines spatially-resolved AO-assisted IFS observations

for a fairly representative sample of sources selected in an unbiased way with respect to the chance of detecting outflows, aiming at investigating the physical properties of AGN outflows and their impact on the star formation activity in the host galaxies as well as connecting the physical properties of AGN and host galaxies to those of ionized outflows. As shown in Figure 3.1, SUPER probes a wide range of AGN bolometric luminosities, up to four orders of magnitude, with spatial resolutions between ~ 1.7 and 4 kpc (i.e., $0.2'' - 0.5''$).

This work is the first of a series of publications dedicated to the survey. It focuses on providing an overview of the survey (i.e., characteristics, goals and sample selection criteria), as well as describing the physical properties of the target sample and the way they have been measured through a uniform multi-wavelength analysis from the X-ray to the radio regime. We derive stellar masses, star formation rates (SFRs) and AGN bolometric luminosities from the multi-wavelength spectral energy distributions (SEDs), X-ray luminosities and column densities from the X-ray spectra and BH masses and Eddington ratios from the optical spectra. The Chapter is organized as follows: in Sec. 3.2 we present the properties and the main goals of the survey as well as the sample selection criteria and its X-ray properties. In Sec 3.3 we describe the multi-wavelength dataset and the SED-fitting code used to derive host galaxy and AGN properties of the targets. These properties are then discussed in Sec. 3.4, with particular emphasis on stellar masses, SFRs and AGN bolometric luminosities as well as the target properties in the radio regime. We finally summarize our results and discuss future follow-up work in Sec. 3.5. In this Chapter we adopt a *WMAP9* cosmology (Hinshaw et al., 2013), $H_0 = 69.3 \text{ km s}^{-1} \text{ Mpc}^{-1}$, $\Omega_M = 0.287$ and $\Omega_\Lambda = 0.713$.

3.2 The survey

SUPER¹ (PI: Mainieri - 196.A-0377) is a Large Programme at the ESO's Very Large Telescope (VLT). The survey has been allocated 280 hours of observing time in AO-assisted mode with the aim of providing high-resolution, spatially-resolved IFS observations of multiple emission lines for a carefully-selected sample of 39 X-ray AGN at $z \sim 2$. The AO correction is performed in Laser Guide Star-Seeing Enhancer (LGS-SE) mode, which has demonstrated the capability to achieve a point spread function (PSF) full width at half maximum (FWHM) of $\sim 0.3''$ under typical weather conditions in Paranal (Förster Schreiber et al., 2018), that is average seeing of $\sim 0.55''$ in *K* band (Sarazin et al., 2008). We have selected for all our targets the 50 mas/pixel scale of SINFONI which corresponds to a total field of view $\text{FOV} = 3.2'' \times 3.2''$. The selected plate scale corresponds to a spectral resolution of about $R \approx 2730$ in *H* band and $R \approx 5090$ in *K* band.

The redshift range covered by SUPER is crucial to investigate AGN feedback, being at the peak epoch of AGN and galaxy assembly. Key emission lines, such as [OIII], $H\beta$ and $H\alpha$, are covered with *H*- and *K*-band observations in this redshift range. We will use asymmetric and spatially-extended [OIII] line emission, traced by *H*-band observations, to

¹<https://www.super-survey.org>

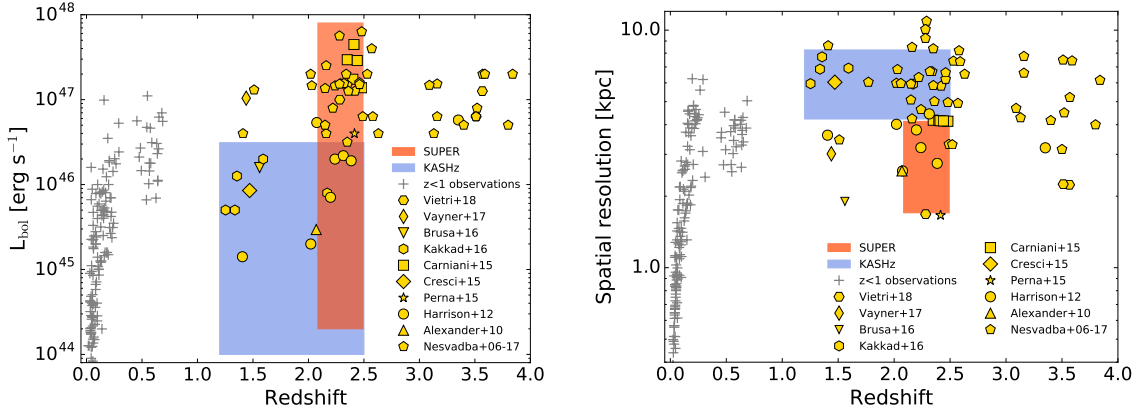


Figure 3.1: Summary of IFS observations from the literature characterizing ionized outflows through the $[\text{OIII}]\lambda 5007$ emission line in AGN host galaxies. *Left*: For each observation we plot the AGN bolometric luminosity of the source, in units of erg s^{-1} , as a function of redshift. The red and blue shaded areas show the parameter space probed by SUPER and KASHz (Harrison et al., 2016a, Harrison et al., in prep.), respectively. Excluding these two surveys, current observations at $z > 1$ are limited to a smaller number of objects, mainly at high luminosity ($L_{\text{bol}} > 10^{46} \text{ erg s}^{-1}$) and focused on targets mostly selected to increase the chances to detect an outflow. SUPER will be able to explore a wide range in bolometric luminosities ($10^{44} < L_{\text{bol}} < 10^{48} \text{ erg s}^{-1}$) for an unbiased sample of AGN. The gray crosses represent observations at $z < 1$ (Bae et al., 2017; Rupke et al., 2017; Karouzos et al., 2016; Harrison, 2014; Husemann et al., 2013, 2014, 2017b; Liu et al., 2013, 2014) covering the parameter space much more uniformly than high-redshift observations available so far (Vietri et al., 2018; Vayner et al., 2017; Brusa et al., 2016; Kakkad et al., 2016; Carniani et al., 2015; Cresci et al., 2015; Perna et al., 2015; Harrison et al., 2012b; Alexander et al., 2010; Nesvadba et al., 2006, 2007, 2008, 2011, 2017a,b). All AGN bolometric luminosities, when not available in the papers, have been obtained consistently either as indicated in the papers themselves or from the observed $[\text{OIII}]$ luminosity adopting a conversion factor of 3500 (Heckman et al., 2004). *Right*: Spatial resolution, in kpc, of the observations shown in the left panel as a function of redshift. The angular resolutions from which the values plotted are derived, are taken from the respective papers and given by the seeing of the observations or from the size of the PSF. SUPER observations will allow us to reach an unprecedented spatial resolution (i.e., $\sim 1.7\text{--}4$ kpc) for a sizeable sample of 39 AGN, obtained just by a few single-object studies so far at similar redshift.

identify outflowing ionized gas as extensively done in the literature (e.g., Alexander et al., 2010; Cresci et al., 2015; Harrison et al., 2016a). The K -band observations will provide the possibility to map the $H\alpha$ emission, with the aim to construct spatially-resolved maps of the on-going star formation in the host from the narrow component of the line, which could be less affected by AGN emission, and compare it with the outflow geometry derived from the [OIII] line profile (see, e.g., Cano-Díaz et al., 2012; Cresci et al., 2015; Carniani et al., 2016). The comparison between these two tracers will give us the opportunity to constrain systematically the role of AGN outflows in regulating star formation. Thanks to the extensive set of AGN and host galaxy physical properties (AGN bolometric luminosity, BH mass, Eddington ratio, obscuring column density, radio emission, stellar mass and SFR), derived in a uniform way for each target as explained in the present Chapter, and outflow parameters which will be extracted from the H -band observations (such as mass outflow rate, kinetic power, momentum rate, size), SUPER will explore the potential relations among these quantities (Fiore et al., 2017).

The science goals of our survey are:

- Systematic study of the occurrence of outflows in AGN host galaxies and investigation of any possible link between the physical properties of both SMBHs and their hosts, and the outflow properties.
- Mapping AGN ionized outflow morphology on kpc scale using [OIII] and constraining their impact on the on-going star formation in the host galaxies using the narrow component of $H\alpha$. If the signal-to-noise of the latter is not good enough to produce spatially-resolved maps of star formation, we should still be able to compare the outflow properties with the integrated SFR (as derived by SED fitting).
- Investigating the variation of outflow properties as a function of the host galaxy location with respect to the main sequence of star-forming galaxies (MS, e.g., Noeske et al., 2007), in order to investigate empirically the relation between galaxy and AGN.

An important further goal of this survey will be the comparison of our results to a mass-matched control sample of normal star-forming galaxies at the same redshift and with similar AO-assisted observations (e.g., the SINS/ z C-SINF survey, Förster Schreiber et al., 2018, see Sec. 3.4.1), to investigate the differences between galaxies hosting active and inactive SMBHs.

In the following we describe the criteria adopted to select our sample.

3.2.1 Sample selection

Our Large Programme is designed to conduct a blind search for AGN-driven outflows on a representative sample of AGN. Therefore, we do not preselect AGN with already known outflows or with characteristics suitable for being in an outflowing phase (Brusa et al., 2015; Kakkad et al., 2016). Instead, aiming at performing a statistical investigation of this phenomenon, the first goal is to cover the widest possible range in AGN properties.

One of the most efficient tracers of AGN activity is offered by their X-ray emission, since it probes directly the active nucleus with a negligible contamination from the host galaxy, providing the largest AGN surface density (e.g., Padovani et al., 2017). We identified our targets by combining X-ray catalogs from several surveys characterized by different depths and areas. While shallow and wide-field surveys provide a better census of the rare high-luminosity AGN, deep and small-area surveys, limited to a few deg^2 , are able to reveal fainter sources (see Fig. 3 in Brandt & Alexander, 2015). By adopting this “wedding cake” approach we are able to cover a wide range in AGN bolometric luminosity, $10^{44} < L_{\text{bol}} < 10^{48} \text{ erg s}^{-1}$ (see Fig. 3.1), spanning both faint and bright AGN. The selection was performed by adopting as a threshold an absorption-corrected X-ray luminosity $L_X \geq 10^{42} \text{ erg s}^{-1}$ from the following surveys:

- The *Chandra* Deep Field-South (CDF-S; Luo et al., 2017), the deepest X-ray survey to date which covers a global area of 484.2 arcmin^2 observed for a total *Chandra* exposure time of ~ 7 Ms, reaching a sensitivity of $\sim 1.9 \times 10^{-17} \text{ erg cm}^{-2} \text{ s}^{-1}$ in the full 0.5 – 7.0 keV band.
- The *COSMOS-Legacy* survey (Civano et al., 2016; Marchesi et al., 2016a), a 4.6 Ms *Chandra* observation of the COSMOS field, which offers a unique combination of deep exposure over an area of about 2.2 deg^2 at a limiting depth of $8.9 \times 10^{-16} \text{ erg cm}^{-2} \text{ s}^{-1}$ in the 0.5 – 10 keV band.
- The wide-area *XMM-Newton* XXL survey (Pierre et al., 2016), where we focus in particular on the equatorial sub-region of the XMM-XXL North, a $\sim 25 \text{ deg}^2$ field surveyed for about 3 Ms by *XMM-Newton* with a sensitivity in the full 0.5 – 10 keV band of $2 \times 10^{-15} \text{ erg cm}^{-2} \text{ s}^{-1}$.
- The Stripe 82 X-ray survey (Stripe82X; LaMassa et al., 2016; Ananna et al., 2017), ~ 980 ks of observing time with *XMM-Newton* covering 31.3 deg^2 of the Sloan Digital Sky Survey (SDSS) Stripe 82 Legacy Field and a flux limit of $2.1 \times 10^{-15} \text{ erg cm}^{-2} \text{ s}^{-1}$ in the full 0.5 – 10 keV band.
- The WISE/SDSS selected Hyper-luminous quasars sample (WISSH; Bischetti et al., 2017; Duras et al., 2017; Martocchia et al., 2017; Vietri et al., 2018), with both proprietary and archival *Chandra* and *XMM-Newton* observations available, described in Martocchia et al. (2017).

The choice of the fields was driven by their visibility from Paranal and the rich multi-wavelength photometric coverage from the UV to the far-infrared (FIR), needed to obtain robust measurements of the target properties by using an SED-fitting technique. Our targets are then selected to meet the following criteria:

1. Spectroscopic redshift in the range $z = 2.0 - 2.5$, whose quality was flagged as “Secure” in the respective catalogs. This redshift range was chosen in order to have $\text{H}\beta$ and $[\text{OIII}]$ included in *H*-band and $\text{H}\alpha$ in *K*-band together with their potential

broad line components, by allowing a margin of $10\,000\text{ km s}^{-1}$ between the peak of the lines and the edges of the filter bands.

2. Observed wavelengths for [OIII] and H α characterized by a low contamination from the strong telluric OH lines, which affect NIR observations.

The resulting sample consists of 39 AGN (namely 6 from CDF-S, 16 from COSMOS, 10 from XMM-XXL, 4 from Stripe82X and 3 from the WISSH sample), whose IDs, coordinates, redshifts as well as H - and K -band magnitudes (AB) are reported in Table 3.1. This sample results from an optimization between size, the amount of observing time required to carry out the observations, and a wide and uniform coverage in AGN bolometric luminosities, Eddington ratios, and column densities. All our targets have spectroscopic redshifts based on optical spectroscopic campaigns: for example VLT/VIMOS and FORS2 surveys for the CDF-S (Balestra et al., 2010; Kurk et al., 2013); for the COSMOS field, a master spectroscopic catalog is available within the COSMOS collaboration (Salvato et al., in prep.) and includes results from several spectroscopic surveys of this field (see Marchesi et al., 2016a); SDSS-BOSS spectra for the XMM-XXL field (Menzel et al., 2016); SDSS-DR12 for Stripe82X (LaMassa et al., 2016); SDSS-DR10 and LBT/LUCI1 redshifts for the WISSH subsample (Bischetti et al., 2017). Thanks to the parameter space covered by the survey (Fig. 3.1, *left panel*), we will be able to probe AGN bolometric luminosities in the range $44 \lesssim \log(L_{\text{bol}}/\text{erg s}^{-1}) \lesssim 48$, not covered so far by a coherent high spatial resolution observing program at this redshift.

| Field | ID | RA[J2000] | DEC[J2000] | z_{spec} | H -band mag | K -band mag |
|---------|--------------------|--------------|--------------|-------------------|---------------|---------------|
| (1) | (2) | (3) | (4) | (5) | (6) | (7) |
| XMM-XXL | X_N_160.22 | 02:04:53.81 | -06:04:07.82 | 2.445 | 19.22 | 18.79 |
| | X_N_81.44 | 02:17:30.95 | -04:18:23.66 | 2.311 | 18.78 | 18.43 |
| | X_N_53.3 | 02:20:29.84 | -02:56:23.41 | 2.434 | 20.60 | - |
| | X_N_66.23 | 02:22:33.64 | -05:49:02.73 | 2.386 | 20.56 | 20.33 |
| | X_N_35.20 | 02:24:02.71 | -05:11:30.82 | 2.261 | 22.07 | 21.70 |
| | X_N_12.26 | 02:25:50.09 | -03:06:41.16 | 2.471 | 19.83 | 19.53 |
| | X_N_44.64 | 02:27:01.46 | -04:05:06.73 | 2.252 | 21.31 | 20.77 |
| | X_N_4.48 | 02:27:44.63 | -03:42:05.46 | 2.317 | 19.57 | 20.43 |
| | X_N_102.35 | 02:29:05.94 | -04:02:42.99 | 2.190 | 18.76 | 18.19 |
| | X_N_115.23 | 02:30:05.66 | -05:08:14.10 | 2.342 | 19.79 | 19.26 |
| CDF-S | XID36 | 03:31:50.77 | -27:47:03.41 | 2.259 | 21.49 | 20.80 |
| | XID57 ^a | 03:31:54.40 | -27:56:49.70 | 2.298 | 23.49 | 22.19 |
| | XID419 | 03:32:23.44 | -27:42:54.97 | 2.145 | 22.44 | 21.84 |
| | XID427 | 03:32:24.20 | -27:42:57.51 | 2.303 | 22.48 | 21.83 |
| | XID522 | 03:32:28.50 | -27:46:57.99 | 2.309 | 22.98 | 22.27 |
| | XID614 | 03:32:33.02 | -27:42:00.33 | 2.448 | 22.59 | 21.82 |
| COSMOS | cid_166 | 09:58:58.68 | +02:01:39.22 | 2.448 | 18.55 | 18.23 |
| | lid_1289 | 09:59:14.65 | +01:36:34.99 | 2.408 | 22.29 | 21.51 |
| | cid_1057 | 09:59:15.00 | +02:06:39.65 | 2.214 | 21.70 | 21.09 |
| | cid_1605 | 09:59:19.82 | +02:42:38.73 | 2.121 | 20.63 | 20.14 |
| | cid_337 | 09:59:30.39 | +02:06:56.08 | 2.226 | 22.12 | 21.54 |
| | cid_346 | 09:59:43.41 | +02:07:07.44 | 2.219 | 19.24 | 18.95 |
| | cid_451 | 10:00:00.61 | +02:15:31.06 | 2.450 | 21.88 | 21.37 |
| | cid_1205 | 10:00:02.57 | +02:19:58.68 | 2.255 | 21.64 | 20.72 |
| | cid_2682 | 10:00:08.81 | +02:06:37.66 | 2.435 | 21.46 | 21.17 |
| | cid_1143 | 10:00:08.84 | +02:15:27.99 | 2.492 | 22.90 | 22.27 |
| | cid_467 | 10:00:24.48 | +02:06:19.76 | 2.288 | 19.34 | 18.91 |
| | cid_852 | 10:00:44.21 | +02:02:06.76 | 2.232 | 21.53 | 21.05 |
| cid_971 | 10:00:59.45 | +02:19:57.44 | 2.473 | 22.58 | 22.10 | |

| | | | | | | |
|-----------|------------|-------------|--------------|-------|-------|-------|
| | cid_38 | 10:01:02.83 | +02:03:16.63 | 2.192 | 20.42 | 20.21 |
| | lid_206 | 10:01:15.56 | +02:37:43.44 | 2.330 | 22.38 | 21.97 |
| | cid_1253 | 10:01:30.57 | +02:18:42.57 | 2.147 | 21.30 | 20.72 |
| WISSH | J1333+1649 | 13:33:35.79 | +16:49:03.96 | 2.089 | 15.72 | 15.49 |
| | J1441+0454 | 14:41:05.54 | +04:54:54.96 | 2.059 | 17.15 | 16.53 |
| | J1549+1245 | 15:49:38.73 | +12:45:09.20 | 2.365 | 15.92 | 15.34 |
| Stripe82X | S82X1905 | 23:28:56.35 | -00:30:11.74 | 2.263 | 19.72 | 19.15 |
| | S82X1940 | 23:29:40.28 | -00:17:51.68 | 2.351 | 20.80 | 20.15 |
| | S82X2058 | 23:31:58.62 | -00:54:10.44 | 2.308 | 19.79 | 19.29 |
| | S82X2106 | 23:32:53.24 | -00:33:35.35 | 2.281 | 20.56 | 20.23 |

Table 3.1: Summary of the target AGN sample. (1) Field where the targets are located. (2) Source identification number from the catalogs corresponding to each field, namely Menzel et al. (2016), Luo et al. (2017), Civano et al. (2016), Martocchia et al. (2017) and LaMassa et al. (2016), respectively (see also Sec. 3.2.1). (3) RA and (4) DEC, given for the optical counterpart: the XMM-XXL targets have an SDSS counterpart whose coordinates are given in Menzel et al. (2016); for the targets in the CDF-S we report the CANDELS coordinates when available (we use the GEMS coordinates from Häussler et al. (2007) for the targets XID36 and XID57 since they are outside the CANDELS area), as given in Luo et al. (2017); for the COSMOS field we list the i -band coordinates taken from Marchesi et al. (2016a); the information for the WISSH subsample are available in Martocchia et al. (2017); for the targets in Stripe82X we give the SDSS coordinates from LaMassa et al. (2016). (5) Spectroscopic redshift, taken from the papers listed above. (6) H -band and (7) K -band AB magnitudes.

^aWe took the redshift available in Xue et al. (2016), since Luo et al. (2017) provide a different redshift flagged as “Insecure”.

3.2.2 X-ray properties of the sample

As described in Sec. 3.2.1, our survey sample is selected from available X-ray AGN surveys. Apart from the source detection, these X-ray observations provide us with important information on the AGN properties from the analysis of their X-ray spectra. Since the obscuring column densities N_{H} and the X-ray luminosities L_{X} available from the various survey catalogs may be affected by inhomogeneities due to the adoption of different analysis methods and spectral models, we decided to perform a new systematic analysis of all the X-ray spectra, by using XSPEC v.12.9.1² (Arnaud, 1996). For this purpose, we followed the method described in Lanzuisi et al. (2013) and Marchesi et al. (2016b) for *XMM-Newton* and *Chandra* data respectively, which have been extensively tested in the low count regime typical of the current data set. *Chandra* and *XMM-Newton* spectra of sources in the COSMOS field are extracted following Lanzuisi et al. (2013) and Mainieri et al. (2011), respectively. For sources in the CDF-S we followed the approach described in Vito et al. (2013), applied to the full 7 Ms data set (Luo et al., 2017). For sources in XMM-XXL, Stripe82X and WISSH (SDSS targets), we extracted new *XMM-Newton* spectra adopting a standard data reduction procedure³ (background flare removal, “single” and “double” event selection, CCD edge and bad pixels removal) and standard source, background and response matrix extraction from circular regions, whose radii were chosen to maximize the signal-to-noise ratio (e.g., Liu et al., 2016, for XMM-XXL). Typical background regions are ~ 10 times the source extraction regions. We considered the 0.5 – 7.0 keV band for *Chandra* and 0.5 – 10 keV band for *XMM-Newton*. All the fits were performed by using the Cash statistic (Cash, 1979) and the direct background option (Wachter et al., 1979). The spectra are binned to 1 count per bin to avoid empty channels.

For sources with more than 30 (50) net counts (reported in Table B.2) for *Chandra* (*XMM-Newton*), we performed a simple spectral fit, modeling the emission with an absorbed power law plus Galactic absorption as well as a secondary power law to reproduce any excess in the soft band, due to scattering or partial covering in obscured sources. In 11 cases out of 39 this second component gave a significant contribution to the fit, while in the other cases its normalization was consistent with 0. The photon index was left free to vary during the spectral analysis for spectra with more than ~ 100 net counts (typical values within $\Gamma = 1.5 - 2.5$), otherwise we fixed it to the canonical value of 1.8 (e.g., Piconcelli et al., 2005), being mainly interested in deriving reliable N_{H} and L_{X} values. For targets with less than 30 (50) counts, we relied on hardness ratios ($HR = \frac{H-S}{H+S}$, where H and S are the number of counts in the hard 2 – 7 keV and soft 0.5 – 2 keV bands, respectively), converted into N_{H} values at the source redshift following Lanzuisi et al. (2009).

Both in the case of spectral analysis and HR , we propagated the uncertainty on N_{H} when deriving the errors on the intrinsic luminosity. This is in fact the main source of uncertainty in L_{X} , at least for obscured sources. We compared our results for the targets in the COSMOS field with those presented by Marchesi et al. (2016b), who performed X-ray spectral analysis for all the targets with more than 30 counts in the 0.5 – 7 keV band.

²<https://heasarc.gsfc.nasa.gov/xanadu/xspec/>

³We used SAS v.16.0.0, https://heasarc.gsfc.nasa.gov/docs/xmm/xmmhp_analysis.html

Ten out of sixteen of our COSMOS targets were analyzed in Marchesi et al. (2016b), for which the comparison results in an average $\langle \log(L_{X, \text{literature}}/L_{X, \text{this work}}) \rangle = -0.08$ dex and $\langle \log(N_{\text{H, literature}}/N_{\text{H, this work}}) \rangle = 0.07$ dex, as well as a standard deviation of 0.2 and 0.3 dex, respectively.

The results derived for column densities and 2 – 10 keV absorption-corrected luminosities are listed in Table B.2 (Appendix B). X-ray luminosities range between $L_X = 1.6 \times 10^{43}$ erg s $^{-1}$ and 6.5×10^{45} erg s $^{-1}$, therefore including AGN with Seyfert-like X-ray luminosities ($L_X \sim 10^{42} - 10^{44}$ erg s $^{-1}$) and quasar-like ones ($L_X > 10^{44}$ erg s $^{-1}$). In terms of column densities, the target sample covers uniformly a range from unobscured ($N_{\text{H}} \leq 10^{20}$ cm $^{-2}$, given by the Galactic value) to obscured and Compton-thick AGN ($N_{\text{H}} > 10^{24}$ cm $^{-2}$), with values up to 2×10^{24} cm $^{-2}$. For the objects whose column density derived from the X-ray spectral analysis is $\sim 10^{20}$ cm $^{-2}$ we provide 90% confidence level upper limits. From an X-ray point of view, AGN are classified as unobscured when $N_{\text{H}} < 10^{22}$ cm $^{-2}$ and obscured vice versa. Overall the sample is split in almost an equal number of unobscured and obscured objects based on the X-ray classification. Further discussion about these results, in relation to other physical properties of our targets, is presented in Sec. 3.4.2.

3.3 Target sample characterization

To draw a wide and complete picture of the physical properties of our AGN and host galaxies, a full multi-wavelength support is needed. We make use of the rich suite of multi-wavelength ancillary data available for these targets, which are unique in terms of amount and depth. They range from the X-rays (Sec. 3.2.1) to the optical, NIR and FIR regimes, and up to the radio (see Sec. 3.4.3). This allows us to gather information about AGN quantities, such as obscuring column density, X-ray and bolometric luminosity, BH mass, as well as galaxy ones, such as stellar mass and SFR.

In this Section we describe the ancillary data collected for this work from the UV to the FIR when available, as well as the code used to perform the SED-fitting analysis of the target sample.

3.3.1 Multi-wavelength dataset

The counterparts to the X-ray sources in the CDF-S and COSMOS are provided along with the optical-to-MIR multi-wavelength photometry by the original catalogs (Hsu et al., 2014; Laigle et al., 2016), where in both cases images were previously registered at the same reference and the photometry was PSF-homogenized. The counterparts to the SUPER targets in XMM-XXL and Stripe82X are known in the SDSS optical images and the corresponding associations to the X-ray sources are likewise given in the original catalogs (Fotopoulou et al., 2016; LaMassa et al., 2016; Ananna et al., 2017). The remaining SDSS targets are WISE selected with follow-up in the X-ray band (Martocchia et al., 2017).

We complemented the UV-to-MIR photometry with further FIR data from *Herschel*/PACS and SPIRE, when available, using a positional matching radius of 2'', taking into

account that we used 24 μm -prior catalogues which in turn are IRAC-3.6 μm prior. Here we briefly describe the multi-wavelength data set used for this study but further information can be found in the specific papers mentioned for each field in the following. In Table 3.2 we summarize the wavelength bands used to build the SEDs of our AGN.

CDF-S

The multi-wavelength catalogue used for this field, presented in Hsu et al. (2014), provides UV-to-MIR photometric data for all the sources detected in the Extended *Chandra* Deep Field-South (E-CDF-S; Xue et al., 2016; Lehmer et al., 2005), combining data from CANDELS (Guo et al., 2013), MUSYC (Cardamone et al., 2010) and TENIS (Hsieh et al., 2012). MIR and FIR photometry at 24 μm with *Spitzer*/MIPS and at 70, 100 and 160 μm with *Herschel*/PACS is presented by Magnelli et al. (2013), combining observations from the PACS Evolutionary Probe (PEP; Lutz et al., 2011) and the GOODS-*Herschel* programs (GOODS-H; Elbaz et al., 2011). *Herschel*/SPIRE fluxes at 250, 350 and 500 μm are taken from the *Herschel* Multi-tiered Extragalactic Survey (HerMES; Roseboom et al., 2010, 2012; Oliver et al., 2012) DR3. We point out that the HerMES team provides also *Herschel*/PACS photometry for the same field. However, we decided to take advantage of the deeper data released by the PEP team, after verifying the consistency of the fluxes obtained by both teams. Two out of the six targets in the CDF-S are outside the area covered by CANDELS (namely XID36 and XID57). Therefore, we adopted FIR observations at 100 and 160 μm from the PEP DR1 (Lutz et al., 2011), since the data products released by Magnelli et al. (2013) cover the GOODS-S field only. The prior information for these FIR catalogues is given by IRAC-3.6 μm source positions. To this data set, we added ALMA data in Band 7 and 3 available from the ALMA Archive and Scholtz et al. (2018).

COSMOS

The UV-to-MIR photometry is taken from the COSMOS2015 catalogue presented in Laigle et al. (2016), combining existing data from previous releases (e.g., Capak et al., 2007; Ilbert et al., 2009, 2013) and new NIR photometry from the UltraVISTA-DR2 survey, Y-band observations from Subaru and infrared data from *Spitzer*. The source detection is based on deep NIR images and all the photometry is obtained from images registered at the same reference. *Spitzer*/MIPS photometry at 24 μm and *Herschel*/PACS at 100 and 160 μm is taken from the PEP DR1 (Lutz et al., 2011) extracted using IRAC-3.6 μm source position priors, as mentioned above. The 24 μm data for the targets cid_971 and lid_206 were provided by Le Floch (priv. comm.), since they are particularly faint in this band and therefore not reported in the original catalogue. *Herschel*/SPIRE photometry at 250, 350 and 500 μm is retrieved from the data products presented in Hurley et al. (2017), who describe the 24 μm prior-based source extraction tool XID+, developed using a probabilistic Bayesian method. The resulting flux probability distributions for each source in the catalogue are described by the 50th, 84th and 16th percentiles. We assumed Gaussian uncertainties by taking the maximum between the 84th-50th percentile and the 50th-16th percentile.

As done for the CDF-S, we added ALMA data in Band 7 and 3 available from the ALMA Archive and Scholtz et al. (2018).

XMM-XXL North

The multi-wavelength photometry from UV-to-MIR for this field is obtained by merging the photometric SDSS and CFHTLenS (Erben et al., 2013) optical catalogs (see Fotopoulou et al., 2016; Georgakakis et al., 2017). These data were complemented with GALEX/NUV photometry, *YZJHK* band photometry from VISTA as well as *u* and *i* bands from CFHT (see Fotopoulou et al., 2016). We considered total magnitudes for CFHTLenS data and model mag for SDSS. As for IRAC, we considered aperture 2 (1.9'') photometry corrected to total. The WISE data are taken from Lang et al. (2016), who provide forced photometry of the WISE All-sky imaging at SDSS positions. *Herschel*/PACS and SPIRE data are those released by the HerMES collaboration in the Data Release 4 and 3 respectively (Oliver et al., 2012). Both sets of data are extracted using the same *Spitzer*/MIPS 24 μm prior catalog, whose fluxes are available along with the SPIRE data. We use aperture fluxes in smaller apertures, that is 4'' diameter.

Stripe82X

We used the photometry that was made public in Ananna et al. (2017) and was used for the computation of the photometric redshifts in the field. The data are homogeneously deep in optical (Fliri & Trujillo, 2016), but in the NIR and MIR a patchwork of surveys was used (see Ananna et al., 2017, and its Fig. 1). Similarly to the XMM-XXL photometry, we took WISE data from Lang et al. (2016).

WISSH

For these targets we collected UV-to-MIR photometry from the WISSH photometric catalog (Duras et al., in prep.), which includes SDSS photometry, NIR data from the 2MASS as well as WISE photometry from 3 to 22 μm (see Duras et al., 2017, for further details).

All the data used in this work are corrected for Galactic extinction (Schlegel et al., 1998). The resulting photometry, from NUV to FIR, spans a maximum of 31, 36, 27, 12 and 17 wavebands overall for XMM-XXL, CDF-S, COSMOS, WISSH and Stripe82X, respectively. However there is some overlap among bands from different surveys, which reduces the number of unique wavebands. As far as the mid and far-IR photometry from 24 to 500 μm is concerned, we considered as detections only photometric points with $S/N > 3$, where the total noise is given by the sum in quadrature of both the instrumental and the confusion ones (Lutz et al., 2011; Oliver et al., 2012; Magnelli et al., 2013). The detections below this threshold were converted to 3σ upper limits. The number of targets with ($\geq 3\sigma$) *Herschel* detections in at least one PACS band is 7 out of 39, while there are 12 out of 39 targets with at least one SPIRE band detection. Five sources present detections in both PACS and SPIRE filters. All the targets have photometric data available from the UV to the MIR.

Although these data enable a detailed SED modeling, they are collected and/or stacked over many years, so that issues related to variability (intrinsic properties of AGN) can potentially arise (e.g., Simm et al., 2016). While we cannot correct for variability in case of stacked images, we were able to correct this issue for the AGN whose photometry was taken in the same wavebands from different surveys. Clear variability was shown by the XMM-XXL targets X_N_4_48, X_N_35_20 and X_N_44.64, for which the SDSS photometry was brighter than the CFHT one by up to two magnitudes. We have taken the latter since it is closer in time to the X-ray observations.

| Field | λ range | Reference | Telescope/Instrument | Bands | | |
|------------------------|--|--|-----------------------------|--|------|-----------------------------------|
| XMM-XXL | UV to MIR | Georgakakis et al. (2017) and Fotopoulou et al. (2016) | GALEX | NUV | | |
| | | | CFHT | u, g, r, i, z | | |
| | | | SDSS | u, g, r, i, z | | |
| | | | VISTA | z, Y, J, H, K | | |
| | | | <i>Spitzer</i> /IRAC | 3.6, 4.5, 5.8, 8.0 μm | | |
| | | | WISE | $W1, W2, W3, W4$ | | |
| | | | <i>Spitzer</i> /MIPS | 24 μm | | |
| 24 – 500 μm | Lang et al. (2016) Oliver et al. (2012) | <i>Herschel</i> /PACS | 70, 100, 160 μm | | | |
| | | <i>Herschel</i> /SPIRE | 250, 350, 500 μm | | | |
| | | CTIO-Blanco/Mosaic-II | | U | | |
| | | VLT/VIMOS | | U | | |
| CDF-S | UV to MIR | Hsu et al. (2014) | HST/ACS | F435W, F606W, F775W, F814W, F850LP | | |
| | | | HST/WFC3 | F098M, F105W, F125W, F160W | | |
| | | | ESO-MPG/WFI | $UU_{38}BVR I$ | | |
| | | | CTIO-Blanco/Mosaic-II | z -band | | |
| | | | NTT/SofI | H -band | | |
| | | | CTIO-Blanco/ISPI | J, K | | |
| | | | VLT/ISAAC | K_S | | |
| | | | VLT/HAWK-I | K_S | | |
| | | | <i>Spitzer</i> /IRAC | 3.6, 4.5, 5.8, 8.0 μm | | |
| | | | <i>Spitzer</i> /MIPS | 24 μm | | |
| | | | <i>Herschel</i> /PACS | 70, 100, 160 μm | | |
| | | | <i>Herschel</i> /SPIRE | 250, 350, 500 μm | | |
| | | | 24 – 160 μm | Magnelli et al. (2013) or Lutz et al. (2011) | ALMA | Band 7 (800–1100 μm) |
| | | | 250 – 500 μm | Oliver et al. (2012) | ALMA | Band 3 (2600–3600 μm) |
| > 1000 μm | Scholtz et al. (2018) and ALMA Archive | | | | | |
| COSMOS | UV to MIR | Laigle et al. (2016) | GALEX | NUV | | |
| | | | CFHT/MegaCam | u^* | | |
| | | | Subaru/Suprime-Cam | B, V, r, i^+, z^{++}, Y | | |
| | | | Subaru/HSC | Y | | |
| | | | VISTA/VIRCAM | Y, J, H, K_s | | |
| | | | CFHT/WIRCam | H, K_s | | |
| | | | <i>Spitzer</i> /IRAC | 3.6, 4.5, 5.8, 8.0 μm | | |
| | | | <i>Spitzer</i> /MIPS | 24 μm | | |
| | | | <i>Herschel</i> /PACS | 70, 100, 160 μm | | |
| | | | <i>Herschel</i> /SPIRE | 250, 350, 500 μm | | |
| | | | 24 – 160 μm | Lutz et al. (2011) | ALMA | Band 7 (800–1100 μm) |
| | | | 250 – 500 μm | Hurley et al. (2017) | ALMA | Band 7 (800–1100 μm) |
| | | | > 1000 μm | Scholtz et al. (2018) and | | |

| ALMA Archive | | | Band 3 (2600–3600 μm) | |
|--------------|-----------|-------------------------|---|---|
| WISSH | UV to MIR | Duras et al. (in prep.) | SDSS 2MASS WISE | u, g, r, i, z J, H, K $W1, W2, W3, W4$ |
| Stripe 82X | UV to MIR | Ananna et al. (2017) | SDSS UKIDSS VISTA <i>Spitzer</i> /IRAC | u, g, r, i, z J, H, K J, H, K 3.6, 4.5 μm |
| | | Lang et al. (2016) | WISE | $W1, W2, W3, W4$ |

Table 3.2: Summary of the photometric data used for the SED-fitting modeling.

3.3.2 Data modeling

The analysis presented in this work is performed by using the Code Investigating GALaxy Emission (CIGALE⁴; Noll et al., 2009), a publicly available state-of-the-art galaxy SED-fitting technique. CIGALE adopts a multi-component fitting approach in order to disentangle the AGN contribution from the emission of its host galaxy and estimate in a self-consistent way AGN and host galaxy properties from the integrated SEDs. Moreover, it takes into account the energy balance between the UV-optical absorption by dust and the corresponding re-emission in the FIR. Here we provide a brief description of the code and we refer the reader to Noll et al. (2009), Buat et al. (2015) and Ciesla et al. (2015) for more details. In this work we used the version 0.11.0.

CIGALE accounts for three main distinct emission components: (i) stellar emission, dominating the wavelength range $0.3 - 5 \mu\text{m}$; (ii) emission by cold dust heated by star formation which dominates the FIR; (iii) AGN emission, appearing as direct energy coming from the accretion disk at UV-optical wavelengths and reprocessed emission by the dusty torus peaking in the MIR. The code assembles the models, according to a range of input parameters, which are then compared to the observed photometry by computing model fluxes in the observed filter bands and performing an evaluation of the χ^2 . The output parameters as well as the corresponding uncertainties are determined through a Bayesian statistical analysis: the probability distribution function (PDF) for each parameter of interest is built by summing the exponential term $\exp(-\chi^2/2)$ related to each model in given bins of the parameter space. The output value of a parameter is the mean value of the PDF and the associated error is the standard deviation derived from the PDF (Noll et al., 2009). The values of the input parameters used for the fitting procedure are listed in Table 3.3. In the following we describe the assumptions and the models adopted.

(i) To create the stellar models we assumed a star formation history (SFH) represented by a delayed τ -model (exponentially declining) with varying e-folding time and stellar population ages (see Table 3.3), defined as:

$$\text{SFR}(t) \propto t \times \exp(-t/\tau) \quad (3.1)$$

where τ is the e-folding time of the star formation burst. The stellar population ages are constrained to be younger than the age of the Universe at the redshift of the source sample. The SFH is then convolved with the stellar population models of Bruzual & Charlot (2003) and a Chabrier (2003) initial mass function (IMF). The metallicity is fixed to solar (0.02)⁵. To account for the role played by dust in absorbing the stellar emission in the UV/optical regime we applied an attenuation law to the stellar component. One of the most used ones, also at high redshift, is the Calzetti et al. (2000) law. However, in the literature there is evidence for shapes of the attenuation law different from the standard Calzetti one (e.g., Salvato et al., 2009; Buat et al., 2011, 2012; Reddy et al., 2015; Lo Faro et al., 2017, but see also Cullen et al. 2018). We used the modified version of the Calzetti et al. (2000) curve,

⁴<https://cigale.lam.fr>

⁵The impact of lower metallicity on the SED-fitting output was tested by fixing the metallicity to a value 0.3 dex lower than the solar one. The results of the fitting procedure are well within the uncertainties.

which is multiplied in the UV range by a power law with a variable slope δ , where the attenuation is given by $A(\lambda) = A(\lambda)_{Calz.} \times (\lambda/550 \text{ nm})^\delta$. In this recipe, negative slopes of the additional power law produce steeper attenuation curves and vice versa positive values give a flatter curve, while a slope equal to 0 reproduces the Calzetti et al. (2000) curve. We did not include the bump feature at 2175 Å. The same law is applied to both old (>10 Myr) and young (<10 Myr; Charlot & Fall 2000) stars. Moreover we took into account that stars of different ages can suffer from differential reddening by applying a reduction factor of the visual attenuation to the old stellar population (Calzetti et al., 2000). The reduction factor, $E(B - V)_{old}/E(B - V)_{young}$, is fixed to 0.93 as derived by Puglisi et al. (2016).

(ii) The reprocessed emission from dust heated by star formation is modeled using the library presented by Dale et al. (2014), which includes the contributions from dust heated by both star formation and AGN activity. In order to treat the AGN emission separately by adopting different models, and therefore estimate the contribution from star formation only with this library, we assumed an AGN contribution equal to 0. This family of models is made of a suite of templates constructed with synthetic and empirical spectra which represent emission from dust exposed to a wide range of intensities of the radiation field. These templates are combined in order to model the total emission and their relative contribution is given by a power law, whose slope is the parameter α_{SF} . For higher values of the slope the contribution of weaker radiation fields is more important and the dust emission peaks at longer wavelengths. The dust templates are linked to the stellar emission by a normalization factor which takes into account the energy absorbed by dust and re-emitted in the IR regime.

(iii) Accounting for the AGN contribution is essential for the determination of the host galaxy properties. To reproduce the AGN emission component we chose the physical models presented by Fritz et al. (2006), who solved the radiative transfer equation for a flared disk geometry with a smooth dust distribution composed by silicate and graphite grains. Although a clumpy or filamentary structure has been observed for nearby AGN (e.g., Jaffe et al., 2004) and is more physical, in this work we focus on the global characterization of the SED, for which both clumpy and smooth models provide good results and are widely used in the literature. As claimed by Feltre et al. (2012), the major differences in the SEDs produced by the two dust distributions are due to different model assumptions and not to their intrinsic properties. The main AGN parameter we want to reliably constrain from the SED is the AGN bolometric luminosity, therefore the details of the dust distribution are not fundamental in this work. The law describing the dust density within the torus is variable along the radial and the polar coordinates and is given by:

$$\rho(r, \theta) = \alpha r^\beta e^{-\gamma|\cos(\theta)|} \quad (3.2)$$

where α is proportional to the equatorial optical depth at 9.7 μm ($\tau_{9.7}$), β and γ are related to the radial and angular coordinates respectively. Other parameters describing the geometry are the ratio between the outer and inner radii of the torus, $R_{\text{max}}/R_{\text{min}}$, and the opening angle of the torus, Θ . The inclination angle of the observer's line of sight with

respect to the torus equatorial plane, the parameter ψ with values in the range between 0° and 90° , allows one to distinguish between type 1 AGN (unobscured) for high inclinations and type 2 AGN (obscured) for low inclinations. Intermediate types are usually associated to $\psi \simeq 40^\circ - 60^\circ$ depending on the dust distribution. The central engine is assumed to be a point-like source emitting isotropically with an SED described by a composition of power laws parameterizing the disk emission. This emission is partially obscured when the line of sight passes through the dusty torus. Another important input parameter that handles the normalization of the AGN component to the host galaxy emission is the AGN fraction, which is the contribution of the AGN emission to the total ($8 - 1000 \mu\text{m}$) IR luminosity and is given by $f_{\text{AGN}} = L_{\text{IR}}^{\text{AGN}} / L_{\text{IR}}^{\text{TOT}}$, with $L_{\text{IR}}^{\text{TOT}} = L_{\text{IR}}^{\text{AGN}} + L_{\text{IR}}^{\text{starburst}}$ (Ciesla et al., 2015). The input values available in the code are based on the results presented by Fritz et al. (2006). However, as described by Hatziminaoglou et al. (2008), using all the possible values would produce degeneracies in the model templates. Therefore we cannot determine the torus geometry in an unequivocal way and the parameter proving to be best constrained is the bolometric luminosity. The values of the above-mentioned physical parameters related to the torus geometry should be taken as indicative. For this reason we decided to narrow down the grid of input values and to fix some of them. Our selected values (see Table 3.3) are partly based on the analysis performed by Hatziminaoglou et al. (2008), who presented a restricted grid of input parameters. Differently from their setup, we fixed $R_{\text{max}}/R_{\text{min}}$ and the opening angle to a single value, as well as using a less dense grid for the optical depth.

To the main emission components described above we also added templates reproducing nebular emission, ranging from the UV to the FIR. These templates are based on the models presented by Inoue (2011) and represent the emission from HII regions. They include recombination lines, mainly from hydrogen and helium, and continuum emission due to free-free, free-bound and 2-photon processes of hydrogen. This SED component is proportional to the rate of Lyman continuum photons ionizing the gas and takes into account the Lyman continuum escape fraction and the absorption of the ionizing photons by dust. The templates do not include lines from photo-dissociation regions and nebular lines due to AGN emission. Therefore they do not reproduce the AGN contribution to the emission lines which may contaminate the photometric data. We fixed the parameters of the nebular emission model (see Table 3.3) as in Boquien et al. (2016).

| Template | Parameter | Value and range | Description |
|--------------------------------------|---------------------------------|---|---|
| <i>Stellar emission</i> | IMF | Chabrier (2003) | |
| | Z | 0.02 | Metallicity |
| | Separation age | 10 Myr | Separation age between the young and the old stellar populations |
| Delayed SFH | Age | 0.10, 0.25, 0.5, 1.0, 1.5, 2.0, 2.5 Gyr | Age of the oldest SSP |
| | τ | 0.10, 0.25, 0.5, 1.0, 3.0, 5.0, 10.0 Gyr | e-folding time of the SFH |
| Modified Calzetti attenuation law | $E(B - V)$ | 0.05, 0.1, 0.3, 0.5, 0.7, 0.9, 1.1, 1.3 | Attenuation of the young stellar population |
| | Reduction factor | 0.93 | Differential reddening applied to the old stellar population |
| | δ | -0.6, -0.4, -0.2, 0.0 | Slope of the power law multiplying the Calzetti attenuation law |
| <i>Dust emission</i> | α_{SF} | 0.5, 1.0, 1.5, 2.0, 2.5, 3.0 | Slope of the power law combining the contribution of different dust templates |
| <i>AGN emission</i> | $R_{\text{max}}/R_{\text{min}}$ | 60 | Ratio of the outer and inner radii |
| | $\tau_{9.7}$ | 0.6, 3.0, 6.0 | Optical depth at 9.7 μm |
| | β | 0.00, -0.5, -1.0 | Slope of the radial coordinate |
| | γ | 0.0, 6.0 | Exponent of the angular coordinate |
| | Θ | 100 degrees | Opening angle of the torus |
| | ψ | 0, 10, 20, 30, 40, 50, 60, 70, 80, 90 degrees | Inclination of the observer's line of sight |
| | f_{AGN} | 0.05, 0.1, 0.15, 0.2, 0.25, 0.3, 0.35, 0.4, 0.45, 0.5, 0.55, 0.6, 0.65, 0.7, 0.75, 0.8, 0.85, 0.9 | AGN fraction |
| <i>Nebular emission</i> | U | 10^{-2} | Ionization parameter |
| | f_{esc} | 0% | Fraction of Lyman continuum photons escaping the galaxy |
| | f_{dust} | 10% | Fraction of Lyman continuum photons absorbed by dust |

Table 3.3: Input parameter values used in the SED-fitting procedure.

3.4 Overall properties of the target sample

In this section we provide a detailed picture of the multi-wavelength properties of our target sample obtained using SED fitting and spectral analysis. In particular, we focus on the main AGN and host galaxy physical parameters that we aim to connect to the outflow properties, as traced by our on-going SINFONI observations.

The AGN sample is characterized by a wide range of column densities, up to $2 \times 10^{24} \text{ cm}^{-2}$, derived from the X-ray spectra (see Section 3.2.2). This translates into different levels of contamination of the AGN to the galaxy emission at UV-to-NIR wavelengths. Therefore, host galaxy properties for the targets where this contamination is low, that is obscured AGN, can be robustly determined. At the same time, AGN properties are better constrained for unobscured targets, whose emission prevails in the UV-to-IR portion of the SED. In general, the classification of AGN into obscured and unobscured sources can be performed based on different criteria, such as X-ray spectral analysis, optical spectral properties, and shape of the UV-to-NIR SED (see Merloni et al., 2014). We adopt the following nomenclature: from an optical point of view, the classification depends on the presence of broad ($\text{FWHM} > 1000 \text{ km s}^{-1}$) or narrow ($\text{FWHM} < 1000 \text{ km s}^{-1}$) permitted lines in their spectra, defining broad-line (BL) or narrow-line (NL) AGN respectively; according to the shape of the UV-to-NIR SED, we can constrain the AGN type based on the inclination of the observer’s line of sight with respect to the obscuring torus; finally, AGN are classified as unobscured or obscured when the column density is smaller or larger than 10^{22} cm^{-2} (see Sec. 3.2.2). As explained later in Sec. 3.4.2, the three classification methods broadly agree with each other. However, as final classification, we decided to adopt the optical spectroscopic classification (BL/NL, Table B.1). In the following we will refer to type 1 and type 2 AGN as based on the optical spectroscopic classification.

3.4.1 SED-fitting results

The main output parameters obtained with CIGALE are reported in Table B.1 and B.2 (Appendix B), that is stellar mass, SFR, and AGN bolometric luminosity together with their 1σ uncertainties. Two representative examples of SEDs are shown in Figure 3.2 for a type 2 (*top panel*) and a type 1 (*bottom panel*) AGN from CDF-S and COSMOS, respectively. The SEDs of the whole sample are presented in Appendix C.

Stellar masses

Stellar masses (M_*) are probed by rest-frame NIR flux densities shifted to the MIR at this redshift, which are dominated by old stellar populations. The uncertainty associated to stellar masses increases with the level of AGN contamination. As shown by the green template in the top panel of Figure 3.2, in type 2s there is a negligible AGN contribution in the UV-to-NIR regime. Conversely, for type 1s the green template in the bottom panel outshines the galaxy emission (orange curve) preventing a derivation of the stellar mass as robust as for type 2s. However, estimates of the stellar mass for type 1 AGN can still

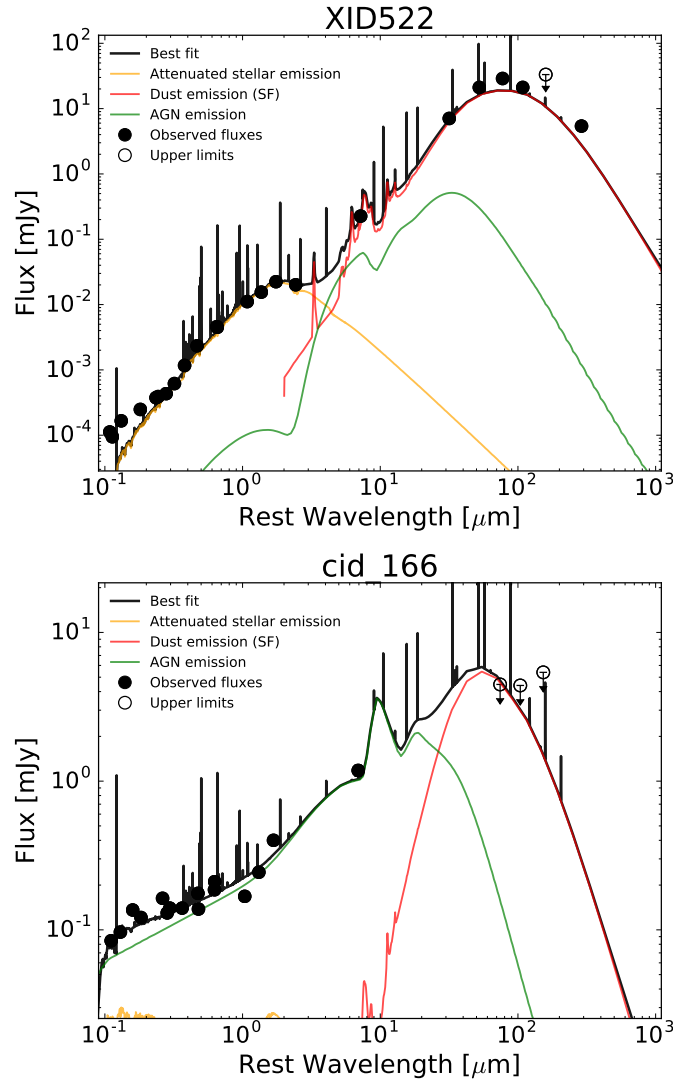


Figure 3.2: Two examples of rest-frame SEDs obtained for a type 2 (XID522, *top*) and a type 1 (cid_166, *bottom*) AGN. The black dots represent the observed multi-wavelength photometry, while the empty dots indicate 3σ upper limits. The black solid line is the total best-fit model, the orange curve represents the stellar emission attenuated by dust, the green template reproduces the AGN emission, the red curve accounts for dust emission heated by star formation. Emission lines in the black curves are part of the nebular emission component, included in the overall SED.

be recovered albeit with larger uncertainties (e.g., Bongiorno et al., 2012), apart from very bright type 1s (e.g., Stripe82X, WISSH and some XMM-XXL targets in our sample) for which the uncertainties on this parameter are much larger than the parameter value itself and therefore an estimate of the stellar mass is meaningless. For these targets, we do not report a value of M_* in Table B.1. Our results range between $\sim 4 \times 10^9 M_\odot$ and $\sim 1.6 \times 10^{11} M_\odot$, with an average 1σ uncertainty of 0.1 dex for type 2s and 0.3 dex for type 1s⁶.

Star Formation Rates

SFRs are derived from the IR luminosity integrated in the rest-frame wavelength range 8 – 1000 μm , when possible, assuming the Kennicutt (1998b) SFR calibration converted to a Chabrier (2003) IMF (i.e., by subtracting 0.23 dex). This value is an indication of the SFR averaged over the last 100 Myr of the galaxy history and is produced by emission from dust heated by young stars as well as from evolved stellar populations. The AGN also contributes to the IR luminosity (whose percentage is given by the AGN fraction, see Sec. 3.3.2), although it usually dominates the emission only up to 30 μm rest-frame as described in Mullaney et al. (2011) (see also Symeonidis et al., 2016). Since our SED fitting allows us to disentangle the contribution of the two components (AGN and SF), we estimate the IR luminosity from SF removing the AGN contamination⁷. However this is affected by intrinsic degeneracies that cannot be solved with the current data sampling at MIR and FIR wavelengths. Therefore an over-estimation of the AGN fraction will result in an under-estimation of the IR emission from the galaxy and thus of the SFR and vice versa (e.g., Ciesla et al., 2015). We provide a 3σ upper limit on the SFR, derived as the 99.7th percentile of the FIR luminosity PDF, for the targets with only upper limits at $\lambda > 24 \mu\text{m}$. For the subset of targets without data at observed $\lambda > 24 \mu\text{m}$ we did not include the dust templates in the fitting procedure. Therefore we report the average SFR over the last 100 Myr of the galaxy history as obtained from the modeling of the stellar component in the UV-to-NIR regime with SED fitting. This has been done for cid_971 and lid_206, since their 24 μm flux was not available in the catalog used as a prior for the extraction of the FIR photometry (see Sec. 3.3.1). The targets without an estimate of the SFR are instead bright type 1s, therefore no information about SFR, and stellar mass, can be retrieved from the UV-optical regime. SFRs determined for our targets are in the range between $\sim 25 M_\odot \text{ yr}^{-1}$ and $\sim 680 M_\odot \text{ yr}^{-1}$ with an average 1σ uncertainty of 0.15 dex for type 1 and 0.06 for type 2 AGN (see footnote 6). The SFRs derived from the FIR luminosity and through the modeling of the stellar emission in the UV-to-NIR regime are in very good agreement (when the comparison is possible), with the low scatter due to the

⁶In general, the statistical uncertainties in the determination of M_* and SFR through SED modeling are typically around 0.3 dex for stellar masses and larger for SFRs (e.g., Mancini et al., 2011; Santini et al., 2015), usually underestimated by the SED-fitting tools. Moreover, systematic differences in the results are due to the models used, degeneracies and a priori assumptions as well as the discrete coverage of the parameter space.

⁷AGN fractions (derived for the targets with FIR detections) range between 0.05 and 0.90, with a median value of 0.36.

energy-balance approach used (see also Bongiorno et al., 2012).

Comparison of M_* and SFRs to literature results

We compared our results with those presented by Santini et al. (2015) for the targets in the CDF-S and Chang et al. (2017), Delvecchio et al. (2017) as well as Suh et al. (2017) for the COSMOS targets. Santini et al. (2015) collected M_* measurements of the targets in the CANDELS field from several teams which used different SED-fitting codes and assumptions, in order to study the influence of systematic effects on the final output. The resulting estimates turned out to be clustered around the median value with a scatter of 25% – 35%. Their results are available for all of our CDF-S targets covered by CANDELS. Chang et al. (2017) derived physical parameters for galaxies over the whole COSMOS field, Delvecchio et al. (2017) dealt with a sub-sample of AGN as part of the VLA-COSMOS 3 GHz Large Project, while Suh et al. (2017) provided physical properties for a sample of X-ray selected type 2s. 16, 6 and 7 out of 16 of our COSMOS targets have a match in these catalogs, respectively. However, the values from Delvecchio et al. (2017) have been recomputed by adopting the same photometry used in this work (Delvecchio, priv. comm.). The overall comparison for stellar masses is quite satisfactory, with the average $\langle \log(M_{*, \text{literature}}/M_{*, \text{this work}}) \rangle$ equal to 0.30 dex (this result includes both type 2 and type 1 AGN), 0.03 dex and 0.18 dex for Chang et al. (2017), Delvecchio et al. (2017) and Suh et al. (2017), and 0.20 dex for Santini et al. (2015). The standard deviation is 0.38, 0.3 and 0.19 dex for the COSMOS targets and 0.19 dex for the CDF-S ones. The fits performed in Santini et al. (2015) do not take into account the AGN contribution. As for the SFRs, the results are similar, with an average $\langle \log(\text{SFR}_{\text{literature}}/\text{SFR}_{\text{this work}}) \rangle = 0.39, -0.30$ and 0.03 dex and standard deviation 0.44, 0.34 and 0.47 dex for Chang et al. (2017), Delvecchio et al. (2017) and Suh et al. (2017), respectively. The AGN contribution was subtracted in all the estimates. For this comparison we did not consider the SFRs reported in Santini et al. (2015), because their SED fitting did not include the FIR fluxes which are crucial to properly constrain the total SFR. The larger discrepancies for SFRs are mainly attributed to different and looser constraints in the FIR regime. In general, other sources of uncertainties are the diverse models used and the sparser data with large error bars (often just upper limits) compared to the UV-to-NIR regime.

Although the SFR is a key quantity to be compared with AGN activity in order to understand the feedback processes, measuring the current SFR in AGN hosts is a well-known challenge, since the tracers are usually contaminated by AGN emission. Thanks to the SINFONI data that will be available for our targets, we will be able to compare various SF tracers (e.g., narrow $\text{H}\alpha$ vs. L_{FIR}) in order to explore the systematic effects in this kind of measurements.

AGN bolometric luminosities

As described in Section 3.3.2, we used the Fritz et al. (2006) models to reproduce the overall AGN emission. According to a comparison discussed in Ciesla et al. (2015), type 2 AGN

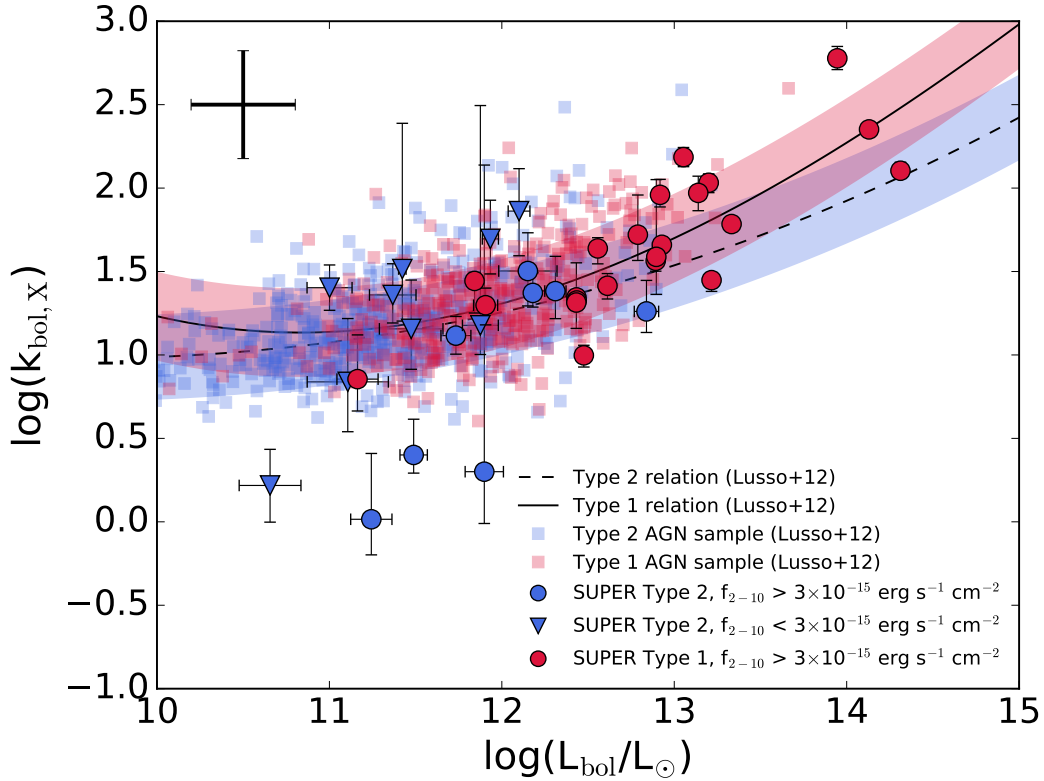


Figure 3.3: Bolometric corrections in the hard 2 – 10 keV band versus bolometric luminosities. Circles and triangles mark the SUPER targets with 2 – 10 keV fluxes higher and lower than $3 \times 10^{-15} \text{ erg s}^{-1} \text{ cm}^{-2}$ respectively, while type 1 and type 2 AGN are plotted in red and blue. The solid and dashed lines show the relations obtained by Lusso et al. (2012) for type 1s and type 2s with fluxes higher than $3 \times 10^{-15} \text{ erg s}^{-1} \text{ cm}^{-2}$, respectively. The shaded areas depict the scatter of these relations. We plot as red and blue squares the sample of type 1 and type 2 AGN, respectively, analyzed by Lusso et al. (2012) to show the dispersion of the data around the best-fit relations. The error bar in the upper-left corner takes into account a systematic error of 0.3 dex on L_{bol} . The SUPER data points are well consistent with the trends found for the bolometric correction.

templates from the Fritz et al. (2006) library are cooler than the SEDs obtained empirically by Mullaney et al. (2011), which may indicate that those models do not reproduce all the physical properties of the AGN obscuring structure. Moreover, there are several models (both theoretical and empirical) in the literature reproducing the dusty torus emission (e.g., Nenkova et al., 2008a; Mor & Netzer, 2012; Stalevski et al., 2012; Lani et al., 2017) and approximations of the intrinsic AGN continuum (e.g., Telfer et al., 2002; Richards et al., 2006; Stevans et al., 2014). Nevertheless, it is important to stress that our main goal is not the detailed determination of the torus or accretion disk specific characteristics but just recovering the AGN bolometric luminosity. To test the reliability of the derived quantity we explored the input parameter space described in Section 3.3.2 (see also Table 3.3) by fixing the input parameters to different values and comparing L_{bol} to those obtained using the whole grid of models used in this work. Even though the best-fit geometry varied through the different runs, the bolometric luminosity proved to be constrained within a variation of 0.2 dex. The same trend emerged for the dust luminosity due to star formation, which is related to the AGN luminosity by the AGN fraction. Moreover, we compared our results with available literature values for the targets in the COSMOS field (from Chang et al., 2017; Delvecchio et al., 2017) and those from the WISSH catalog (Duras, priv. comm., Duras et al., 2017). Duras et al. (2017) modeled the AGN emission combining models from Feltre et al. (2012) and Stalevski et al. (2016); Chang et al. (2017) used empirical templates by Richards et al. (2006), Polletta et al. (2007), Prieto et al. (2010) and Mullaney et al. (2011); Delvecchio et al. (2017) adopted the Feltre et al. (2012) library. In spite of the variety of models used by the different authors, the comparison is satisfactory and all the results are within 0.3 dex scatter: the average $\langle \log(L_{\text{bol, literature}}/L_{\text{bol, this work}}) \rangle$ is equal to 0.03, 0.18 and -0.09 dex for Chang et al. (2017), Delvecchio et al. (2017) and Duras (priv. comm.) respectively, with standard deviation 0.26, 0.30 and 0.14 dex. From our SED fitting, average 1σ uncertainties of the bolometric luminosity are on the order of 0.03 and 0.1 dex for type 1s and type 2s respectively, with best-fit values in the range $2 \times 10^{44} - 8 \times 10^{47}$ erg s $^{-1}$. As pointed out for M_* and SFRs, the uncertainties estimated through SED fitting can be underestimated. According to the comparison mentioned above, a more realistic typical uncertainty can be fixed to 0.3 dex.

The physical quantities available for the SUPER sample give us the opportunity to study the distribution of the X-ray bolometric correction in the hard 2 – 10 keV band (defined as $k_{\text{bol, X}} = L_{\text{bol}}/L_{[2-10 \text{ keV}]}$) versus L_{bol} . This can be done over a wide range of bolometric luminosities with a set of values determined in a uniform way. In Figure 3.3 we compare our results to the relation derived by Lusso et al. (2012) for a sample of more than 900 AGN (both type 1 and type 2) selected from the COSMOS field (see also Lusso & Risaliti, 2016). At variance with their AGN selection, which includes sources with hard X-ray fluxes larger than 3×10^{-15} erg s $^{-1}$ cm $^{-2}$, 23% of our targets reach fainter values (down to $\approx 5 \times 10^{-17}$ erg s $^{-1}$ cm $^{-2}$, triangles in Fig. 3.3). Moreover, we can probe the $k_{\text{bol, X}} - L_{\text{bol}}$ relation for targets with bolometric luminosities an order of magnitude higher (see also Martocchia et al., 2017). We plot the relations obtained by Lusso et al. (2012) for type 1 and type 2 AGN (solid and dashed lines respectively), although they do not differ too much. The shaded areas depict the dispersion of these relations, while the red and

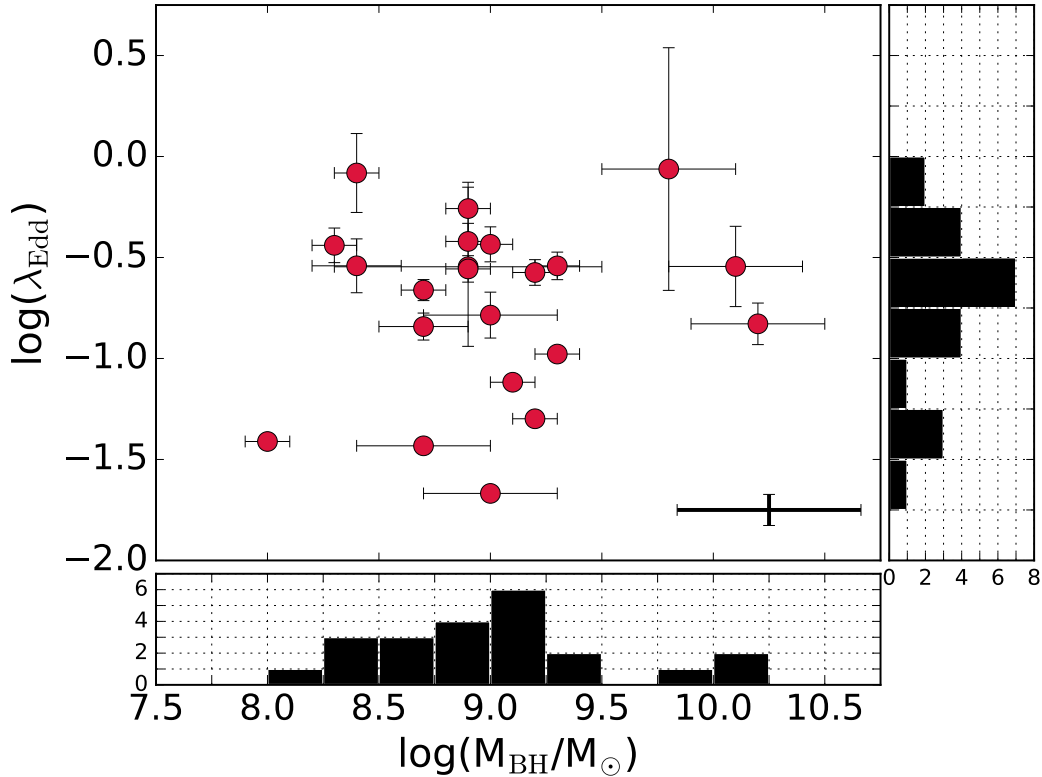


Figure 3.4: Eddington ratios versus BH masses of the 22 type 1 AGN in the target sample. The Eddington ratio is given by $\lambda_{\text{Edd}} = L_{\text{bol}}/L_{\text{Edd}}$, with bolometric luminosities estimated through SED-fitting analysis. BH masses (given in Table B.2) are derived via the “virial method” mainly using the broad CIV emission line and the calibration of Vestergaard & Peterson (2006). We plot a representative error bar at the bottom-right corner of the plot which takes into account a systematic error of 0.4 dex on M_{BH} . The black histograms show the projected distribution of the two quantities along each axis. SUPER will allow us to sample both accretion rates close to the Eddington limit and more moderate ones and to connect these quantities to the potential outflows detected by SINFONI.

blue squares represent the sample of type 1 and type 2 AGN, respectively, from which the relations were obtained. Our results for both type 1 (shown in red) and type 2 (shown in blue) are well consistent with the trends found by Lusso et al. (2012) with only the presence of three targets outside the $\pm 1\sigma$ scatter, according to the errorbars. The rest of the SUPER targets are within the scatter shown by their sample and also the most luminous AGN are well represented by those curves. One of the outliers has faint hard-band flux (marked by different symbols to distinguish the targets below the threshold adopted by Lusso et al. 2012) and a total number of X-ray counts < 60 . We note that the error bars in the plot are given by the error on L_{bol} provided by the SED-fitting code. In the upper-left corner of the panel we plot a median error bar taking into account a systematic error of 0.3 dex on L_{bol} which is more representative. Accounting for the scatter of the data presented by Lusso et al. (2012) around the best fits and the underestimated error bars for our L_{bol} , our estimates result to be in agreement with the literature trends and therefore we can consider L_{bol} and L_X obtained with our analysis reliable parameters.

Bolometric luminosities can be also combined with black hole masses, when available, in order to obtain the Eddington ratio $\lambda_{\text{Edd}} = L_{\text{bol}}/L_{\text{Edd}}$, where $L_{\text{Edd}} = 1.5 \times 10^{38} (M_{\text{BH}}/M_{\odot})$ erg s $^{-1}$. BH masses for type 1 AGN, ranging between 8×10^7 and $1.6 \times 10^{10} M_{\odot}$, are reported in Table B.2 together with the respective references. These values are derived via the “virial method” mainly using the broad CIV $\lambda 1549$ emission line and the calibration of Vestergaard & Peterson (2006). Such method is affected by well-known limitations since the CIV emitting gas could be affected by non-virial motion (Trakhtenbrot & Netzer, 2012). However, in the present work we only want to give a broad idea of the coverage in the $\lambda_{\text{Edd}}-M_{\text{BH}}$ plane that will be provided by our survey. As shown in Fig. 3.4, where we plot the distribution of BH masses and Eddington ratios, we will be able to sample both accretion rates close to the Eddington limit and more moderate ones ($\sim 10^{-2}$ the Eddington limit) and to connect these quantities to the potential outflows that will be detected by SINFONI. To take into account the heavy uncertainties CIV-based BH mass estimates are affected by, we assume in Fig. 3.4 a systematic error on M_{BH} equal to 0.4 dex and plot a median error bar as a reference. Importantly, SINFONI observations will allow us to derive accurate estimates of M_{BH} combining broad H β and H α line profiles with continuum luminosities verifying, and improving upon, the CIV-based measurements.

Comparison to the Main Sequence of star-forming galaxies

In Figure 3.5 we show the location of our targets in the SFR- M_* plane for the objects with an estimate of both parameters, that is obscured AGN and a subsample of unobscured ones (24 targets, those for which we provide M_* and SFR in Table B.1). SFRs are already corrected for the AGN contribution. The distribution of our targets is compared to the so-called main sequence of star-forming galaxies (e.g., Noeske et al., 2007). We adopted the parametrization derived by Schreiber et al. (2015), who performed a stacking analysis of deep *Herschel* data in several extragalactic fields (GOODS, UDS, COSMOS), finding a flattening of the MS at high stellar masses ($\log(M_*/M_{\odot}) > 10.5$) and a SFR dispersion of 0.3 dex. Our sample covers in a quite uniform way the SFR- M_* plane, probing a wide

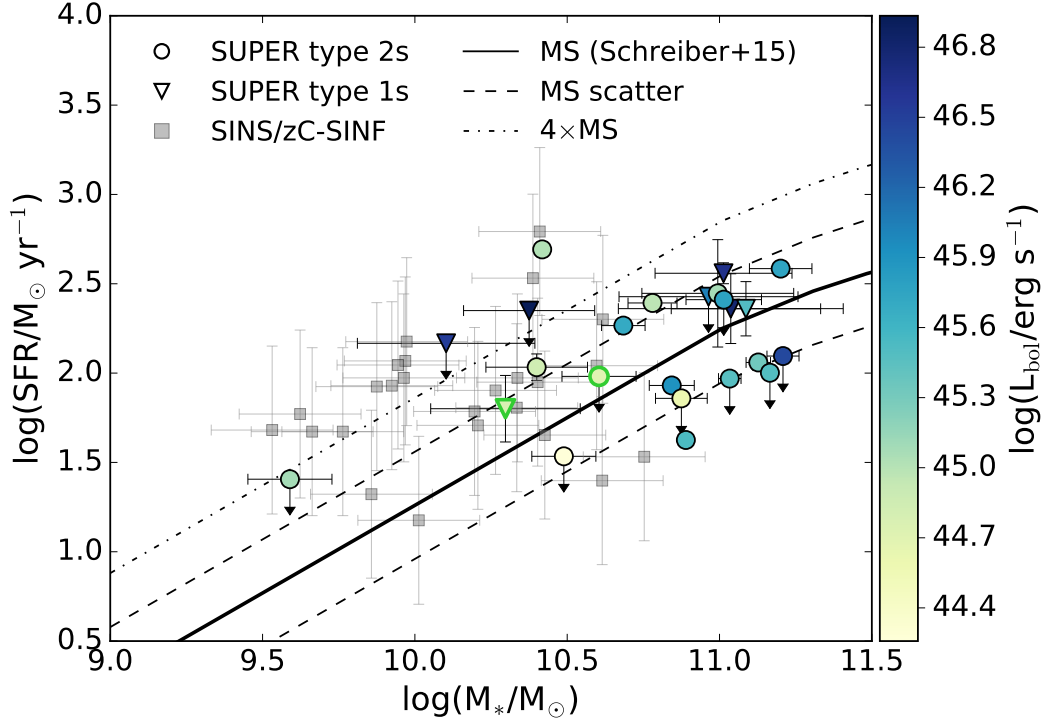


Figure 3.5: Distribution of host galaxy properties in the SFR- M_* plane for the 24 AGN (type 1s marked by triangles and type 2s marked by circles) with star formation constraints in our sample as given in Table B.1. The two data points with green edges represent the targets with SFR derived through modeling of the stellar emission with SED fitting. The color coding indicates the AGN bolometric luminosity for each object of this subsample. The black solid line reproduces the main sequence (MS) of star-forming galaxies from Schreiber et al. (2015) at the average redshift of our target sample (i.e., ~ 2.3). The dashed lines mark the scatter of the main sequence (equal to 0.3 dex) while the dot-dashed line represents the locus 4 times above the main sequence along the SFR axis (as defined by Rodighiero et al., 2011). The gray squares trace the properties of the 25 star-forming galaxies targeted by the SINS/zC-SINF survey (Förster Schreiber et al., 2018) without AGN signatures. We note that their selection based on a minimum SFR or $H\alpha$ flux results in a preferentially higher sSFRs than the overall population of normal galaxies at those redshifts (see discussion in Förster Schreiber et al., 2009; Mancini et al., 2011). These galaxies, with IFU data comparable to the SUPER ones, will be our non-AGN comparison sample in future analyses (see text for more details).

range in terms of SFRs. About 46% of the targets are within the $\pm 1\sigma$ scatter of the main sequence at the average redshift of the sample $z \sim 2.3$, while the rest are subdivided above (33%) and below (20%) it. As far as the stellar mass range is concerned, our AGN reside in massive hosts (median M_* of $10^{10.88} M_\odot$). This can be ascribed to a selection effect, as already pointed out by, e.g., Bongiorno et al. (2012) and Aird et al. (2012). In particular, they found that AGN with a low Eddington ratio are more numerous than AGN with a high one. At a fixed X-ray flux limit there is a bias toward galaxies hosting an AGN with higher stellar masses, given the relation between L_{Edd} , M_{BH} and M_* . Over a sample of 1700 AGN in the COSMOS field analyzed by Bongiorno et al. (2012), the host galaxy masses range from 10^{10} to $10^{11.5} M_\odot$, with a peak at $\sim 10^{10.9} M_\odot$. The color coding in Figure 3.5 refers to the AGN bolometric luminosity of each target. The detailed analysis of potential outflows in our AGN, as a function of their position in the SFR– M_* plane and their bolometric luminosity, will expand the physical understanding of the impact of AGN outflows on host galaxies by investigating the variation of outflow properties (such as mass outflow rates and energetics) moving from above to below the MS.

Currently the largest AO-assisted NIR IFU observations of galaxies in the same redshift range covered by SUPER is represented by the SINS/zC-SINF survey (Förster Schreiber et al., 2018). These observations focus on the H α and [NII] emission lines, probing their distribution and kinematics in the galaxy, with a spatial resolution of ~ 1.5 kpc. Excluding objects classified as AGN in Förster Schreiber et al. (2018), this SINFONI survey includes 25 objects, shown in Figure 3.5, in the redshift range $2 < z < 2.5$ of the SUPER sample. The total stellar mass and SFR intervals, used to match the SINS/zC-SINF sample to the SUPER one, span a range which takes into account also the uncertainties on these quantities. As can be seen from Figure 3.5, the SUPER and SINS/zC-SINF (excluding AGN) samples have an overlap in this plane, in the stellar mass range $\log(M_*/M_\odot) = [9.5 - 10.8]$, which will enable an interesting comparison of the properties of galaxies hosting active and inactive SMBHs.

3.4.2 X-ray vs. optical spectroscopic and SED-fitting classification

In Fig. 3.6 we plot the distribution of our targets in the AGN bolometric luminosity and column density plane. The coverage of this parameter space is quite uniform. The bolometric luminosity probed by our survey ranges from $\sim 10^{44}$ erg s $^{-1}$ up to $\sim 10^{48}$ erg s $^{-1}$, spanning almost 4 orders of magnitude. In terms of column density, the sample covers uniformly a range from unobscured ($N_{\text{H}} \leq N_{\text{H}}^{\text{gal}}$) to heavily obscured objects, with values up to 2×10^{24} cm $^{-2}$. We adopt a separation value of 10^{22} cm $^{-2}$ between obscured and unobscured AGN (Mainieri et al., 2002; Szokoly et al., 2004). In Fig. 3.6 we also compare the X-ray and optical (spectroscopy and SED fitting) diagnostics to distinguish between obscured and unobscured AGN as introduced at the beginning of Sec. 3.4. The diagnostic recovered from the SED fitting is the inclination of the observer’s line of sight with respect to the torus equatorial plane, shown by the color coding in Fig. 3.6. The optical spec-

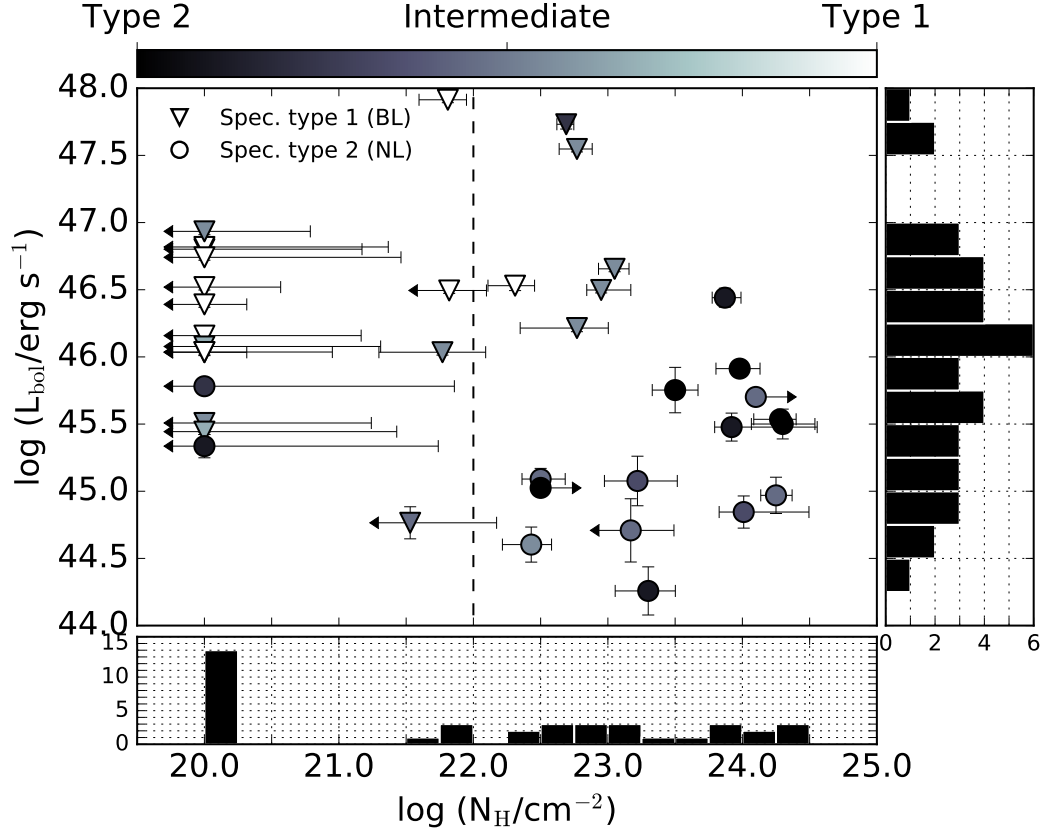


Figure 3.6: AGN bolometric luminosities versus column densities of the whole target sample. These quantities are derived through SED-fitting modeling and X-ray spectral analysis, respectively. The dashed line at $\log(N_{\text{H}}/\text{cm}^{-2}) = 22$ marks the assumed separation between X-ray unobscured and obscured AGN. The black histograms show the projected distribution of the two quantities along each axis. The gray color scale depicts the inclination of the observer’s line of sight with respect to the dusty torus equatorial plane derived from the SED-fitting analysis, which corresponds to type 2 for dark colors, type 1 for light colors and intermediate (i.e., the transition between the two classes of AGN) in between. The AGN type as derived from the optical spectra is depicted by the different symbols, triangles for type 1s and circles for type 2s. The comparison of the color coding and the different symbols to the location of the targets in the $L_{\text{bol}} - N_{\text{H}}$ plane suggests an agreement between the three classification methods and provides extra confidence in the SED-fitting results. The sample results to be almost equally divided in type 1 and type 2 AGN.

troscopic diagnostic (i.e., the presence of broad or narrow lines in the spectra) is depicted with different markers for broad- and narrow-line AGN. As can be clearly seen in Fig. 3.6, the three diagnostics agree rather well. Upper limits refer mainly to objects for which the column density derived from the X-ray spectral analysis is consistent with $\sim 10^{20} \text{ cm}^{-2}$ (given by Galactic absorption) and are therefore classified as unobscured from an X-ray point of view, even if the formal upper limit for N_{H} is larger than 10^{22} cm^{-2} . In some cases, the SED-fitting procedure is affected by significant degeneracies, since the same SED can sometimes be fit by either a type 1 AGN template and a negligible contribution from the host galaxy or an absorbed AGN template together with a very young and UV-bright set of stellar populations. In most cases the results of the SED fitting were in agreement with the overall classification of the target, returning a robust estimate of the AGN type. For some of the bright (type 1) AGN we restricted the range of inclinations based on the obscuration type suggested by the spectroscopic diagnostic in order to overcome the degeneracy. There are also some ambiguous cases. We find 2 targets classified as unobscured in the X-rays but showing obscured characteristics in the optical regime (both in the spectra and in the SEDs), although the upper error for N_{H} is very large. Six targets show an obscured X-ray spectrum ($10^{22} < N_{\text{H}} < 10^{23} \text{ cm}^{-2}$) but with broad lines in the optical spectrum and Intermediate/Type 1 characteristics in the SED (see Merloni et al., 2014). The final classification is performed according to the optical spectroscopic diagnostic, which divides the sample in almost an equal number of type 1 (22) and type 2 AGN (17).

3.4.3 Radio regime

All our AGN are located in fields targeted by radio surveys. In particular, the E-CDF-S has been observed with the Very Large Array (VLA) at 1.4 GHz (Miller et al., 2013), with a typical rms of $7.4 \mu\text{Jy beam}^{-1}$ ($2''.8 \times 1''.6$ beam size). A catalog of optical and IR counterparts for this survey is provided by Bonzini et al. (2012). As for the COSMOS field, we took advantage of the deep 3 GHz VLA-COSMOS project (Smolčić et al., 2017), characterized by an average rms sensitivity of $2.3 \mu\text{Jy beam}^{-1}$ and an angular resolution of $0''.75$. The other targets (from XMM-XXL, Stripe 82X and WISSH) are part of the VLA’s FIRST survey at 1.4 GHz (Becker et al., 1995), with a typical 5σ sensitivity of $0.15 \text{ mJy beam}^{-1}$ and a resolution of $5''$.

We want to study the radio properties of our targets to see, in particular, which ones are jetted and non-jetted⁸. We do this by comparing their FIR and radio luminosities. Namely, when an object lies along the FIR-radio correlation both its radio and FIR emission are supposed to be driven by recent star-formation (Yun et al., 2001). Instead, if an object is off the correlation its “radio excess” is interpreted as evidence for radio emission from strong jets (Padovani, 2017). In Figure 3.7 (*top panel*) we plot these quantities for the 24 targets with detections or upper limits in the FIR regime for which we could derive FIR luminosities through SED-fitting modeling (Section 3.3.2). The values are reported in

⁸We follow Padovani (2017) and use this new nomenclature, which supersedes the old “radio-loud/radio-quiet” distinction.

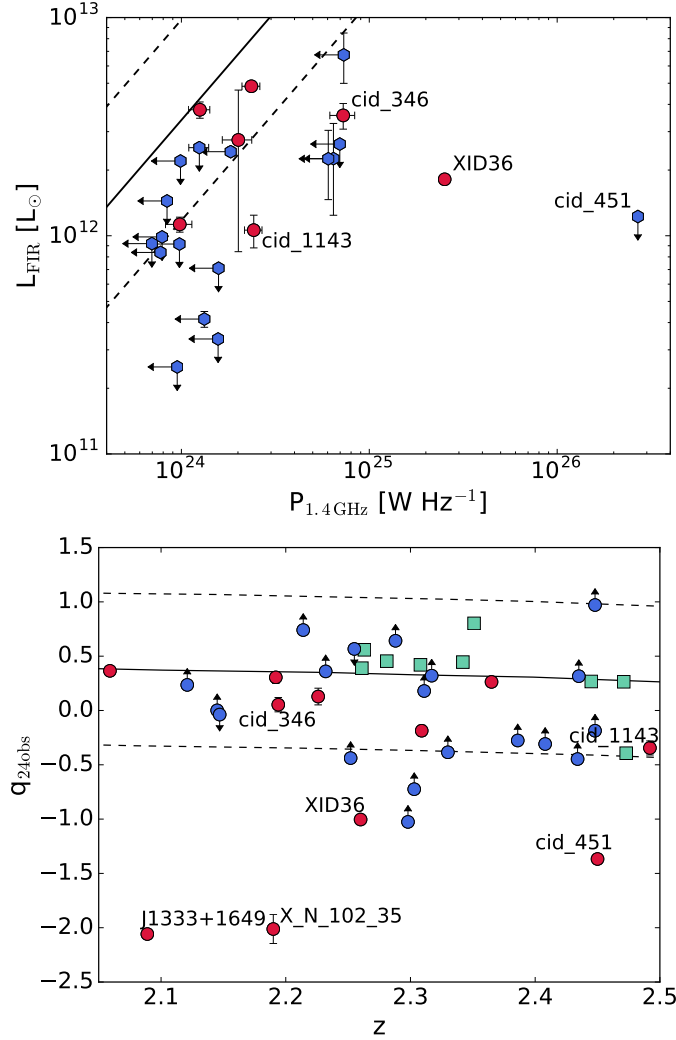


Figure 3.7: Radio properties of the target sample. *Top*: FIR luminosities due to star formation versus radio power at 1.4 GHz. The solid line shows the Kennicutt (1998a) relation, given by $\log P_{1.4\text{GHz}} = \log L_{\text{FIR}} + 11.47$, while the dashed lines represent its 2σ dispersion. Red circles depict targets with radio detections, while blue hexagons mark targets with upper limits in the radio regime and/or in the FIR. The four AGN outside the 2σ dispersion and classified as jetted are marked by their ID. *Bottom*: $q_{24\text{obs}} = \log(S_{24\mu\text{m}}/S_r)$ plotted as a function of redshift for the whole AGN sample. Red dots mark targets with detections both in the MIR and radio regime; blue-dot upper and lower limits represent sources with detections only in the radio or in the MIR, respectively; green squares depict AGN with upper limits both in the MIR and in the radio. The solid line displays $q_{24\text{obs}}$ versus redshift for M82 (from Bonzini et al., 2013), while dashed lines mark the $\pm 2\sigma$ dispersion. The six AGN classified as jetted, either from this plot or from the left panel of the figure, are marked by their ID.

Table B.2. We computed the radio power at 1.4 GHz for all sources, converting the 3 GHz flux for the COSMOS targets assuming a radio spectral index $\alpha_r = 0.7$. For the objects without radio detections (blue hexagons in the top panel of Figure 3.7) we used the 5σ sensitivity flux values (0.02, 0.037 and 0.15 mJy beam $^{-1}$ for the COSMOS, CDF-S and XMM-XXL/Stripe82X/WISSH targets respectively) to estimate upper limits for the radio power. The plot includes $\sim 62\%$ of the sample although most of the datapoints are actually radio and/or FIR upper limits. The comparison with the FIR-radio correlation and its 2σ dispersion shows the presence of 4 outliers: cid_451, cid_346, cid_1143 and XID36.

Since FIR luminosities are not available for the whole AGN sample, we further explored its radio properties by deriving the so-called q parameter, defined as the logarithm of the ratio between IR monochromatic and radio flux densities. The photometric band at the longest wavelength which allows us to use actual detections for most of the sample by keeping the number of upper limits as low as possible, is 24 μm . We therefore use $q_{24\text{ obs}} = \log(S_{24\mu\text{m}}/S_r)$, where $S_{24\mu\text{m}}$ is the observed flux density at 24 μm and S_r is that at 1.4 GHz (see, e.g., Bonzini et al., 2013). For the only target which is undetected at 24 μm and without an upper limit, S82X1940, we used an upper limit of 6 mJy given by the WISE All-sky survey 5σ sensitivity in the 22 μm W_4 filter. The distribution of $q_{24\text{ obs}}$ as a function of redshift is plotted in Figure 3.7 (*bottom panel*). Red dots mark targets with detections both in the MIR and radio regime; blue-dot upper and lower limits represent sources with detections only in the radio or in the MIR, respectively; green squares depict AGN with upper limits both in the MIR and in the radio, for which the two limits go in opposite directions. As done by Bonzini et al. (2013), we compare our results to the $q_{24\text{ obs}}$ of M82 (as representative of SFGs) and compute $q_{24\text{ obs}}$ from its SED as a function of redshift (for more details see Section 3.1.1 and Figure 2 in Bonzini et al., 2013). The SFG locus is defined as the region of $\pm 2\sigma$ around the M82 template (dashed lines in the plot) and sources below this region show a radio excess. We are fully aware of the fact that, using the 24 μm flux density (which corresponds to $\lambda \sim 7.3 \mu\text{m}$ rest-frame at the average z of the sample), we are actually probing a wavelength regime where the AGN can dominate the total energy budget. To have an estimate of the increase in $q_{24\text{ obs}}$ the AGN emission may produce, we evaluate the average AGN contribution to the total 24 μm flux from the SEDs where we can model all the emission components (i.e., 24 targets, 62% of the sample). The median value of this fraction is $\sim 86\%$ which, when subtracted from $q_{24\text{ obs}}$, would produce a down shift of the data points by ~ 0.8 dex. In the bottom panel of Figure 3.7 the datapoints are already downshifted by such value. After accounting for this correction we find that four of our targets display a clear radio excess: the COSMOS target cid_451, whose jetted nature is confirmed also from the FIR-radio comparison; the CDF-S target XID36, which was inside the 2σ area before the correction but an outlier in the FIR-radio plane; the targets J1333+1649 and X.N.102.35, not plotted in the top panel of Figure 3.7 because they lack an FIR detection. The targets cid_346 and cid_1143 are still within the dispersion after the correction, but classified as jetted according to the position in the FIR-radio plane. Combining the results of the two panels in Fig. 3.7, we estimate a jetted AGN fraction of 10 – 15%, which is consistent with the typical values observed in X-ray selected samples.

3.5 Summary and future work

We have presented the sample targeted by SUPER, an on-going ESO’s VLT/SINFONI Large Programme assisted by AO facilities, designed to map the ionized gas kinematics down to ~ 2 kpc spatial resolution in a representative sample of 39 AGN at $2 < z < 2.5$. It will provide a systematic investigation of AGN ionized outflows and their effects on star formation in the host galaxies, by exploring a wide range in AGN and host galaxies properties. The sample was selected in an unbiased way with respect to the chance of detecting outflows, with the aim to cover the widest possible range in AGN properties. In this first work we fully characterized the physical properties of the AGN sample, drawn from X-ray surveys (i.e., CDF-S, COSMOS, XMM-XXL, Stripe82X, WISSH) which benefit from a wealth of multi-wavelength data, from the radio to the X-rays as follows:

- By collecting UV to FIR photometric data we built up the AGN SEDs and performed a detailed SED-fitting modeling which allowed us to derive stellar masses, $\log(M_*/M_\odot) = [9.59 - 11.21]$, SFR = $[25 - 680] M_\odot \text{ yr}^{-1}$, and AGN bolometric luminosities, $\log(L_{\text{bol}}/\text{erg s}^{-1}) = [44.3 - 47.9]$.
- A detailed X-ray spectral fitting was performed to determine column densities N_{H} up to $2 \times 10^{24} \text{ cm}^{-2}$ and X-ray 2–10 keV luminosities, $\log(L_{\text{X}}/\text{erg s}^{-1}) = [43.2 - 45.8]$.
- For AGN characterized by broad lines in their optical spectra we reported BH masses obtained using the “virial method” on the C IV and H β lines, with results in the range $\log(M_{\text{BH}}/M_\odot) = [7.9 - 10.2]$. These values were combined with the bolometric luminosity to compute Eddington ratios for this subsample of AGN which includes BHs accreting at the Eddington limit and down to 10^{-2} times λ_{Edd} .
- Finally, we retrieved the radio fluxes (or upper limits) for each target and, by comparing their FIR luminosities (when available) or their 24 μm fluxes, we inferred the presence of at least 6 jetted AGN in our sample.

As clear from the wide parameter ranges given above, our survey probes a representative sample of AGN, in terms of both host galaxy properties, such as stellar mass and SFR, and AGN ones, like column density, AGN bolometric luminosity, BH mass and Eddington ratio. This will give us the context to place our IFS studies and the opportunity to investigate possible links among all these quantities and connect them to the outflow properties.

To achieve one of the main goals of the survey, namely inferring the impact that outflows may have on the ability of the host galaxy to form stars, we need to quantify their gas content. Molecular gas represents indeed the principal fuel for star formation in galaxies and the fundamental link between SF and AGN activity. In AGN host galaxies, molecular gas fractions ($f_{\text{gas}} = M_{\text{gas}}/M_*$) and depletion timescales ($t_{\text{dep}} = M_{\text{gas}}/\text{SFR}$) appear to be

smaller than the values measured for the parent population of SF galaxies (e.g., Kakkad et al., 2017; Brusa et al., 2018, but see also Husemann et al. 2017a; Rosario et al. 2018). The interpretation of these quantities is non-trivial and requires a joint characterization of the cold molecular and ionized gas phase. SUPER will achieve this goal by combining the SINFONI observations with two on-going programs with ALMA and APEX:

- SUPER-ALMA (PI: Mainieri; see Chapter 4), which has been allocated 12.6 and 19.5 hours of ALMA Band-3 observing time in Cycle 4 and 5 respectively, to target the CO(3-2) emission line with 1'' angular resolution over a sample constructed to include the SUPER sources. This project will perform a systematic study of the gas content of AGN hosts, in order to derive gas fractions and depletion timescales, but will also complement the goals of our SINFONI survey. In fact, information about the possible presence of outflows in these targets will be available and will allow us to infer whether there is a causal connection between a lower gas fraction and the presence of an AGN-driven outflow.
- SUPER-APEX (PI: Cicone), a pilot project with the APEX PI230 Rx receiver that was allocated 28.2 hours to observe, in two of our targets, the [C_I](2-1) transition as a tracer of the total amount of cold H_2 and the CO($J=7-6$) transition, which will trace the warmer and denser phase of H_2 .

Recent studies showed that a significant fraction of the mass and momentum of AGN-driven outflows can be contained in the molecular gas phase (e.g., Cicone et al., 2014; Carniani et al., 2015; Fiore et al., 2017). To obtain a comprehensive picture of the feedback processes, it is crucial to investigate the molecular gas properties. The next step will be to map the molecular gas, tracing the fuel for star formation and feedback, with the same \sim kpc spatial resolution of the ionized gas (e.g., Cicone et al., 2018). A comprehensive and dynamic view of the evolution of the star formation process and the impact of AGN feedback across the host galaxy, at the peak epoch of galaxy assembly, will be finally possible. This will have far reaching implications on theoretical models and simulations of galaxy-AGN evolution. The final goal of the SUPER project is to be a reference legacy survey for future work and to establish a unique statistical sample at high redshift characterized by a wide set of ancillary data. The systematic approach adopted will reveal key clues about outflow physics and feedback in AGN host galaxies.

Chapter 4

The molecular gas content of active galactic nuclei at $z \sim 2$

4.1 Introduction

The discovery of correlations between the mass of supermassive black holes (SMBHs) and their host galaxy properties (e.g., bulge masses, Magorrian et al. 1998, and velocity dispersions, Ferrarese & Merritt 2000) provided indirect evidence for a connection between them. It is still unclear which physical processes are responsible for such correlations. However, a key role is attributed to active phases which SMBHs go through while accreting material, when they are visible as active galactic nuclei (AGN). During these phases the central engine releases a huge amount of energy which is injected into the surrounding interstellar medium (ISM). This energy, if efficiently coupled, could remove, heat and/or dissociate the molecular gas, which is the fuel out of which stars form. Such process may regulate the growth of the host galaxy and establish the observed correlations between SMBH and galaxy properties (for a review, see Kormendy & Ho, 2013). The mechanisms by which the energy produced by the AGN is coupled to the ISM is called AGN feedback (Fabian, 2012; King & Pounds, 2015; Harrison, 2017). Theoretically, AGN feedback is invoked to reproduce the observed properties of the galaxy population, for example the lack of very massive galaxies in the most massive galaxy haloes (Somerville et al., 2008), the bimodal color distribution of galaxies (Strateva et al., 2001) and the correlations between SMBH mass and host galaxy properties. Although AGN feedback is a necessary ingredient in models of galaxy evolution, proving its role observationally remains a challenge. In particular, outflows from AGN have been observed in many galaxies (e.g., Cicone et al., 2014; Carniani et al., 2015; Cresci et al., 2015; Kakkad et al., 2016; Brusa et al., 2018), but their impact on the global star-forming activity of the hosts is still an open issue.

To understand the link between AGN and star formation, previous studies compared a proxy of AGN activity (e.g., the X-ray luminosity) and the star-formation rate (SFR). While no correlation was found for moderate-luminosity AGN ($L_{X, 2-8 \text{ keV}} \leq 10^{44} \text{ erg s}^{-1}$; e.g., Lutz et al. 2010; Harrison et al. 2012b), the conclusions were contradictory for high

luminosity AGN ($L_{X, 2-8 \text{ keV}} \geq 10^{44} \text{ erg s}^{-1}$), reporting no correlation (e.g. Harrison et al., 2012b; Rosario et al., 2012; Stanley et al., 2015), a negative (e.g., Page et al., 2012) or a positive one (e.g., Rovilos et al., 2012; Delvecchio et al., 2015; Harris et al., 2016). The discrepancies are due to selection effects and the different timescales of the AGN phase (few Myr) and star formation activity in the host galaxy (hundred of Myr; Hickox et al., 2014; Scholtz et al., 2018).

A promising approach to move forward requires direct observations of the cold gas reservoir of galaxies, which fuels both star formation and AGN activity. Recent results constrain the cosmic evolution of the molecular gas density (Decarli et al., 2019). This seems to closely match the evolution of the cosmic SFR density and the black hole accretion rate (Madau & Dickinson, 2014; Aird et al., 2015), therefore supporting the relevance of the gas reservoir as a key ingredient in galaxy evolution and SMBH accretion history. The molecular gas provides an instantaneous measure of the raw fuel to form stars and a more direct tracer of potential feedback effects since it is less affected by the timescale issue, unlike the SFR. However, our current understanding of the molecular gas content for the galaxy and AGN population is incomplete, especially for AGN. During the last years, large observational efforts have been devoted to map the molecular gas reservoir of galaxies (e.g., García-Burillo et al., 2012; Bauermeister et al., 2013; Cicone et al., 2017; Saintonge et al., 2017; Tacconi et al., 2018). These studies are largely based on observations of carbon monoxide (CO) rotational emission lines, used as a tracer of molecular hydrogen H_2 (in particular the ground-state rotational transition best traces the total molecular gas). The main targets of such CO campaigns have primarily been “inactive” galaxies that mostly lie on the main sequence of star-forming galaxies (MS; e.g., Noeske et al., 2007; Schreiber et al., 2015), where the majority of the cosmic star-formation activity occurs. Starburst galaxies lie above the MS and contribute to $\sim 10\%$ of the cosmic SFR density (Rodighiero et al., 2011).

The fundamental relationship between SFR and molecular gas content of galaxies provides precious information about how efficiently galaxies turn their gas into stars. Such star-formation law (or Schmidt-Kennicutt relation; Schmidt, 1959; Kennicutt, 1989) is usually presented in terms of surface densities, therefore requiring resolved measurements of galaxies. However, in high-redshift studies, an integrated form of this relation with global measurements of SFR and molecular mass is normally used (e.g., Carilli & Walter, 2013; Sargent et al., 2014). As in the SFR- M_* plane, star-forming galaxies and starbursts show different properties in terms of SFR and gas mass. Whether the difference is driven by the molecular gas content and/or the gas consumption timescale is still matter of debate (e.g., Daddi et al., 2010; Genzel et al., 2015; Scoville et al., 2016). The timescale needed to consume the available galaxy molecular gas content given the current SFR is called depletion time, $t_{\text{dep}} = M_{\text{mol}}/\text{SFR}$. Main-sequence galaxies typically have $t_{\text{dep}} > 100 \text{ Myr}$, while starbursts show $t_{\text{dep}} < 10 \text{ Myr}$ (e.g., Daddi et al., 2010).

A similar observational effort is needed to characterize the cold gas phase of AGN host galaxies to understand whether this is different from inactive galaxies and quantify any potential effect of AGN feedback on the host galaxy ISM. Currently, there is no consensus in the literature. Some local studies report no clear evidence for AGN to affect the ISM

component of the host, by tracing the molecular phase (e.g., Husemann et al., 2017a; Saintonge et al., 2017; Rosario et al., 2018), the atomic one (e.g., Ellison et al., 2019), and the dust mass as a proxy of the gas mass (e.g., Shangguan & Ho, 2019). AGN appear to follow the same star-formation law of normal galaxies. Since the redshift $1 < z < 3$ corresponds to the peak of accretion activity of SMBHs, when the energy injected into the host galaxy may be maximized, this cosmic epoch is a crucial laboratory to look for AGN feedback effects. Interestingly, studies at redshift $z > 1$ present contrasting results. In particular, some found reduced molecular gas fractions (i.e., the molecular gas mass per unit stellar mass, $f_{\text{gas}} = M_{\text{mol}}/M_*$) and depletion timescales of AGN compared to the parent population of normal galaxies (Carilli & Walter, 2013; Kakkad et al., 2016; Fiore et al., 2017; Brusa et al., 2018; Perna et al., 2018). This has been interpreted as an evidence for highly efficient gas consumption possibly related to AGN feedback affecting the gas reservoir of the host galaxies. For a few targets, fast outflows were also detected (e.g., Fiore et al., 2017; Brusa et al., 2018). Complementary observations tracing the possible presence of outflows are needed to generally confirm such conclusions.

Nevertheless, these studies are affected by several assumptions and limitations. CO measurements at $z > 1$ are usually performed using high-J transitions, and excitation corrections are needed to estimate the luminosity of the ground-state transition. The CO spectral line energy distribution (SLED) of a given target is rarely known and therefore the excitation correction is typically highly uncertain. In addition, calculating gas masses from CO luminosities (L'_{CO}) requires the assumption of a conversion factor α_{CO} , that depends on the conditions of the ISM and typically ranges between 0.8 and $4 M_{\odot}/(\text{K km s}^{-1} \text{ pc}^2)$ (Carilli & Walter, 2013). When dealing with SFRs of AGN hosts, an additional complication is the difficulty to properly account for the AGN contribution to the far-infrared (FIR) luminosity. As recently shown by Kirkpatrick et al. (2019), different methods to estimate the AGN contribution can lead to completely different results and place the AGN population on the same star-formation law of normal galaxies. Finally, AGN samples at high redshift are usually small and likely biased toward brighter objects (e.g., Brusa et al., 2018) or are heterogeneous when assembled from literature data (e.g., Fiore et al., 2017; Perna et al., 2018; Kirkpatrick et al., 2019).

In this Chapter we present the first systematic and uniform analysis of the molecular gas content of AGN at $z \sim 2$ to infer whether their activity affects the ISM of the host galaxy. As a tracer, we use the CO(3-2) emission line, which is the lowest-J transition accessible with ALMA at $z \sim 2$. We compare the CO emission properties of our AGN as traced by ALMA with those of star-forming galaxies. Differently from previous work, our comparison sample only includes galaxies observed in the same transition of our targets. We then use the observed CO luminosities without making uncertain assumptions on conversion factors to retrieve the gas masses, which could bias our conclusions.

The Chapter is structured as follows: in Sec. 4.2 we describe the sample selection criteria and the target multi-wavelength properties, as well as the control sample used for comparison; Sec. 4.3 presents the multi-wavelength properties of our AGN sample; in Sec. 4.4 the ALMA observations and data analysis are outlined; we discuss our results in Sec. 4.5 and we present our conclusions in Sec. 4.6. In this work we adopt a *WMAP9*

cosmology (Hinshaw et al., 2013), $H_0 = 69.3 \text{ km s}^{-1} \text{ Mpc}^{-1}$, $\Omega_M = 0.287$ and $\Omega_\Lambda = 0.713$.

4.2 The sample

4.2.1 Target selection

The main aim of our ALMA program was to perform a follow-up of the AGN targeted by the SUPER survey, presented in Chapter 3. The goal is to have a complete picture of the ionized gas component as well as AGN-driven outflows traced by [OIII] VLT/SINFONI and the molecular gas properties of the host traced by ALMA. Part (25%) of the ALMA targets were excluded from the SUPER sample due to time constraints on the SINFONI observations, nevertheless they share the same properties and selection criteria of the rest of the sample. As a tracer of AGN activity we used X-ray emission, which is very efficient thanks to the low contamination from the host galaxy. We combined catalogs from a deep and small-area as well as a shallow and wide-area X-ray survey, in order to include in our sample both high- and low-luminosity AGN and cover a wide range in AGN bolometric luminosity L_{bol} (Brandt & Alexander, 2015; Circosta et al., 2018). The targets were drawn from the following surveys, by adopting as a threshold an absorption-corrected X-ray luminosity $L_X \geq 10^{42} \text{ erg s}^{-1}$:

- The *COSMOS-Legacy* survey (Civano et al., 2016; Marchesi et al., 2016a), a 4.6 Ms *Chandra* observation of the COSMOS field, with a deep exposure over an area of about 2.2 deg^2 at a limiting depth of $8.9 \times 10^{-16} \text{ erg cm}^{-2} \text{ s}^{-1}$ in the 0.5 – 10 keV band.
- The wide-area *XMM-Newton* XXL survey North (Menzel et al., 2016; Pierre et al., 2016), a $\sim 25 \text{ deg}^2$ field surveyed for about 3 Ms by *XMM-Newton*, with a sensitivity in the full 0.5 – 10 keV band of $2 \times 10^{-15} \text{ erg cm}^{-2} \text{ s}^{-1}$.

These fields are covered by a rich multi-wavelength set of ancillary data spanning from the X-rays to the radio regime, which are essential to obtain robust measurements of the target properties. Our AGN are then selected to have spectroscopic redshift in the range $z = 2.0 - 2.5$, whose quality was flagged as “Secure” in the respective catalogs as well as a coverage of AGN and galaxy properties as wide and uniform as possible. Overall, our sample consists of 25 AGN, namely 4 from XMM-XXL and 21 from COSMOS. 18 out of 25 are targeted by the SUPER survey (see Chapter 3; Circosta et al. 2018). IDs, coordinates and redshift of the sources are reported in Table 4.1.

4.2.2 Comparison sample of star-forming galaxies

We complemented our sample with data from the literature, building a comparison sample which consists of star-forming galaxies. In particular we drew targets from the PHIBSS sample, presented by Tacconi et al. (2018). This sample is made of main-sequence galaxies

| ID | RA[J2000] | DEC[J2000] | z_{spec} |
|-----------------------|-------------|--------------|-------------------|
| (1) | (2) | (3) | (4) |
| X_N_81.44 | 02:17:30.95 | −04:18:23.66 | 2.311 |
| X_N_53.3 | 02:20:29.84 | −02:56:23.41 | 2.434 |
| X_N_6.27 ^a | 02:23:06.32 | −03:39:11.07 | 2.263 |
| X_N_44.64 | 02:27:01.46 | −04:05:06.73 | 2.252 |
| lid_1852 ^a | 09:58:26.57 | +02:42:30.22 | 2.444 |
| lid_3456 ^a | 09:58:38.40 | +01:58:26.83 | 2.146 |
| cid_166 | 09:58:58.68 | +02:01:39.22 | 2.448 |
| lid_1289 | 09:59:14.65 | +01:36:34.99 | 2.408 |
| cid_1057 | 09:59:15.00 | +02:06:39.65 | 2.214 |
| cid_1605 | 09:59:19.82 | +02:42:38.73 | 2.121 |
| cid_337 | 09:59:30.39 | +02:06:56.08 | 2.226 |
| cid_346 | 09:59:43.41 | +02:07:07.44 | 2.219 |
| cid_357 ^a | 09:59:58.02 | +02:07:55.10 | 2.136 |
| cid_451 | 10:00:00.61 | +02:15:31.06 | 2.450 |
| cid_1205 | 10:00:02.57 | +02:19:58.68 | 2.255 |
| cid_2682 | 10:00:08.81 | +02:06:37.66 | 2.435 |
| cid_247 ^a | 10:00:11.23 | +01:52:00.27 | 2.412 |
| cid_1215 ^a | 10:00:15.49 | +02:19:44.58 | 2.450 |
| cid_467 | 10:00:24.48 | +02:06:19.76 | 2.288 |
| cid_852 | 10:00:44.21 | +02:02:06.76 | 2.232 |
| cid_970 ^a | 10:00:56.52 | +02:21:42.35 | 2.501 |
| cid_971 | 10:00:59.45 | +02:19:57.44 | 2.473 |
| cid_38 | 10:01:02.83 | +02:03:16.63 | 2.192 |
| lid_206 | 10:01:15.56 | +02:37:43.44 | 2.330 |
| cid_1253 | 10:01:30.57 | +02:18:42.57 | 2.147 |

Table 4.1: Summary of the target AGN sample. (1) Source identification number from the catalogs corresponding to each field, namely Menzel et al. (2016) for XMM-XXL and Civano et al. (2016) for COSMOS (see also Sec. 4.2.1). (2) RA and (3) DEC, given for the optical counterpart: the XMM-XXL targets have an SDSS counterpart whose coordinates are given in Menzel et al. (2016); for the COSMOS field we list the *i*-band coordinates taken from Marchesi et al. (2016a). (4) Spectroscopic redshift, taken from the papers listed above.

^a These targets were not presented in Chapter 3 (Circosta et al., 2018).

observed with IRAM PdB to target the CO($J=3-2$) transition as well as other literature sources. From the PHIBSS parent sample, we selected for our purposes galaxies with $z = 2 - 2.5$, the same redshift range of our targets, whose molecular gas mass was derived through CO($J=3-2$) observations. By requiring that also the control sample is observed in CO($J=3-2$), we are free from assumptions on the excitation correction, which can be crucial when comparing CO luminosities and bias the results (Kirkpatrick et al., 2019). The literature sample, satisfying these selection criteria, is made of 59 objects. It is relevant to mention that these targets cover the same range of stellar mass of our AGN sample. For each bin of stellar mass we further matched in SFR, therefore selecting all the galaxies within the range of SFR shown by our AGN. The final comparison sample used in this work is composed of 47 star-forming galaxies.

4.3 Multi-wavelength properties of the sample

We characterized the physical properties of our sources by exploiting the multi-wavelength coverage, from the X-ray to the radio regime, available for the fields where our targets lie. In particular, we followed the same procedure described in Chapter 3 (Circosta et al., 2018) to collect the multi-wavelength data and derive the properties of the targets that were not analyzed in our previous work, through X-ray spectral analysis and broad-band SED fitting.

The results of the SED-fitting analysis are reported in Tables B.1 and B.2 (Appendix B), together with the optical spectroscopic classification in broad-line (BL) and narrow-line (NL) AGN, depending on the presence of broad (FWHM $> 1000 \text{ km s}^{-1}$) or narrow (FWHM $< 1000 \text{ km s}^{-1}$) permitted emission lines in their spectra, respectively. From now on, we will refer to type 1 and type 2 AGN according to the optical spectroscopic classification. The SEDs of the whole sample are provided in Appendix C. When possible, SFRs are derived by assuming the Kennicutt (1998b) calibration, converted to a Chabrier (2003) IMF, from the IR luminosity integrated in the rest-frame wavelength range 8–1000 μm , after removing the AGN contribution. When only upper limits at observed $\lambda > 24 \mu\text{m}$ are available, we provide a 3σ upper limit on the SFR, derived as the 99.7th percentile from the probability distribution function of the FIR luminosity. For the targets with no data at observed $\lambda > 24 \mu\text{m}$, the dust templates were not included in the fitting routine. We therefore provide the SFR as derived from the modeling of the stellar component in the UV-to-NIR regime with SED fitting, averaged over the last 100 Myr of the galaxy star-formation history. We measured stellar masses in the range $\log(M_*/M_\odot) = 9.6 - 11.2$, FIR luminosities $\log(L_{\text{FIR}}/\text{erg s}^{-1}) = 45.3 - 46.4$, SFRs $< 686 M_\odot/\text{yr}$, and AGN bolometric luminosities $\log(L_{\text{bol}}/\text{erg s}^{-1}) = 44.7 - 46.9$ probing two orders of magnitude. In Fig. 4.1 we show the distribution of our targets in the SFR- M_* plane, as well as the control sample. Of our targets, 44% sit on the MS, 40% above and 16% at the lower boundary of the MS.

From the analysis of the X-ray spectra we derived obscuring column densities N_{H} and X-ray luminosities L_{X} . Again, we followed the same procedure described in Chapter 3. The results derived for column densities and 2 – 10 keV absorption-corrected luminosities

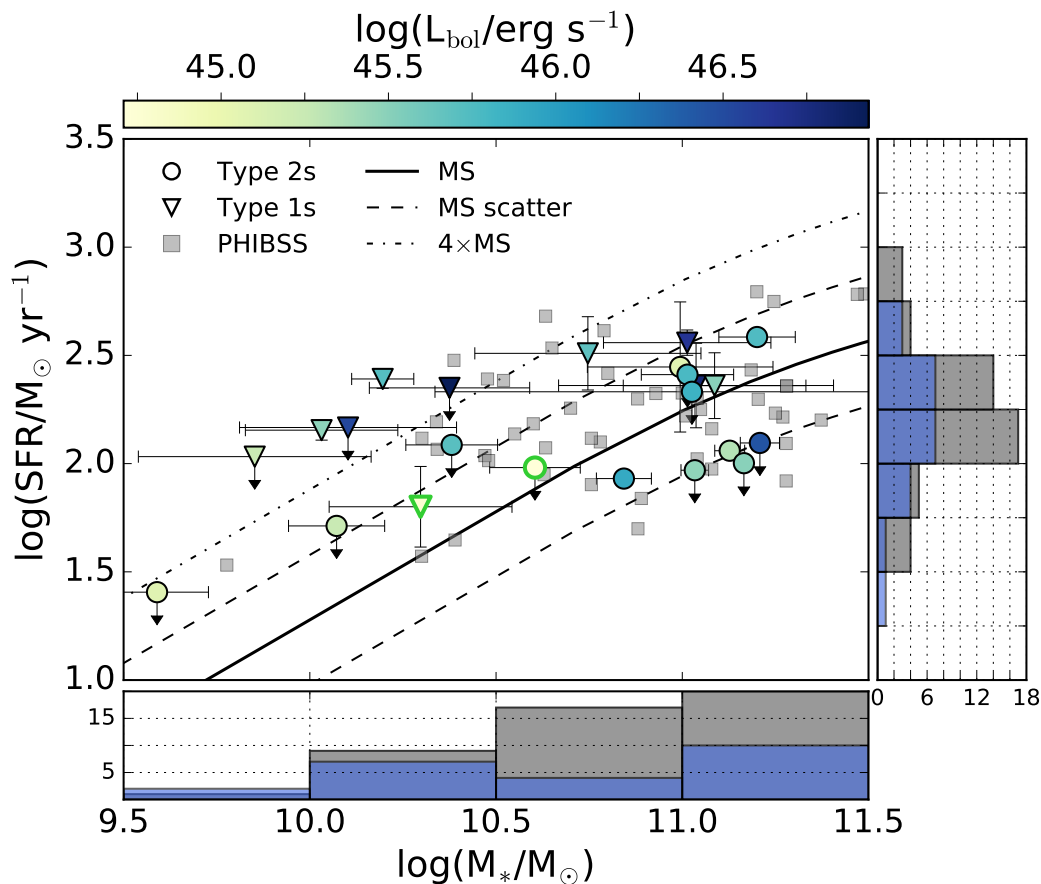


Figure 4.1: Distribution of host galaxy properties in the SFR- M_* plane for the 25 AGN (type 1s marked by triangles and type 2s marked by circles) in our sample and the comparison sample of normal star-forming galaxies (gray squares). The two data points with green edges represent the targets with SFR derived through modeling of the stellar emission with SED fitting. The color coding indicates the AGN bolometric luminosity for each object. The black solid line reproduces the main sequence of star-forming galaxies from Schreiber et al. (2015) at the average redshift of our target sample (i.e., ~ 2.3). The dashed lines mark the scatter of the main sequence (equal to 0.3 dex) while the dot-dashed line represents the locus 4 times above the main sequence along the SFR axis (as defined by Rodighiero et al., 2011). The histograms show the projected distribution of the two quantities along each axis, in blue for our sample and gray for the comparison one.

are listed in Table B.2. Our sample spans a range of obscuration properties including unobscured targets ($N_{\text{H}} < 10^{22} \text{ cm}^{-2}$) up to Compton-thick ones ($N_{\text{H}} > 10^{24} \text{ cm}^{-2}$) and X-ray luminosities in the range $\log(L_{[2-10 \text{ keV}]}/\text{erg s}^{-1}) = 43.0 - 45.4$.

4.4 ALMA data: observations and analysis

The ALMA observations of the targets were carried out in Cycle 4 and 5 (Project codes: 2016.1.00798.S and 2017.1.00893.S; PI: V. Mainieri) using 42–47 antennas and maximum baselines between 704 m and 1.1 km. Observations were taken in Band 3 between November 2016 and May 2017 (Cycle 4) and in March 2018 (Cycle 5). In each observation, one spectral window, with a bandwidth of 1.875 GHz, was centered at the expected frequency of the redshifted CO($J=3-2$) emission line (the rest-frame frequency is 345.8 GHz), while the other three spectral windows were used to sample the continuum emission. Each spectral window is divided in 240 channels and has a spectral resolution of 7.8 MHz, corresponding to 21–23 km/s at the line frequency. The exposure time on-source varied between ~ 9 and ~ 80 minutes, reaching a sensitivity of 0.1–0.5 mJy per 100 km/s velocity bin. The requested angular resolution was $1''$ in order to probe the total gas reservoir of our targets.

ALMA visibilities were calibrated using the CASA software¹ version 4.7.0 for Cycle 4 data and 5.1.1 for Cycle 5, as originally used for the reduction with the pipeline. The final datacubes have been generated with the CASA task TCLEAN in velocity mode and using a “natural” weighting, which optimizes the point-source sensitivity in the image plane, and a cellsize of $0.25''$. The velocity bin width was kept between 50 and 100 km/s to maximize the signal-to-noise ratio S/N and yet sample the line with at least four bins assuming a FWHM of 400 km/s (e.g., Daddi et al., 2010). After a first analysis, the targets cid_166 and cid_1605 showed a tentative broad line (FWHM $\gtrsim 600$ km/s) in the 100 km/s-binned cube and, to increase the S/N we reiterated the imaging with a velocity bin width of 200 km/s. Final products, generated from the continuum-subtracted uv-datasets, have angular resolutions of $0.6-1.4''$ depending on the dataset. The beam size for each target is reported in Table 4.2. We considered as a detection a line with S/N of the line peak over the rms of the spectrum $\gtrsim 3$. The line is detected in 12 out of 25 targets. The continuum remained undetected for all targets but cid_451, which is a jetted source with a high radio power (see Table B.2). Therefore, the detected ALMA continuum could be possibly produced by synchrotron emission from jets.

Moment 0 maps (i.e., the frequency-integrated flux maps) were constructed by using the task IMMOMENTS and collapsing along the channels with CO detections. The rms was computed on the source spectrum where there is no line or on the spectrum where we would expect to detect the line, in case of non-detections. We reached a sensitivity of 0.1–0.5 mJy, as listed in Table 4.2. For the targets with a CO($J=3-2$) detection, the spectra were extracted from the ALMA cubes using an aperture which maximizes the S/N ($\sim 1-2''$). We fit the line using a Gaussian model (Python package LMFIT) in order to retrieve the velocity-integrated fluxes and the width of the line. Moment 0 maps and spectra of the

¹<https://casa.nrao.edu>

targets with a detected line are reported in Appendix D. The results of our analysis, namely the line flux, the FWHM and central frequency of the line, together with the details of the observations (expected observed frequency of the line and beam size), are reported for each target in Table 4.2. For the non-detections, we provide a 3σ upper limit calculated from the sensitivity reached over a channel width of 100 km/s in the spectral window where we expect the CO($J=3-2$) line, and assuming a line width of 416 km/s, which is the average of the FWHM values measured for our detections. We finally derive CO luminosities (in Table 4.2) as given by Solomon & Vanden Bout (2005):

$$L'_{\text{CO}} = 3.25 \times 10^7 I_{\text{CO}} \nu_{\text{obs}}^{-2} D_{\text{L}}^2 (1+z)^{-3} \quad (4.1)$$

where I_{CO} is the velocity-integrated flux, D_{L} is the luminosity distance and ν_{obs} is the observed frequency of the line. We measured FWHM in the range 150–870 km/s and CO($J=3-2$) luminosities $\log(L'_{\text{CO}}/\text{K km/s pc}^2) = 9.28 - 10.69$. Gas masses were derived assuming the excitation factor measured for AGN, $R_{31} = L'_{\text{CO}(3-2)}/L'_{\text{CO}(1-0)} = 0.92 \pm 0.44$ (Kirkpatrick et al., 2019) and $\alpha_{\text{CO}} = 3.6$, commonly used in the literature for star-forming galaxies at a similar redshift as our AGN sample (Daddi et al., 2010; Tacconi et al., 2013; Kakkad et al., 2016).

| ID | ν_{obs} | Beam size | rms | I_{CO} | FWHM | ν_0 | $\log(L'_{\text{CO}(3-2)})$ | $\log(M_{\text{mol}})$ |
|-----------|--------------------|------------------|-------|-----------------|---------------|---------|-----------------------------|------------------------|
| (1) | [GHz] | [" \times ""] | [mJy] | [mJy km/s] | [km/s] | [GHz] | [K km/s pc ²] | [M_{\odot}] |
| (1) | (2) | (3) | (4) | (5) | (6) | (7) | (8) | (9) |
| X_N_81.44 | 104.44 | 1.4 \times 1.1 | 0.138 | <89 | - | - | <9.42 | <10.01 |
| X_N_53.3 | 100.70 | 1.4 \times 1.2 | 0.228 | 189 \pm 41 | 562 \pm 197 | 100.71 | 9.79 \pm 0.19 | 10.38 \pm 0.28 |
| X_N_6.27 | 105.97 | 1.3 \times 1.2 | 0.200 | <129 | - | - | <9.79 | <10.16 |
| X_N_44.64 | 106.33 | 1.2 \times 1.2 | 0.134 | 242 \pm 51 | 401 \pm 120 | 106.55 | 9.92 \pm 0.15 | 10.51 \pm 0.26 |
| lid_1852 | 100.40 | 1.4 \times 1.2 | 0.109 | <70 | - | - | <9.36 | <9.95 |
| lid_3456 | 109.9 | 1.3 \times 1.2 | 0.395 | <254 | - | - | <9.82 | <10.41 |
| cid_166 | 100.29 | 1.3 \times 0.9 | 0.159 | 454 \pm 57 | 810 \pm 153 | 99.89 | 10.17 \pm 0.11 | 10.77 \pm 0.23 |
| lid_1289 | 101.47 | 1.5 \times 1.2 | 0.091 | <59 | - | - | <9.27 | <9.86 |
| cid_1057 | 107.59 | 1.7 \times 1.2 | 0.239 | <154 | - | - | <9.63 | <10.22 |
| cid_1605 | 110.80 | 1.2 \times 1.2 | 0.145 | 266 \pm 43 | 467 \pm 135 | 110.96 | 9.83 \pm 0.15 | 10.43 \pm 0.26 |
| cid_337 | 107.19 | 1.3 \times 1.1 | 0.218 | 227 \pm 42 | 587 \pm 216 | 106.84 | 9.80 \pm 0.16 | 10.39 \pm 0.26 |
| cid_346 | 108.27 | 1.2 \times 1.1 | 0.255 | 720 \pm 88 | 239 \pm 34 | 107.39 | 10.30 \pm 0.10 | 10.88 \pm 0.23 |
| cid_357 | 110.27 | 1.3 \times 1.1 | 0.183 | <118 | - | - | <9.48 | <10.08 |
| cid_451 | 100.23 | 1.6 \times 1.4 | 0.393 | 167 \pm 36 | 165 \pm 66 | 100.37 | 9.73 \pm 0.19 | 10.32 \pm 0.28 |
| cid_1205 | 106.24 | 1.5 \times 1.1 | 0.161 | <104 | - | - | <9.47 | <10.06 |
| cid_2682 | 100.67 | 1.3 \times 1.3 | 0.219 | 165 \pm 34 | 209 \pm 79 | 100.68 | 9.73 \pm 0.18 | 10.32 \pm 0.27 |
| cid_247 | 101.35 | 1.4 \times 1.3 | 0.230 | <148 | - | - | <9.67 | <10.27 |
| cid_1215 | 100.23 | 1.8 \times 1.3 | 0.545 | 1092 \pm 120 | 672 \pm 161 | 100.37 | 10.55 \pm 0.10 | 11.14 \pm 0.23 |
| cid_467 | 105.17 | 0.9 \times 0.7 | 0.129 | <83 | - | - | <9.38 | <9.98 |
| cid_852 | 106.99 | 1.4 \times 1.1 | 0.157 | <101 | - | - | <9.45 | <10.04 |
| cid_970 | 98.80 | 1.5 \times 1.2 | 0.096 | <62 | - | - | <9.32 | <9.91 |
| cid_971 | 99.57 | 0.8 \times 0.8 | 0.058 | 62 \pm 25 | 151 \pm 33 | 99.67 | 9.30 \pm 0.38 | 9.89 \pm 0.43 |
| cid_38 | 108.33 | 1.4 \times 1.3 | 0.175 | <113 | - | - | <9.48 | <10.08 |
| lid_206 | 103.84 | 1.6 \times 1.4 | 0.092 | 61 \pm 27 | 184 \pm 55 | 103.77 | 9.28 \pm 0.41 | <10.08 |
| cid_1253 | 109.88 | 1.3 \times 1.2 | 0.428 | 1857 \pm 140 | 871 \pm 96 | 109.73 | 10.69 \pm 0.11 | 11.27 \pm 0.22 |

Table 4.2: Summary of ALMA observations and analysis. (1) Source identification number; (2) Expected observed frequency of the CO($J=3-2$) line based on the redshift given in Table 4.1; (3) Beam size in arcsec; (4) Rms calculated using a velocity channel of 100 km/s; (5) Velocity-integrated CO fluxes and 1σ error, as well as upper limits for non-detections; (6) FWHM of the CO line and 1σ error; (7) Frequency of the detected CO line; (8) Luminosity of the CO($J=3-2$) line and 1σ error, as well as upper limits for non-detections; (9) Molecular gas mass and 1σ error, as well as upper limits for non-detections.

4.5 Results and discussion

As previously said, we focus on the CO($J=3-2$) luminosity for both our sample and the comparison one with the aim to avoid a priori assumptions on excitation correction factors which can be very uncertain. In the following, we use the CO($J=3-2$) luminosity as a proxy of the molecular gas mass. Similarly, we use the FIR luminosity, subtracted by the contribution of the AGN, as a proxy of the SFR. The PHIBSS data release provides the final gas masses and we derived CO luminosities following the prescriptions given in Tacconi et al. (2018) for the metallicity-dependent α_{CO} and an excitation factor $R_{13} = L'_{\text{CO}(1-0)}/L'_{\text{CO}(3-2)} = 1.8$. In Fig. 4.2 we plot CO and FIR luminosities for our sample and the comparison one. We used as reference the relationships derived for normal galaxies and starbursts by Sargent et al. (2014). These were originally derived by converting the luminosities of all targets to the CO($J=1-0$) transition, therefore we rescaled them to the CO($J=3-2$) luminosity to compare with our measurements, by adopting the ratio $R_{13} = 1.8$, normally used for star-forming and submillimeter galaxies (Bothwell et al., 2013; Carilli & Walter, 2013; Tacconi et al., 2018). The solid line and its dispersion in Fig. 4.2 can be interpreted as the region of the parameter space where most normal galaxies lie. The dashed line instead marks the region of the plot where starbursts are located. We color code the points by their offset in SFR with respect to the MS at the corresponding redshift (Schreiber et al., 2015). The sources with an offset in SFR within ± 0.3 dex sit on the main sequence in the SFR- M_* plane (see Fig. 4.1). Despite a number of upper limits in L_{FIR} and therefore SFR (color-coded in gray in Fig. 4.2), our AGN appear to be underluminous in CO compared to the population of normal galaxies, especially in the lower range of FIR luminosity.

Since a homogeneous characterization of the multi-wavelength properties of our targets was performed, we exploited this set of physical parameters by investigating potential trends of the distribution of our AGN in the $L'_{\text{CO}} - L_{\text{FIR}}$ plane, with respect to AGN bolometric luminosity or obscuring column density. We did not find any significant correlation with these properties. As for the bolometric luminosity, there is a known limitation due to different timescales between L_{FIR} and L_{bol} . Star-forming activity as traced by FIR observations has a timescale of ~ 100 Myr while AGN activity can vary on much shorter time intervals, < 10 Myr (e.g., Hickox et al., 2014; Stanley et al., 2015). As for the column density, evolutionary scenarios of powerful AGN predict that the unobscured phase follows the obscured one after that the AGN has removed some gas and dust from the galaxy because of feedback mechanisms. However, previous studies in the literature looked at this possibility but no trend with obscuration was found (Perna et al., 2018; Shangguan & Ho, 2019). Identifying the evolutionary phase of an AGN based on the amount of obscuration is challenging, because of the non-uniform distribution of the absorbing material and rapid variations of the AGN duty cycle. Therefore, potential trends may be washed out in the scatter.

We now compare the distribution of L'_{CO} with the stellar masses of AGN and normal galaxies, as shown in Fig. 4.3 (*top panel*), color-coded by the offset in SFR with respect to the MS. Overall there is an increase in CO luminosity with stellar mass and, for a

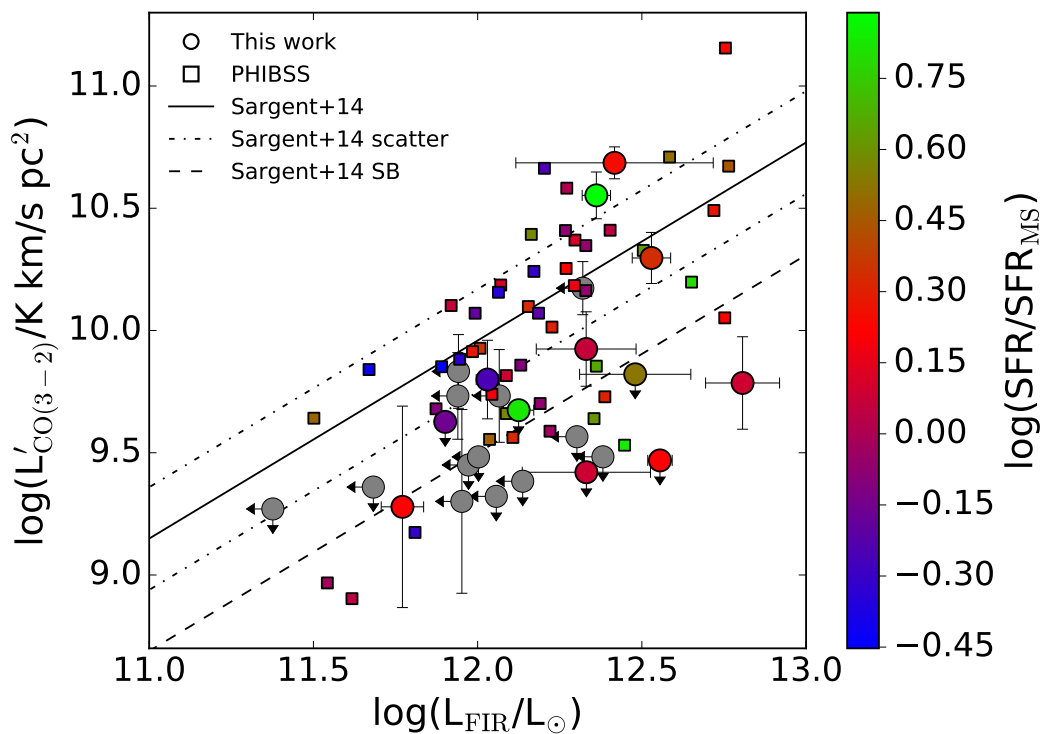


Figure 4.2: L'_{CO} as a function of L_{FIR} for our sample (circles) and the PHIBSS targets (squares; Tacconi et al. 2018). The color coding shows the deviation of the targets with respect to the MS (Schreiber et al., 2015). The targets with an upper limit in L_{FIR} and therefore SFR are colored in gray. The solid line depicts the relation derived by Sargent et al. (2014) for normal galaxies (the dot-dashed lines show the dispersion of 0.21 dex), while the dashed line represents the sequence for starburst galaxies. They were both rescaled to the CO($J=3-2$) transition by a factor 1.8.

given value of stellar mass, the CO luminosity increases for galaxies above the MS. To quantify the differences between the two samples, in Fig. 4.3 (*bottom panel*), we divided the targets in bins of stellar mass (width of 0.5 dex) and for each we computed the average L'_{CO} . Since in our sample 13 out of 25 targets have an upper limit for this quantity, we performed a survival analysis in order to take them into account. We used the function KMESTM within the ASURV package, which gives the Kaplan-Meier estimator for the distribution function of a sample with upper limits. As for the comparison sample, the quantities shown in the plot are the mean values and the errorbars represent the standard deviation of the distribution. The difference is not statistically significant in the lower mass bins ($\log(M_*/M_\odot) < 10.5$), in particular the first (low-) mass bin contains only one normal galaxy and two AGN (upper limits). However, there is a difference in L'_{CO} at the high mass end, which is particularly clear for $\log(M_*/M_\odot) > 11$. Normal galaxies appear to have CO luminosities higher than AGN, with a difference of more than 0.5 dex in the high-mass bin. The result holds even considering the sample of normal galaxies not matched in SFR (i.e., the 59 targets representing our initial literature sample, as described in Sec. 4.2.2). The results shown in Fig. 4.3 represent a first attempt to quantify the differences of the two populations of sources, although we are aware that the assumption of random distribution of the upper limits characterizing the survival analysis does not exactly hold in our case, because we are restricted to a narrow redshift range. We plan to explore the characterization of the distribution of upper limits by using an MCMC algorithm (Bernhard et al., 2018).

Previous works (Förster Schreiber et al., 2019), studying outflows in galaxies through the H α emission line, found that incidence, strength, and velocity of AGN-driven winds is strongly correlated with stellar mass. In particular, high-velocity ($\sim 1000\text{--}2000$ km s $^{-1}$) AGN-driven outflows are commonly detected at masses above $\log(M_*/M_\odot) = 10.7$. This is the same stellar-mass threshold above which the difference in CO luminosity between the population of AGN and star-forming galaxies in our results is significant. A deficit of CO emission in the CO($J=3-2$) transition has been recently found by Kirkpatrick et al. (2019). They performed a study of CO emission properties of AGN as a function of AGN contribution in the MIR regime, for an heterogeneous sample of targets collected from the literature. Their sample spanned from very low AGN contribution (essentially inactive galaxies) to powerful AGN. They derived representative SLEDs for normal galaxies and AGN and compared the CO line fluxes for several transitions. Although the results were not statistically robust for some transitions because of substantial uncertainties and small sample sizes, they found significant differences for CO($J=3-2$) and CO($J=1-0$) for which they had a higher number of detections. In particular, the line fluxes of AGN were lower than for normal galaxies. Such result is in agreement with what we found for our samples and would translate in lower gas masses in high-redshift AGN. Similarly, Fiore et al. (2017) compared molecular gas and stellar masses for an heterogeneous AGN sample collected from the literature and found lower gas masses in AGN than in star-forming galaxies.

The difference in CO luminosity between the population of AGN and normal galaxies could be ascribed to the presence of the AGN. The central engine could have a role in heating, exciting, dissociating and/or ejecting the gas. However, understanding the mechanism

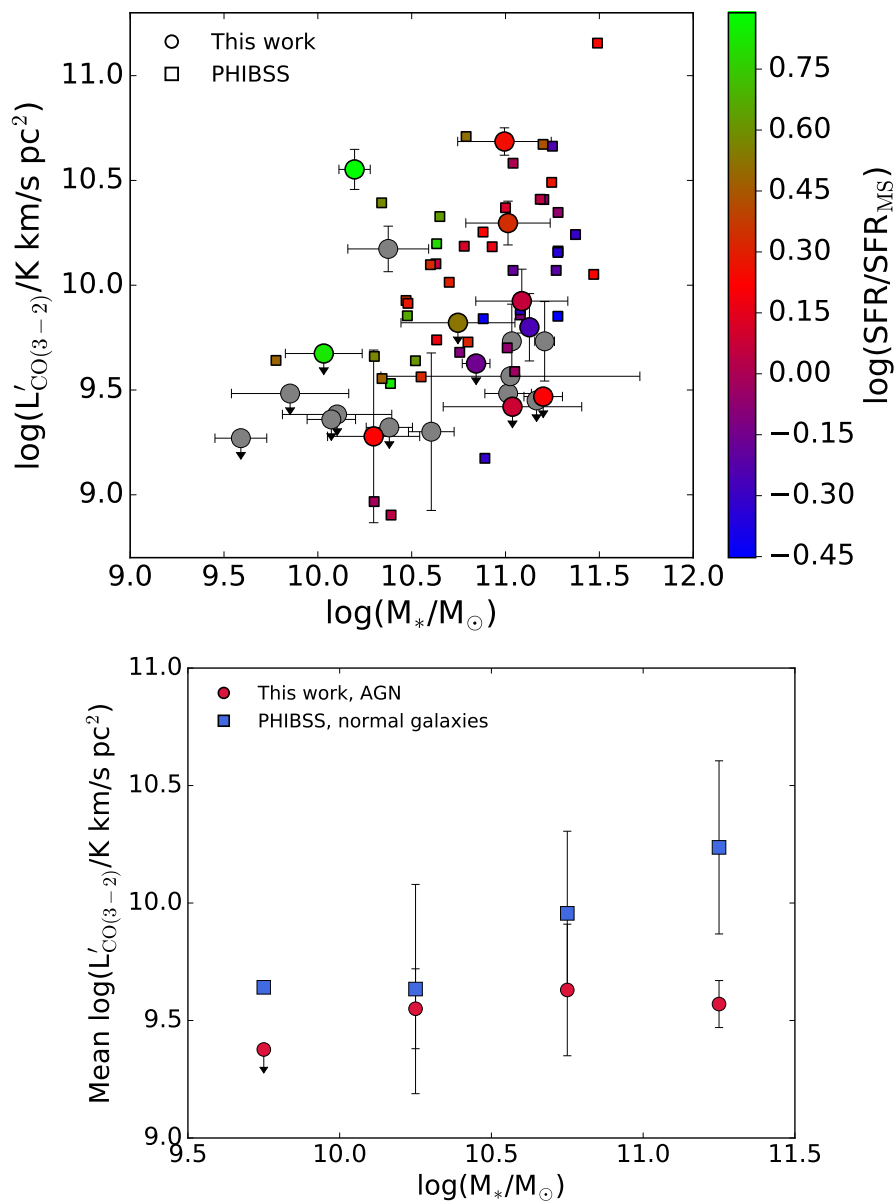


Figure 4.3: *Top panel:* L'_{CO} versus stellar masses for our sample of AGN (circles) and normal galaxies (squares; Tacconi et al. 2018). The color coding shows the deviation of the targets with respect to the MS (Schreiber et al., 2015). Overall there is an increase in CO luminosity with stellar mass and, for a given value of stellar mass, the CO luminosity increases for galaxies above the MS. *Bottom panel:* mean L'_{CO} in bins of stellar mass (0.5 dex width) for AGN (circles) and normal galaxies (squares). Normal galaxies appear to have CO luminosities higher than AGN, with a difference of more than 0.5 dex in the high-mass bin.

producing such difference requires further data, tracing different gas phases and several CO transitions. With the dataset in hand, we can only focus on one specific CO transition. We provide in the following possible scenarios to interpret our results.

The gas is excited by the AGN to higher- J transitions. Previous works found a difference in the CO SLEDs of AGN compared to those of star-forming galaxies at high redshift, with the former peaking at higher- J transitions (e.g., Weiß et al., 2007; Carilli & Walter, 2013). The molecular gas of AGN could therefore be more excited than in normal galaxies and, as a consequence, we observe less CO emission in the lower- J transitions. However, for low- J transitions it is difficult to distinguish between the effects of star formation and AGN activity if SLED excitation can already be explained by high SFR densities (Narayanan & Krumholz, 2014). Overall, large collections of local CO SLEDs display a wide variation in their overall shape (e.g., Mashian et al., 2015), with some trends of the strength of high- J CO transitions which increases with the AGN bolometric luminosity. At high redshift the sampling of the SLED is usually sparser than the local Universe, but variations in the SLEDs connected with the presence of an AGN were reported (e.g., Carilli & Walter, 2013; Brusa et al., 2018; Carniani et al., 2019). Studies of CO SLEDs over large AGN samples, especially out to high- J transitions, are needed to understand the role of AGN ionization in shaping the properties of the molecular gas reservoir. We plan to perform a detailed CO SLED analysis for some of our objects with a follow-up ALMA program (see Chapter 5).

The gas is heated/dissociated by the AGN. An interesting example of this scenario was recently presented by Rosario et al. (2019). Thanks to spatially-resolved observations of different gas phases (both molecular and ionized) for a local AGN, they identified a central region which is weak in CO($J=2-1$) emission but filled with ionized and warm molecular gas (H_2 MIR rotational lines). They concluded that the energy liberated by the AGN may influence the molecular gas properties and suppress the CO($J=2-1$) emission by heating and dissociating the molecular gas. Although the action of the central engine is limited to the innermost region (<200 pc) for this target, we notice that it is a nearby Seyfert 2 galaxy, whose properties are different from the bulk of the AGN population at the peak of SMBH activity. At high redshift, when the overall AGN population is more active, the central engine could have an impact over larger spatial scales. Whether this effect of the AGN would be observed in integrated measurements of the molecular gas content is not clear and we currently miss the data to further investigate this possibility.

AGN-driven outflows affect the gas reservoir. Another possible effect of the AGN activity on the molecular gas is through outflows. This possibility is supported by observations of individual objects. For example, Brusa et al. (2018) found low gas fraction in a powerful AGN at $z \sim 1.6$ hosting also a high-velocity molecular and ionized outflow. AGN feedback in action in this target could be depleting the molecular gas reservoir. As for our sample, we are performing a systematic investigation of the ionized gas phase with SINFONI as part of the SUPER survey (see Chapter 3). These dataset, available for 19 out of 25 targets, will reveal the presence of outflows (see Chapter 5).

Distinguishing among the different scenarios is challenging. AGN feedback could proceed in different ways and different mechanisms may overlap in shaping the properties of the molecular gas reservoir. For example, AGN radiation could both excite the molecular

gas altering the SLED and dissociate CO molecules. In this case, AGN would produce a feedback mechanism that does not require outflows. As for AGN-driven outflows, they could impact the gas content by ejecting material out of the galaxy. Additionally, numerical simulations predict that AGN-driven outflows may heat via shocks a significant quantity of the gas in the ISM, reaching the high temperatures required for the excitation of high- J CO transitions (Costa et al., 2018). As part of our future efforts, we will start investigating these different possibilities by tracing ionized outflows and their properties for our targets and probing the CO SLEDs with ALMA (see Chapter 5).

4.6 Conclusions

In this work we presented the first systematic investigation of the molecular gas content of AGN at $z \sim 2$. We analyzed ALMA observations of the CO($J=3-2$) transitions for a sample of 25 AGN, selected from deep and shallow X-ray surveys, in order to cover a wide range in AGN and galaxy properties. To infer whether AGN activity affects the ISM of the host galaxy, we compared the CO properties of our sample with those of star-forming galaxies. Our findings can be summarized as follows.

- For our sample we characterized the multi-wavelength properties of both AGN and their host galaxies through SED-fitting and X-ray spectral analysis. We measured stellar masses ($\log(M_*/M_\odot) = 9.6 - 11.2$), FIR luminosities ($\log(L_{\text{FIR}}/\text{erg s}^{-1}) = 45.3 - 46.4$), AGN bolometric luminosities ($\log(L_{\text{bol}}/\text{erg s}^{-1}) = 44.7 - 46.9$), column densities ($N_{\text{H}} < 2 \times 10^{24} \text{ cm}^{-2}$) and X-ray luminosities ($\log(L_{[2-10 \text{ keV}]}/\text{erg s}^{-1}) = 43.0 - 45.4$).
- The control sample of star-forming galaxies was drawn from the PHIBSS survey (Tacconi et al., 2018), matching the same range of redshift, stellar mass and SFR of our targets. Additionally, we only selected targets with observations of the CO($J=3-2$) transition. This requirement allowed us to avoid uncertain assumptions on conversion factors to retrieve the gas masses, which could bias our conclusions. We then used the CO($J=3-2$) luminosities for our comparisons.
- We detected CO emission in 12 out of 25 targets and carried out a Gaussian fit to measure velocity-integrated fluxes and line widths. The emission line widths are in the range 150–870 km/s. For the targets without a detection we provided 3σ upper limits.
- By comparing the CO and FIR luminosities of our AGN and the control sample, as well as their stellar masses, we found that AGN are overall underluminous in CO. We further quantified this difference by dividing our samples in bin of stellar mass and computing mean CO luminosities for each bin. The difference resulted to be particularly significant in the high-mass bins, especially for $\log(M_*/M_\odot) > 11$, where AGN are more than 0.5 dex less luminous than star-forming galaxies.

- We interpreted our result as an evidence for the effect of AGN activity, which may be able to excite, dissociate or deplete the gas reservoir of the host galaxies. Whether the driving mechanisms are AGN radiation and/or outflows cannot be established with the current dataset. Future and ongoing observations will allow us to start pinpointing the contribution of different mechanisms.

Chapter 5

Conclusions and Future prospects

This thesis presented a multi-wavelength approach to the evolution of AGN and their host galaxies at cosmic noon ($1 < z < 3$). In particular, I adopted observational methods to study the ISM of AGN, investigating AGN obscuration and the effects of AGN activity on the ISM of the hosts, by using broad-band SED fitting, X-ray spectral analysis and submm spectroscopy. This Chapter summarizes the main results from the work presented and the main outstanding issues that are still to be addressed, as well as an overview of ongoing and future projects.

5.1 Summary of this thesis

- **Contribution of the host galaxy to the obscuration of high-redshift AGN.**
The aim of Chapter 2 was to investigate whether the obscuration observed in the X-ray spectra of AGN can be produced by the ISM of the host galaxy. To test this scenario, I performed a multi-wavelength study of seven $z > 2.5$ AGN in the CDF-S, selected to have good FIR detections. The highest-quality data currently available for a deep field were exploited by following a parallel approach. On the one hand, by modeling the X-ray spectra of our targets, I obtained a direct measurement of the total hydrogen column density along the line of sight. On the other hand, the column density associated with the ISM of the host was estimated by combining gas masses (derived through SED-fitting analysis) and galaxy sizes. The obtained values are in the range $N_{\text{H}} \sim 10^{23-24} \text{ cm}^{-2}$. Overall, these results show that the column densities as derived from the X-ray regime and SED-fitting analysis are similar. This unveiled the key role of the ISM of the host, which appeared to be capable of providing significant absorption on kpc scales, at least at high redshift. Such absorption adds to (or even replaces) that produced on pc scales by any circumnuclear material. This result challenges the view of the obscured/unobscured AGN dichotomy as due to inclination effects only, and attributes to the host galaxy a crucial role in obscuring the AGN emission.
- **A multi-wavelength approach to constrain the properties of AGN and their**

host galaxies, laying the foundations for SUPER. In Chapter 3 I performed a uniform and systematic analysis of the multi-wavelength (from X-rays to the radio regime) properties of AGN and host galaxies for a sample of 39 X-ray selected AGN at $z \sim 2$. SED-fitting and X-ray spectral analysis were used to measure a wide set of parameters, including stellar masses, SFRs, AGN bolometric luminosities, obscuring column densities and X-ray luminosities. This comprehensive characterization of the AGN sample carried out in this work is pivotal to set the scene for the SUPER survey, which traces ionized outflows through IFS observations for such AGN. SUPER is performing the first high-resolution spatially-resolved systematic investigation of outflows at cosmic noon. A key feature of the survey is the range in AGN bolometric luminosity probed (up to four orders of magnitude), much wider than in previous work. One of the main goals is to connect the properties of outflows with those of AGN and their hosts, derived in this work. At the same time I proved the importance of a multi-wavelength approach. By combining information from different spectral regimes I constrained, for example, the AGN type and bolometric luminosity, as well as the distinction in jetted and non-jetted AGN. Comparing insights from different techniques/observations is crucial to confirm and provide extra confidence in SED-fitting as well as spectroscopic results. Moreover, a wide set of multi-wavelength physical parameters is necessary to place samples of targets in the broad context of AGN and galaxy evolution.

- **Tracing the molecular gas content of AGN, a promising approach to look for feedback effects.** Chapter 4 presented a systematic analysis of the molecular gas content of 25 AGN at $z \sim 2$ by using ALMA observations of the CO($J=3-2$) transition. I compared the properties of the AGN sample with those of a control sample of normal star-forming galaxies matched in redshift, stellar mass and SFR. Additionally, the comparison sample only consisted of targets observed in the same CO($J=3-2$) transition, to avoid the uncertainties connected with a priori assumptions on excitation factors, which can affect the conclusions. I compared CO and FIR luminosities as well as stellar masses, derived through the same multi-wavelength characterization presented in Chapter 3. The key result of this analysis is that AGN appear to be underluminous in CO with respect to normal galaxies and this can be clearly quantified once dividing in bins of stellar mass. The difference is statistically significant especially at high masses, $\log(M_*/M_\odot) > 11$. These observations demonstrated that the AGN may have an effect on the ISM of the hosts, although the exact mechanisms in place in these sources require further observations to be understood. Possibly, the AGN radiation is able to excite, heat or dissociate the CO molecules, or outflows are depleting the molecular gas reservoir. Distinguishing among different scenarios is the focus of future work.

The work presented in this thesis has demonstrated the need for a multi-wavelength approach to determine the properties of AGN at high redshift, investigate the role of the host ISM in obscuring the AGN emission and the effects of AGN on the gas reservoir. Importantly, the samples studied in this thesis were chosen to cover a wide range of properties

(especially AGN bolometric luminosity) compared to the objects studied in the majority of previous work. However, this work provides indirect observational evidence for the impact of AGN on galaxy evolution and a clear requirement to establish their long-term role is to have strong observational constraints. There are outstanding issues that still need to be addressed and which I will focus on in the future.

5.2 Future work

As a result of the work presented in this thesis, a number of follow-up observational projects are now underway. The main focus is to quantify the impact of AGN activity on galaxy evolution as well as the relation between AGN and star-formation activity, by using different tracers and moving to larger physical scales. We are carrying on and planning future campaigns which will exploit current cutting-edge facilities such as ALMA and the VLT (e.g., instruments like MUSE and X-shooter).

5.2.1 Unveiling the causes behind low molecular gas contents in AGN

As found in Chapter 4, the sample of AGN appeared to be underluminous in CO compared to a sample of inactive galaxies. Although this difference was ascribed to an effect of the AGN, the exact mechanisms behind this result cannot be disentangled with the current dataset. My future work will explore two possible scenarios: a) the presence of outflows responsible for the depletion of the gas content; b) the effect of AGN radiation on the CO SLED with respect to galaxies lacking AGN activity.

AGN outflows. To understand whether AGN-driven outflows can be key candidates in affecting the gas reservoir of galaxies, I will exploit the unique dataset already in hand, as part of the SUPER survey. The high spatial resolution ($\sim 0.3''$, i.e. 2 kpc) SINFONI observations targeting the [OIII] emission line will be combined with the ALMA observations presented in Chapter 4 and the wide set of multi-wavelength properties presented in Chapter 3, for the 19 targets followed-up by both the SINFONI and ALMA programs. I will investigate any potential link between a lower gas content, the presence of AGN-driven outflows, and AGN/galaxy properties (e.g., AGN luminosity, SFR, M_*). The results presented by previous analyses are controversial, since they have been conducted on few individual objects, biased samples or do not have a proper characterization of the outflow properties. Now I have the data to characterize the ionized outflow properties by using SINFONI observations. Fig. 5.1 shows one example of the SINFONI data in hand, namely flux and velocity H -band [OIII] maps for one of the AGN targeted also by the ALMA program. This study represents a step forward in finding direct observational evidence of the impact of AGN feedback, since it traces both the molecular gas content and the ionized outflows, which could affect the gas reservoir. I will complement this observational approach with state-of-the-art cosmological simulations (e.g., Nelson et al., 2019) and the expectations in terms of AGN gas content and outflow properties with cosmic time.

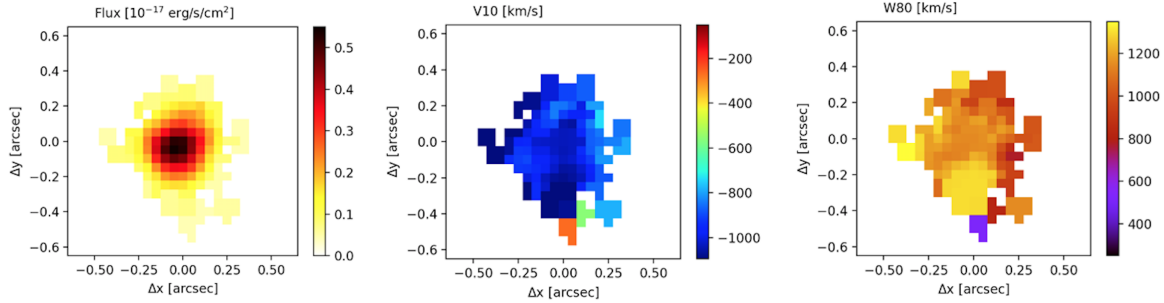


Figure 5.1: SINFONI maps of the [OIII] line of the target cid_451 from the SUPER Large Programme (Chapter 3; Circosta et al., 2018), showing the flux (*left*), velocity at the 10th percentile (*middle*) and the width containing 80% of the total flux (*right*). Combined with the ALMA observations presented in Chapter 4, these data will trace both the molecular gas content and the ionized outflows, which could affect the gas reservoir.

AGN SLEDs. The work presented in Chapter 4 triggered a follow-up project to construct a unique set of CO SLEDs of galaxies at $z \sim 2$ from CO($J=3-2$) to CO($J=10-9$). I have proposed ALMA observations in Bands 5, 6, and 7 (Project code: 2019.1.00892.S, PI: Circosta, pending) to conduct this experiment for a sample including both normal star-forming galaxies, as well as AGN with and without powerful outflows. For the sample selection, I have capitalized on the ALMA and SINFONI/VLT campaigns described in this thesis to observe the best targets in terms of physical characterization of the host galaxy and kinematics of the ionized gas. This unique dataset will be used to determine the physical conditions of the ISM (temperature, density) as a function of galaxy-AGN properties (presence of AGN and/or ionized outflows) and assess how AGN activity may influence such physical conditions. Median CO SLEDs as a function of AGN contribution have been recently presented by Kirkpatrick et al. (2019) by collecting an heterogeneous sample from the literature, as shown in Fig. 5.2. As can be seen from their plot, the results are very uncertain. I am planning to perform a detailed analysis of CO SLEDs, by taking advantage of a set of carefully-derived multi-wavelength properties as carried out in this work.

5.2.2 Moving to different sizes: study of the impact of AGN on large scale

Another limitation of AGN studies in the key $z \sim 2$ epoch is that they have mainly focused either on outflowing gas on kpc-scales within the host (e.g., Kakkad et al., 2016; Brusa et al., 2018), or on the status of the gas on scales of hundreds of kpc (e.g., Prochaska et al., 2013; Lau et al., 2018). On kpc scales, such outflows have been observed to affect different gas phases (Cicone et al., 2018) and reach scales of ~ 10 kpc (Cresci et al., 2015) as well as very high velocities (Carniani et al., 2016). However, the effects of AGN activity may propagate out to larger scales (up to 1 Mpc), through ionizing radiation, jets, energy and

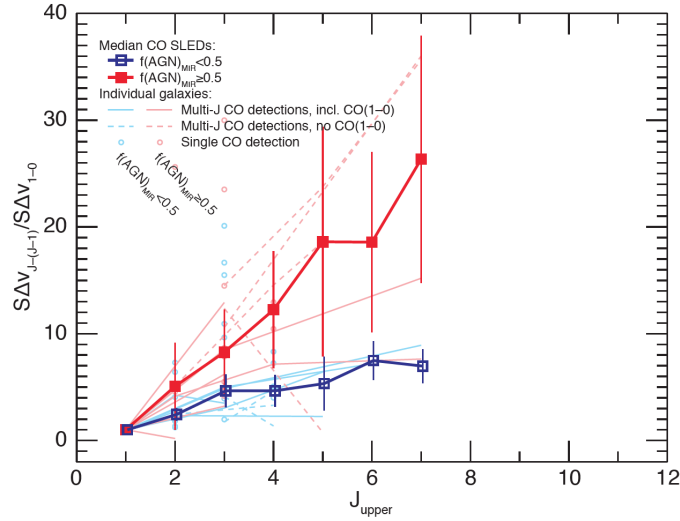


Figure 5.2: Median CO SLEDs for sources with mid-IR AGN fractions $>50\%$ (red filled squares/thick lines) and $<50\%$ (blue open squares/thick lines), from Kirkpatrick et al. (2019). The sample is a collection of literature observations. Light color circles show sources with only a single reported CO detection. Dashed lines show the SLED of sources that lack $\text{CO}(J=1-0)$ measurements. The large uncertainties support the need for a detailed analysis of CO SLEDs for both AGN and normal galaxies.

material injected into the surrounding medium (Prochaska et al., 2013). On scales >100 kpc, observations revealed that quasar halos are characterized by large reservoirs of cool gas as well as a high incidence of metal-line absorption and may trace processes such as infalling of gas, turbulence or outflows (Farina et al., 2013). The latter studies are mainly performed through absorption lines of the diffuse foreground gas against background quasar spectra.

The influence that an AGN has on its environment on kpc up to Mpc scale is an open issue. In particular, the connection between the AGN as well as outflow properties and those of the gas on scales of hundreds of kpc is still missing. Is the gas kinematics affected by AGN outflows on very large scales? Is this large-scale gas already polluted with metals exported by outflows at this epoch? To address these questions, I have been awarded 16 hours of observing time at the VLT/X-shooter (Project code: 0103.B-0779, PI: Circosta). I designed a pilot project to link the ISM studies on kpc scales to the large-scale gas (hundreds of kpc). The targets of this observation are three background AGN in projected quasar-quasar pairs with the SUPER targets as a foreground (impact parameter in the range 200–500 kpc). The X-shooter dataset will be used to search for HI and metal absorption lines in the background quasar spectra, which are fundamental to place constraints on the physical properties of the gas around the foreground AGN (e.g. gas column density, presence of inflows/outflows).

The uniqueness of this approach is that, for the first time, the gas kinematics on small scales for AGN with powerful known outflows will be linked to observations in absorption

on scales of hundreds of kpc. Simulations indicate that the influence of quasars could be extended up to 2 Mpc (Sorini et al., 2018). This project represents a first step to start pinpointing this possibility. A potential Ly α absorption is detected in an archival VIMOS spectrum of one of the background quasars (shown in Fig. 5.3), at the redshift of the foreground source. However, the detection of several metal lines, other than the Ly α absorption, requires a wider wavelength range (given by, e.g., X-shooter). Observations will be completed in September 2019.

We are also attempting to expand this study by using different tracers and perform analyses of the environment surrounding AGN through the CIV and Ly α emission lines with VLT/MUSE and FLAMES (PIs: Vietri; Kakkad). Remarkably, combining these experiments with our in-hand SINFONI data opens up the possibility to simultaneously look at the interplay between nuclear activity and gas content in a galaxy over several orders of magnitudes in radial distance (from a few up to hundreds of kpc).

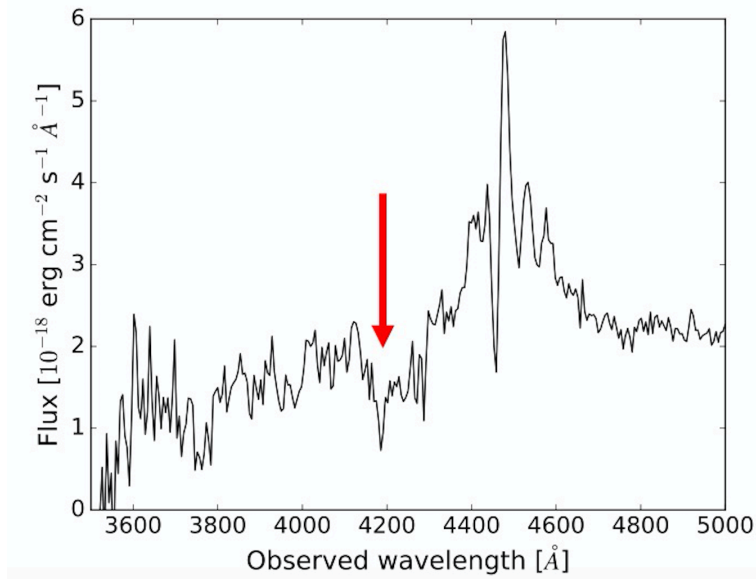


Figure 5.3: VIMOS spectrum of one of the background quasars ($z = 2.673$). Ly α absorption is observed at $\lambda \sim 4195$ Å (red arrow), consistent with being produced by the foreground quasar ($z = 2.45$). The HI column density associated with this absorption is $\sim 10^{20}$ cm⁻². X-shooter observations will extend the wavelength range covered and allow the detection of other metal absorption lines.

5.2.3 Investigating the correlation between AGN activity and SFR through high-resolution observations

Although SMBH activity and star formation in the host galaxy seem to be intimately linked as suggested by the correlation between their properties, the physical mechanisms

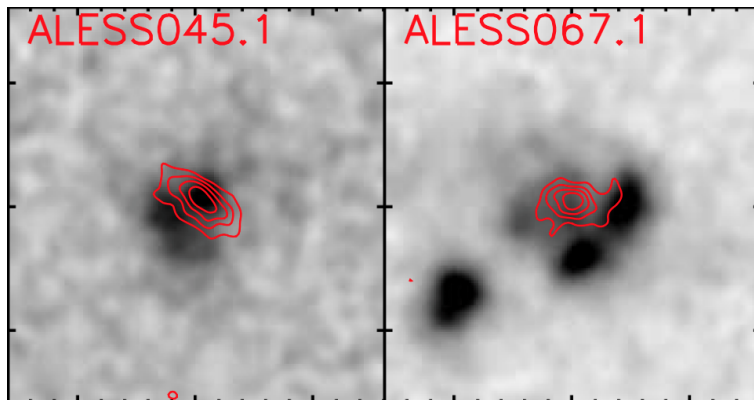


Figure 5.4: Comparisons of the ALMA 870 μm emission (contours) and *HST* *H*-band emission (grayscale) at $\sim 0.15''$ resolution for inactive galaxies, from Hodge et al. (2016). A similar set of observations will be used to perform a systematic comparison of sizes and spatial distribution of star formation for a sample of AGN and inactive galaxies to understand the connection between AGN activity and star formation.

triggering (e.g., mergers versus internal secular processes) and connecting these two processes are not clear. As mentioned earlier, FIR studies of high-redshift AGN hosts using *Herschel* have revealed that average SFRs are almost independent of AGN luminosity, after taking into account redshift evolution (Stanley et al., 2015). However, these results are characterized by poor spatial resolution (e.g., $\text{FWHM} \sim 5\text{--}30''$ at $\sim 70\text{--}500 \mu\text{m}$) which corresponds to physical scales of >40 kpc at $z \sim 2$. Due to the very different timescales of AGN activity and star formation, this may result in intrinsic correlations being washed out in these average measurements (e.g., Hickox et al., 2014). Indeed, locally there is evidence that nuclear (<1 kpc) SFRs are more closely correlated to AGN activity than galaxy-wide SFRs (Diamond-Stanic & Rieke, 2012), consistent with some theoretical models that predict a stronger correlation on smaller scales (e.g., Hopkins & Quataert, 2010). The high resolution offered by ALMA can actually provide unique insights into how AGN activity and star formation are connected, at the peak epoch of AGN and star formation activity. ALMA observations already in hand at $150\text{--}350 \mu\text{m}$ rest frame will be used to perform a systematic comparison of sizes and spatial distribution of star formation, at ~ 1 kpc resolution, for a sample of AGN and inactive galaxies at $z = 1.5\text{--}5$. Previous work targeting inactive galaxies showed that the stellar morphologies appear significantly more extended and disturbed than the dust ones, suggesting that major mergers may be responsible for driving the formation of the compact dust disks observed (see Fig. 5.4; Hodge et al., 2016). By studying the dust distribution (clumpy vs. smooth disks) compared to the stellar one as observed by *HST* (Harrison et al., 2016b), I will test the connection between mergers and/or disturbed disks, star formation, and crucially AGN activity.

5.3 Final remarks

Over the last two decades AGN became key protagonists in the field of galaxy evolution. Since the first results finding a correlation between SMBH and galaxy properties, huge progress has been made. Theoretical models predict that AGN play a pivotal role in shaping the evolution of massive galaxies but, observationally, the details of how this occurs are still not fully understood. As shown in this thesis, it is fundamental to look at the properties of the ISM of AGN host galaxies by adopting a multi-wavelength approach and using different techniques. However, we still lack direct observational evidence of whether AGN are an indispensable requirement to create the properties of the galaxies observed today. To address this outstanding issue, we have started observational campaigns by exploiting cutting-edge facilities, such as ALMA and the VLT, as explained in this Chapter. An important effort to be pursued in the next future has to aim at probing different tracers and gas phases as well as reaching higher resolution. In addition, state-of-the-art simulations should constantly represent a benchmark to better understand observational results.

In the next decades, revolutionary multi-wavelength observational facilities will deliver a considerable amount of high-quality data from X-rays to radio wavelengths. For example, with the advent of the James Webb Space Telescope (JWST) it will be possible to carry out studies of ionized outflows in $z > 4$ sources, while we are currently limited at $z \sim 3$. The Square Kilometre Array (SKA) will open a window to understand the drivers of AGN outflows (e.g., jets) in the radio regime with high resolution, at the peak of cosmic star formation. Finally, the next generation of IFS of the Extremely Large Telescopes (ELTs) will allow to trace AGN-driven winds down to very low luminosities and on large statistical samples. Thanks to these exciting developments, we will be able to reach further detailed insight into the influence of active galactic nuclei on the evolution of galaxies.

Appendix A

Notes on the targets of Chapter 2

XID42

This target has the largest off-axis angle of the sample in the CDF-S, therefore it is strongly background dominated, and the useful energy range for a spectral analysis is reduced to 0.8 – 3 keV. A second power law emerging in the soft X-rays was not required by the fit. We note a difference by a factor ~ 2 in the observed flux derived using the reflection model with respect to the transmission and MYTorus models. This might be ascribed to the different shape of this model compared to the others outside the covered energy range. The Fe $K\alpha$ line is detected at a rest-frame energy of about 6.5 keV at $\sim 2.2\sigma$; its EW is characterized by large errors that are due to the poor spectral quality.

XID170

The X-ray data of XID170 are well fit by the transmission and MYTorus models, but not by the reflection model, whose best-fit parameters significantly differ from those derived with the other two models. A second power law was not required to improve the fit quality in the soft X-ray regime. The iron line is poorly constrained.

XID337

The best-fit parameters obtained by analyzing the X-ray spectrum with the whole set of models agree well. The Fe $K\alpha$ line parameters are constrained in the transmission and MYTorus models, while its energy was fixed to the best-fit value in the reflection model; in this case, only an upper limit on its EW is computed. We added a soft component to the transmission and MYTorus models, and the resulting fraction of scattered emission, computed as the ratio between the power-law normalizations in the MYTorus model, is $\sim 3\%$. The derived best-fit column densities point to a Compton-thick emission.

The SED of this target represents a particular case in our sample. Thanks to the high

resolution ($\sim 0.2''$) of the ALMA image at $870 \mu\text{m}$, we have found that this source, which was thought to be a single object in the *Spitzer*/MIPS and *Herschel* maps (and in SCUBA observations, Mainieri et al., 2005), is actually a blend of two sources. The MIR and FIR photometry is dominated by a bright source at $3.5''$ from the target and forced us to convert these data points into upper limits. As a result, this translates into a very uncertain AGN contribution.

XID539

This source lies at a very large off-axis position with respect to the center of the CDF-S and is characterized by low photon statistics. The iron emission line is detected at $\sim 6.9 \text{ keV}$ (at $\sim 2\sigma$) with the transmission model, while is kept fixed to the best-fit value in the reflection model. As for MYTorus, we added a Gaussian component to reproduce the line at such energies because the default line energy is 6.4 keV (i.e., due to neutral iron). The energy of the line can be interpreted as emission from highly ionized iron (i.e., hydrogen-like iron) and is also very prominent according to the derived EW.

XID551

This target lies in the inner region of the CDF-S area and has reasonably good photon statistics. The secondary power law accounts for about 3% of the unobscured flux at 1 keV . The emission line, detected at $\sim 3\sigma$ and at $\sim 6.6 \text{ keV}$ rest-frame, could be ascribed to emission from either neutral or ionized iron (i.e., helium-like iron) or a mixture of the two.

XID666

XID666 is the most obscured source of the sample. The high column density results in a lower limit in MYTorus because of the low photon statistics. The resulting fraction of scattered emission in the soft X-rays is smaller than 1%. The target is characterized by a flat spectrum and an extremely strong iron $K\alpha$ line at $\sim 6.4 \text{ keV}$, clearly detected at $\sim 4.5\sigma$. The EW is well constrained and larger than 1 keV . All models are in agreement in terms of flux and luminosities. This is suggestive of a spectrum dominated by reflected emission.

XID746

Like XID170, the reflection model of XID746 does not provide a good fit to the spectral data. The transmission model provides a best-fit column density of $\sim 5.5 \times 10^{23} \text{ cm}^{-2}$. The iron line is not required by the data, therefore only an upper limit on the EW is reported.

Appendix B

Multi-wavelength properties of the targets presented in Chapters 3 and 4

| ID (1) | AGN type (2) | $\log \frac{M_*}{M_\odot}$ (3) | $\log \frac{L_{\text{FIR}}}{\text{erg s}^{-1}}$ (4) | SFR [$M_\odot \text{ yr}^{-1}$] (5) |
|-------------------------|-----------------|-----------------------------------|--|--|
| X.N.160.22 | BL | - | - | - |
| X.N.81.44 | BL | 11.04 ± 0.37 | 45.93 ± 0.20 | 229 ± 103 |
| X.N.53.3 | BL | - | 46.41 ± 0.11 | 686 ± 178 |
| X.N.66.23 | BL | 10.96 ± 0.29 | < 46.00 | < 268 |
| X.N.6.27 | NL | 11.03 ± 0.59 | < 45.90 | < 215 |
| X.N.35.20 | BL | - | - | - |
| X.N.12.26 | BL | - | - | - |
| X.N.44.64 | BL | 11.09 ± 0.25 | 45.93 ± 0.15 | 229 ± 80 |
| X.N.4.48 | BL | - | - | - |
| X.N.102.35 ^a | BL | - | - | - |
| X.N.115.23 | BL | - | - | - |
| XID36 | NL | 10.68 ± 0.07 | 45.84 ± 0.02 | 184 ± 9 |
| XID57 | NL | 10.49 ± 0.11 | < 45.10 | < 34 |
| XID419 | NL | 10.89 ± 0.02 | 45.20 ± 0.04 | 42 ± 4 |
| XID427 | NL | 10.87 ± 0.08 | < 45.43 | < 72 |
| XID522 | NL | 10.42 ± 0.02 | 46.26 ± 0.02 | 492 ± 25 |
| XID614 | NL | 10.78 ± 0.08 | 45.97 ± 0.02 | 247 ± 12 |
| lid.1852 | NL | 10.07 ± 0.13 | < 45.28 | < 52 |
| lid.3456 | BL | 10.75 ± 0.30 | 46.08 ± 0.17 | 323 ± 126 |
| cid.166 | BL | 10.38 ± 0.22 | < 45.92 | < 224 |
| lid.1289 | NL | 9.59 ± 0.14 | < 44.98 | < 25 |
| cid.1057 | NL | 10.84 ± 0.07 | 45.50 ± 0.02 | 85 ± 4 |
| cid.1605 | BL | - | < 45.54 | < 94 |
| cid.337 | NL | 11.13 ± 0.04 | 45.63 ± 0.03 | 115 ± 9 |
| cid.346 | BL | 11.01 ± 0.22 | 46.13 ± 0.06 | 362 ± 49 |

| | | | | |
|------------|----|------------------|------------------|---------------|
| cid_357 | BL | 9.85 ± 0.31 | < 45.60 | < 108 |
| cid_451 | NL | 11.21 ± 0.05 | < 45.67 | < 125 |
| cid_1205 | NL | 11.20 ± 0.10 | 46.16 ± 0.04 | 384 ± 33 |
| cid_2682 | NL | 11.03 ± 0.04 | < 45.54 | < 93 |
| cid_1143 | NL | 10.40 ± 0.17 | 45.61 ± 0.07 | 108 ± 18 |
| cid_247 | BL | 10.03 ± 0.20 | 45.73 ± 0.05 | 143 ± 15 |
| cid_1215 | BL | 10.20 ± 0.08 | 45.96 ± 0.04 | 246 ± 24 |
| cid_467 | BL | 10.10 ± 0.29 | < 45.74 | < 147 |
| cid_852 | NL | 11.17 ± 0.02 | < 45.57 | < 100 |
| cid_970 | NL | 10.38 ± 0.12 | < 45.66 | < 122 |
| cid_971 | NL | 10.60 ± 0.12 | - | $< 96^a$ |
| cid_38 | NL | 11.01 ± 0.12 | < 45.98 | < 258 |
| lid_206 | BL | 10.30 ± 0.25 | - | 63 ± 27^a |
| cid_1253 | NL | 10.99 ± 0.25 | 46.02 ± 0.30 | 280 ± 194 |
| J1333+1649 | BL | - | - | - |
| J1441+0454 | BL | - | - | - |
| J1549+1245 | BL | - | - | - |
| S82X1905 | BL | - | - | - |
| S82X1940 | BL | - | - | - |
| S82X2058 | BL | - | - | - |
| S82X2106 | BL | - | - | - |

Table B.1: Summary of the properties of AGN host galaxies derived in Chapters 3 and 4. (1) Target ID, see also Tables 3.1 and 4.1; (2) AGN classification into broad line (BL) and narrow line (NL) according to the optical spectra; (3) Galaxy stellar mass and 1σ error; (4) FIR luminosity in the $8 - 1000 \mu\text{m}$ range and 1σ error; (5) SFR from the FIR luminosity and 1σ error.

^aAverage SFR over the last 100 Myr of the galaxy history as obtained from the modeling of the stellar component with SED fitting.

| ID | AGN type | $\log \frac{L_{\text{bol}}}{\text{erg s}^{-1}}$ | X-ray net counts | $\log \frac{N_{\text{H}}}{\text{cm}^{-2}}$ | $\log \frac{L_{[2-10 \text{ keV}]}}{\text{erg s}^{-1}}$ | $\log \frac{M_{\text{BH}}}{M_{\odot}}$ | $\log \frac{P_{1.4 \text{ GHz}}}{\text{W Hz}^{-1}}$ |
|-------------------------|----------|---|------------------|--|---|--|---|
| (1) | (2) | (3) | (4) | (5) | (6) | (7) | (8) |
| X_N_160_22 | BL | 46.74 ± 0.02 | 24.5 ± 4.9 | < 22.32 | $44.77^{+0.14}_{-0.19}$ | 8.9 ± 0.2 | < 24.87 |
| X_N_81_44 | BL | 46.80 ± 0.03 | 94.8 ± 9.7 | < 21.86 | $44.77^{+0.07}_{-0.09}$ | 9.2 ± 0.1 | < 24.81 |
| X_N_53_3 | BL | 46.21 ± 0.03 | 25.8 ± 5.1 | $22.77^{+0.37}_{-0.67}$ | $44.80^{+0.10}_{-0.13}$ | 8.7 ± 0.1 | < 24.86 |
| X_N_66_23 | BL | 46.04 ± 0.02 | 118.7 ± 10.9 | < 21.51 | $44.71^{+0.06}_{-0.08}$ | 8.3 ± 0.2 | < 24.84 |
| X_N_6_27 | NL | 45.85 ± 0.05 | 26 ± 5 | < 22.64 | $44.36^{+0.22}_{-0.24}$ | - | - |
| X_N_35_20 | BL | 45.44 ± 0.02 | 38.1 ± 6.2 | < 22.27 | $44.00^{+0.07}_{-0.40}$ | 8.7 ± 0.1 | < 24.79 |
| X_N_12_26 | BL | 46.52 ± 0.02 | 61.3 ± 7.8 | < 20.90 | $44.56^{+0.13}_{-0.12}$ | 8.9 ± 0.1 | < 24.88 |
| X_N_44_64 | BL | 45.51 ± 0.07 | 51.8 ± 7.2 | < 21.97 | $44.21^{+0.11}_{-0.17}$ | 9.1 ± 0.2 | < 24.78 |
| X_N_4_48 | BL | 46.16 ± 0.02 | 58.2 ± 7.6 | < 21.85 | $44.52^{+0.09}_{-0.16}$ | 9.1 ± 0.2 | < 24.81 |
| X_N_102_35 ^a | BL | 46.82 ± 0.02 | 79.0 ± 8.9 | < 22.17 | $45.37^{+0.05}_{-0.11}$ | 8.9 ± 0.1 | 27.05 ± 0.01 |
| X_N_115_23 | BL | 46.49 ± 0.02 | 131.8 ± 11.5 | < 22.26 | $44.93^{+0.08}_{-0.10}$ | 8.4 ± 0.1 | < 24.82 |
| XID36 ^a | NL | 45.70 ± 0.06 | 47.2 ± 6.9 | $b > 24.1$ | $43.84^{+0.31}_{-0.63}$ | - | 25.40 ± 0.01 |
| XID57 | NL | 44.26 ± 0.18 | 58.9 ± 7.7 | $b 23.30^{+0.32}_{-0.39}$ | $44.04^{+0.17}_{-0.24}$ | - | < 24.20 |
| XID419 | NL | 45.54 ± 0.05 | 70.2 ± 8.4 | $b 24.28^{+0.19}_{-0.31}$ | $43.84^{+0.29}_{-0.44}$ | - | < 24.12 |
| XID427 | NL | 44.60 ± 0.13 | 324.2 ± 18.0 | $22.43^{+0.24}_{-0.34}$ | $43.20^{+0.06}_{-0.06}$ | - | < 24.20 |
| XID522 | NL | 45.02 ± 0.02 | 35.1 ± 5.9 | $b > 22.5$ | $43.51^{+0.76}_{-0.87}$ | - | 24.37 ± 0.05 |
| XID614 | NL | 44.97 ± 0.13 | 78.3 ± 8.8 | $24.25^{+0.19}_{-0.18}$ | $43.61^{+0.18}_{-0.18}$ | - | < 24.26 |
| lid_1852 | NL | 45.25 ± 0.09 | 53 ± 7 | $22.92^{+0.36}_{-0.74}$ | $44.46^{+0.15}_{-0.15}$ | - | - |
| lid_3456 | BL | 45.68 ± 0.07 | 5 ± 2 | < 22.0 | $43.00^{+0.50}_{-0.50}$ | - | - |
| cid_166 | BL | 46.93 ± 0.02 | 717.8 ± 26.8 | < 21.25 | $45.15^{+0.03}_{-0.02}$ | 9.3 ± 0.1^c | < 24.00 |
| lid_1289 | NL | 45.09 ± 0.08 | 123.4 ± 11.1 | $22.50^{+0.29}_{-0.22}$ | $44.69^{+0.26}_{-0.13}$ | - | < 23.98 |
| cid_1057 | NL | 45.91 ± 0.06 | 36.1 ± 6.0 | $23.98^{+0.24}_{-0.28}$ | $44.53^{+0.26}_{-0.30}$ | - | < 23.89 |
| cid_1605 | BL | 46.03 ± 0.02 | 327.9 ± 18.1 | $21.77^{+0.51}_{-0.75}$ | $44.69^{+0.06}_{-0.04}$ | 8.4 ± 0.2 | < 23.84 |
| cid_337 | NL | 45.34 ± 0.09 | 83.1 ± 9.1 | < 22.76 | $44.22^{+0.11}_{-0.12}$ | - | 23.99 ± 0.07 |
| cid_346 ^a | BL | 46.66 ± 0.02 | 124.1 ± 11.1 | $23.05^{+0.17}_{-0.19}$ | $44.47^{+0.08}_{-0.09}$ | 8.9 ± 0.1^c | 24.86 ± 0.07^d |
| cid_357 | BL | 45.25 ± 0.06 | 110 ± 11 | < 22.87 | $44.44^{+0.19}_{-0.15}$ | - | - |
| cid_451 ^a | NL | 46.44 ± 0.07 | 136.9 ± 11.7 | $23.87^{+0.19}_{-0.15}$ | $45.18^{+0.23}_{-0.19}$ | - | 26.43 ± 0.01^d |
| cid_1205 | NL | 45.75 ± 0.17 | 33.9 ± 5.8 | $23.50^{+0.27}_{-0.27}$ | $44.25^{+0.21}_{-0.23}$ | - | 24.10 ± 0.06 |
| cid_2682 | NL | 45.48 ± 0.10 | 35.5 ± 6.0 | $23.92^{+1.01}_{-0.20}$ | $44.30^{+0.96}_{-0.27}$ | - | < 23.99 |
| cid_1143 ^a | NL | 44.85 ± 0.12 | 51.3 ± 7.2 | $24.01^{+0.77}_{-0.29}$ | $44.83^{+0.43}_{-0.36}$ | - | 24.39 ± 0.05 |

| | | | | | | | |
|-------------------------|----|------------------|-------------------|-------------------------|-------------------------|------------------|--------------------|
| cid_247 | BL | 45.49 ± 0.04 | 158 ± 13 | < 22.43 | $44.43^{+0.11}_{-0.06}$ | - | - |
| cid_1215 | BL | 45.73 ± 0.05 | 78 ± 9 | $22.86^{+0.31}_{-0.50}$ | $44.34^{+0.14}_{-0.14}$ | - | - |
| cid_467 | BL | 46.53 ± 0.04 | 446.8 ± 21.1 | $22.31^{+0.23}_{-0.32}$ | $44.87^{+0.04}_{-0.05}$ | 8.9 ± 0.6 | < 23.92 |
| cid_852 | NL | 45.50 ± 0.11 | 25.0 ± 5.0 | $24.30^{+0.38}_{-0.37}$ | $45.20^{+1.14}_{-0.76}$ | - | < 23.90 |
| cid_970 | NL | 45.71 ± 0.04 | 287 ± 17 | < 22.25 | $44.69^{+0.07}_{-0.04}$ | - | - |
| cid_971 | NL | 44.71 ± 0.24 | 33.1 ± 5.8 | < 23.68 | $43.87^{+0.36}_{-0.38}$ | - | < 24.01 |
| cid_38 | NL | 45.78 ± 0.04 | 159.4 ± 12.6 | < 22.95 | $44.41^{+0.16}_{-0.13}$ | - | 24.10 ± 0.05 |
| lid_206 | BL | 44.77 ± 0.12 | 40.2 ± 6.3 | < 22.55 | $43.91^{+0.39}_{-0.29}$ | 7.9 ± 0.1 | < 23.94 |
| cid_1253 | NL | 45.08 ± 0.18 | 36.1 ± 6.0 | $23.22^{+0.47}_{-0.39}$ | $43.92^{+0.29}_{-0.31}$ | - | 24.30 ± 0.08^d |
| J1333+1649 ^a | BL | 47.91 ± 0.02 | 174.5 ± 13.2 | $21.81^{+0.22}_{-0.34}$ | $45.81^{+0.07}_{-0.06}$ | 9.79 ± 0.3 | 28.15 ± 0.01 |
| J1441+0454 | BL | 47.55 ± 0.02 | 74.5 ± 8.6 | $22.77^{+0.18}_{-0.21}$ | $44.77^{+0.10}_{-0.11}$ | 10.2 ± 0.3 | 25.78 ± 0.03 |
| J1549+1245 | BL | 47.73 ± 0.04 | 1023.1 ± 32.0 | $22.69^{+0.09}_{-0.11}$ | $45.38^{+0.02}_{-0.02}$ | 10.1 ± 0.3^e | 25.91 ± 0.03 |
| S82X1905 | BL | 46.50 ± 0.02 | 31.3 ± 5.6 | $22.95^{+0.35}_{-0.17}$ | $44.91^{+0.50}_{-0.50}$ | 9.3 ± 0.1 | < 24.79 |
| S82X1940 | BL | 46.03 ± 0.02 | 33.7 ± 5.8 | < 20.50 | $44.72^{+0.30}_{-0.30}$ | 8.7 ± 0.2 | < 24.83 |
| S82X2058 | BL | 46.39 ± 0.02 | 29.5 ± 4.3 | < 20.50 | $44.67^{+0.30}_{-0.30}$ | 8.9 ± 0.3 | < 24.81 |
| S82X2106 | BL | 46.08 ± 0.03 | 94.5 ± 9.7 | < 22.08 | $45.08^{+0.08}_{-0.11}$ | 9.2 ± 0.1 | < 24.80 |

Table B.2: Summary of the properties of AGN derived in Chapters 3 and 4. (1) Target ID, see also Tables 3.1 and 4.1; (2) AGN classification into broad line (BL) and narrow line (NL) according to the optical spectra; (3) AGN bolometric luminosity and 1σ error, derived from SED fitting; (4) X-ray net counts (i.e., background subtracted) in the full band and respective error, computed assuming a Poisson statistic; (5) Absorbing hydrogen column density and 90% confidence level error; (6) Absorption-corrected X-ray luminosity in the hard band (2 – 10 keV) and 90% confidence level error; (7) Black hole mass and 1σ error. For the XMM-XXL and Stripe82X targets the values are from Shen et al. (2015), for the WISSH targets are from Weedman et al. (2012), and for COSMOS we have re-analyzed zCOSMOS and FMOS spectra (Schulze et al., 2018); (8) Radio power at 1.4 GHz and 1σ error.

^aTargets classified as “jetted” (Padovani, 2017), according to the comparison between their IR and radio properties (see Fig. 3.7).

^bTargets fit with the physical model MYtorus (Murphy & Yaqoob, 2009) that self-consistently takes into account photoelectric absorption, Compton scattering, cold reflection and fluorescent emission in a fixed toroidal geometry. The analysis was performed as described in Lanzuisi et al. (2018).

^cBH mass derived using the $H\beta$ emission line from Subaru/FMOS spectroscopy (Schulze et al., 2018).

^dTargets detected at 1.4 GHz as part of the VLA-COSMOS survey (Schinnerer et al., 2007). The luminosities reported here for these targets are derived from the 1.4 GHz fluxes. The predicted 3 GHz fluxes (assuming $\alpha = 0.7$) are consistent with the observed 1.4 GHz ones for cid_1253 and cid_346, while for cid_451 the predicted flux is a factor of 2 higher than the measured 1.4 GHz one. The measurements reported for the other COSMOS targets are derived from 3 GHz fluxes (see Sec. 3.4.3).

^eBH mass derived using the $H\beta$ emission line from Bischetti et al. (2017).

Appendix C

Spectral energy distributions of the targets presented in Chapters 3 and 4

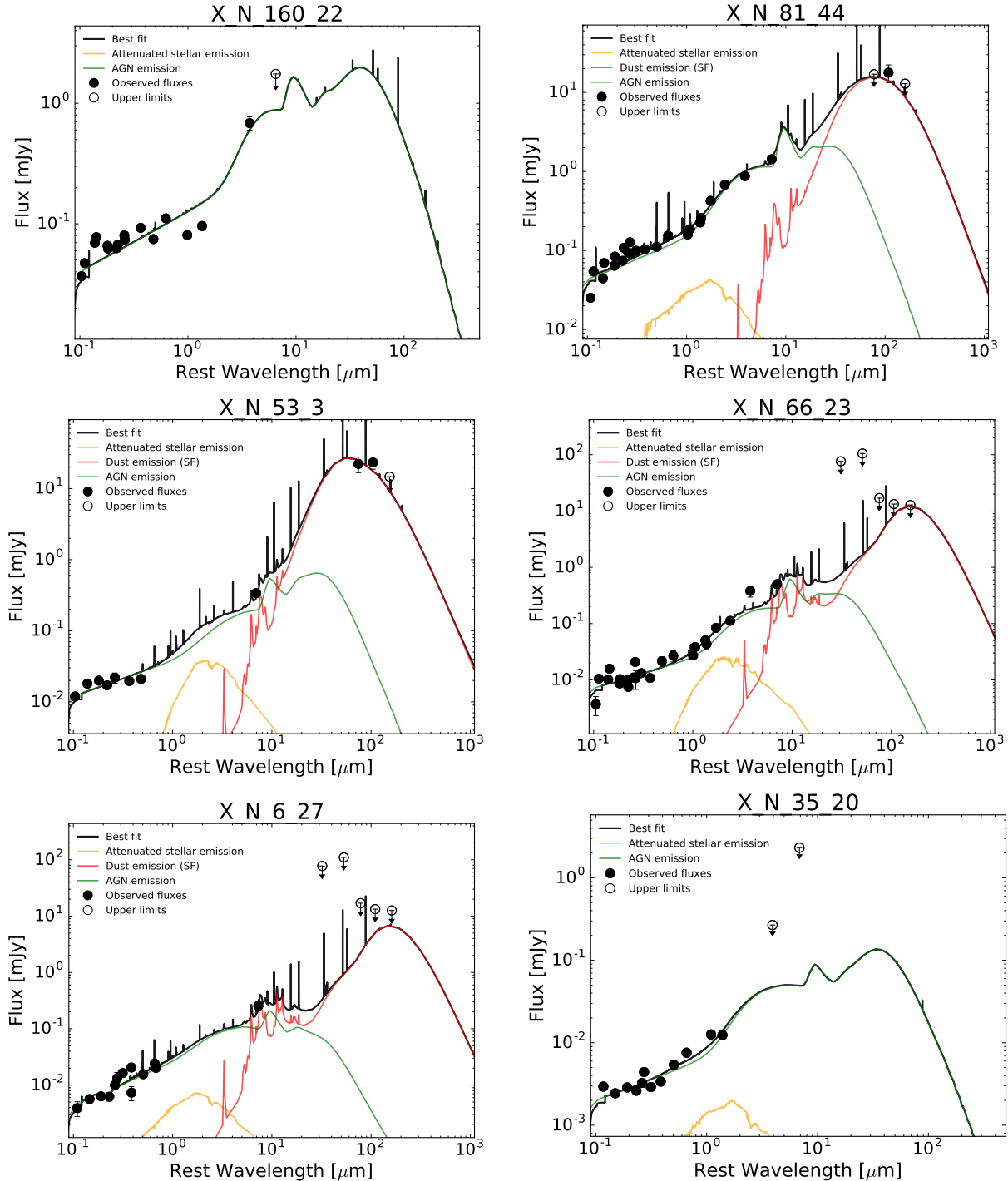
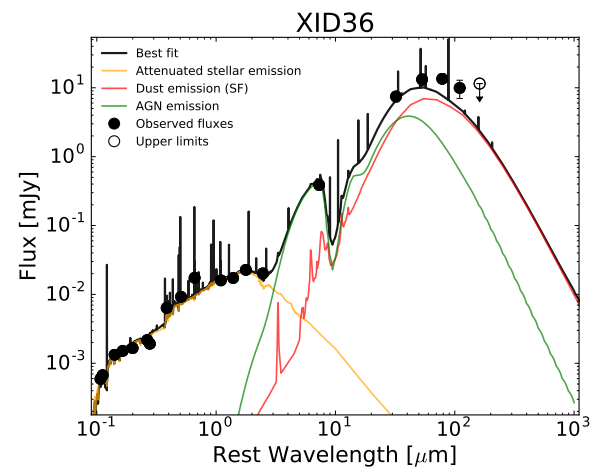
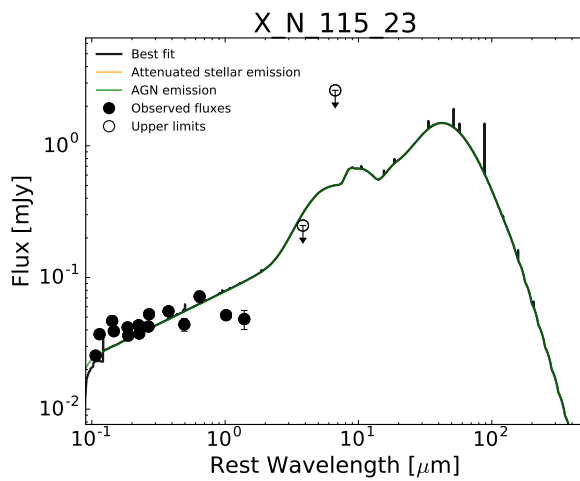
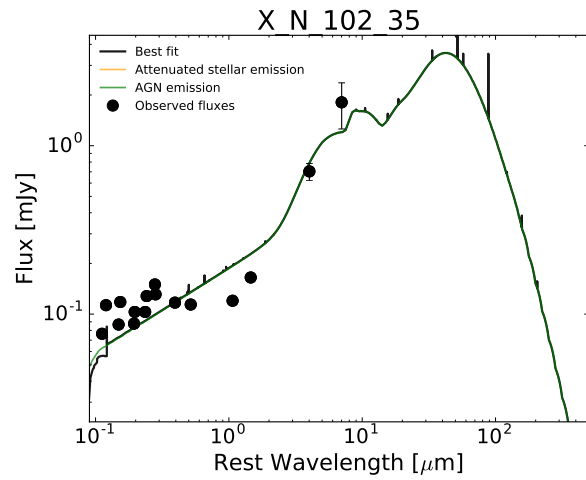
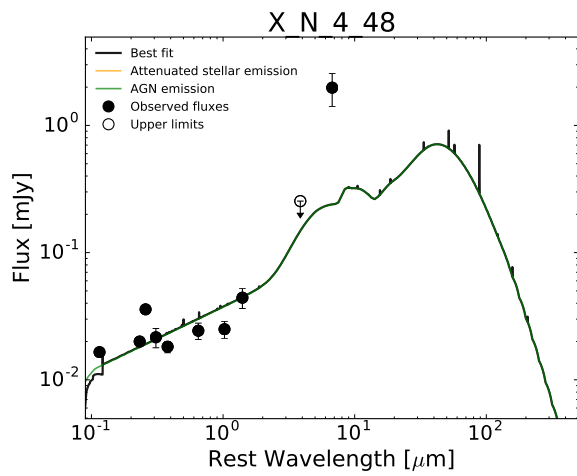
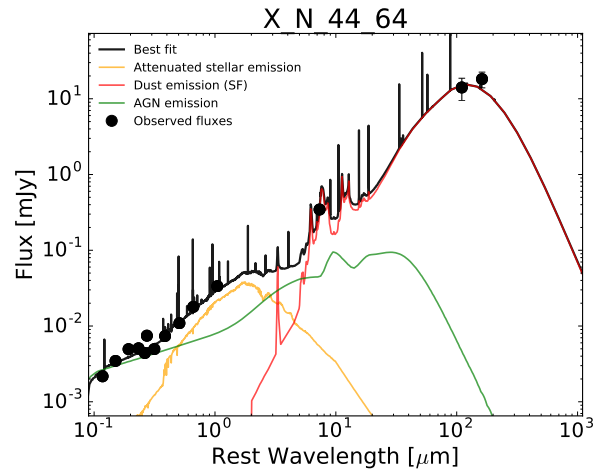
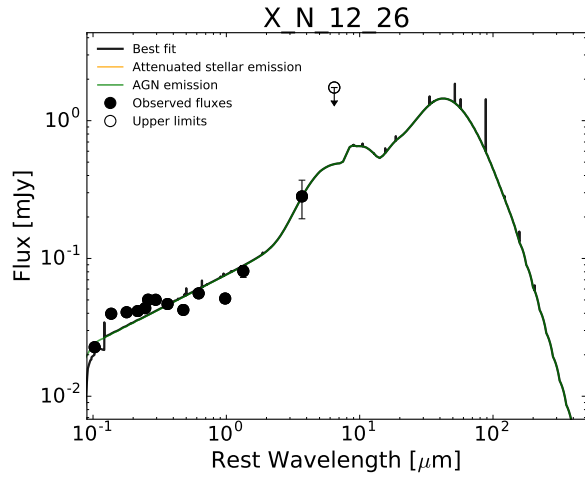
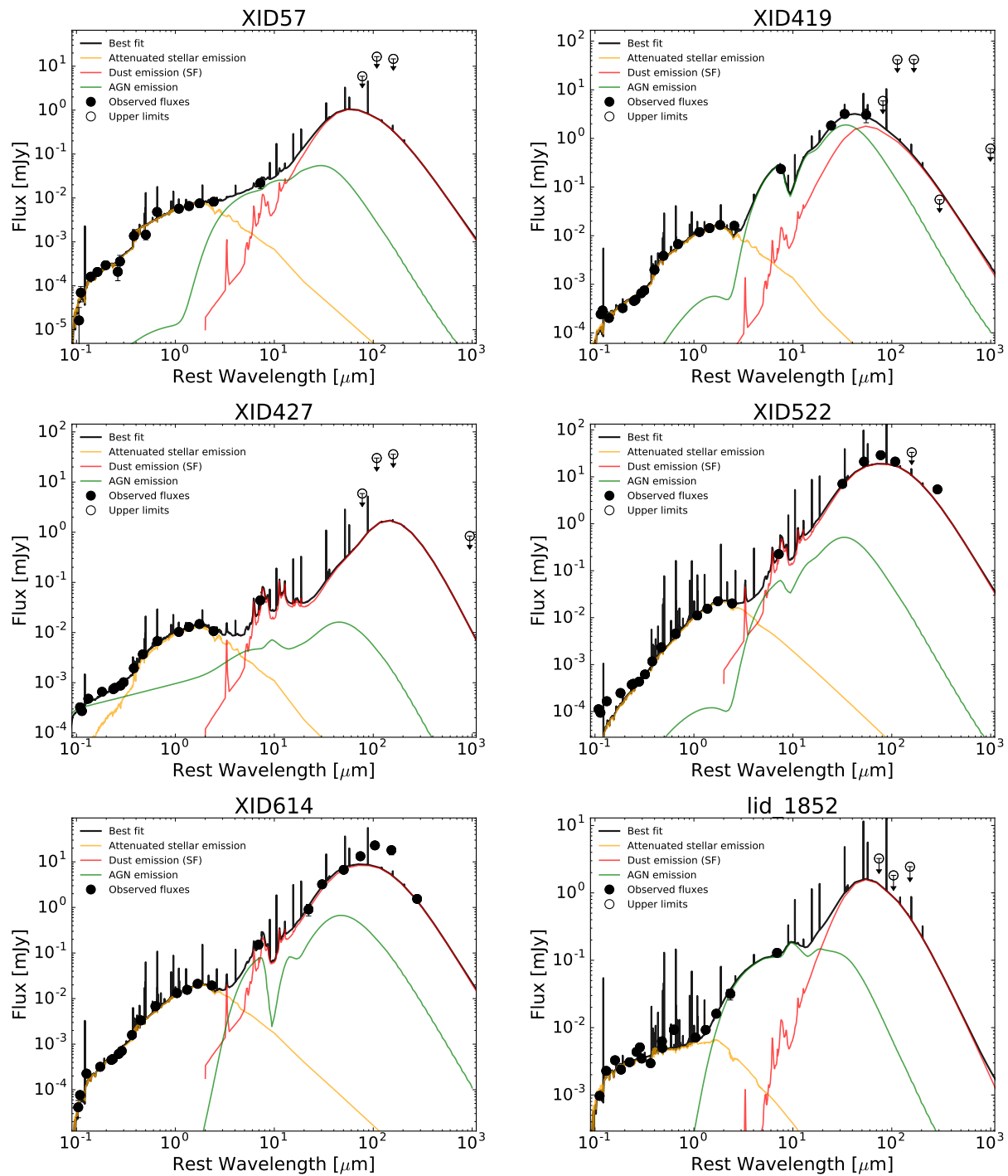
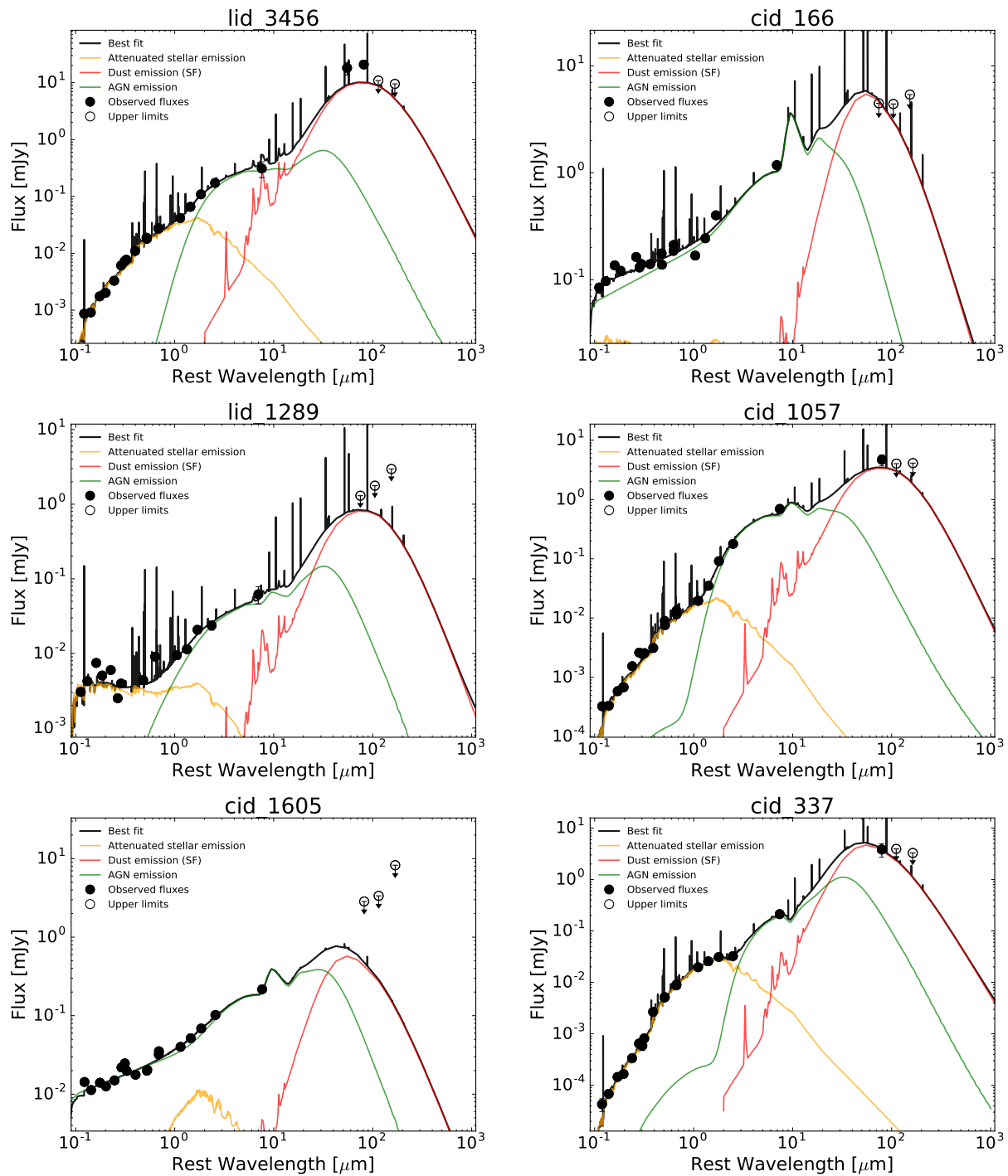
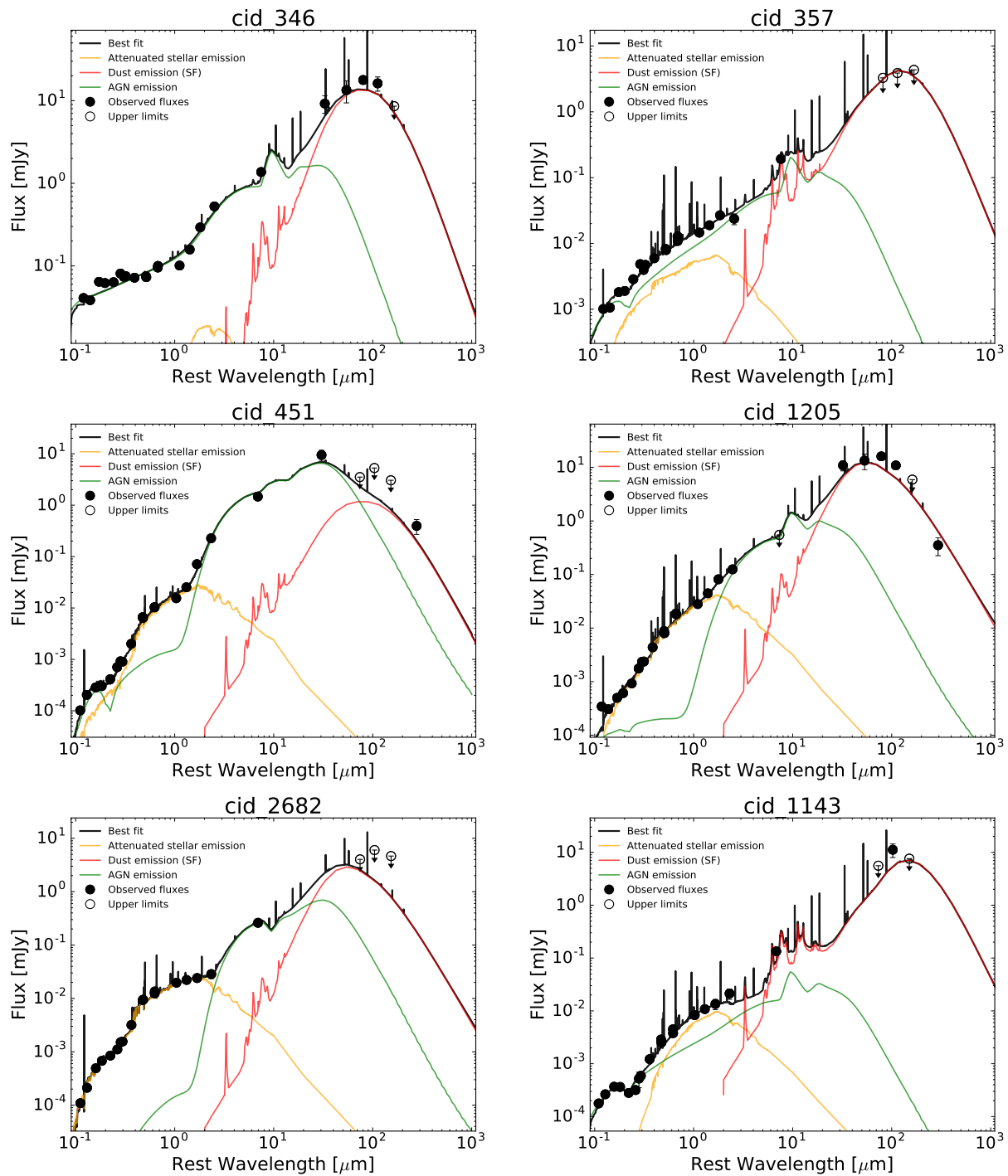


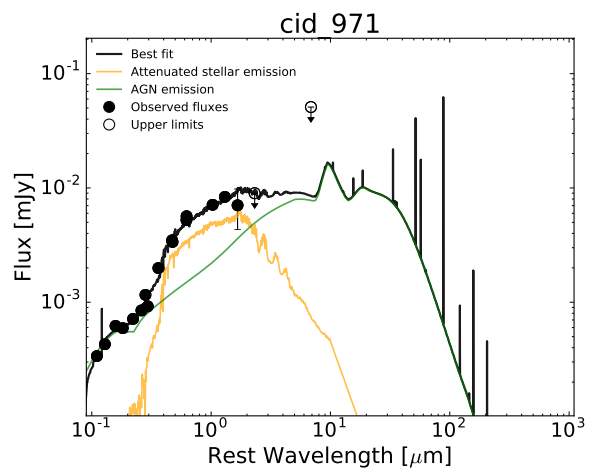
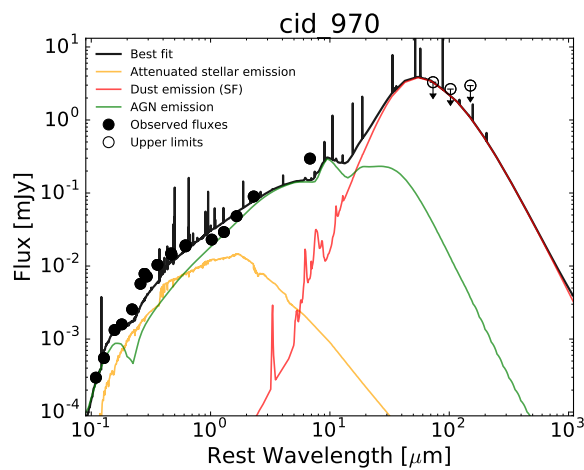
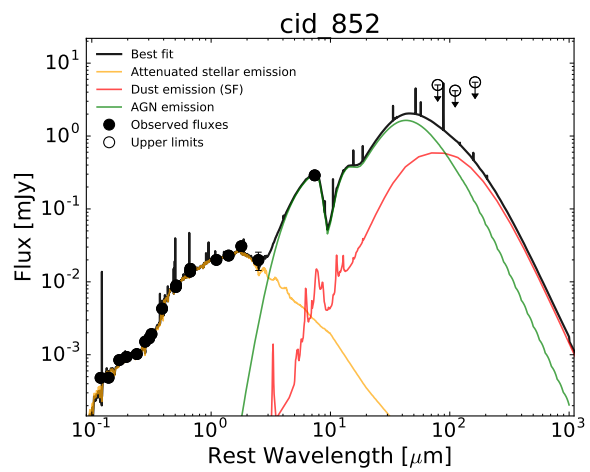
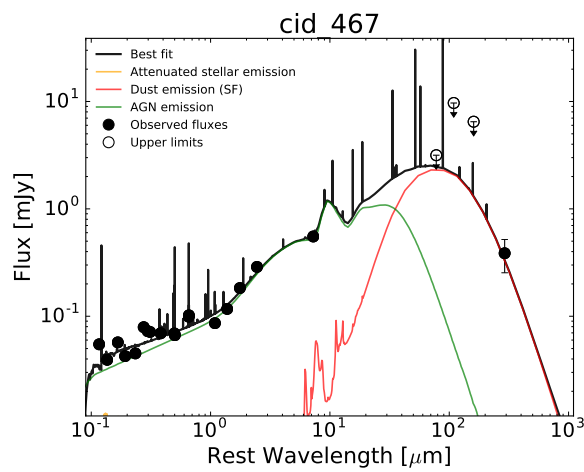
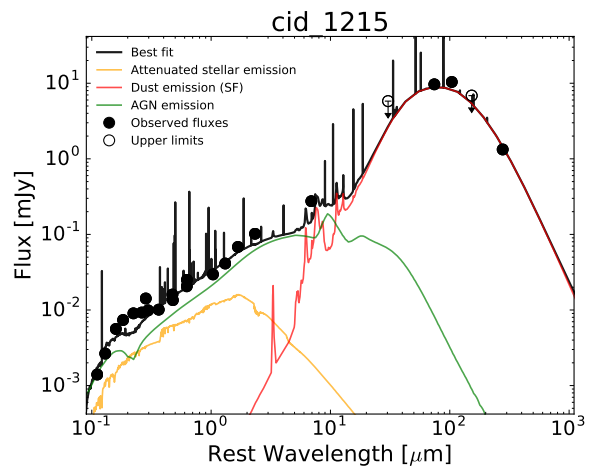
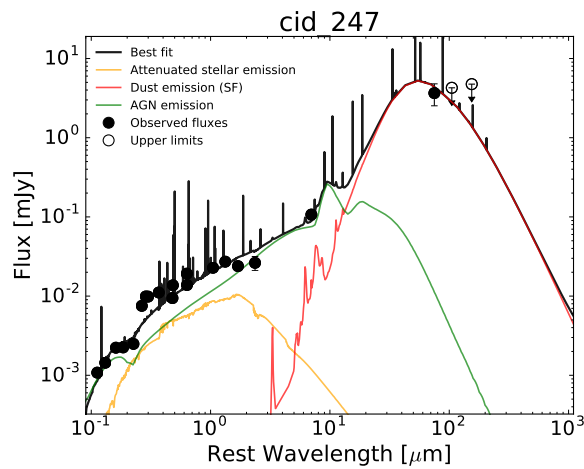
Figure C.1: Rest-frame SEDs of the target samples presented in Chapters 3 and 4. The black dots represent the observed multi-wavelength photometry, while the empty dots indicate 3σ upper limits. The black solid line is the total best-fit model, the orange curve represents the stellar emission attenuated by dust, the green template reproduces the AGN emission, the red curve accounts for dust emission heated by star formation. Emission lines in the black curves are part of the nebular emission component, included in the overall SED.

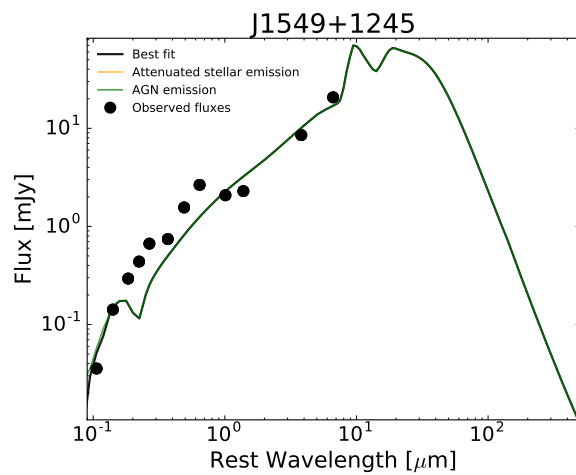
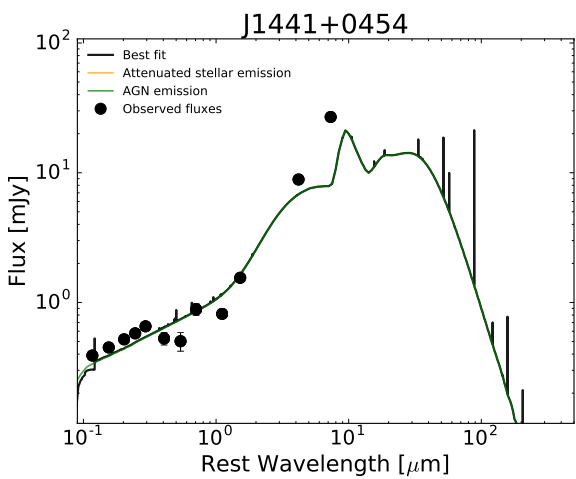
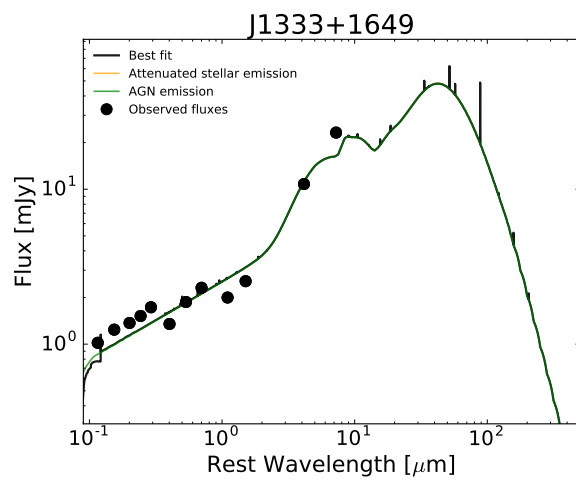
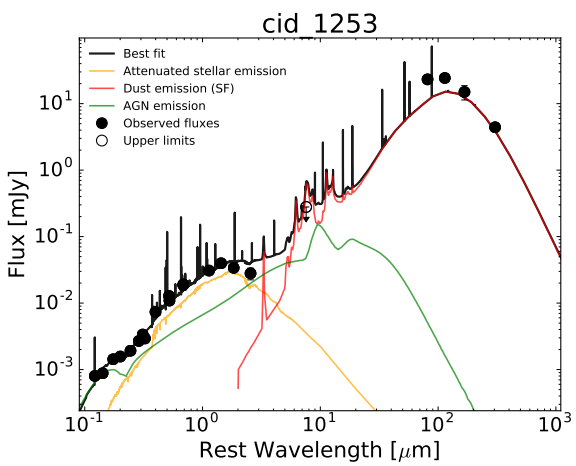
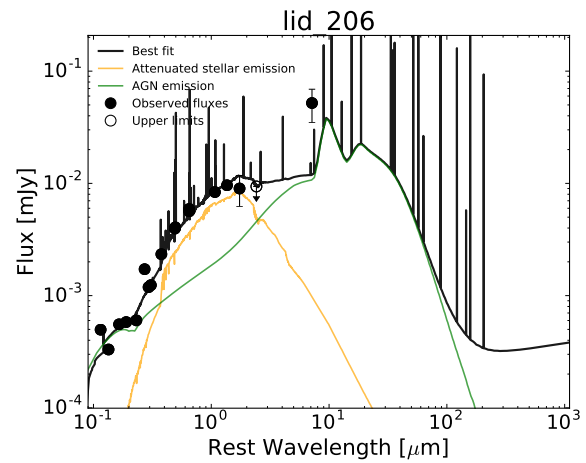
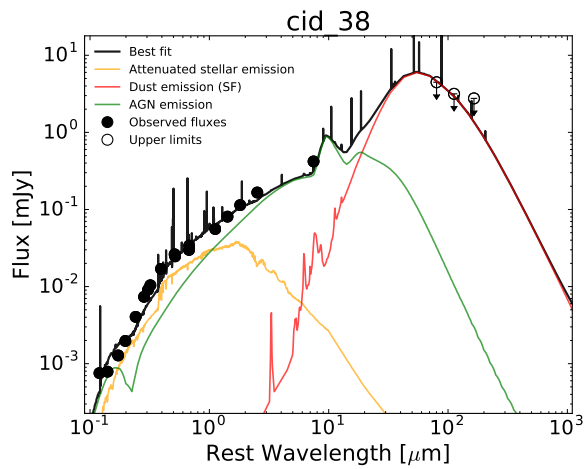


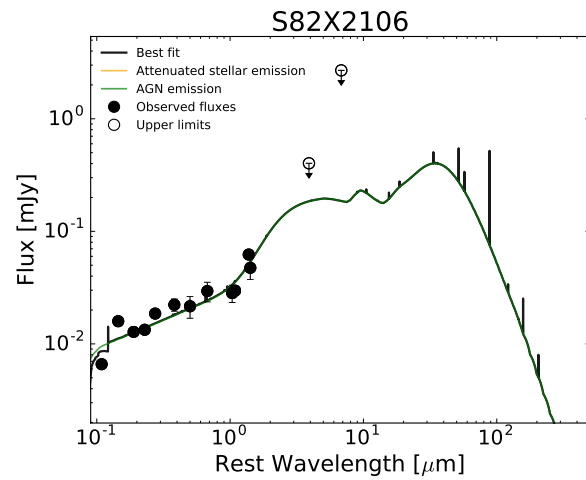
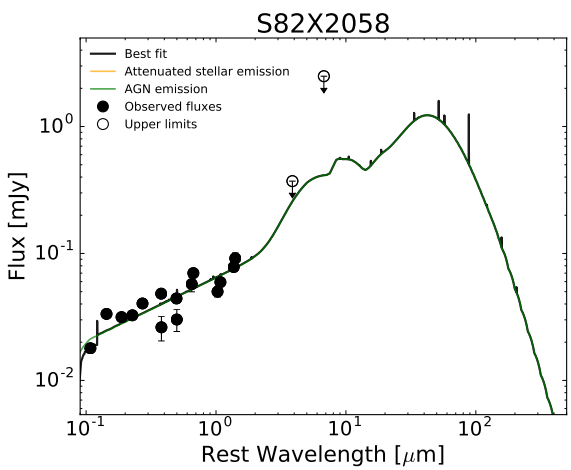
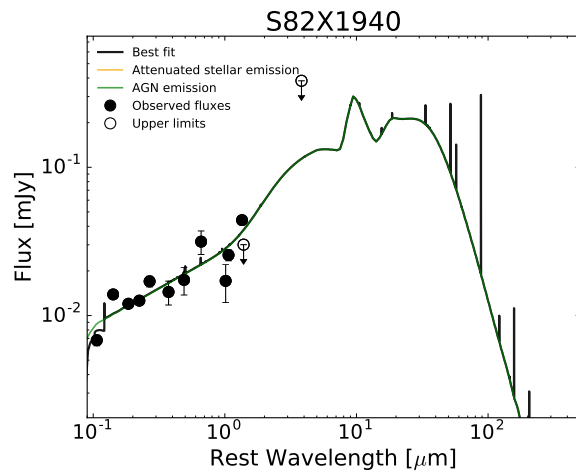
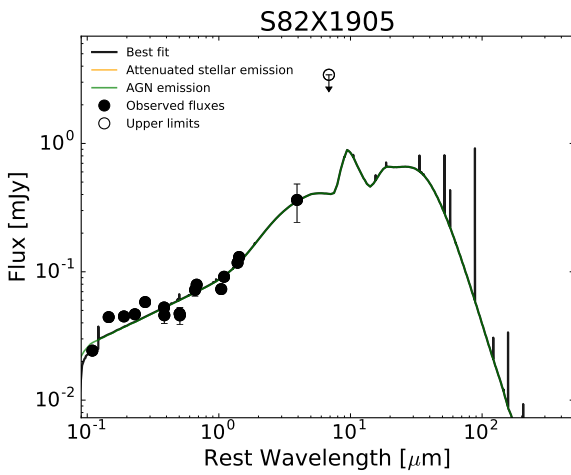












Appendix D

Flux maps and spectra of the ALMA observations

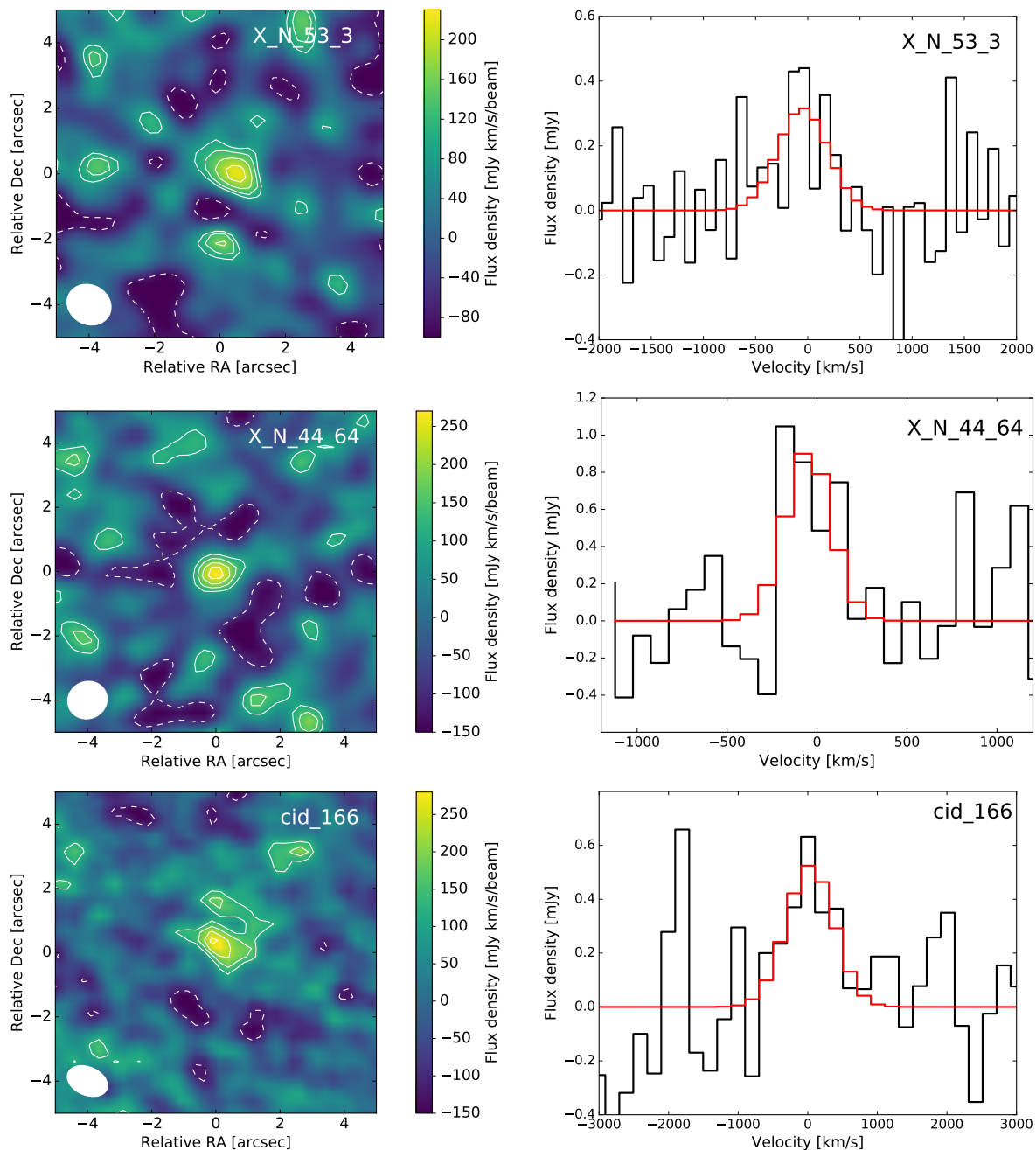
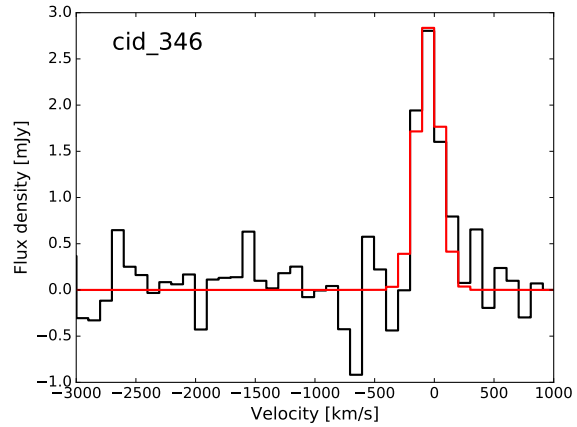
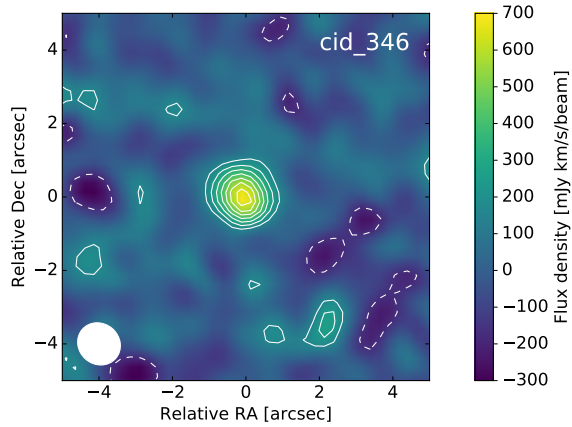
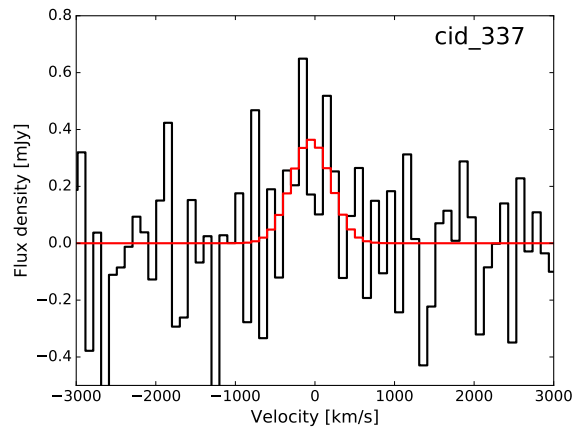
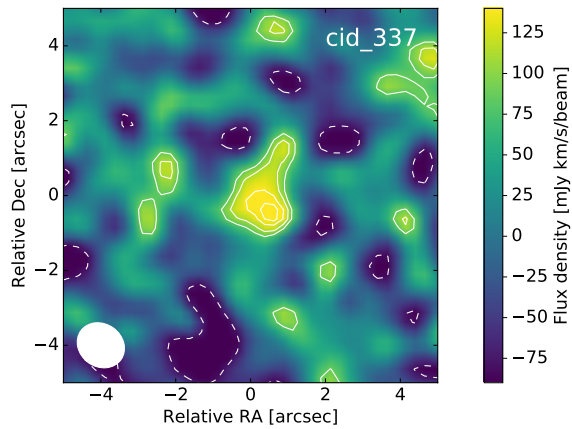
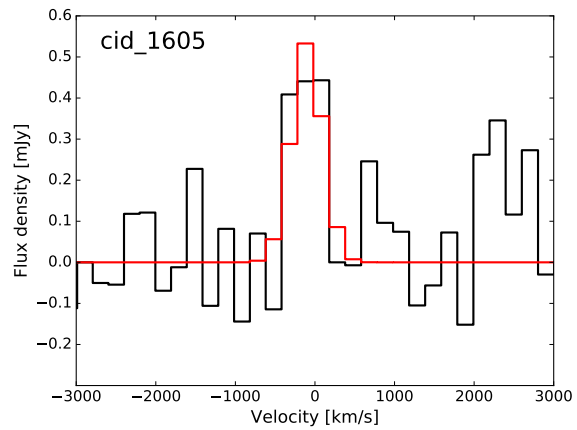
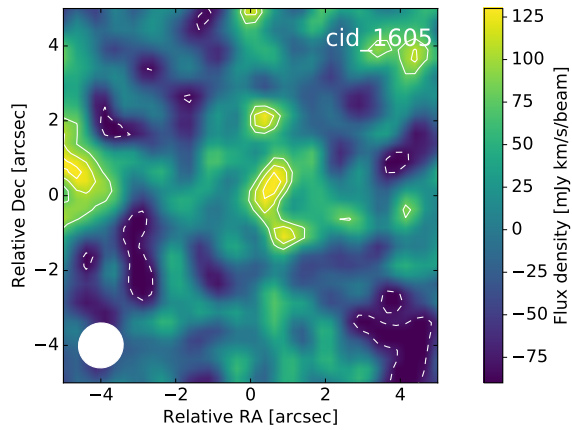
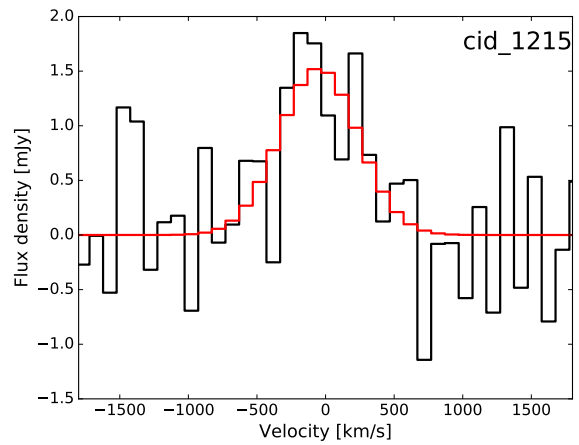
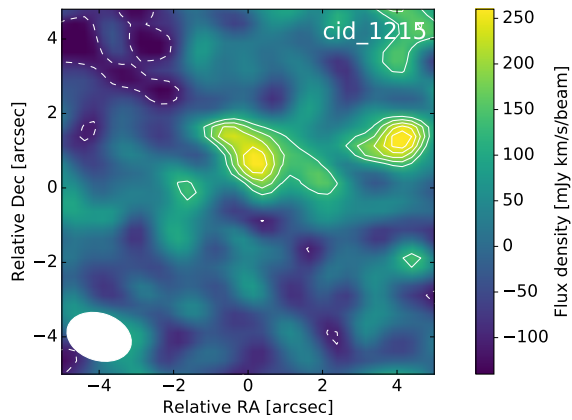
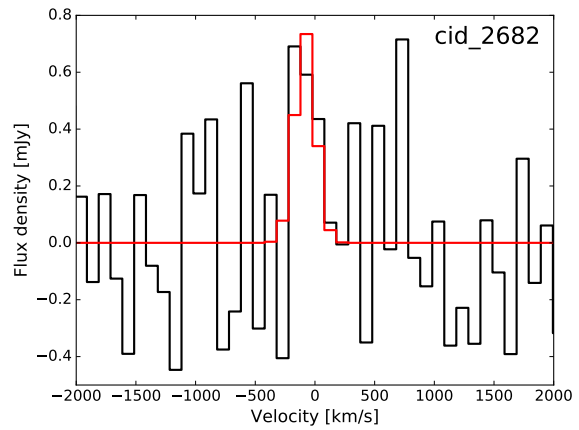
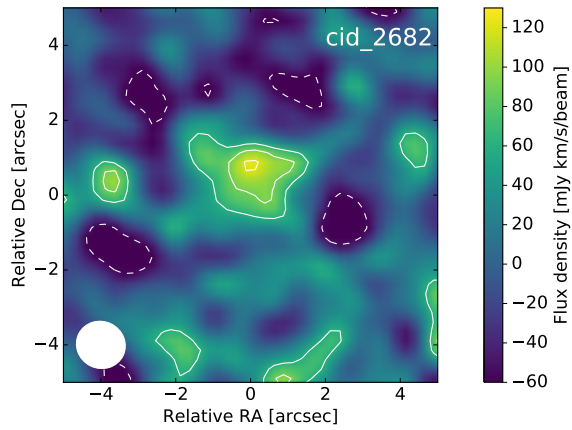
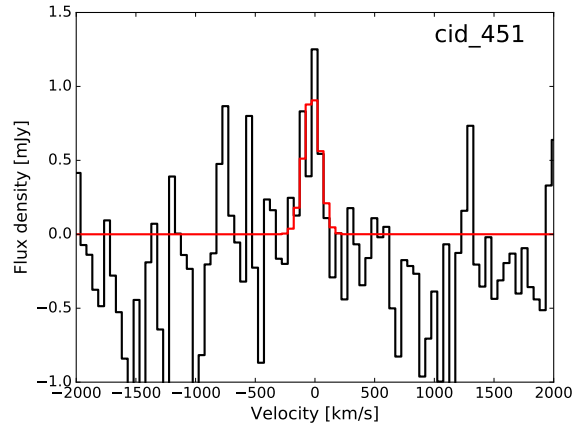
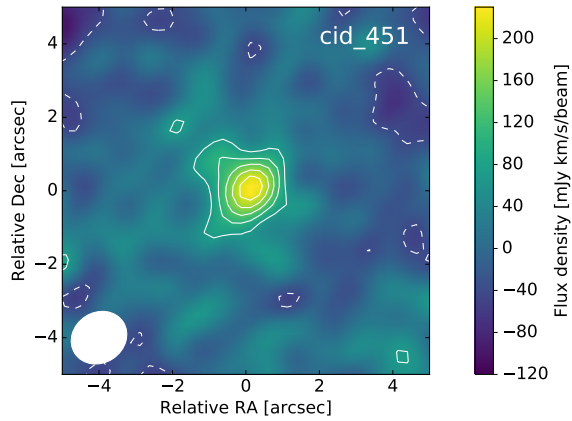
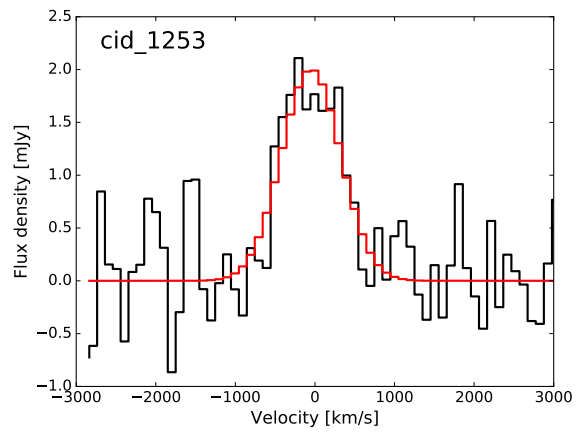
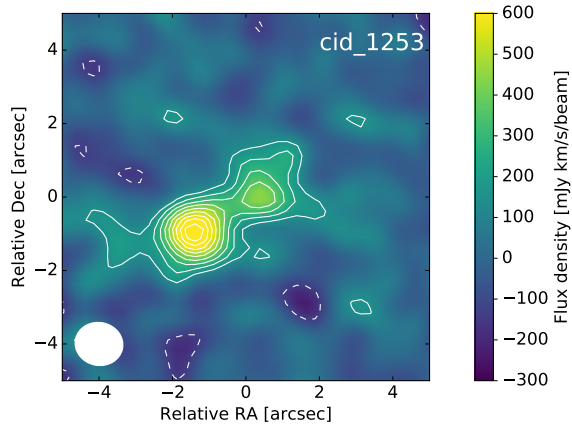
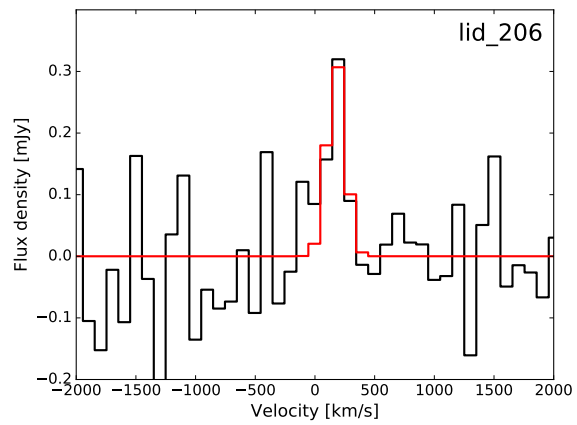
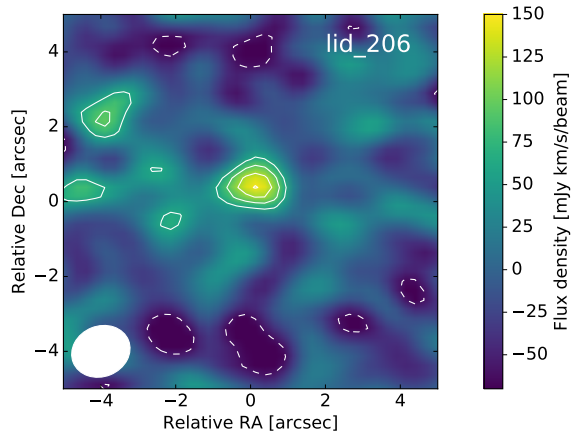
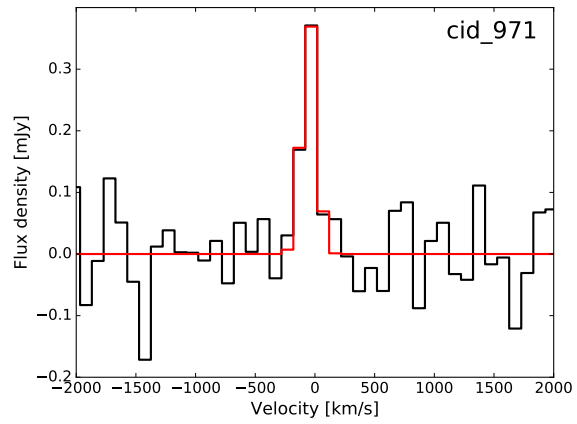
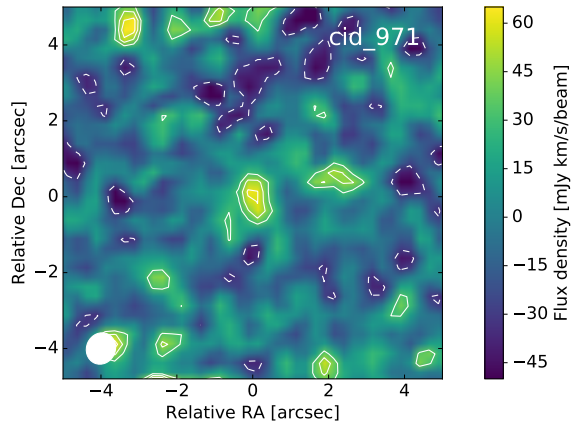


Figure D.1: CO velocity-integrated maps (*left*) and CO spectra (*right*) of the 12 detections described in Chapter 4. *Left*: contours are -2, 2, 3, 4, etc. σ . Dashed lines represent negative contours while solid lines depict positive contours. The synthetic beam is indicated at the bottom-left corner of each map by a white ellipse. North is up and East is toward left. *Right*: the black line corresponds to the observed spectrum while the red line represents the Gaussian fit.







Bibliography

- Ade, P. A. R., Aghanim, N., Arnaud, M., et al. 2016, , 594, A13
- Aird, J., Coil, A. L., Georgakakis, A., et al. 2015, , 451, 1892
- Aird, J., Coil, A. L., Moustakas, J., et al. 2012, , 746, 90
- Aird, J., Nandra, K., Laird, E. S., et al. 2010, , 401, 2531
- Akylas, A., Georgakakis, A., Georgantopoulos, I., Brightman, M., & Nandra, K. 2012, , 546, A98
- Alexander, D. M., Smail, I., Bauer, F. E., et al. 2005, , 434, 738
- Alexander, D. M., Swinbank, A. M., Smail, I., McDerimid, R., & Nesvadba, N. P. H. 2010, , 402, 2211
- Allen, R. J., Kacprzak, G. G., Glazebrook, K., et al. 2017, , 834, L11
- Ananna, T. T., Salvato, M., LaMassa, S., et al. 2017, , 850, 66
- Antonucci, R. 1993, , 31, 473
- Arnaud, K. A. 1996, in *Astronomical Society of the Pacific Conference Series*, Vol. 101, *Astronomical Data Analysis Software and Systems V*, ed. G. H. Jacoby & J. Barnes, 17
- Avni, Y. 1976, , 210, 642
- Baade, W. & Minkowski, R. 1954, , 119, 215
- Bae, H.-J., Woo, J.-H., Karouzos, M., et al. 2017, , 837, 91
- Balestra, I., Mainieri, V., Popesso, P., et al. 2010, , 512, A12
- Baloković, M., Comastri, A., Harrison, F. A., et al. 2014, , 794, 111
- Barro, G., Faber, S. M., Pérez-González, P. G., et al. 2013, , 765, 104
- Bauermeister, A., Blitz, L., Bolatto, A., et al. 2013, , 768, 132

- Becker, R. H., White, R. L., & Helfand, D. J. 1995, , 450, 559
- Behroozi, P. S., Wechsler, R. H., & Conroy, C. 2013, , 770, 57
- Bennert, V. N., Auger, M. W., Treu, T., Woo, J.-H., & Malkan, M. A. 2011, , 726, 59
- Benson, A. J., Bower, R. G., Frenk, C. S., et al. 2003, , 599, 38
- Bernhard, E., Mullaney, J. R., Aird, J., et al. 2018, , 476, 436
- Bianchi, S. 2013, , 552, A89
- Bischetti, M., Piconcelli, E., Vietri, G., et al. 2017, , 598, A122
- Blain, A. W., Smail, I., Ivison, R. J., Kneib, J.-P., & Frayer, D. T. 2002, , 369, 111
- Bongiorno, A., Merloni, A., Brusa, M., et al. 2012, , 427, 3103
- Bonzini, M., Mainieri, V., Padovani, P., et al. 2012, , 203, 15
- Bonzini, M., Padovani, P., Mainieri, V., et al. 2013, , 436, 3759
- Boquien, M., Kennicutt, R., Calzetti, D., et al. 2016, , 591, A6
- Bothwell, M. S., Smail, I., Chapman, S. C., et al. 2013, , 429, 3047
- Bournaud, F., Chapon, D., Teyssier, R., et al. 2011a, , 730, 4
- Bournaud, F., Dekel, A., Teyssier, R., et al. 2011b, , 741, L33
- Brandt, W. N. & Alexander, D. M. 2015, , 23, 1
- Brusa, M., Bongiorno, A., Cresci, G., et al. 2015, , 446, 2394
- Brusa, M., Cresci, G., Daddi, E., et al. 2018, , 612, A29
- Brusa, M., Perna, M., Cresci, G., et al. 2016, , 588, A58
- Bruzual, G. & Charlot, S. 2003, , 344, 1000
- Buat, V., Giovannoli, E., Heinis, S., et al. 2011, , 533, A93
- Buat, V., Noll, S., Burgarella, D., et al. 2012, , 545, A141
- Buat, V., Oi, N., Heinis, S., et al. 2015, , 577, A141
- Buchner, J. & Bauer, F. E. 2017, , 465, 4348
- Buchner, J., Georgakakis, A., Nandra, K., et al. 2015, , 802, 89
- Burtscher, L., Meisenheimer, K., Tristram, K. R. W., et al. 2013, , 558, A149

- Calistro Rivera, G., Hodge, J. A., Smail, I., et al. 2018, , 863, 56
- Calura, F., Gilli, R., Vignali, C., et al. 2014, , 438, 2765
- Calzetti, D., Armus, L., Bohlin, R. C., et al. 2000, , 533, 682
- Cano-Díaz, M., Maiolino, R., Marconi, A., et al. 2012, , 537, L8
- Capak, P., Aussel, H., Ajiki, M., et al. 2007, , 172, 99
- Cardamone, C. N., van Dokkum, P. G., Urry, C. M., et al. 2010, , 189, 270
- Carilli, C. L. & Walter, F. 2013, , 51, 105
- Carniani, S., Gallerani, S., Vallini, L., et al. 2019, arXiv e-prints, arXiv:1902.01413
- Carniani, S., Marconi, A., Maiolino, R., et al. 2015, , 580, A102
- Carniani, S., Marconi, A., Maiolino, R., et al. 2016, , 591, A28
- Cash, W. 1979, , 228, 939
- Chabrier, G. 2003, , 115, 763
- Chang, Y.-Y., Le Floc'h, E., Juneau, S., et al. 2017, , 233, 19
- Charlot, S. & Fall, S. M. 2000, , 539, 718
- Chen, C.-C., Smail, I., Swinbank, A. M., et al. 2015a, , 799, 194
- Chen, C.-T. J., Hickox, R. C., Alberts, S., et al. 2015b, , 802, 50
- Cicone, C., Bothwell, M., Wagg, J., et al. 2017, , 604, A53
- Cicone, C., Brusa, M., Ramos Almeida, C., et al. 2018, *Nature Astronomy*, 2, 176
- Cicone, C., Maiolino, R., Gallerani, S., et al. 2015, , 574, A14
- Cicone, C., Maiolino, R., Sturm, E., et al. 2014, , 562, A21
- Ciesla, L., Charmandaris, V., Georgakakis, A., et al. 2015, , 576, A10
- Cimatti, A., Cassata, P., Pozzetti, L., et al. 2008, , 482, 21
- Ciotti, L. & Ostriker, J. P. 1997, , 487, L105
- Circosta, C., Mainieri, V., Padovani, P., et al. 2018, , 620, A82
- Circosta, C., Vignali, C., Gilli, R., et al. 2019, , 623, A172
- Civano, F., Marchesi, S., Comastri, A., et al. 2016, , 819, 62

- Comastri, A., Iwasawa, K., Gilli, R., et al. 2010, , 717, 787
- Comastri, A., Ranalli, P., Iwasawa, K., et al. 2011, , 526, L9
- Combes, F., García-Burillo, S., Audibert, A., et al. 2019, , 623, A79
- Concas, A., Popesso, P., Brusa, M., et al. 2017, , 606, A36
- Conselice, C. J., Wilkinson, A., Duncan, K., & Mortlock, A. 2016, , 830, 83
- Coppin, K. E. K., Chapman, S. C., Smail, I., et al. 2010, , 407, L103
- Costa, T., Rosdahl, J., Sijacki, D., & Haehnelt, M. G. 2018, , 479, 2079
- Costa, T., Sijacki, D., & Haehnelt, M. G. 2014, , 444, 2355
- Crenshaw, D. M. & Kraemer, S. B. 2007, , 659, 250
- Cresci, G., Hicks, E. K. S., Genzel, R., et al. 2009, , 697, 115
- Cresci, G., Mainieri, V., Brusa, M., et al. 2015, , 799, 82
- Cresci, G. & Maiolino, R. 2018, *Nature Astronomy*, 2, 179
- Cullen, F., McLure, R. J., Khochfar, S., et al. 2018,
- Curtis, H. D. 1918, *Publications of Lick Observatory*, 13, 9
- Daddi, E., Elbaz, D., Walter, F., et al. 2010, , 714, L118
- Dale, D. A., Helou, G., Magdis, G. E., et al. 2014, , 784, 83
- Das, V., Crenshaw, D. M., Hutchings, J. B., et al. 2005, , 130, 945
- De Breuck, C., Williams, R. J., Swinbank, M., et al. 2014, , 565, A59
- Debuhr, J., Quataert, E., & Ma, C.-P. 2012, , 420, 2221
- Decarli, R., Walter, F., González-López, J., et al. 2019, *arXiv e-prints*
- Decarli, R., Walter, F., Venemans, B. P., et al. 2018, , 854, 97
- Del Moro, A., Alexander, D. M., Bauer, F. E., et al. 2016, , 456, 2105
- Delvecchio, I., Gruppioni, C., Pozzi, F., et al. 2014, , 439, 2736
- Delvecchio, I., Lutz, D., Berta, S., et al. 2015, , 449, 373
- Delvecchio, I., Smolčić, V., Zamorani, G., et al. 2017, , 602, A3
- Di Matteo, T., Springel, V., & Hernquist, L. 2005, , 433, 604

- Diamond-Stanic, A. M. & Rieke, G. H. 2012, , 746, 168
- Duras, F., Bongiorno, A., Piconcelli, E., et al. 2017, , 604, A67
- Elbaz, D., Dickinson, M., Hwang, H. S., et al. 2011, , 533, A119
- Ellison, S. L., Brown, T., Catinella, B., & Cortese, L. 2019, , 482, 5694
- Elvis, M., Wilkes, B. J., McDowell, J. C., et al. 1994, , 95, 1
- Erben, T., Hildebrandt, H., Miller, L., et al. 2013, , 433, 2545
- Evans, I., Koratkar, A., Allen, M., Dopita, M., & Tsvetanov, Z. 1999, , 521, 531
- Event Horizon Telescope Collaboration, Akiyama, K., Alberdi, A., et al. 2019, , 875, L1
- Fabbiano, G., Elvis, M., Paggi, A., et al. 2017, , 842, L4
- Fabian, A. C. 2012, , 50, 455
- Fabian, A. C., Iwasawa, K., Reynolds, C. S., & Young, A. J. 2000, , 112, 1145
- Fabian, A. C. & Miniutti, G. 2005, ArXiv:astro-ph/0507409
- Farina, E. P., Falomo, R., Decarli, R., Treves, A., & Kotilainen, J. K. 2013, , 429, 1267
- Fath, E. A. 1909, , 21, 138
- Feltre, A., Hatziminaoglou, E., Fritz, J., & Franceschini, A. 2012, , 426, 120
- Feltre, A., Hatziminaoglou, E., Hernán-Caballero, A., et al. 2013, , 434, 2426
- Ferrarese, L. & Merritt, D. 2000, , 539, L9
- Feruglio, C., Daddi, E., Fiore, F., et al. 2011, , 729, L4
- Feruglio, C., Maiolino, R., Piconcelli, E., et al. 2010, , 518, L155
- Fiore, F., Feruglio, C., Shankar, F., et al. 2017, , 601, A143
- Fliri, J. & Trujillo, I. 2016, , 456, 1359
- Fluetsch, A., Maiolino, R., Carniani, S., et al. 2019, , 483, 4586
- Förster Schreiber, N. M., Genzel, R., Bouché, N., et al. 2009, , 706, 1364
- Förster Schreiber, N. M., Genzel, R., Newman, S. F., et al. 2014, , 787, 38
- Förster Schreiber, N. M., Renzini, A., Mancini, C., et al. 2018, ArXiv e-prints
- Förster Schreiber, N. M., Übler, H., Davies, R. L., et al. 2019, , 875, 21

- Fotopoulou, S., Pacaud, F., Paltani, S., et al. 2016, , 592, A5
- Fritz, J., Franceschini, A., & Hatziminaoglou, E. 2006, , 366, 767
- Fu, H., Cooray, A., Feruglio, C., et al. 2013, , 498, 338
- Fu, H., Isbell, J., Casey, C. M., et al. 2017, , 844, 123
- Fujimoto, S., Ouchi, M., Shibuya, T., & Nagai, H. 2017, , 850, 83
- Gandhi, P., Horst, H., Smette, A., et al. 2009, , 502, 457
- García-Burillo, S., Usero, A., Alonso-Herrero, A., et al. 2012, , 539, A8
- Genzel, R., Tacconi, L. J., Gracia-Carpio, J., et al. 2010, , 407, 2091
- Genzel, R., Tacconi, L. J., Lutz, D., et al. 2015, , 800, 20
- Georgakakis, A., Salvato, M., Liu, Z., et al. 2017, , 469, 3232
- Giavalisco, M., Ferguson, H. C., Koekemoer, A. M., et al. 2004, , 600, L93
- Gilli, R., Comastri, A., & Hasinger, G. 2007, , 463, 79
- Gilli, R., Norman, C., Vignali, C., et al. 2014, , 562, A67
- Gilli, R., Salvati, M., & Hasinger, G. 2001, , 366, 407
- Gilli, R., Su, J., Norman, C., et al. 2011, , 730, L28
- Gnerucci, A., Marconi, A., Cresci, G., et al. 2011, , 528, A88
- Gravity Collaboration, Abuter, R., Amorim, A., et al. 2018, , 618, L10
- Greene, J. E., Zakamska, N. L., Ho, L. C., & Barth, A. J. 2011, , 732, 9
- Grogin, N. A., Kocevski, D. D., Faber, S. M., et al. 2011, , 197, 35
- Guo, Y., Ferguson, H. C., Giavalisco, M., et al. 2013, , 207, 24
- Haardt, F. & Maraschi, L. 1993, , 413, 507
- Harris, K., Farrah, D., Schulz, B., et al. 2016, , 457, 4179
- Harrison, C. 2014, PhD thesis, Durham University
- Harrison, C. M. 2017, *Nature Astronomy*, 1, 0165
- Harrison, C. M., Alexander, D. M., Mullaney, J. R., et al. 2012a, , 760, L15
- Harrison, C. M., Alexander, D. M., Mullaney, J. R., et al. 2016a, , 456, 1195

- Harrison, C. M., Alexander, D. M., Swinbank, A. M., et al. 2012b, , 426, 1073
- Harrison, C. M., Costa, T., Tadhunter, C. N., et al. 2018, *Nature Astronomy*, 2, 198
- Harrison, C. M., Simpson, J. M., Stanley, F., et al. 2016b, , 457, L122
- Hatziminaoglou, E., Fritz, J., Franceschini, A., et al. 2008, , 386, 1252
- Hatziminaoglou, E., Omont, A., Stevens, J. A., et al. 2010, , 518, L33
- Häussler, B., McIntosh, D. H., Barden, M., et al. 2007, , 172, 615
- Heckman, T. M., Kauffmann, G., Brinchmann, J., et al. 2004, , 613, 109
- Herschel, W. 1786, *Philosophical Transactions of the Royal Society of London Series I*, 76, 457
- Hickox, R. C. & Alexander, D. M. 2018, , 56, 625
- Hickox, R. C., Mullaney, J. R., Alexander, D. M., et al. 2014, , 782, 9
- Hinshaw, G., Larson, D., Komatsu, E., et al. 2013, , 208, 19
- Hodge, J. A., Karim, A., Smail, I., et al. 2013, , 768, 91
- Hodge, J. A., Riechers, D., Decarli, R., et al. 2015, , 798, L18
- Hodge, J. A., Swinbank, A. M., Simpson, J. M., et al. 2016, , 833, 103
- Hopkins, P. F., Bundy, K., Hernquist, L., Wuyts, S., & Cox, T. J. 2010, , 401, 1099
- Hopkins, P. F., Hernquist, L., Cox, T. J., et al. 2005, , 630, 705
- Hopkins, P. F., Hernquist, L., Cox, T. J., et al. 2006, , 163, 1
- Hopkins, P. F. & Quataert, E. 2010, , 407, 1529
- Hsieh, B.-C., Wang, W.-H., Hsieh, C.-C., et al. 2012, , 203, 23
- Hsu, L.-T., Salvato, M., Nandra, K., et al. 2014, , 796, 60
- Hubble, E. P. 1925, *Popular Astronomy*, 33
- Huggins, W. & Miller, W. A. 1864, *Philosophical Transactions of the Royal Society of London Series I*, 154, 437
- Hurley, P. D., Oliver, S., Betancourt, M., et al. 2017, , 464, 885
- Husemann, B., Davis, T. A., Jahnke, K., et al. 2017a, , 470, 1570
- Husemann, B., Jahnke, K., Sánchez, S. F., et al. 2014, , 443, 755

- Husemann, B., Tremblay, G., Davis, T., et al. 2017b, *The Messenger*, 169, 42
- Husemann, B., Wisotzki, L., Sánchez, S. F., & Jahnke, K. 2013, , 549, A43
- Ilbert, O., Capak, P., Salvato, M., et al. 2009, , 690, 1236
- Ilbert, O., McCracken, H. J., Le Fèvre, O., et al. 2013, , 556, A55
- Inoue, A. K. 2011, , 415, 2920
- Iwasawa, K., Sanders, D. B., Teng, S. H., et al. 2011, , 529, A106
- Jaffe, W., Meisenheimer, K., Röttgering, H. J. A., et al. 2004, , 429, 47
- Jarvis, M. E., Harrison, C. M., Thomson, A. P., et al. 2019, , 485, 2710
- Juneau, S., Dickinson, M., Bournaud, F., et al. 2013, , 764, 176
- Kakkad, D., Mainieri, V., Brusa, M., et al. 2017, , 468, 4205
- Kakkad, D., Mainieri, V., Padovani, P., et al. 2016, , 592, A148
- Karouzos, M., Woo, J.-H., & Bae, H.-J. 2016, , 819, 148
- Kennicutt, Jr., R. C. 1989, , 344, 685
- Kennicutt, Jr., R. C. 1998a, , 36, 189
- Kennicutt, Jr., R. C. 1998b, , 498, 541
- King, A. 2005, , 635, L121
- King, A. & Pounds, K. 2015, , 53, 115
- Kirkpatrick, A., Sharon, C., Keller, E., & Pope, A. 2019, arXiv e-prints
- Kormendy, J. & Ho, L. C. 2013, , 51, 511
- Kurk, J., Cimatti, A., Daddi, E., et al. 2013, , 549, A63
- La Franca, F., Fiore, F., Comastri, A., et al. 2005, , 635, 864
- Lagos, C. D. P., Baugh, C. M., Lacey, C. G., et al. 2011, , 418, 1649
- Laigle, C., McCracken, H. J., Ilbert, O., et al. 2016, , 224, 24
- LaMassa, S. M., Urry, C. M., Cappelluti, N., et al. 2016, , 817, 172
- Lampton, M., Margon, B., & Bowyer, S. 1976, , 208, 177
- Lang, D., Hogg, D. W., & Schlegel, D. J. 2016, , 151, 36

- Lani, C., Netzer, H., & Lutz, D. 2017, , 471, 59
- Lanzuisi, G., Civano, F., Elvis, M., et al. 2013, , 431, 978
- Lanzuisi, G., Civano, F., Marchesi, S., et al. 2018, , 480, 2578
- Lanzuisi, G., Delvecchio, I., Berta, S., et al. 2017, , 602, A123
- Lanzuisi, G., Gilli, R., Cappi, M., et al. 2019, , 875, L20
- Lanzuisi, G., Piconcelli, E., Fiore, F., et al. 2009, , 498, 67
- Lanzuisi, G., Ranalli, P., Georgantopoulos, I., et al. 2015, , 573, A137
- Lapi, A., Pantoni, L., Zanisi, L., et al. 2018, , 857, 22
- Lapi, A., Raimundo, S., Aversa, R., et al. 2014, , 782, 69
- Lau, M. W., Prochaska, J. X., & Hennawi, J. F. 2018, , 857, 126
- Lauer, T. R., Gebhardt, K., Faber, S. M., et al. 2007, , 664, 226
- Lehmer, B. D., Brandt, W. N., Alexander, D. M., et al. 2005, , 161, 21
- Liu, G., Arav, N., & Rupke, D. S. N. 2015, , 221, 9
- Liu, G., Zakamska, N. L., & Greene, J. E. 2014, , 442, 1303
- Liu, G., Zakamska, N. L., Greene, J. E., Nesvadba, N. P. H., & Liu, X. 2013, , 430, 2327
- Liu, T., Tozzi, P., Wang, J.-X., et al. 2017, , 232, 8
- Liu, Z., Merloni, A., Georgakakis, A., et al. 2016, , 459, 1602
- Lo Faro, B., Buat, V., Roehlly, Y., et al. 2017, , 472, 1372
- Luo, B., Brandt, W. N., Xue, Y. Q., et al. 2017, , 228, 2
- Lusso, E., Comastri, A., Simmons, B. D., et al. 2012, , 425, 623
- Lusso, E. & Risaliti, G. 2016, , 819, 154
- Lutz, D., Mainieri, V., Rafferty, D., et al. 2010, , 712, 1287
- Lutz, D., Poglitsch, A., Altieri, B., et al. 2011, , 532, A90
- Lynden-Bell, D. 1969, , 223, 690
- Madau, P. & Dickinson, M. 2014, , 52, 415
- Magdis, G. E., Daddi, E., Béthermin, M., et al. 2012, , 760, 6

- Magdziarz, P. & Zdziarski, A. A. 1995, , 273, 837
- Magnelli, B., Popesso, P., Berta, S., et al. 2013, , 553, A132
- Magnelli, B., Saintonge, A., Lutz, D., et al. 2012, , 548, A22
- Magorrian, J., Tremaine, S., Richstone, D., et al. 1998, , 115, 2285
- Mainieri, V., Bergeron, J., Hasinger, G., et al. 2002, , 393, 425
- Mainieri, V., Bongiorno, A., Merloni, A., et al. 2011, , 535, A80
- Mainieri, V., Rigopoulou, D., Lehmann, I., et al. 2005, , 356, 1571
- Maiolino, R. & Rieke, G. H. 1995, , 454, 95
- Maiolino, R., Salvati, M., Bassani, L., et al. 1998, , 338, 781
- Mancini, C., Förster Schreiber, N. M., Renzini, A., et al. 2011, , 743, 86
- Marchesi, S., Civano, F., Elvis, M., et al. 2016a, , 817, 34
- Marchesi, S., Lanzuisi, G., Civano, F., et al. 2016b, , 830, 100
- Marconi, A., Risaliti, G., Gilli, R., et al. 2004, , 351, 169
- Martocchia, S., Piconcelli, E., Zappacosta, L., et al. 2017, , 608, A51
- Mashian, N., Sturm, E., Sternberg, A., et al. 2015, , 802, 81
- Mateos, S., Barcons, X., Carrera, F. J., et al. 2005, , 444, 79
- Matthews, T. A. & Sandage, A. R. 1963, , 138, 30
- Menzel, M.-L., Merloni, A., Georgakakis, A., et al. 2016, , 457, 110
- Merloni, A., Bongiorno, A., Brusa, M., et al. 2014, , 437, 3550
- Messier, C. 1781, *Catalogue des Nébuleuses et des Amas d'Étoiles (Catalog of Nebulae and Star Clusters)*, Tech. rep.
- Miller, N. A., Bonzini, M., Fomalont, E. B., et al. 2013, , 205, 13
- Molnár, D. C., Sargent, M. T., Elbaz, D., Papadopoulos, P. P., & Silk, J. 2017, , 467, 586
- Mor, R. & Netzer, H. 2012, , 420, 526
- Mullaney, J. R., Alexander, D. M., Aird, J., et al. 2015, , 453, L83
- Mullaney, J. R., Alexander, D. M., Goulding, A. D., & Hickox, R. C. 2011, , 414, 1082

- Murphy, K. D. & Yaqoob, T. 2009, , 397, 1549
- Nandra, K. & Pounds, K. A. 1994, , 268, 405
- Narayanan, D. & Krumholz, M. R. 2014, , 442, 1411
- Nelson, D., Pillepich, A., Springel, V., et al. 2019, arXiv e-prints, arXiv:1902.05554
- Nenkova, M., Sirocky, M. M., Ivezić, Ž., & Elitzur, M. 2008a, , 685, 147
- Nenkova, M., Sirocky, M. M., Nikutta, R., Ivezić, Ž., & Elitzur, M. 2008b, , 685, 160
- Nesvadba, N. P. H., De Breuck, C., Lehnert, M. D., Best, P. N., & Collet, C. 2017a, , 599, A123
- Nesvadba, N. P. H., Drouart, G., De Breuck, C., et al. 2017b, , 600, A121
- Nesvadba, N. P. H., Lehnert, M. D., De Breuck, C., Gilbert, A., & van Breugel, W. 2007, , 475, 145
- Nesvadba, N. P. H., Lehnert, M. D., De Breuck, C., Gilbert, A. M., & van Breugel, W. 2008, , 491, 407
- Nesvadba, N. P. H., Lehnert, M. D., Eisenhauer, F., et al. 2006, , 650, 693
- Nesvadba, N. P. H., Polletta, M., Lehnert, M. D., et al. 2011, , 415, 2359
- Netzer, H. 2013, *The Physics and Evolution of Active Galactic Nuclei*
- Noeske, K. G., Weiner, B. J., Faber, S. M., et al. 2007, , 660, L43
- Noll, S., Burgarella, D., Giovannoli, E., et al. 2009, , 507, 1793
- Norman, C., Hasinger, G., Giacconi, R., et al. 2002, , 571, 218
- Oesch, P. A., Brammer, G., van Dokkum, P. G., et al. 2016, , 819, 129
- Oliver, S. J., Bock, J., Altieri, B., et al. 2012, , 424, 1614
- Osterbrock, D. E. & Ferland, G. J. 2006, *Astrophysics of gaseous nebulae and active galactic nuclei*
- Padovani, P. 2017, *Nature Astronomy*, 1, 0194
- Padovani, P., Alexander, D. M., Assef, R. J., et al. 2017, , 25, 2
- Page, M. J., Symeonidis, M., Vieira, J. D., et al. 2012, , 485, 213
- Papadopoulos, P. P., van der Werf, P. P., Xilouris, E. M., et al. 2012, , 426, 2601

- Perna, M., Brusa, M., Salvato, M., et al. 2015, , 583, A72
- Perna, M., Lanzuisi, G., Brusa, M., Mignoli, M., & Cresci, G. 2017, , 603, A99
- Perna, M., Sargent, M. T., Brusa, M., et al. 2018, , 619, A90
- Peterson, B. M. 2003, *An Introduction to Active Galactic Nuclei*
- Peterson, B. M., Ferrarese, L., Gilbert, K. M., et al. 2004, , 613, 682
- Piconcelli, E., Jimenez-Bailón, E., Guainazzi, M., et al. 2005, , 432, 15
- Pier, E. A. & Krolik, J. H. 1992, , 401, 99
- Pierre, M., Pacaud, F., Adami, C., et al. 2016, , 592, A1
- Polletta, M., Courvoisier, T. J. L., Hooper, E. J., & Wilkes, B. J. 2000, , 362, 75
- Polletta, M., Tajer, M., Maraschi, L., et al. 2007, , 663, 81
- Pozzi, F., Vignali, C., Gruppioni, C., et al. 2012, , 423, 1909
- Prieto, M. A., Reunanen, J., Tristram, K. R. W., et al. 2010, , 402, 724
- Privon, G. C., Narayanan, D., & Davé, R. 2018, *ArXiv e-prints*
- Prochaska, J. X., Hennawi, J. F., Lee, K.-G., et al. 2013, , 776, 136
- Puglisi, A., Rodighiero, G., Franceschini, A., et al. 2016, , 586, A83
- Ramos Almeida, C. & Ricci, C. 2017, *Nature Astronomy*, 1, 679
- Reddy, N. A., Kriek, M., Shapley, A. E., et al. 2015, , 806, 259
- Ricci, C., Trakhtenbrot, B., Koss, M. J., et al. 2017, , 233, 17
- Richards, G. T., Lacy, M., Storrie-Lombardi, L. J., et al. 2006, , 166, 470
- Rigopoulou, D., Mainieri, V., Almaini, O., et al. 2009, , 400, 1199
- Risaliti, G. & Elvis, M. 2004, in *Astrophysics and Space Science Library*, Vol. 308, *Supermassive Black Holes in the Distant Universe*, ed. A. J. Barger, 187
- Rodighiero, G., Daddi, E., Baronchelli, I., et al. 2011, , 739, L40
- Rosario, D. J., Burtscher, L., Davies, R. I., et al. 2018, , 473, 5658
- Rosario, D. J., Santini, P., Lutz, D., et al. 2013, , 771, 63
- Rosario, D. J., Santini, P., Lutz, D., et al. 2012, , 545, A45

- Rosario, D. J., Togi, A., Burtscher, L., et al. 2019, , 875, L8
- Roseboom, I. G., Ivison, R. J., Greve, T. R., et al. 2012, , 419, 2758
- Roseboom, I. G., Oliver, S. J., Kunz, M., et al. 2010, , 409, 48
- Rovilos, E., Comastri, A., Gilli, R., et al. 2012, , 546, A58
- Rupke, D. S. N., Gültekin, K., & Veilleux, S. 2017, , 850, 40
- Rupke, D. S. N. & Veilleux, S. 2013, , 775, L15
- Saintonge, A., Catinella, B., Tacconi, L. J., et al. 2017, , 233, 22
- Salpeter, E. E. 1955, , 121, 161
- Salpeter, E. E. 1964, , 140, 796
- Salvato, M., Hasinger, G., Ilbert, O., et al. 2009, , 690, 1250
- Sanders, D. B., Soifer, B. T., Elias, J. H., et al. 1988, , 325, 74
- Santini, P., Ferguson, H. C., Fontana, A., et al. 2015, , 801, 97
- Santini, P., Rosario, D. J., Shao, L., et al. 2012, , 540, A109
- Sarazin, M., Melnick, J., Navarrete, J., & Lombardi, G. 2008, *The Messenger*, 132, 11
- Sargent, M. T., Daddi, E., Béthermin, M., et al. 2014, , 793, 19
- Schinnerer, E., Smolčić, V., Carilli, C. L., et al. 2007, , 172, 46
- Schlegel, D. J., Finkbeiner, D. P., & Davis, M. 1998, , 500, 525
- Schmidt, M. 1959, , 129, 243
- Schmidt, M. 1963, , 197, 1040
- Scholtz, J., Alexander, D. M., Harrison, C. M., et al. 2018, , 475, 1288
- Schreiber, C., Pannella, M., Elbaz, D., et al. 2015, , 575, A74
- Schulze, A., Silverman, J. D., Kashino, D., et al. 2018, , 239, 22
- Scoville, N., Lee, N., Vanden Bout, P., et al. 2017, , 837, 150
- Scoville, N., Sheth, K., Aussel, H., et al. 2016, , 820, 83
- Seyfert, C. K. 1943, , 97, 28
- Shakura, N. I. & Sunyaev, R. A. 1973, , 24, 337

- Shangguan, J. & Ho, L. C. 2019, , 873, 90
- Shen, Y., Greene, J. E., Ho, L. C., et al. 2015, , 805, 96
- Shibuya, T., Ouchi, M., & Harikane, Y. 2015, , 219, 15
- Silk, J. & Rees, M. J. 1998, , 331, L1
- Simm, T., Salvato, M., Saglia, R., et al. 2016, , 585, A129
- Simpson, J. M., Swinbank, A. M., Smail, I., et al. 2014, , 788, 125
- Smith, R. W. 2008, *Journal for the History of Astronomy*, 39, 91
- Smolčić, V., Novak, M., Bondi, M., et al. 2017, , 602, A1
- Solomon, P. M. & Vanden Bout, P. A. 2005, , 43, 677
- Somerville, R. S., Hopkins, P. F., Cox, T. J., Robertson, B. E., & Hernquist, L. 2008, , 391, 481
- Sorini, D., Oñorbe, J., Hennawi, J. F., & Lukić, Z. 2018, , 859, 125
- Speagle, J. S., Steinhardt, C. L., Capak, P. L., & Silverman, J. D. 2014, , 214, 15
- Spilker, J. S., Bezanson, R., Marrone, D. P., et al. 2016, , 832, 19
- Springel, V., Di Matteo, T., & Hernquist, L. 2005, , 361, 776
- Stalevski, M., Fritz, J., Baes, M., Nakos, T., & Popović, L. Č. 2012, , 420, 2756
- Stalevski, M., Ricci, C., Ueda, Y., et al. 2016, , 458, 2288
- Stanley, F., Harrison, C. M., Alexander, D. M., et al. 2015, , 453, 591
- Stark, A. A., Gammie, C. F., Wilson, R. W., et al. 1992, , 79, 77
- Stevans, M. L., Shull, J. M., Danforth, C. W., & Tilton, E. M. 2014, , 794, 75
- Strateva, I., Ivezić, Ž., Knapp, G. R., et al. 2001, , 122, 1861
- Suh, H., Civano, F., Hasinger, G., et al. 2017, , 841, 102
- Swinbank, A. M., Smail, I., Chapman, S. C., et al. 2010, , 405, 234
- Symeonidis, M., Giblin, B. M., Page, M. J., et al. 2016, , 459, 257
- Szokoly, G. P., Bergeron, J., Hasinger, G., et al. 2004, , 155, 271
- Tacconi, L. J., Genzel, R., Saintonge, A., et al. 2018, , 853, 179

- Tacconi, L. J., Genzel, R., Smail, I., et al. 2008, , 680, 246
- Tacconi, L. J., Neri, R., Genzel, R., et al. 2013, , 768, 74
- Tadaki, K.-i., Genzel, R., Kodama, T., et al. 2017a, , 834, 135
- Tadaki, K.-i., Kodama, T., Nelson, E. J., et al. 2017b, , 841, L25
- Tadhunter, C. N., Fosbury, R. A. E., & Quinn, P. J. 1989, , 240, 225
- Talia, M., Pozzi, F., Vallini, L., et al. 2018, , 476, 3956
- Telfer, R. C., Zheng, W., Kriss, G. A., & Davidsen, A. F. 2002, , 565, 773
- Toft, S., Smolčić, V., Magnelli, B., et al. 2014, , 782, 68
- Tombesi, F., Meléndez, M., Veilleux, S., et al. 2015, , 519, 436
- Tombesi, F., Sambruna, R. M., Reeves, J. N., et al. 2010, , 719, 700
- Tozzi, P., Gilli, R., Mainieri, V., et al. 2006, , 451, 457
- Trakhtenbrot, B. & Netzer, H. 2012, , 427, 3081
- Trebitsch, M., Volonteri, M., & Dubois, Y. 2019, arXiv e-prints, arXiv:1901.01261
- Tristram, K. R. W., Meisenheimer, K., Jaffe, W., et al. 2007, , 474, 837
- Trujillo, I., Conselice, C. J., Bundy, K., et al. 2007, , 382, 109
- Ueda, Y., Akiyama, M., Hasinger, G., Miyaji, T., & Watson, M. G. 2014, , 786, 104
- Urry, C. M. & Padovani, P. 1995, , 107, 803
- van der Wel, A., Bell, E. F., Häussler, B., et al. 2012, , 203, 24
- van der Wel, A., Franx, M., van Dokkum, P. G., et al. 2014, , 788, 28
- Vayner, A., Wright, S. A., Murray, N., et al. 2017, , 851, 126
- Veilleux, S., Bolatto, A., Tombesi, F., et al. 2017, , 843, 18
- Venemans, B., Decarli, R., Walter, F., et al. 2018, ArXiv e-prints
- Vestergaard, M. & Peterson, B. M. 2006, , 641, 689
- Vietri, G., Piconcelli, E., Bischetti, M., et al. 2018, ArXiv e-prints
- Vignali, C., Piconcelli, E., Lanzuisi, G., et al. 2011, , 416, 2068
- Vito, F., Brandt, W. N., Yang, G., et al. 2018, , 473, 2378

- Vito, F., Gilli, R., Vignali, C., et al. 2014, , 445, 3557
- Vito, F., Vignali, C., Gilli, R., et al. 2013, , 428, 354
- Wachter, K., Leach, R., & Kellogg, E. 1979, , 230, 274
- Wang, R., Wagg, J., Carilli, C. L., et al. 2013a, , 773, 44
- Wang, S. X., Brandt, W. N., Luo, B., et al. 2013b, , 778, 179
- Weedman, D., Sargsyan, L., Lebouteiller, V., Houck, J., & Barry, D. 2012, , 761, 184
- Wei, A., Downes, D., Neri, R., et al. 2007, , 467, 955
- Whitaker, K. E., van Dokkum, P. G., Brammer, G., & Franx, M. 2012, , 754, L29
- Woo, J.-H., Bae, H.-J., Son, D., & Karouzos, M. 2016, , 817, 108
- Wylezalek, D. & Morganti, R. 2018, *Nature Astronomy*, 2, 181
- Xue, Y. Q., Luo, B., Brandt, W. N., et al. 2016, , 224, 15
- Xue, Y. Q., Luo, B., Brandt, W. N., et al. 2011, , 195, 10
- Yaqoob, T. 1997, , 479, 184
- Yun, M. S., Reddy, N. A., & Condon, J. J. 2001, , 554, 803